Numerical Simulations of Planetesimal Formation

Numerical Simulations of Planetesimal Formation

By

JOSEF J. RUCSKA, M.SC.

A Thesis Submitted to the School of Graduate Studies in the Partial Fulfillment of the Requirements for the Degree of Doctor of Philosophy in Physics
McMaster University

Descriptive Note

DOCTOR OF PHILOSOPHY (PHYSICS and ASTRONOMY) 2022

McMaster University (Physics and Astronomy) Hamilton, Ontario

AUTHOR: Josef J. Rucska , M.Sc. (McMaster University)

SUPERVISOR: Dr. James Wadsley

NUMBER OF PAGES: xxi, 208

Abstract

A long-standing question in planet formation is the origin of planetesimals, the kilometre-sized precursors to protoplanets. Asteroids and distant Kuiper Belt objects are believed to be remnant planetesimals from the beginnings of our Solar system. A leading mechanism for explaining the formation of these bodies directly from centimetre-sized dust pebbles is the streaming instability (SI). Using high resolution numerical simulations of protoplanetary discs, we probe the behavior of the non-linear SI and planetesimal formation in previously unexplored configurations. Small variations in initial state of the disc can lead to different macroscopic outcomes such as the total mass converted to planetesimals, or the distribution of planetesimal masses. These properties can vary considerably within large simulations, or across smaller simulations re-run with different initial perturbations. However, there is a similar spread in outcomes between multiple smaller simulations and between smaller sub-regions in larger simulations. In small simulations, filaments preferentially form rings while in larger simulations they are truncated. Larger domains permit dynamics on length scales inaccessible to the smaller domains. However, the overall mass concentrated in filaments across various length scales is consistent in all simulations. Small simulations in our suite struggle to resolve dynamics at the natural filament separation length scale, which restricts the possible filament configurations in these simulations. We also model discs with multiple grain species, sampling a size distribution predicted from theories of grain coagulation and fragmentation. The smallest grains do not participate in the formation of planetesimals or filaments, even while they co-exist with dust that readily forms such dense features. For both single-grain and multiple-grain models, we show that the clumping of dust into dense features results in saturated thermal emission, requiring an observational mass correction factor that can be as large as 20-80%. Finally, we present preliminary work showing that the critical dust-to-gas mass ratio required to trigger the SI can vary between 3D and 2D simulations.

Declaration of Authorship

Chapters 2, 3, 4 and 5 present original research written by myself, Josef Rucska. I ran the simulations studied on supercomputing clusters, performed the analyses of the simulation data, and created the figures presented. In all work, my supervisor Prof. James Wadsley provided guidance on the direction and objectives of the research, in the interpretation of the results, and in the writing and editing process of the manuscripts.

Acknowledgements

I would like to thank my supervisor Dr. James Wadsley for his support and guidance during my time as a graduate student at McMaster. I would also like to thank my committee members Dr. Alison Sills and Dr. Ralph Pudritz. I have learned so much about how to effectively conduct research and about a wide assortment of fields in astrophysics. I could not have accomplished this work without their help.

Thank you to all the friends I have made at McMaster over the years. Many of you have moved on to the next stage of your lives already—unfortunately, unceremoniously for some, because of the pandemic. I know I will look back at this phase of my life fondly because of the memories we made together, at house parties, on the softball team, to the micro-interactions so dearly missed when we had to work from home. I cherish all of it. I could not have found a better set of roommates to share these experiences with. I will never forget the first lockdown where we turned that house of questionable structural integrity into a home.

Thank you to my girlfriend, Nat, for her bottomless patience and support this summer while writing this thesis. It was a bumpy ride at times, and you were there to pick me up through the worst of it. I couldn't have gotten across the finish line without you.

Lastly, to Dad, Mum, and my brother Ben, for their infinite, unwavering support in everything I do. I am so lucky to have you all in my life. When I was fifteen, my parents bought me a 10" backyard telescope for Christmas. The sky at the cottage is covered with stars when the weather is clear. As that eager, sparkly-eyed teen, night after night, by the fire, I'd regale them with anything I could tell them about the stars, and how deep the mysteries of space seemed to me. The first time I saw Saturn through that telescope changed my life. I had never seen something so majestic. I had to know its

story. I think it was that moment that kicked me onto a path that lead, several years later, towards graduate school.

I don't know what is next for me, but I know, Mum, Dad, Ben, that you will be there for me, and for that I am eternally grateful.

“Every quest takes place in both the sphere of the actual, which is what maps reveal to us, and in the sphere of the symbolic, for which the only maps are the unseen ones in our heads.”

— Salman Rushdie, *Quichotte*

Contents

List of Figures

List of Tables

Chapter 1

Introduction

The study of astronomy is, at least in part, the study of origins. Where did we come from? What process created the Sun and the stars, the Moon, the Earth, or the atoms that make up everything on our planet, both living and not? In this thesis, our target is planets. The neighbouring planets in the Solar System—Jupiter, Saturn, and the rest—are easily identifiable by their slow, predictable march in front of the background stars. Hellenic observers named this class of objects for their wandering behaviour, and to this day, in western cultures, the individuals bear the Roman names of deities from their mythology. Planets are wondrous objects for backyard and academic astronomers alike, and the story of where they come from is fraught with surprise and mystery.

But before there are planets, there must come stars. The birthplace of stars is the interstellar medium (ISM): the gas, dust and radiation that pervades the space between stars and star clusters in a galaxy. The formation of stars begins with the gravitational collapse of dense clouds of ISM material (see Pineda et al. 2022, for a review). Observations of young stellar objects undergoing this process display a significant amount of radiation in the infrared spectrum (IR) and at longer millimetre wavelengths, more than is expected from the star alone. This IR/mm excess can be explained by the presence of a substantial dust structure surrounding the star, absorbing optical light and re-emitting it at longer wavelengths (e.g. Lada & Wilking 1984; Adams et al. 1987; Greene et al. 1994; Calvet et al. 1994). Note, however, that the dust represents only a small fraction of the mass of the system. The ratio of dust mass to gas mass in the ISM is around 1% (Bohlin et al. 1978). The diversity of IR flux and spectral indices seen in young stellar objects invites a classification scheme that describes how the circumstellar environment evolves from an enveloping shell to a disc that becomes progressively less pronounced until it is nonexistent (Lada 1987; Adams et al. 1987; Andre et al. 2000; Williams & Cieza 2011). The evolution of the cloud geometry towards a flattened disc results from the conservation of any angular momentum initially present in the pre-collapse cloud. Further evidence of the evolution of the young stellar environment are bursts of optical and X-ray photons associated with the accretion of gas onto the star (e.g Gullbring et al. 1997) Observations of these objects in optical light with the Hubble Space Telescope reveal dark, disc-shaped silhouettes against the background light of the star-forming nebulae (e.g. Bally et al. 2000; Smith et al. 2005). The dusty discs around young stars, which can span hundreds of AU in diameter, absorb optical radiation strongly, and are most easily seen when the disc is edge-on and obscuring the star at the centre of the disc.

These objects are referred to as protoplanetary discs, and it is within these structures—which are composed of the gas and dust once dispersed in the ISM—where planets are born. The typical lifetime of protoplanetary discs around young stars, seen in both accretion signatures (Hartmann et al. 1998) and IR/mm radiation (Haisch et al. 2001; Ribas et al. 2014) has been observed to be between 5-10 million years. For stars beyond that age, these signatures cease to exist, indicating the dispersal of the protostellar envelope, likely due to a combination of the accretion of material onto the star due to a turbulent viscosity, or dispersal of the upper gaseous disc atmosphere via magnetically driven winds (Pascucci et al. 2022; Manara et al. 2022). This places a stringent constraint on timescales for planet formation. It is just one of many recent observational breakthroughs that have challenged paradigms and invigorated the field of planet formation.

1.1 Planet Formation in the Modern Era

Over the last 10 years, the Kepler and K2 NASA space missions have revealed thousands of exoplanets orbiting nearby stars, expanding our conceptions of what is possible in planet formation. This has inspired follow up missions with ambitions such as the Transiting Exoplanet Survey Satellite (TESS), which promises to add thousands of entries to the exoplanet catalogue by surveying an area of the sky 400 times larger than the Kepler mission. In Figure 1.1, we present data on all confirmed exoplanets in the parameter space of orbital semi-major axis versus planet mass. These data are retrieved from the NASA exoplanet archive[1] and summarize the current findings from every technique in exoplanet discovery.

Each discovery method comes with individual biases and strengths. We will briefly describe them here, following Armitage (2020) Section 1.7, and associate each method with the locations of points in Figure 1.1. Planets that orbit far from their stars can be directly imaged at infrared wavelengths by telescopes with high resolving power and the assistance of a coronagraph, an instrument which blocks the light from the star at the centre of planetary system (see mauve circles at $>$ 1000 Earth Masses, M_E, with a semi-major axis of $a \gtrsim 30$ AU). The radial velocity method tracks the gravitational influence of close-in, massive planets, which can induce a periodic "wobble" in stellar motions. The component of these motions along the line of sight—the radial velocity—is discernible in stellar spectra. This signal is most apparent for planets that are massive, $\gtrsim 100 M_E$ or on orbits $\lesssim$1 AU (green circles). The same wobbling motions of the star can also be observed directly via astrometry, a technique which makes use of precise

[1] `https://exoplanetarchive.ipac.caltech.edu/`

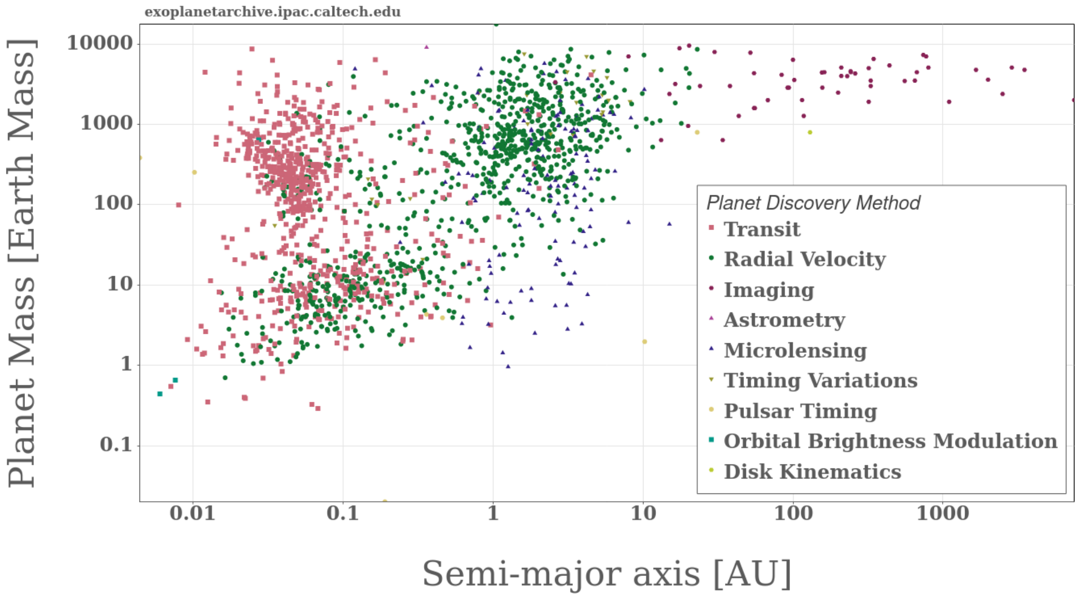

FIGURE 1.1: Known exoplanets in the Mass - semi-major axis (M-a) parameter space. Each data point is coloured by the method used to detect the planet. Error bars are not shown. Data retrieved on August 15, 2022 from the NASA Exoplanet Archive, which is operated by the California Institute of Technology, under contract with the National Aeronautics and Space Administration under the Exoplanet Exploration Program.

measurements of the position of stars on the sky (pink triangles). High spatial resolution is required to resolve the relatively short distances travelled by stars as they orbit the system centre of mass. Hence, to date this technique has not been as fruitful as the radial velocity method. Measurements of the line-of-sight stellar velocity directly with spectroscopic instrumentation are typically more accessible. The transit method, employed by Kepler/K2 and TESS, observes the periodic dimming of starlight due to the transit of an exoplanet across the line of sight (pink squares). Properties of the occulted starlight signal are useful in constraining the planet radius and properties of the planet atmosphere. Gravitational microlensing makes use of the gravitational focusing of background starlight by foreground planets. This technique requires somewhat serendipitous observations but is useful for detecting lower mass planets between 1-10 AU, where the other techniques are not sensitive (purple squares—note the two data points with Earth-like properties!). Further details on these detection techniques are available in a review by Fischer et al. (2014).

A compelling feature of Figure 1.1 is the separated clusters of data points, suggesting distinct categories of exoplanets. There are the so-called Hot Jupiters: planets greater than 100 Earth masses on very tight, $\lesssim 0.1$ AU orbits; gas giants on orbits between 1-3 AU; massive $> 1000 M_E$ giant planets on distant, > 100 AU orbits; and a group collectively known as super-Earths or sub-Neptunes, with masses between $3 - 20 M_E$ on orbits $\lesssim 1$ AU. Recall the transit technique can also reveal the planet radii, and within the super-Earth/sub-Neptunes, there is a distinct deficiency of planets with radii around $\sim$1.7 Earth radii (R_E) (Fulton et al. 2017; Fulton & Petigura 2018). As the name implies, this category hence represents two subgroups: super-Earths with radii $< 1.7 R_E$, which, based on calculations of the bulk density (assuming a sphere of uniform density), are believed to be terrestrial, rocky worlds; and sub-Neptunes[2] with radii $\sim 1.7 - 3.0 R_E$, which are believed to have rocky cores with varying amounts of ice, water, or gaseous

[2]The mass of Neptune is ~ 17.15 Earth masses and has a radius of $\sim$3.8 Earth radii (Data courtesy of D. Williams, online NSSDCA planetary fact sheets).

atmospheres. Whether these planets are—for example—worlds with substantial liquid oceans, or rocky planets with Hydrogen/Helium envelopes, is a topic of ongoing research (e.g. Zeng et al. 2019). Leading theories for the cause of the radius gap itself include the removal of lighter elements from gaseous atmospheres due to the radiation pressure from a bright, cooling rocky core (Ginzburg et al. 2018), or the photoevaporation of atmospheres from incident high-energy photons from the central star (Owen & Wu 2017).

Another interesting observation from Figure 1.1 is the relative dearth of Solar System analogues: Venus (0.72 AU, $0.82 M_E$), Earth (1 AU, 1 M_E), Mars (1.52 AU, $0.11 M_E$), Jupiter (5.2 AU, $318 M_E$), Saturn (9.6 AU, $95 M_E$), Neptune (30 AU, $17 M_E$) (Data courtesy of D. Williams, online NSSDCA planetary fact sheets). This may simply be because current observational facilities are not particularly sensitive to extrasolar objects at these masses and orbital distances. Yet, it is worthwhile to acknowledge the abundance of exoplanets unlike the Solar System planets, such as Hot Jupiters, extremely distant gas giants, and super-Earths or sub-Neptunes, which represent the most populous exoplanet category (Fulton & Petigura 2018). Further, before the landmark discovery of Mayor & Queloz (1995), for which the authors were awarded the 2019 Nobel Prize in Physics, the Solar System constituted the only known planets around sun-like stars. Early models of planet formation presumed the solar system architecture—e.g., with inner rocky planets, and outer gas and ice giants—was ordinary. A decade of exoplanet discoveries has determined the opposite.

This has lead to the ongoing refinement of planet formation models. It is believed that rocky planets form from vast populations of smaller, $\sim$km-sized objects (of which the asteroids are likely Solar System remnants) via gravitational interactions that drive collisions (Wetherill & Stewart 1989; Kokubo & Ida 1996; Pollack et al. 1996; Raymond et al. 2006; Wallace & Quinn 2019). The growth of rocky cores can also be driven by the rapid accretion of millimetre to centimetre-sized pebbles (Johansen & Lambrechts

2017). Once the core reaches 5-10 M_E or larger, the planet gravity can cause the rapid accretion of gaseous material from the protoplanetary disc onto the planet, creating gas giants (Perri & Cameron 1974; Pollack et al. 1996; Ayliffe & Bate 2012). The formation of the Hot Jupiters specifically could occur via multiple channels (Dawson & Johnson 2018): in-situ formation in the inner disk (given a large concentration of solids), the migration of the planet from intermediate disc radii, or the tidal evolution of high eccentricity orbits driven by gravitational interactions with other planets post disc dispersal. Migration could also cause the orbital evolution of smaller, super-Earth/sub-Neptunes, which could explain their close-in $\lesssim 1$ AU orbits (e.g. Alessi et al. 2020). The likely formation mechanism for the extremely massive, distant gas giants is via the direct collapse of outer disc material in massive protoplanetary discs with large radial extents (e.g. Mayer et al. 2004; Backus & Quinn 2016). In Section 1.2.4, we further discuss the growth of protoplanets into full planets, including the above processes.

1.1.1 Protoplanetary discs

New observational facilities have also revolutionized our conceptions of protoplanetary discs themselves. The Atacama Large Millimeter/submillimeter Array (ALMA) has provided high resolution images of the disc gas as well as the millimetre sized dust in the orbital midplane, commonly referred to as pebbles in the literature. The first object observed with this instrument was HL Tau (ALMA Partnership et al. 2015). Planets are expected to form within the disc midplane, thus observations of the millimetre dust provides an invaluable probe into the ongoing planet formation process. In Figure 1.2, we show images from a survey of protoplanetary discs that display a stunning variety of rings, gaps, spiral-like features, and other asymmetries in the dust/pebble disc. Similar features have since been found in many other objects (e.g. Pérez et al. 2016; Cazzoletti et al. 2018; Macías et al. 2019; Maucó et al. 2021; van der Marel et al. 2021). Embedded protoplanets within the disc are a proposed explanation for these gaps and spirals (e.g.

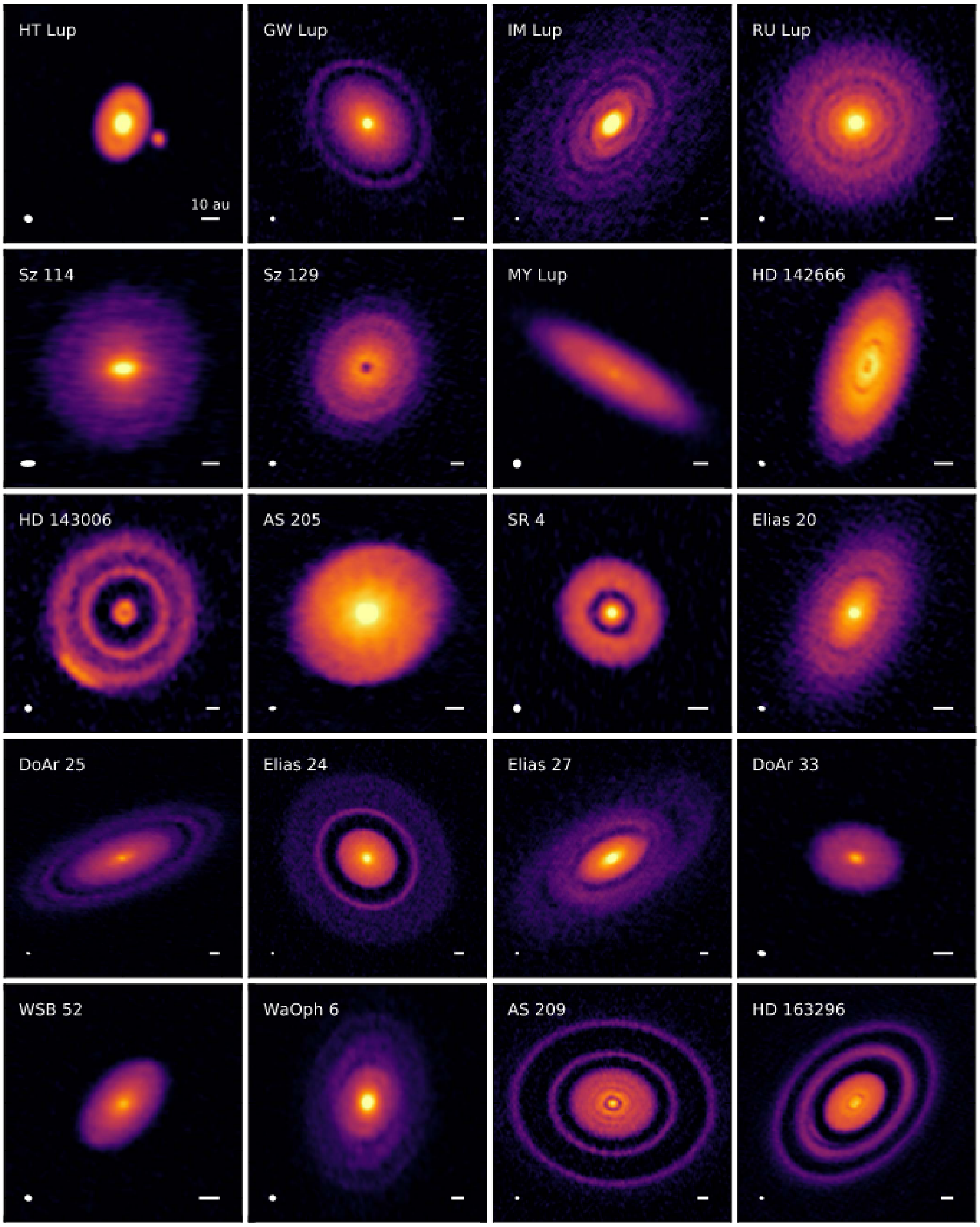

FIGURE 1.2: 1.25 mm continuum emission in protoplanetary discs from the Disk Substructures at High Angular Resolution Project (DSHARP) survey, data recorded with ALMA. The scale bar in the bottom right of each panel represents 10 AU. Reproduced with permission from Andrews, S., Huang, J., Pérez, L. et al. (2018), ApJL **869**, L41. DOI:10.3847/2041-8213/aaf741, Figure 3. ©AAS.

Dipierro et al. 2015; Dong et al. 2015; Pinilla et al. 2016; Yang & Zhu 2020; Speedie et al. 2022a), though alternative explanations exist, as we discuss in Section 1.2.2.

Recent studies have shown that the majority of protoplanetary discs do not display rings or gaps in the dust pebbles. Van der Marel & Mulders (2021) combine several surveys to show that most discs are compact and unlike the $\sim$100 AU discs like HL Tau (ALMA Partnership et al. 2015). The DSHARP survey (Andrews et al. 2018) contains both large discs with rings and gaps (e.g. AS 209, HD 163296 in Fig. 1.2) as well as compact discs (DoAr 33, WSB 52 in Fig. 1.2). The disc sample in van der Marel & Mulders (2021) includes hundreds of discs from several star forming regions, and they find rings and gaps beyond 25 AU primarily appear in only the most massive discs (greater than 10 Earth masses) and around stars more massive than a solar mass. (It is worth noting that for most discs thus far, ALMA observations have typically been limited to a resolution of $\sim$20 AU, so it is possible that compact discs have structure that is unresolved. The closest objects are resolvable at $\lesssim$ 5 AU.) Interestingly, exoplanet observations also show an increased number of giant planets around massive stars (Johnson et al. 2010). Thus, van der Marel & Mulders (2021) suggest a simple explanation for their observed trends: massive disks around larger stars are more capable of forming giant planets, which leads to the gaps and rings seen in a minority of the protoplanetary disc population. The less massive, more common compact discs ($<$40 AU) can be explained by the inward radial drift of dust in a disc unperturbed by massive planets (See Section 1.2.2 for further discussion).

The SPHERE instrument at the Very Large Telescope is capable of incredible spatial resolution at near-IR wavelengths which reveals the distribution of smaller $\sim$µm grains in the protoplanetary disc. We present images from a recent survey of young stellar objects from this facility in Figure 1.3. These images record the light of the central star scattering off micron-sized dust grains. These observations and others (e.g. Muto et al.

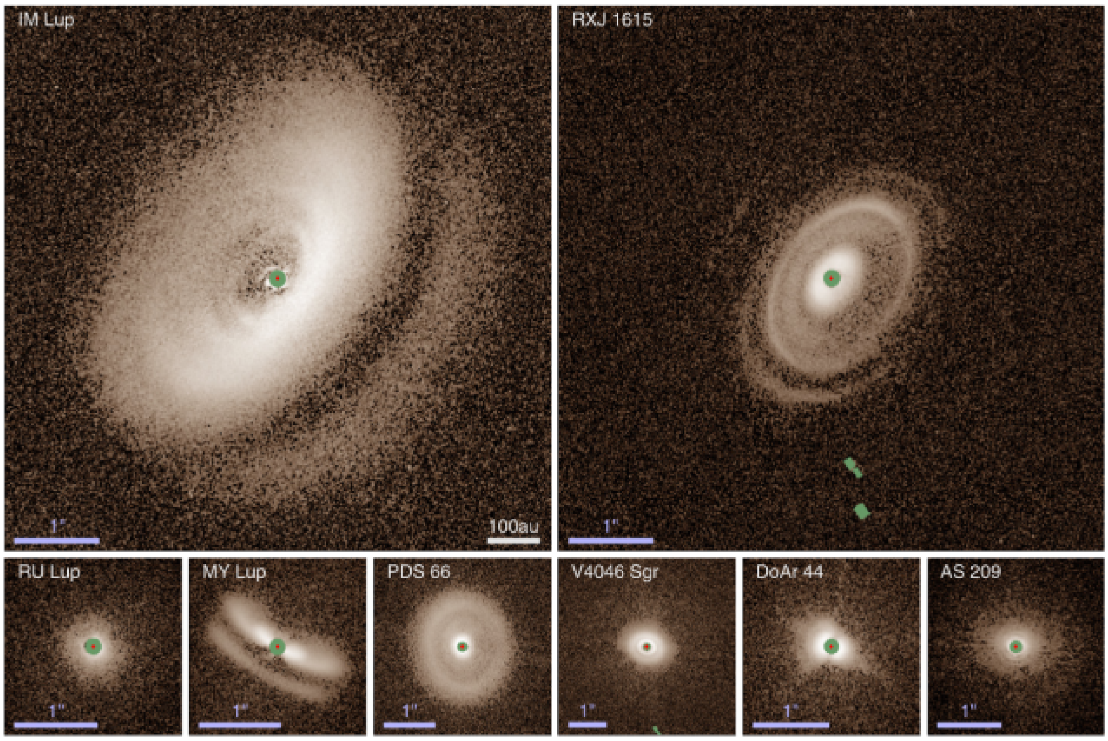

FIGURE 1.3: H-band (1.65 µm, infrared) images of various young stellar objects. The white 100 AU scale bar applies for all panels. Reproduced with permission from Avenhaus, H., Quanz, S. P., Garufi, A. et al. (2018), ApJ **863**, 44. DOI:10.3847/1538-4357/aab846, Figure 1. ©AAS.

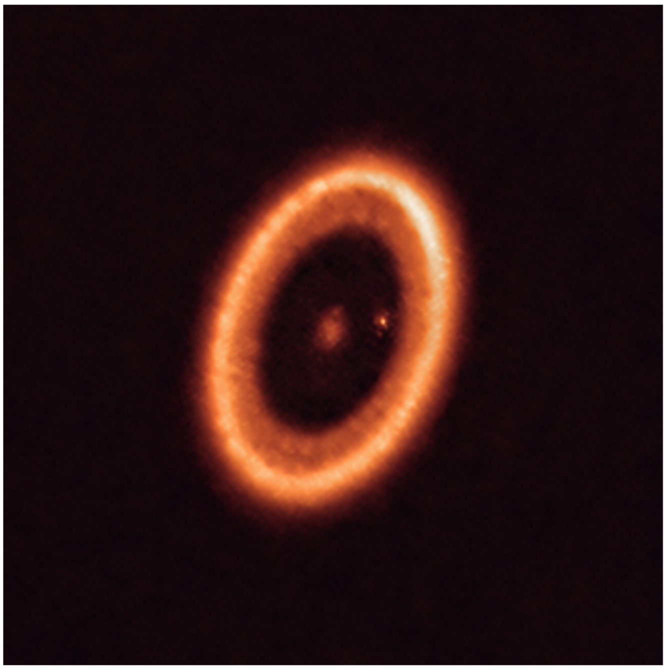

FIGURE 1.4: The PDS 70 planet forming system at 855 μm. Image credit: ALMA (ESO/NAOJ/NRAO)/Benisty et al. Reproduced under Creative Commons license (CC BY 4.0).

2012; Benisty et al. 2015; Benisty et al. 2017; Avenhaus et al. 2018) reveal a rich variety of discs, both in size (80 − > 400 AU) and structure. Some discs reveal flared profiles and shadows, a sign that the smaller grains are vertically extended throughout those discs, unlike the millimetre dust in the midplane seen by ALMA (See Benisty et al. 2022 for a review of the observational techniques and discoveries at these wavelengths.)

Most disc observations offer indirect constraints, as planets are difficult to detect directly. The system PDS 70 is an exciting and rare exception. Multiple observations at various wavelengths have revealed two planetary companions orbiting a young star in the inner cavity of protoplanetary disc (Keppler et al. 2018; Müller et al. 2018; Haffert et al. 2019), and even a circumplanetary disc around one of the companions (Benisty et al. 2021). This system offers a rare glimpse into active planet-disc interactions in nature. In Figure 1.4, we present an image of this system.

There are multiple components to models of protoplanetary disc structure, in how the gas mass, dust mass, and temperature vary with radius and vertical position away from the midplane. A widely used result for discs evolving via viscous processes from Lynden-Bell & Pringle (1974) gives an initial gaseous surface density profile described by a power law, $\Sigma_g(r) \propto (r/r_c)^{-1}$, combined with an exponential cut-off at a characteristic radius r_c. Constraints on the total disc mass have come from observations of gaseous molecular emission lines (e.g. Long et al. 2017; Kama et al. 2020), or from a reconstruction of the protosolar disc by considering the gas profile needed to produce the planets in the solar system (minimum mass solar nebula, Weidenschilling 1977b; Hayashi 1981).

Estimates of the dust mass in observed disc populations range from 1-100 Earth masses, depending on the age of the disc (see Drążkowska et al. 2022, Fig. 2). The interstellar medium predicts a dust-to-gas mass ratio of ~0.01 (Bohlin et al. 1978), but estimates of this ratio from observations of protoplanetary discs can be as high as 0.1 (Long et al. 2017; Kama et al. 2020). However, there are currently large uncertainties in these estimates, especially in measurements based on carbon monoxide (CO) emission lines, due in part to difficulties in constraining the amount of CO that exists in the gaseous versus solid (ice) phase (Long et al. 2017).

In planet formation literature, the dust content in the disc is often characterized as the dust-to-gas surface density ratio. This quantity differs from the common definition of metallicity for gaseous nebula, which is usually defined as the mass ratio of all elements heavier than helium to the total gas mass (which is nearly 99% hydrogen and helium). From measurements of the Solar photosphere spectra, meteoritic chemical abundances, and models of heavy element settling in the interior of the Sun, ~1.5% of the protosolar nebula mass was potentially solid material (Lodders 2003). Roughly 1/3 was rocky material, with the rest being gas species that could have condensed in the outer Solar System, where low temperatures permit the freeze-out of volatile gases onto solid rock grains. Thus, in the outer Solar System disc, the solids-to-gas mass ratio was ≈ 0.015, and in the inner disc this ratio was ≈ 0.005. Many processes in planet formation are driven by the amount of solid material locally. A leading mechanism for the formation of planetesimals (which is the focus of this thesis, introduced in Section 1.3) generally requires a super-solar solids-to-gas mass ratio initially. Hence, a different mechanism may need to create regions of concentrated dust before planetesimal formation can occur. We discuss candidate processes for dust concentration in Section 1.2.2.

The temperature within a protoplanetary disc can vary between the vertical surface layer and the midplane. The vertical surface of the disc is irradiated by photons from the central star, which is absorbed by a layer of small dust grains suspended in the upper disc atmosphere. This layer then reradiates about half of this energy into empty space, and the other half towards the interior of the disc, driving gas heating and consequent vertical flaring of the disc (Chiang & Goldreich 1997). In observed discs, flared profiles are often seen in the small grains which are tightly aerodynamically coupled to the gas and hence trace gas structure (Figure 1.3). Hence, models of protoplanetary disc temperature often describe the disc with three components (Armitage 2020): a hot, low density upper atmosphere, a warm surface layer where the gas can be substantially hotter than the dust, and a relatively cool midplane layer where the dust and gas are in thermal equilibrium. A popular analytical model (Chiang & Goldreich 1997) predicts a cool interior temperature profile (applicable to dust and gas) of $T = 150\ (r/\mathrm{AU})^{-3/7}$ K and a warm surface layer with $T_{\mathrm{dust}} = 550\ (r/\mathrm{AU})^{-2/7}$ K, with gas disc photosphere height profile that increases with radius (i.e. flared), given by $h_p/r = 0.17\ (r/\mathrm{AU})^{2/7}$.

Protoplanetary discs are not static structures, however. Observations of the accretion of material onto the star (Hartmann et al. 1998) and the decrease in IR/mm excess radiation with age (Haisch et al. 2001; Ribas et al. 2014) confirm that discs evolve and have limited lifetimes. A long-standing question in theory of protoplanetary discs and accretion discs more broadly is what process causes material to lose angular momentum and cause accretion. A commonly invoked mechanism is the macroscopic mixing of disc material due to turbulent motions, which can result in an effective turbulent viscosity. As this process is generally difficult to model in detail. Shakura & Sunyaev (1973) provide a simple parameterization for this viscosity. Assuming motions occur at velocities no larger than the sound speed (c_s), with a typical length scale given by the gas scale height (H_g), the viscosity ν can be crudely modelled as,

$$\nu = \alpha_t c_s H_g, \tag{1.1}$$

where α_t is a dimensionless scaling parameter. This so-called alpha-disc model is ubiquitous in the field of planet formation. It is used widely to estimate angular momentum transport, accretion, and local turbulent velocities, but it is not expected to be correct in detail. In protoplanetary discs, recent observations of gas turbulence and analyses of dust ring widths suggest $\alpha_t \approx 1 \times 10^{-4}$ to 1×10^{-3} for discs in nature (Pinte et al. 2016; Flaherty et al. 2017; Teague et al. 2018b; Dullemond et al. 2018; Trapman et al. 2020). This value is generally considered to represent weak turbulence in the context of the models that depend on it, such as the local growth and fragmentation of dust grains due to collisions (e.g. Birnstiel et al. 2011), global dust evolution in discs (Drążkowska et al. 2016), and the migration of planets (Speedie et al. 2022b).

The physical source of this turbulent viscosity remains an ongoing topic of research. In the inner $\lesssim 0.1$ AU, gas temperatures $\gtrsim 1000$ K can thermally ionize the gas, leading to the development of turbulence via the magnetorotational instability (MRI; Balbus & Hawley 1991) at levels of $\alpha_t \sim 0.01$ (Simon et al. 2012) that are consistent with observed accretion rates of the disc material at the inner radial edge (Hartmann et al. 1998). Beyond this point, out to $\gtrsim 50$ AU, the midplane gas is not expected to be strongly ionized (Turner & Drake 2009), supported by observations of ion abundances in the disc TW Hya (Cleeves et al. 2015). This leads to a "dead zone" of low ionization fraction where magnetic fields can only interact with the gas indirectly through non-ideal effects of magnetohydrodynamics (MHD). Models of MRI turbulence in the regime of non-ideal MHD leads to predictions for $\alpha_t \sim 0.01$ (Simon et al. 2013; Simon et al. 2015), which is slightly too high for the aforementioned observed values, suggesting another mechanism drives midplane turbulence in the midplane disc region between 0.1-50 AU that is applicable to planet formation. Candidate large scale hydrodynamic instabilities include the vertical shear instability, convective overstability, or the zombie vortex instability (see Lyra & Umurhan 2019, for a review).

In the proceeding section, we will outline the full growth of dust in protoplanetary discs, from ∼µm to millimetre sized grains, to asteroid-sized planetesimals (which are the focus of this thesis), to protoplanets, and finally how these rocky cores evolve into the rich diversity of exoplanets seen in the Solar neighbourhood.

1.2 The Stages of Growth in Planet Formation

In protoplanetary discs, the journey of planet formation begins with micron-sized dust aggregates and ends with objects that are over 1000 kilometres in radius, spanning an incredible 12 orders of magnitude in size and over 30 orders of magnitude in mass. This growth process is best subdivided into distinct regimes, each a full sub-field of study on their own. In this section we will discuss the research devoted to each stage.

1.2.1 Micrometre-sized Grains

Dust pervades the interstellar medium (ISM), the baryonic material between stars. By mass, the ISM is almost entirely gas: approximately 75% in hydrogen, in atomic, ionized, and molecular forms, ∼23% in helium, and just a trace few percent of the material is in atoms heaver that helium, which includes the solid material referred to as dust.

Observations of attenuated/reddened starlight, the polarization of starlight, and infrared thermal emission from these dust grains have provided constraints on the properties of the ISM dust. Generally speaking, models agree that this dust is made up of a combination of silicates, carbonaceous/graphite-based grains, and polycyclic aromatic hydrocarbons—planar molecules consisting of hexagonal carbon rings. The size of these grains ranges from about 0.001 micrometre to 1 micrometre (see Ch. 21-23 of Draine 2011).

Within the protoplanetary disc environment, micron-sized dust grains (as seen in Figure 1.3) will collide and stick together due to electrostatic forces (Blum & Wurm 2008). At these sizes, the dominant influence on the relative velocity in collisions is Brownian motion (Birnstiel et al. 2011; Birnstiel et al. 2016). Beyond micrometres, local turbulent motions in the gas become increasingly important, increasing the relative velocity between the grains, yet still driving the net growth of the grains to larger objects. A summary of the various sources of relative velocity between dust objects in protoplanetary discs is provided in Figure 1.5. Processes such as relative radial and azimuthal drift become important for dust objects near centimetre sizes, and further considerations regarding the material strength of the dust can determine whether the centimetre-sized dust will stick together or fragment as a result of collisions. We will discuss these ideas further at the end of the Section 1.2.2.

It is widely believed that the growth of micron-sized ISM dust grains to $\sim$centimetre sizes is efficient. Once the disc is established from the protostellar cloud, the central gravity of the forming star will pull dust to the midplane. During this process, the different settling rates of grains of slightly different sizes can drive the growth of micron-sized grains to centimetre sizes in less than 1000 years (Dullemond & Dominik 2005). Recent observations of protostellar envelopes (Galametz et al. 2019) suggests that grain growth to millimetre sizes could begin even in the pre-disc phase of star formation.

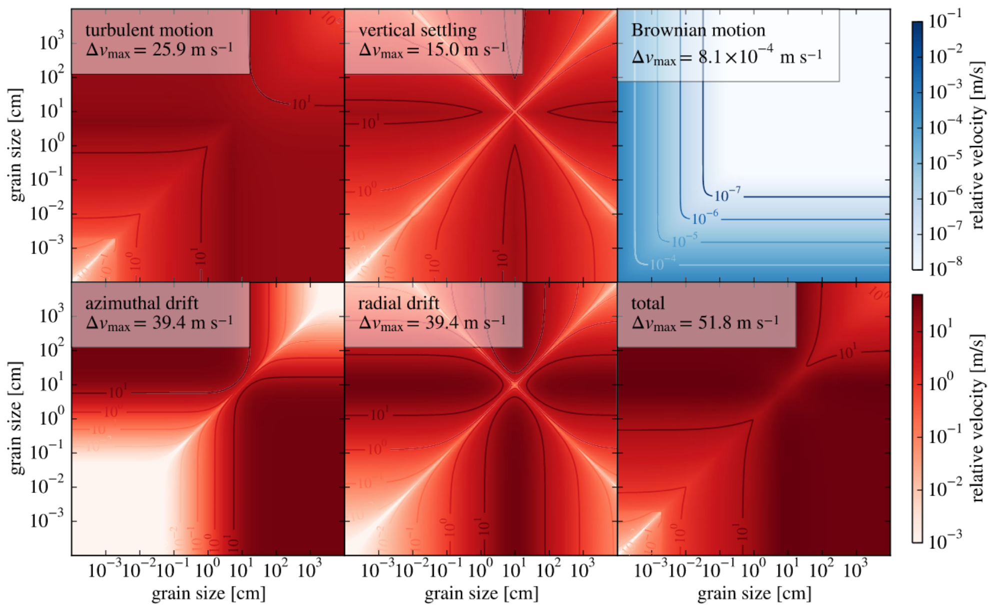

FIGURE 1.5: A summary of contributions to the relative velocities between colliding dust grains in protoplanetary discs. Each axis represents the size of one of the objects in the collision. Reproduced under Creative Commons license (CC BY 4.0) from Birnstiel, T., Fang, M. & Johansen, A., 2016, Space Sci Rev **205**, 41–75. DOI:10.1007/s11214-016-0256-1, Figure 1.

Further, as seen in Figure 1.2, there is a wealth of protoplanetary disc observations revealing significant dust mass near millimetre sizes.

1.2.2 Millimetre-sized Pebbles

The images in Figure 1.2 exemplify the diversity of structure—rings, gaps, asymmetries—seen in the millimetre-sized dust in protoplanetary discs. Many other observations with ALMA see similar features (e.g. van der Marel et al. 2015; Cazzoletti et al. 2018; Ansdell et al. 2018; van der Marel et al. 2021). As mentioned previously, embedded planets provide a plausible explanation for the rings, but alternate explanations exist. In the outer regions of discs, even with weak levels of magnetization in the gas, the presence of magnetic fields can create a circumferential gas pressure maximum (Bai 2015; Béthune et al. 2016), in which the dust can concentrate and form a ring (Riols & Lesur 2018). Also, at certain radii, the temperature in the gas drops below the condensation point for trace volatile chemical species such as CO and NH_3, and gases freeze-out onto the dust grains. These condensation fronts, also called ice lines, represent a steep change in the physical structure of the dust which affects the outcomes of collisions and can cause local radial concentrations of dust (Zhang et al. 2015; Okuzumi et al. 2016). In the outer regions of discs, where the gas density is lower, the dust layer midplane can be unstable to slow, secular gravitational instability that can lead to the formation of rings (Youdin 2011; Tominaga et al. 2018; Tominaga et al. 2020).

Pebble-sized dust is also subject to radial drift, which is a natural consequence of the headwind all solid material feels as it orbits within the gaseous component of protoplanetary discs. The gas is subject to hydrodynamic pressure, and since the gas surface density decreases with radius (Weidenschilling 1977b), there is a radially-outward pressure force that results in a sub-Keplerian orbital speed for the gas. The dust feels no such pressure directly, and thus attempts to orbit at the Keplerian speed, resulting in a headwind that removes angular momentum from the dust and causes inward orbital drift (Weidenschilling 1977a; Nakagawa et al. 1986). This radial drift effect is an essential component of models of dust evolution in protoplanetary discs (e.g Brauer et al. 2008; Birnstiel et al. 2012). It also offers a simple explanation for observed compact dust discs, which in some surveys have approximately half the radius of their associated gas disc (Ansdell et al. 2018).

This radial drift also contributes to constraints on the growth of solid material beyond centimetre sizes. The magnitude of the effects of radial drift—like any process rooted in aerodynamic drag—depends on the physical size of the solids that interact with the fluid. The small, micron-sized ISM dust in the protostellar environment feels strong drag forces relative to their mass, and are hence tightly coupled to the gas motions, which do not involve significant radial motions. Millimetre-sized pebbles are more susceptible to drift, with characteristic timescales for falling into the central star $\gtrsim$100,000 years.

However, at metre sizes drift is maximally efficient, and can remove these objects from the disc in less than 1000 years (Weidenschilling 1977a). This timescale is much too short for simple growth pathways such as collisions.

Further, collisional outcomes based on the relative velocities between objects at that size (Figure 1.5) have been shown to be primarily destructive under the conditions expected in the midplane of protoplanetary discs (Güttler et al. 2010; Zsom et al. 2010; Windmark et al. 2012). The material strength of the pebbles is not strong enough to resist fragmentation, or erosion, which results in a net decrease in the size of colliding objects. These results have largely come from laboratory experiments, and recent work is reviewed in Blum (2018). In Figure 1.6, we present their summary of collisional outcomes between two objects of varying sizes. We see that beyond $\sim$10 centimetres in size, collisions generally do not result in net growth.

The results of the combined collisional and radial drift barriers is a dust grain size distribution that peaks (or at least has a maximum size) near $\sim$ 1cm in the inner disc ($<$ 10 AU) and near $\sim$ 1mm in the outer disc (Birnstiel et al. 2012, see Fig. 4 of Birnstiel et al. 2016). In inner disc, regions grain sizes are limited by efficient fragmentation and in the outer regions by efficient radial drift. Locally, within fragmentation limited regions, an equilibrium between growth and fragmentation is achieved such that most of the dust mass is in the largest $\gtrsim$mm sizes.

Together, the collisional growth barrier and the radial drift barrier present a serious impediment to the continued growth of solids towards planetary sizes. It is believed that some process must efficiently and rapidly produce kilometre-sized objects (planetesimals) directly from millimetre/centimetre sized pebbles. Kataoka et al. (2013) show that fluffy, icy solid aggregates can avoid the radial drift barrier and form icy planetesimals. There have been many studies on the sorting of dust from turbulent motions due to the difference in drag forces at different grain sizes that could result in local concentrations

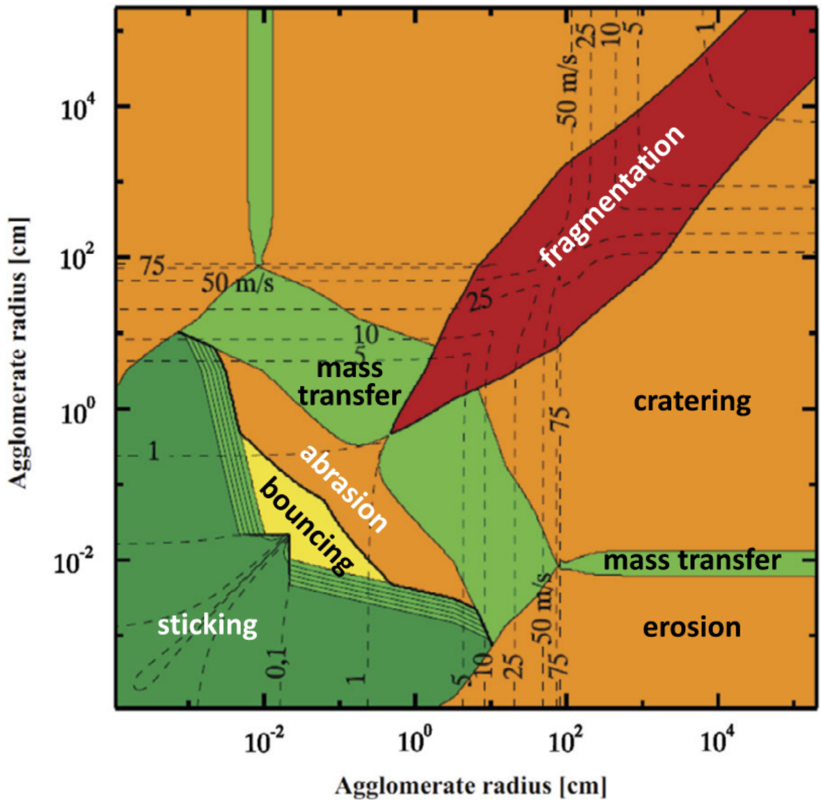

FIGURE 1.6: Collisional outcomes between two solid objects/agglomerates of different sizes. The axes are the same as in Figure 1.5, and each represent the size of one of the objects in the collision. The Reproduced with permission from Blum, J., 2018, Space Sci Rev **214**, 52. DOI:10.1007/s11214-018-0486-5, Figure 1.

leading to the formation of planetesimals (e.g. Cuzzi et al. 2001; Cuzzi et al. 2010; Hartlep & Cuzzi 2020). The concentration of dust into rings from the aforementioned mechanisms (magnetic fields: Riols & Lesur 2018, large scale gravitational instabilities: Youdin 2011; Tominaga et al. 2018; Tominaga et al. 2020), or into hydrodynamic vortices (Lyra et al. 2008), can create strong enough concentrations of the dust such that its own self gravity can lead to planetesimal formation. Xu & Bai (2022a) and Xu & Bai (2022b) demonstrate this process with high resolution numerical simulations for the case of pressure bumps formed from magnetic fields.

Arguably, the leading mechanism for the formation of planetesimals in protoplanetary disks is the streaming instability (SI; Youdin & Goodman 2005). The SI is an instability driven by the momentum exchange between dust and gas via aerodynamic drag. In protoplanetary discs, the settling of pebble-sized dust can lead to a thin midplane dust layer that can become unstable to the SI, leading to the direct formation of planetesimals (Johansen et al. 2007). This process has been the target of numerous studies over the last decade, and is the focus of this thesis. We discuss the existing literature on the streaming instability in Section 1.3. For now, we will accept that planetesimals are capable of efficiently forming directly from mm-cm sized pebbles via the SI and/or a combination of other mechanisms. This is consistent with observations of Solar system asteroids, which are commonly described as rubble piles: an unorganized collection of smaller material of various sizes, bound together by self-gravity (Walsh 2018).

1.2.3 Planetesimals

In the Solar system, remnants of the primordial planetesimal population are believed to be the asteroids and minor bodies beyond Neptune known as trans-Neptunian objects, of which Kuiper Belt Objects (KBOs) are a subset. These populations represent objects between $\sim$1 km and 1000 km. Together, they provide our best observational constraints on planetesimal objects in nature, as our ability to gather information on such small, cold objects beyond the Solar system is limited.

Excluding the very largest objects $\gtrsim$ 400 km in radius which dominate the total asteroid mass budget, the observed size distribution of asteroids peaks near 140 km (Cuzzi et al. 2010). Some authors have suggested this means asteroids were preferentially born big (at that size) (Morbidelli et al. 2009), or born near that size and grew via the rapid accumulation of remnant pebbles in their local environment (Johansen et al. 2015). Some studies claim that this peak can be produced from the growth of a vast population of much smaller bodies near 1km in size (Weidenschilling 2011). Current models of planetesimal formation via the streaming instability suggest that this process readily forms $\gtrsim$100 km sized objects directly (e.g. Simon et al. 2016; Schäfer et al. 2017; Li et al. 2019; Rucska & Wadsley 2021). A recent survey of the Cold Classical Kuiper belt objects (Kavelaars et al. 2021) finds an exponential cut off in the size distribution at the large mass end, which is consistent with SI predictions. Further, Nesvorný et al. (2019) and Nesvorný et al. (2021) show with numerical models that the SI-formed planetesimal distribution exhibits the same fraction of retrograde vs. prograde orbits seen in KBO binaries.

Interestingly, samples of meteorites have displayed a geochemical dichotomy in the abundances of isotopes of elements such as Ti and Cr (Leya et al. 2008; Warren 2011). This dichotomy can be explained if there were two spatially and temporally distinct epochs of planetesimal formation in the Solar system (Lichtenberg et al. 2021). Measurements of the optical and near-infrared colour of KBOs also shows a distinct dichotomy between the Cold-Classical population (low inclinations $\lesssim 5°$, low eccentricity) and the excited population, which hints at geochemical differences and perhaps distinct formation histories between these populations (e.g. Schwamb et al. 2019). This suggests that the process that forms planetesimals, such as the streaming instability, is efficient throughout the lifetime of the protoplanetary disc.

Perhaps the most visually stunning data on planetesimals in recent years has come from the NASA New Horizons mission, which made a close encounter with Pluto and Charon in 2015 and the KBO (486958) Arrokoth. The surfaces of Pluto and Charon are believed to contain pristine records of impacts from the early solar system. Analyses of the crater size distribution reveal an impactor population consistent with observations of the KBOs today (Shankman et al. 2016), and with a turnover near 1-2 km that suggests a deficit of objects below that size (Singer et al. 2019). Unfortunately, neither observational techniques applicable to viewing KBOs or numerical techniques for modelling the streaming instability are capable of providing constraints at small sizes.

Another main target of the New Horizons mission was the KBO (486958) Arrokoth, pictured in Figure 1.7. The object displays two distinct lobes, and models suggest this structure is the result of a low-velocity impact between two different objects on a slowly decaying binary orbit (McKinnon et al. 2020; Grishin et al. 2020; Marohnic et al. 2021). The spatial crater densities on this object suggests the primordial planetesimal number density in our Solar system was not much higher than the number density of KBOs seen today, and this number density is too low to drive a significant collision rate between those objects (Greenstreet et al. 2019). Thus, while the asteroids are known to represent a significantly evolved population of minor bodies, the Cold Classical KBOs are believed to be fair representations of the primordial planetesimal disc from the outer Solar system.

Another space mission to a minor Solar System body came from the European Space Agency's Rosetta mission to the comet 67P/Churyumov-Gerasimenko. Results from this mission show that the comet likely formed from the gentle gravitational collapse of a cloud of mm-sized dust aggregates (Blum et al. 2017; Fulle & Blum 2017). This is further observational support for the streaming instability and the other mechanisms of planetesimal formation from dense pebble clouds we discussed at the end of the previous

FIGURE 1.7: Image of (486958) Arrokoth captured by the New Horizons mission. Image from NASA/Johns Hopkins Applied Physics Laboratory, processing by P. Budassi for Wikimedia.org. Reproduced here under Creative Commons license (CC BY 4.0).

section.

Global models of protoplanetary disc dust evolution show that planetesimal formation via the SI can be efficient throughout the disc under various scenarios that can cause the local concentration of pebbles (Drążkowska et al. 2016; Drążkowska & Alibert 2017; Drążkowska & Dullemond 2018). Once a population of some billions of planetesimals exists, gravitational interactions can lead to the runaway growth of a few > 1000 km bodies (Wetherill & Stewart 1989; Kokubo & Ida 1996) which leads into a phase of oligarchic growth where the planetary embryos interact with each other and dominate the disc dynamics (e.g. Pollack et al. 1996; Raymond et al. 2006; Wallace & Quinn 2019). Recent studies have taken outputs from models of planetesimal formation via the SI and used them as inputs for their initial planetesimal population (Liu et al. 2019; Jang et al. 2022). At sizes $>$1000 km, these objects are capable of significantly perturbing the surrounding gas and dust disc, driving further growth and evolution.

1.2.4 Protoplanets & Planetary Embryos

Massive, rocky protoplanets (or planetary embryos) can interact with their host disc through a variety of complex mechanisms. Broadly speaking, it is these interactions that will determine the mass, composition, and final orbital position of planets in the assembled, post-disc planetary system. This is a relatively young, active field of research. Up-to-date and thorough reviews are available in Drążkowska et al. (2022) and Paardekooper et al. (2022).

If a rocky planetary core is to become a gas giant, the process must occur within the 5-10 Myr lifetime of the disc inferred from observations of accretion signatures and IR/mm excess (Hartmann et al. 1998; Haisch et al. 2001; Ribas et al. 2014). These results have ruled out older theories for the formation of gas giants that require hundreds of millions of years, and inspired new models of protoplanet evolution that are compatible with this stringent time constraint.

The core accretion model of giant planet formation begins with a massive protoplanet which accretes gas from the protoplanetary nebula, forming an envelope that is initially in hydrostatic equilibrium. If gas continues to accrete and the core achieves a mass beyond a critical threshold near 5-10 Earth masses, the envelope can rapidly collapse onto the core, and rapid accretion begins in a runaway process (Perri & Cameron 1974; Pollack et al. 1996; Ayliffe & Bate 2012). This of course requires the existence of bodies more massive than Earth early in the disc lifetime, so that there is sufficient gas within the disc available to the gas giant in the first place. This core likely forms from the oligarchic growth process mentioned in the previous section. The early growth of massive solid bodies can also be enhanced by the process of pebble accretion, where millimetre sized pebbles that are abundant in protoplanetary discs are effectively accreted onto planetary embryos due to enhanced effective collisional cross-sections from the aerodynamic coupling of pebbles to the disc gas (see Johansen & Lambrechts 2017, for a review).

Numerical models shows that the direct formation of giant planets from the collapse of dense clumps is possible in discs that are gravitationally unstable (e.g. Rice et al. 2003; Mayer et al. 2004; Backus & Quinn 2016). This mechanism is likely only applicable in the outer regions of massive discs that are able to cool efficiently (Rogers & Wadsley 2011). Interestingly, there have been observations of several exoplanets orbiting at $\gtrsim$100 AU distances from their star (Figure 1.1), for which formation via gravitational instability is a viable explanation.

For protoplanets near an Earth mass, gravitational torque interactions between the planet and the disc gas can drive substantial inward radial migration of the planet (Type I migration; Goldreich & Tremaine 1980; Tanaka et al. 2002; Paardekooper et al. 2011). Depending on the planet mass and local disc properties such as gas surface density, temperature, and gradients in these properties, the net torque on the planet could also direct the planet outwards, in cases of low turbulent viscosity (Speedie et al. 2022b). Once the protoplanet becomes sufficiently massive (Saturn mass for solar mass stars), the planet can clear the gas material around its orbit, forming a gap (Type II; Lin & Papaloizou 1986). At this point, migration is much slower, and develops as the viscous evolution time scale for the disc (see Paardekooper et al. 2022 for a review: Section 2 for the classic migration picture and Section 3 for recent developments). Catastrophically rapid Type I migration of planets into the central star can be halted at planet traps caused by inhomogeneities in disc surface density or temperature profiles, ice-lines where certain volatile gas species are prone to freezing onto the solid material, and boundaries between inner regions with low turbulence (i.e. midplane to $\sim$50 AU) and outer regions undergoing magnetically driven turbulence (e.g. Alessi & Pudritz 2018; Alessi et al. 2020).

As mentioned in Section 1.2.2, the gaps, rings, and asymmetries seen in observations of millimetre pebbles have been used to guide theories of planet-disc interactions. Some discs have large cavities with smaller, interior discs, and some of these inner discs are inclined with respect to the outer disc, likely due to the influence of a massive companion (Francis & van der Marel 2020). Features in the kinematics of gas discs have also been interpreted as the influence of massive, perturbing planets (Pinte et al. 2018; Pérez et al. 2018; Dong et al. 2019; Teague et al. 2018a; Teague et al. 2019).

The whole of Figure 1.1 can also be used to constrain statistical outcomes of planet growth and formation models. The techniques of populations synthesis (Ida & Lin 2004, Alessi & Pudritz 2018; Alessi et al. 2020, see Benz et al. 2014 for a review) involve generating thousands of individual planetary embryo growth tracks in 1-D models of protoplanetary discs. These techniques are powerful tools for discerning the dominant physical processes that affect protoplanets as they grow to full planets.

1.3 The Streaming Instability

The streaming instability (SI) was first explored and applied to the context of planetesimal formation by Youdin & Goodman (2005). This study demonstrated that the SI is present when solid particles move through a fluid with a steady relative velocity. This condition arises naturally in a protoplanetary disc. The gas phase feels a hydrodynamic force from the global gas radial pressure gradient that pushes the gas to slightly sub-Keplerian speeds, while the dust feels no such force and attempts to orbit at the Keplerian speed, providing the persistent, steady-state relative velocity between the two phases (Nakagawa et al. 1986).

A seminal result from Johansen et al. (2007) showed conclusively with numerical simulations that, under ideal conditions, the SI could form objects as massive as Ceres directly from clouds of $\sim$10 cm sized objects in just tens of orbits. This cemented the SI as a leading candidate to overcome the aforementioned radial drift and collisional barriers discussed at the end of Section 1.2.2. In Figure 1.8, we show the evolution of the dust surface density and the formation of a gravitationally bound clump in a simulation from Johansen et al. (2007).

Since then, much effort has been dedicated to characterizing the SI in both the linear, small perturbation phase and the non-linear phase applicable to planetesimal formation. In this section we summarize this body of work.

1.3.1 Linear and pre-planetesimal non-linear phase

Youdin & Goodman (2005) introduced the SI as a linear instability with small, 2D plane-wave perturbations and analytical analyses that determined the fastest growing eigenmodes of the system. The perturbations are in the radial-vertical plane, denoting axisymmetric rings globally. The growth rates are largest for dust-to-gas mass volume ratios $\mu \gtrsim 1$, and when the characteristic stopping time for the aerodynamic drag ($t_{\rm stop}$) is resonant with the dynamical or epicyclic timescale of the disc (Ω^{-1}, the orbital period is $T_{\rm orb} = 2\pi/\Omega^{-1}$), commonly expressed in terms of a dimensionless stopping time: $\tau_s = t_{\rm stop}\Omega = 1$. These growth rates were explored in my Master's thesis (Rucska 2018), and a plot of the SI growth rates as a function of the perturbation wavevector for various dust conditions is shown in Figure 1.9.

The resonance interpretation for the peak SI growth rates was introduced by Squire & Hopkins (2018), who identified the SI as a specific case of a broader class of resonant drag instabilities. They also identified a faster growing mode of the SI, when a steady vertical velocity is included for the dust, which follows the physical scenario of dust grains settling to the disc midplane due to the gravity of the central star (Chiang & Youdin 2010). Growth rates in this scenario are plotted in the bottom panel of Figure 1.9. Notice that, especially for small τ_s dust (which corresponds to smaller grains in physical size, see discussion below), the growth rates of the SI are greatly enhanced, suggesting clumping of dust via the SI can occur during settling, especially given that smaller grains

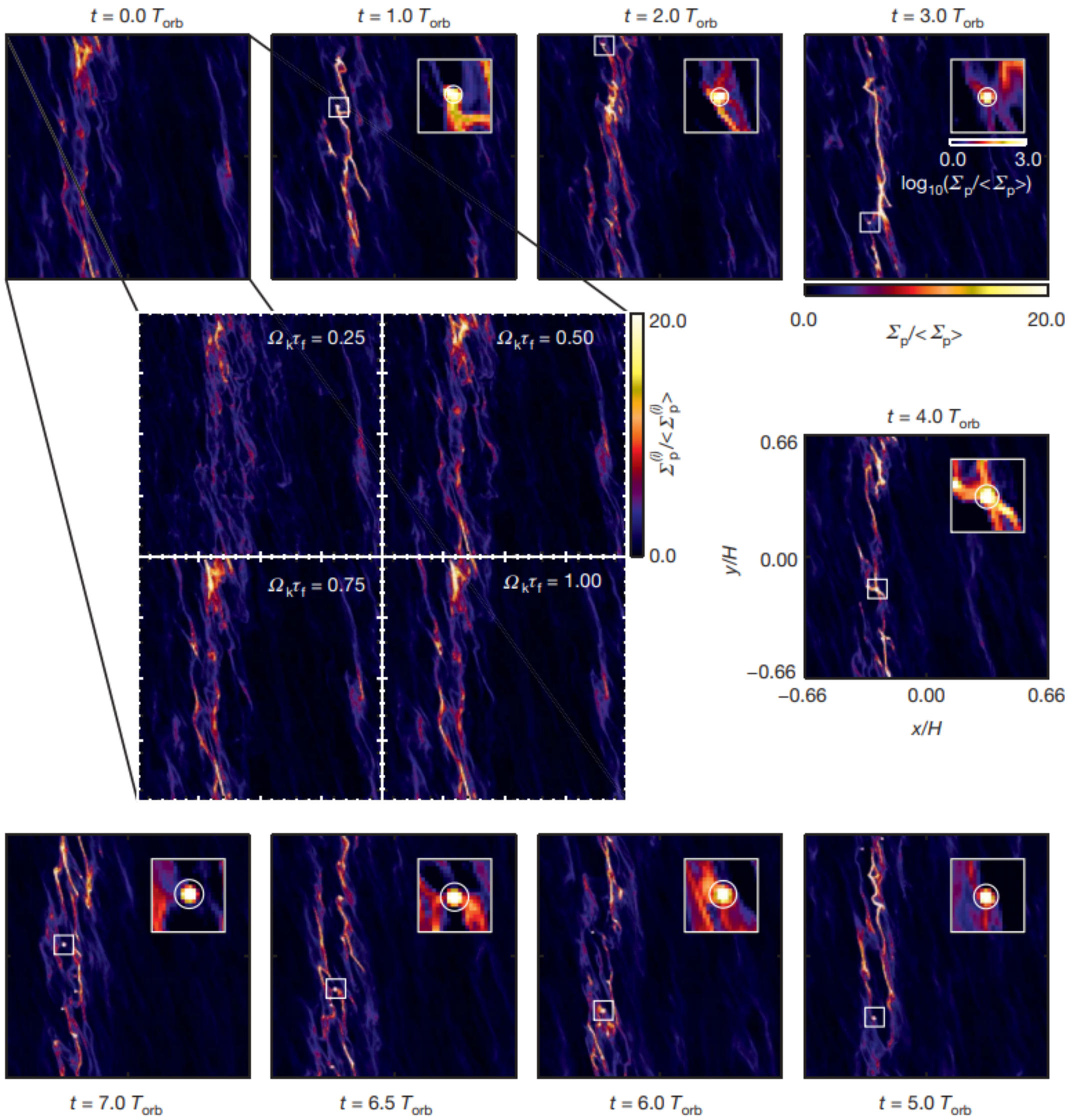

FIGURE 1.8: Surface density of dust particles in the radial-azimuthal (x-y) plane over time in simulation from Johansen et al. (2007), highlighting the collapse of dense dust clumps into bound planetesimals. The inset is centered on the most massive bound clump, the white circle denotes the clump Hill sphere. The colourbar is normalized to the mean surface density in the grid. The time for each panel is in units of the orbital period, and $t = 0$ corresponds to the time self-gravity was turned on. The middle four panels show the surface density in each grain species considered (differentiated by the parameter τ_f). Reproduced with permission from Johansen, A., Oishi, J., Mordecai-Mark, M. L., et al. (2007), Nature **448**, 1022. DOI:10.1038/nature06086, Figure 12.

experience longer settling times. With $\tau_s \ll 1$, $t_{\rm settle} \propto \tau_s^{-1}$ (see Rucska 2018, Section 4.1.5).

The equation for $t_{\rm stop}$ depends on the regime of drag considered. In all but the innermost regions of protoplanetary discs, the applicable regime is the Epstein regime (Epstein 1924), where the dust grain size is smaller than the mean free path of the gas (Birnstiel et al. 2016). The form of $t_{\rm stop}$ in this regime is

$$t_{\rm stop} = \frac{\rho_s}{\rho_g c_s} s, \tag{1.2}$$

where ρ_s is the material density of the particles, ρ_g is the local gas density, c_s is the local sound speed and s is the radius of the dust grains. For $\rho_s \approx 2.6\,{\rm g\,cm^{-3}}$ (applicable to silicates Moore & Rose 1973), and with $\Sigma_g(r) = 1000\ (r/{\rm AU})^{-3/2}\ {\rm g/cm^2}$ (e.g. minimum mass solar nebula model; Weidenschilling 1977b), then at 5 AU, $\tau_s = 1$ corresponds to ~ 35 cm.

Youdin & Johansen (2007) confirmed the streaming instability growth rates in a numerical dust-fluid scheme in the Pencil grid code (Brandenburg et al. 2021), which uses a finite difference discretization that is non-conservative and sixth-order accurate in spatial derivatives, third-order in time. Bai & Stone (2010b) also confirmed growth rates from the SI in the Athena grid code (Stone et al. 2008) which is based on a finite volume Godunov scheme that conserves quantities like mass and momentum and is 2nd-order accurate in spatial and time derivatives. Both methods use Lagrangian particles to represent the dust phase. Particle properties are interpolated onto the grid when computing aerodynamic forces that couple the dust and gas phases. Pencil and Athena have each been used in numerous studies of the SI. Outcomes regarding clumping and planetesimal formation are broadly consistent across the two codes, suggesting the main outcomes of the SI are not sensitive to the numerical choices associated with the hyrdodynamic scheme. Notably, the linear streaming instability has yet to be studied in a

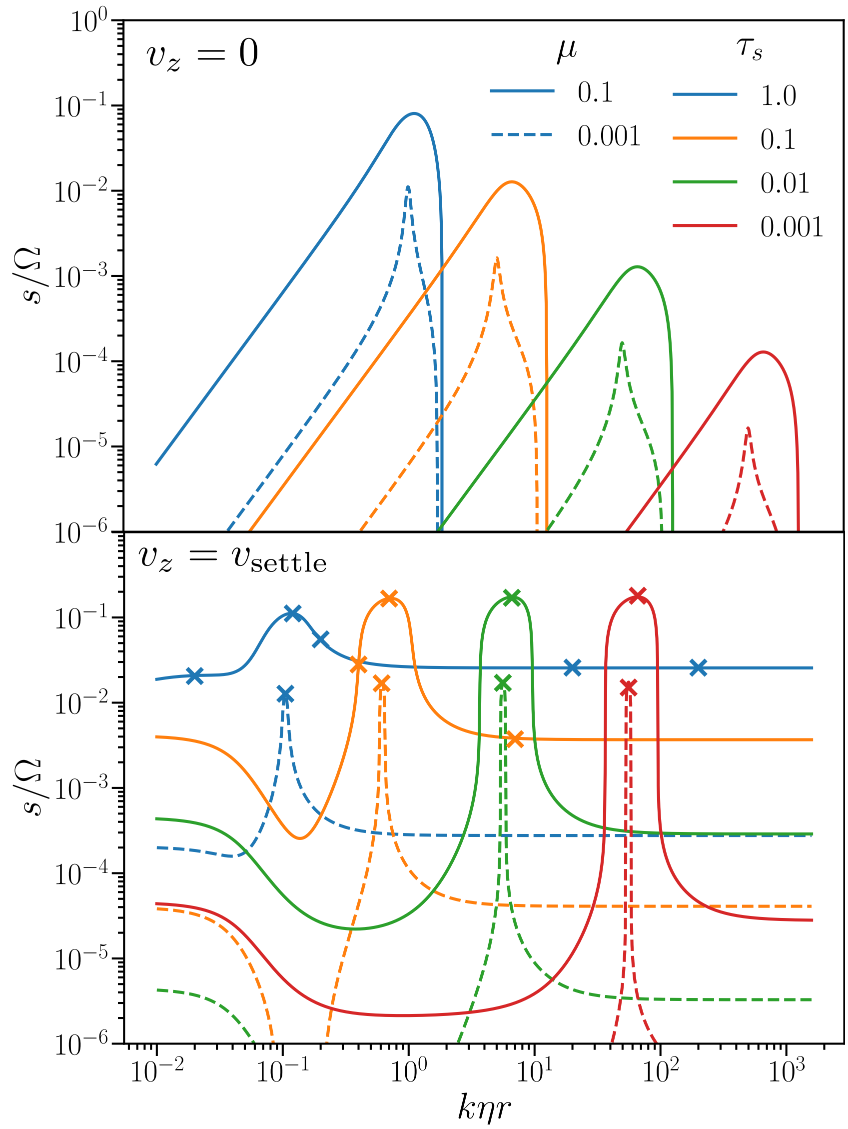

FIGURE 1.9: *Top.* Growth rates of the fastest growing mode in the linear streaming instability. The growth rate s is normalized to the orbital dynamical frequency Ω. The plane wave wavevector has a component in the radial (x) and vertical (z) directions, and the angle is set to $\theta_k \equiv \tan^{-1}(k_x/k_z) = 30°$, and $k \equiv \sqrt{k_x{}^2 + k_z{}^2}$. The growth rates are plotted as a function of k, with the x-axis scaled by the (dimensionless) radial pressure gradient parameter η (see Section 2.2.1) and the global disk radius r. Each curve represents SI growth rates for different combinations of the dust-to-gas density ratio $\mu \equiv \rho_d/\rho_g$ and the dimensionless stopping time parameter $\tau_s = t_{\rm stop}\Omega$ (equation 1.2). *Bottom.* As in the top panel, but a steady vertical settling velocity (Chiang & Youdin 2010) is included. The `X` marks represent confirmations of growth rates in numerical calculations. Reproduced from Figure 4.2 (top) and Figure 4.6 (bottom) of my Master's Thesis (Rucska 2018), results match Squire & Hopkins (2018).

Lagrangian hydrodynamics scheme, e.g. smoothed particle hydrodynamics (Gingold & Monaghan 1977; Wadsley et al. 2017; Price et al. 2018)

There have been recent expansions to the original linear perturbation paradigm of (Youdin & Goodman 2005). When isotropic turbulence is applied to the local disc environment, the viable regimes of rapid growth are restricted, suggesting that global turbulence inhibits the SI, especially for small particles and the interior regions of discs (Umurhan et al. 2020; Chen & Lin 2020). Lin (2021) considered a vertically stratified disk model, i.e. with vertical length scales beyond the disc midplane, so that both gas density and the rotational velocity vary with height, setting up a vertical shear gradient. They find that the vertically stratified SI has faster growth rates and operates on larger length scales than the unstratified SI. Lin & Hsu (2022) consider magnetized discs and find that magnetic torques drive rapid growth even in the absence of the radial gas pressure gradient, which is required for growth in the classic SI. The studies by Li & Youdin (2021) and Lin & Hsu (2022) suggest the SI is a viable mechanism for dust clumping in a broader range of physical conditions than originally considered.

The classic studies of the SI considered only a single size of dust grains, but given the discussion from Sections 1.2.1 and 1.2.2, there is reason to believe a distribution of dust sizes can exist locally within a protoplanetary disc. There are several studies of the linear phase of the SI with multiple species (Krapp et al. 2019; Paardekooper et al. 2020; Paardekooper et al. 2021; McNally et al. 2021; Zhu & Yang 2021), which generally conclude that the growth rates in this case are primarily driven by the largest grains in the distributions, and, like the classic SI, growth rates are high so long as the local concentration of dust mass is roughly equal to or high than the local gas mass. Numerical, non-linear studies of the multi-species SI in 2D (Schaffer et al. 2018; Schaffer et al. 2021; Yang & Zhu 2021) and 3D (Bai & Stone 2010a) reach similar conclusions. They also find that the large dust grains readily clump or settle to the disc midplane, while the smaller, more aerodynamically coupled grains clump less, leading to a spatial separation between dust of different sizes and potentially a population of planetesimals that would only be composed of the largest grains in a given size distribution.

All of the above multi-species SI models considered a size distribution given by a power law, following observed properties of ISM grains (Mathis et al. 1977). However, in protoplanetary discs, grain growth and fragmentation can lead to an equilibrium size distribution with a peak at large sizes (Birnstiel et al. 2011). McNally et al. (2021) studied this size distribution in their linear study of the SI, and in Chapter 4 of this thesis we study this distribution in the context of 3D simulations of planetesimal formation.

Analytical studies of 2D, radial-azimuthal plane-wave perturbations provide useful information on the physical conditions that are most unstable to the SI, but the non-localized nature of the plane waves and the 2D geometry cannot directly relate to localized behavior such as planetesimal formation. Localized clumping can be studied in 3D numerical simulations of the non-linear phase SI, such as in Johansen & Youdin (2007) and Bai & Stone (2010b). Both studies show that perturbations from an initial random distribution of dust can grow via the SI until they clump into dense filaments that merge and interact with complex dynamics. In just 100 dynamical timescales a uniform dust distribution can develop into filaments with local densities two orders of magnitude greater than the initial average. When self-gravity is included, these density fluctuations are large enough to gravitationally collapse into bound clumps, demonstrating the viability of the SI as a mechanism for forming planetesimals directly from pebble clouds.

1.3.2 Planetesimal formation via the SI

In this section we discuss the existing literature on planetesimal formation via the SI from studies of numerical simulations of protoplanetary discs. Pebble-sized dust settles efficiently to the disc midplane, creating a dense, vertically narrow midplane layer. This layer imparts significant momentum onto the gas, modifying the velocity of the gas locally, leading to the development of vertical shear. Thus, in the context of the streaming instability in stratified disc models, the growth of the first perturbations maybe be assisted by the Kelvin-Helmholtz instability (Gerbig et al. 2020; Lin 2021). Yet, the SI does play as critical role, as Johansen et al. (2007) show clumping to the scale of planetesimal formation is not seen in models that do not include the influence of dust imparting momentum back onto the gas.

Once the initial perturbations grow, dust rapidly collects into dense, azimuthally oriented (ring-like) filaments (e.g. Johansen et al. 2007; Bai & Stone 2010a; Yang & Johansen 2014; Simon et al. 2016; Simon et al. 2017; Li et al. 2018; Abod et al. 2019; Carrera et al. 2021). Within those filaments, local clumps of high density form, seeding planetesimal formation. The width of these features appears to depend on dust grain size (Simon et al. 2017) and the radial pressure gradient (Abod et al. 2019), though a systematic study of these correlations has not been conducted. Yang & Johansen (2014) and Li et al. (2018) represent some of the more dedicated studies of the filaments to date, and they find that over time, filaments merge and these interactions produce strong clumping. The filaments represent the mass reservoir available to planetesimal formation via the SI, and hence the total amount of mass in formed planetesimals, which places an upper limit on the mass of protoplanets that can form from via the runaway accretion of the planetesimal population (Liu et al. 2019; Jang et al. 2022). Thus, constraining the filament mass reservoir is essential to inform the future stages of planet formation beyond planetesimals. This is the focus of our work in Chapter 3.

Early work from Johansen et al. (2009b) demonstrated the dependence of non-linear SI clumping in discs on the local concentration of solids. They conclude that a slightly super-solar concentration of solids is required in order to achieve strong enough particle clumping to initiate planetesimal formation for ~1-10 cm sized pebbles. In the literature, this is typically translated to a critical surface density ratio of dust-to-gas mass, and this critical ratio has been shown to depend on grain size/drag stopping times (Carrera et al. 2015, Yang et al. 2017, Li & Youdin 2021). For sufficiently large concentrations of solids, however, planetesimal formation in 3D simulations is possible across a few orders of magnitude in grain size, from roughly centimetre to 0.1 millimetres in size (Simon et al. 2017).

To address the requirement of super-solar solid concentrations, Carrera et al. (2021) and Carrera et al. (2022) study whether an axisymmetric pressure bump could concentrate dust locally. The pressure bump creates a gradient in the radial pressure force on the gas, resulting in reduced radial dust drift speeds near the pressure maximum that can cause a local pile up of solids that triggers the SI. This occurs even though the overall ratio of solid mass in the simulation domain is below the threshold to trigger the SI in models without a pressure bump. Carrera et al. (2021) and Carrera et al. (2022) demonstrate that for a variety of bump amplitudes, cm-sized dust can collect to large local dust-to-gas mass ratios that initiates planetesimal formation. However, Carrera & Simon (2022) show this does not occur for slightly smaller grains near millimetres in size, raising questions about the viability of pressure bumps as a mechanism to collect dust mass and induce the SI for mm-sized dust.

Like the linear and non-linear phases of the SI, planetesimal formation appears to be minimally affected by numerical treatments. Johansen et al. (2012) show that including particle-particle collisions (only kinematics, without grain growth) does not significantly influence planetesimal formation outcomes. Simon et al. (2016) first studied the planetesimal formation phase of the SI in the code Athena. They find that properties of the formed planetesimals agree well with prior work from A. Johansen and collaborators, who use Pencil.

A primary target of these studies has been to constrain the properties of the mass distribution of SI-formed planetesimals—e.g. power-law slopes, characteristic masses, maximum or minimum masses. These properties are useful inputs for models of post-planetesimal formation evolution (Liu et al. 2019; Jang et al. 2022). Many studies explore how these properties vary with numerical or physical parameters, such as gravity versus rotational shear (Simon et al. 2016), grain size and dust-to-gas mass ratio (Simon et al. 2017), radial pressure gradient (Abod et al. 2019), global turbulence (Gole et al. 2020), numerical domain size (Schäfer et al. 2017; Rucska & Wadsley 2021), different perturbations to the initial dust density (Rucska & Wadsley 2021), and how the outcomes change with varying functional fits to the mass distribution (Li et al. 2019). The growing consensus appears to be that the properties of the SI-formed planetesimal mass distribution are remarkably consistent across these varied conditions, hinting at some universality in this process. However, fixed grid resolution models are limited in their ability to constrain the small-mass end of the distribution due to limits in computational resources.

Planetesimal formation also appears to be robust to changes in physical conditions beyond the local dust concentration and drag stopping time/dust grain size. Simon et al. (2016) show that the planetesimal mass distribution is not strongly influenced by the relative strength of self-gravity versus tidal shear—equivalent to considering different radial positions in the disc. More dust mass is converted to planetesimals in regions with stronger gravity vs. shear (i.e. the outer disc), as expected, but planetesimals still form in lower gravity vs. shear environments. Abod et al. (2019) study models with varying strengths for the radial pressure gradient which drives the relative velocity between the dust and gas phase, and, ultimately, the streaming instability. They find the power-law slope that characterizes the planetesimal mass distribution is relatively consistent for different gradient strengths, while weaker gradients form more small planetesimals. At zero pressure gradient, the growth of dust perturbations are driven by the secular gravitational instability instead (e.g. Youdin 2011).

The presence of external turbulence is one mechanism that can suppress planetesimal formation. Gole et al. (2020) find even low levels of external turbulence (external to the simulation domain, i.e. global in terms of the disc) can influence planetesimal formation. The turbulence prevents the settling of dust to a thin midplane later, and from achieving the local dust-to-gas mass volume ratio $\gtrsim$0.5 (from their results) required to achieve strong clumping via the SI. However, upper limits on the levels of turbulence present in observed discs are also low (Pinte et al. 2016; Flaherty et al. 2017; Teague et al. 2018b; Dullemond et al. 2018; Trapman et al. 2020), and within limits that suggest turbulence may not pose a serious issue for the SI (See Section 1.3.3 for further discussion).

As mentioned in Section 1.2.3, the properties of SI-formed planetesimals have been shown to be consistent with observations of asteroids as well as Kuiper Belt Objects (KBOs). The latter are believed to represent a pristine population of planetesimals from the early solar system. Recent studies find that the fraction of retrograde to prograde orbits seen in KBO binaries is consistent with SI-formed binaries (Nesvorný et al. 2019), and that the angular momentum distribution among KBOs is also similar to SI-formed clumps (Nesvorný et al. 2021). The size distribution of the Cold Classical KBOs features an exponential cut-off at the high-mass end (Kavelaars et al. 2021) that is consistent with SI models (e.g. Simon et al. 2016; Schäfer et al. 2017; Li et al. 2019; Rucska & Wadsley 2021). The KBO (486958) Arrokoth also displays a two-lobe structure that is consistent with the slow orbital decay of a planetesimal binary (McKinnon et al. 2020;

Grishin et al. 2020; Marohnic et al. 2021). Further, the "rubble-pile" physical structure of asteroids (Walsh 2018), as well as the comet 67P/Churyumov-Gerasimenko (Blum et al. 2017; Fulle & Blum 2017), suggests these objects formed from the collapse of a dense pebble cloud, consistent with the SI. Analysis of the crater size distribution on Pluto and Charon suggests that the primordial planetesimal population in the outer Solar system had a low number of objects below $\sim$ 1-2 km. Unfortunately, as mentioned previously, the minimum mass of planetesimals formed in simulations of the SI with increasingly high numerical resolution is not converged. The smallest size objects produced with current techniques (i.e. fixed numerical grid size) is $\sim$50 km. The broad agreement between the predictions of the SI and the observational tests put forth thus far provides support to the claim that the SI is a productive mechanism for producing planetesimals from pebble-sized dust.

1.3.3 Challenges to the SI

The requirement of local concentrations of dust to trigger planetesimal formation via the streaming instability is well-documented (Johansen et al. 2009b; Carrera et al. 2015; Yang et al. 2017; Li & Youdin 2021). The logical question arises of how that concentration occurs.

The strong dust pebble features seen in many ALMA observations (Section 1.2.2) have often been cited as regions of local dust concentration where the SI could be active. Interestingly, recent observations of dust rings have shown that this emission is likely not optically thick (Dullemond et al. 2018; Huang et al. 2018; Cazzoletti et al. 2018; Macías et al. 2019; Maucó et al. 2021). Further studies have explained that this may be due to the initiation of planetesimal formation via the SI within the dust ring (Stammler et al. 2019; Maucó et al. 2021). Observed axisymmetric pebble dust bumps (van der Marel et al. 2021) have often been attributed to hydrodynamic vortices, which have also been shown to be capable of concentrating pebble-sized dust to levels compatible with the SI (e.g. Lyra et al. 2008). Magnetized discs are also capable of producing zonal flows, or circumferential pressure bumps (Johansen et al. 2009a; Bai & Stone 2014), and dust can concentrate dust within these structures and result in the formation of planetesimals, even when these bumps are locally turbulent and the SI is believed to be suppressed (Xu & Bai 2022a; Xu & Bai 2022b).

Recent studies regarding both the linear SI (Umurhan et al. 2020; Chen & Lin 2020) and 3D hydrodynamic simulations (Gole et al. 2020), show that planetesimal formation is suppressed in the presence of global disc turbulence. The degree to which gas motions in the midplane protoplanetary discs are turbulent has been an essential question for many aspects of planet formation theory. According to Umurhan et al. (2020), Chen & Lin (2020), and Gole et al. (2020), the levels of turbulence from recent observations of discs (Pinte et al. 2016; Flaherty et al. 2017; Teague et al. 2018b; Dullemond et al. 2018; Trapman et al. 2020) which give $\alpha \sim 1 \times 10^{-4}$ to 1×10^{-3} (see equation 1.1 and surrounding discussion) does not fully suppress the SI. However, these observational constraints come from only a few objects thus far. More work is needed to discern the level of turbulence in disc midplanes where the SI is believed to occur.

1.4 Thesis Overview

As shown in the previous section, much progress in understanding the behavior of the SI in the context of planetesimal formation has come from empirical studies of data collected from 3D numerical simulations. Our work makes use of this strategy, exploring the SI in previously unexplored numerical contexts, configurations for the dust size distribution, and with novel analyses. Here, we outline the methods and results for each chapter of this thesis.

In chapter 2, we explore variance in the planetesimal formation process within large numerical domains and re-run simulations with smaller domains that are otherwise identical except for the initial perturbations to the dust density. Most prior work has used small domains for computational expedience. We see that the non-linear nature of the SI leads to a large variability in the planetesimal mass distribution and the total dust mass converted to planetesimals. This is seen in the multiple re-run small simulations as well as in subdomains within the individual larger simulations. However, the power-law slope that describes the mass distributions is consistent between the populations of planetesimals from all small simulations taken together and the full populations from the larger simulation. The slope we find is also consistent with prior work.

In chapter 3, we study the same suite of simulations from Chapter 2, but with an additional, larger run. We analyze the pre-planetesimal formation, filament-dominated epoch of the SI. We identify dust filaments as contours in the surface density maps, and find that the filaments in the smaller domains primarily span the full azimuthal length of their domain, which translates to ring-like structures globally. In the largest domains, the filaments are truncated. Fourier spectra of the dust surface density in 1D reveal the largest power in the azimuthal direction is at the box scale, regardless of domain size. Hence, large scale dynamics break up the filaments in larger domains, while small domains cannot represent dynamics on that scale.

The Fourier spectra in the radial direction identify a natural radial filament spacing of approximately 0.1 gas scale heights, which is half the length of the smallest domains. Thus, the small domains have low dynamical resolution at this length scale, which leads to configurations of dust filaments that are not seen in the larger domain simulations. We also conduct a novel mock signal analysis procedure to explain features of Fourier spectra from the simulation filament profiles that are difficult to explain with analytical fits. We find these spectral features can be explained by a configuration of filaments that is nearly evenly spaced, but, crucially, with a small level of variation.

In chapter 4, we run simulations using multiple species (or grains sizes) of dust with a grain size distribution guided by outcomes from theories of grain growth and fragmentation and equilibrium. Prior work on the multi-species SI has used distributions set by single power laws. We compare these multi-size models to our previous models with single sizes from Chapters 2 and 3. We find that the largest grains in our distribution readily form clumps and filaments, while the smallest grains do not. The planetesimals are primarily composed of the largest grains. The 2nd smallest grains (out of 6 species) exhibit in-between behavior—they form filaments readily, but not clumps.

We also show that the clumping driven by the SI would result in optically thick thermal emission in observations. The single size models clump more readily than the multi-size models, for which 1/6 of the dust mass does not clump at all. We compute an expected mass correction factor to account for this saturated emission, and find values between 40-90% for single-size (or strongly peaked) models, and 20-50% for the multi-size models.

In chapter 5, we build on prior work which explored the boundary for strong clumping via the SI in the parameter space set by the drag stopping time (or grain size) and the dust-to-gas mass surface density ratio. Strong clumping via the non-linear SI seeds planetesimal formation. Prior work primarily used 2D (radial-vertical) calculations. Motivated by the dynamical behavior seen in the azimuthal direction in the non-linear SI, we perform a parameter sweep in these parameters with 3D calculations. Interestingly, we find disagreement with recent work (Li & Youdin 2021), which generally predict lower critical surface density ratios (at a fixed grain size). Possible reasons for this disagreement include the wider numerical domains in the radial direction used by Li & Youdin (2021), or the vertical outflow boundary conditions used in their numerical work. Additional work is needed to discern the cause of this discrepancy.

Lastly, in chapter 6, we summarize the results, discuss their impact on the field and avenues for future research.

Chapter 2

Streaming instability on different scales. I. Planetesimal mass distribution variability

Josef Rucska & James Wadsley

What follows has been published in Monthly Notices of the Royal Astronomical Society (MNRAS). See: Rucska & Wadsley (2021), *MNRAS*, **500**, 520.

Abstract

We present numerical simulations of dust clumping and planetesimal formation initiated by the streaming instability with self-gravity. We examine the variability in the planetesimal formation process by employing simulation domains with large radial and azimuthal extents and a novel approach of re-running otherwise identical simulations with different random initializations of the dust density field. We find that the planetesimal mass distribution and the total mass of dust that is converted to planetesimals can vary substantially between individual small simulations and within the domains of

larger simulations. Our results show that the non-linear nature of the developed streaming instability introduces substantial variability in the planetesimal formation process that has not been previously considered and suggests larger scale dynamics may affect the process.

2.1 Introduction

Planet formation requires solid growth over a dozen orders of magnitude, from micron-sized grains embedded in protostellar clouds to centimetre or ten-centimetre sized dust pebbles in protoplanetary disks to terrestrial planets and planetary cores thousands of kilometres across. It is widely accepted that the first stage of growth, from micron-sized grains to centimetre-sized pebbles, is achieved by collisions. Similarly, once a large population of kilometre and tens of kilometre-sized planetesimals are present, these objects will interact gravitationally to build protoplanets and the final planetary system (Armitage 2020). The intermediate growth phase, from centimetre sized pebbles to kilometre sized planetesimals, however, faces two key constraints known as the metre-barrier.

The first barrier is rapid radial drift. All solid material feels a headwind as it orbits through the gaseous component of the disk. The gas orbits at sub-Keplerian speeds due to a radial pressure gradient, while dust attempts to orbit at the Keplerian speed. This headwind removes angular momentum from the dust, so that the dust orbit decays towards the star with a net inward radial drift. This effect is small for micron-sized dust grains that are tightly coupled to the gas, as well as for kilometre-sized objects. However, for intermediate sized objects, near one-metre, the radial drift timescale can be as short as a few hundred years (Weidenschilling 1977a).

The second barrier is related to collisional growth. Relative velocities in collisions between dust grains are strongly dependent on their size. When the objects approach one metre in size, the combination of turbulence and lower drag leads to fast collisions that are always destructive, resulting in net mass loss for both objects (Zsom et al. 2010; Windmark et al. 2012).

These barriers act to exclude metre-sized objects from the disk. The formation of kilometre-sized planetesimals thus requires a specific mechanism that is capable of rapidly concentrating solid mass without relying on collisions between dust grains.

2.1.1 The Streaming Instability and Planetesimal Formation

The streaming instability (SI) (Youdin & Goodman 2005) provides a promising mechanism to enhance dust concentrations. The SI is always present in shearing, dust-gas mixtures. It is one of a class of resonant drag instabilities (RDI) present in protoplanetary disks (Squire & Hopkins 2018; Squire & Hopkins 2020). At high dust to gas ratios it can operate faster than radial drift timescales (Youdin & Goodman 2005; Youdin & Johansen 2007).

The formation of planetesimals via the SI requires local dust densities that exceed the Roche density (Li et al. 2019), so that they can condense under their own gravity. Localized collapse occurs at local dust surface densities 2-3 orders of magnitude larger than the local average in the disk. This represents a non-linear, evolved state of the SI that must be treated numerically (Youdin & Johansen 2007; Bai & Stone 2010b). Prior work has established that the non-linear phase consistently produces azimuthally oriented (i.e. globally ring-like) dust filaments (Johansen et al. 2007; Bai & Stone 2010a; Yang & Johansen 2014; Simon et al. 2016; Simon et al. 2017; Li et al. 2018).

In an influential paper, Johansen et al. (2007) showed that these filaments can produce local dust densities high enough to initiate gravitational collapse and planetesimal formation. The timescale for this process is just tens of orbits. This result highlighted the promise of SI for overcoming the metre barrier. 3D hydrodynamical simulations of shearing patches of protoplanetary disks are now well-established as a way to predict the properties of planetesimals formed by the non-linear SI (Johansen et al. 2009b; Johansen et al. 2012; Johansen et al. 2015; Simon et al. 2016; Simon et al. 2017; Schäfer et al. 2017; Abod et al. 2019; Li et al. 2019; Nesvorný et al. 2019; Gole et al. 2020). These studies have explored how this process depends on parameters such as the dust mass (Johansen et al. 2009b; Simon et al. 2017), dust grain size (Simon et al. 2017), radial pressure gradient (Abod et al. 2019) and local gas turbulence (Gole et al. 2020).

Ideally, the streaming instability would operate directly within simple (e.g. smooth, axisymmetric) models based on observations of protoplanetary disks. However, achieving growth rates relevant to planetesimal formation may require local dust-to-gas mass density ratios greater than unity (Youdin & Goodman 2005; Youdin & Johansen 2007). In simulations of local patches of protoplanetary disks this translates to a requirement of super-solar dust-to-gas surface densities in order to achieve sufficient dust clumping for gravitational collapse (Johansen et al. 2009c; Bai & Stone 2010a; Bai & Stone 2010c). Local concentrations of dust in the disk would circumvent this issue. Large-scale gas structures such as pressure bumps and vortices could create large scale dust traps with enhanced local dust-to-gas mass surface density ratios (see Birnstiel et al. 2016, for a review). Observations show protoplanetary disks in nature can have non-uniform dust distributions, including rings (e.g. Dullemond et al. 2018) and non-axisymmetric bumps (van der Marel et al. 2013; van der Marel et al. 2015)[1]. Drążkowska & Dullemond (2014) and Drążkowska et al. (2016) presented global models of dust in protoplanetary disks using semi-analytic prescriptions for planetesimal formation via the SI, and conclude that planetesimal formation via the SI is most efficient in regions with enhanced solid abundances such as beyond the snow line, or where dust pebbles can accumulate due to radial drift pile-up.

[1]Note: features in the dust surface density formed directly by the non-linear SI are much too small to be observed directly.

Planetesimals formed by the streaming instability are sand-piles and initially lack cohesion other than their own self-gravity. This fits the emerging consensus that asteroids are rubble piles and represent somewhat evolved planetesimals (Walsh 2018). For example, data from the recent fly-by of the New Horizon's space mission of Kuiper Belt object 486958, Arrokoth, supports the gravitational collapse scenario. McKinnon et al. (2020) and Grishin et al. (2020) report that this object, which is characterized by two distinct lobes, was likely formed by a low-velocity impact resulting from the slow decay of a binary orbit of two smaller Kuiper Belt objects. Additionally, Nesvorný et al. (2019) compared the observed distribution of prograde vs. retrograde binary orbits in trans-Neptunian objects with similar, planetesimal-sized objects formed via the SI in local simulations of patches of protoplanetary disks, and find that the observed data agree with the simulation. Earlier work (Morbidelli et al. 2009) modeled the gravitational interactions within a population of planetesimals and planetary embryos and finds that to produce a final size distribution consistent with the present day asteroid belt, the initial planetesimal size distribution was dominated by bodies with a minimum size of approximately 100 km, suggesting smaller objects were not present to build planetesimals hierarchically.

Prior models for planetesimal formation usually assume the hierarchical build-up of kilometre-sized objects from smaller objects via collisions (Kataoka et al. 2013). However, this build-up phase would have to occur incredibly efficiently to avoid the aforementioned metre barrier constraints. Thus, the mechanism of planetesimal formation via the gravitational collapse of over-dense clouds of dust pebbles that were generated by the non-linear phase of the streaming instability has become a leading model for this phase of the process of planet formation.

2.1.2 Simulating the planetesimal mass distribution

A primary objective of many studies of planetesimal formation via the SI is to characterize the mass and size distribution of the formed planetesimals (Johansen et al. 2015; Simon et al. 2016; Simon et al. 2017; Schäfer et al. 2017; Abod et al. 2019; Li et al. 2019; Gole et al. 2020). Such results are useful inputs for models of the evolution protoplanets and planetary cores in the presence of planetesimal disks (e.g. Pollack et al. 1996). However, there is still much about simulations of the streaming instability in protoplanetary disks that remains to be understood.

The SI operates on scales that are a tiny fraction of a protoplanetary disk ($\lesssim 0.01\, AU$), as might be expected of a process that can make ~ 100 km-sized bodies. Thus, published 3D numerical simulations have focused on tiny patches in protoplanetary disks. As might be expected, prior work has also focused on regions of parameter space with favourable growth rates which greatly limits the computational expense. In addition, the ubiquitous turbulence and large stopping-distance of dust grains makes the phase space of the dust very complex and difficult to model. This precludes simple adaptive strategies and explains the use of fixed meshes with the associated limits on dynamical range. Thus it is an expensive and ongoing process to explore the full parameter space of dust grain sizes, dust mass, total disk mass, global gas pressure gradient and the role of disk structures. Global disk simulations which resolve the key scales for SI are still far out of reach.

Key questions remain regarding numerical convergence. For example, establishing a minimum planetesimal mass, the detailed properties of the dust density distribution and the turbulent velocity field. We would also like to investigate the non-linear interactions between the non-linear SI and the full, evolving distribution of grain sizes. Generally, there is much work to be done in characterizing the non-linear SI, including perturbation growth rates, characteristic length scales, the interaction between newly collapsed planetesimals and dust, the amount of dust converted to planetesimals, the collapse process for individual planetesimals, their resultant properties and the roles of mergers and collisions.

Due to these challenges and the associated computational expense, most studies using 3D simulations to study the planetesimal mass distribution from the SI considered a numerical domain size that was at most 0.2 gas scale heights on a side ($\sim 0.02\,AU$). Thus the impact of larger domains is relatively unstudied. Yang & Johansen (2014) and Li et al. (2018) used larger domains in a study of the non-linear SI, but their simulations did not consider gravitational forces between the dust mass, and thus did not follow the development of the non-linear SI all the way to planetesimal formation. Schäfer et al. (2017) used larger domains that were twice and four times as large in the radial and azimuthal directions and studied the population of planetesimals in the full domain. They constrain parameters of the planetesimal mass distribution in the full domain of the simulation, and they find disagreement in some parameters for the simulations of different sizes, and agreement in other parameters. Carrera et al. (2021) used domains with large radial extents to study planetesimal formation via the SI within large-scale, background pressure bumps associated with axisymmetric rings in protoplanetary disks. Larger domains permit new dynamical modes which may impact the planetesimal formation process, but not much research has been done in exploring this impact.

In this paper, we confirm the basic results of Schäfer et al. (2017), with a different code and hydrodynamical treatment, using similarly large domains. We expand on their results by running multiple simulations with parameters that are identical but for different random perturbations in initial dust density. We also briefly examine convergence via enhanced resolution in the largest domain simulation. Through a novel analytical approach we probe the spatial variability in the planetesimal mass distribution and conversion rate of the dust mass to planetesimals throughout the larger domains. We also consider the mass distributions on the scale of the full domain to compare to prior work.

The paper is organized as follows. In Section 2.2 we outline our methods and parameters of our simulations. In Section 2.3 we describe our methods for analyzing our simulation data and our results. Sections 2.3.1 to 2.3.2 focuses on the properties of the mass distributions and Section 2.3.3 focuses on the quantifying the total amount of dust that is converted to planetesimals. In Section 2.4 we summarize and discuss our results and their impact on the field, as well as future work.

2.2 Methods and initial conditions

We model the dynamics of localized portion of a protoplanetary disk, using the shearing sheet approximation (Goldreich & Lynden-Bell 1965) to simulate a local portion of a near-Keplerian, protoplanetary disk with a co-rotating Cartesian frame (x, y, z). Relative to the central star, the box centre is at (r, θ_0, z_0) in cylindrical coordinates. The box is centred on the midplane so that $z_0 = 0$. Points within the box are at global coordinates $(r + x, \theta_0 + y, z)$. This approximation neglects the effects of azimuthal curvature in the orbit.

The equations that describe the gas and dust evolution in this non-inertial reference frame are

$$\frac{\partial \rho_g}{\partial t} + \nabla \cdot (\rho_g \boldsymbol{u}) = 0 \tag{2.1}$$

$$\frac{\partial \rho_g \boldsymbol{u}}{\partial t} + \nabla \cdot (\rho_g \boldsymbol{u}\boldsymbol{u}) = -\nabla P_g + \rho_g \left[-2\boldsymbol{\Omega} \times \boldsymbol{u} + 2q\,\Omega^2 x\,\hat{\boldsymbol{x}} - \Omega^2 z\,\hat{\boldsymbol{z}} + \mu \frac{\overline{\boldsymbol{v}} - \boldsymbol{u}}{t_{\rm stop}} \right] \tag{2.2}$$

$$\frac{d\boldsymbol{v}_i}{dt} = 2\boldsymbol{v}_i \times \boldsymbol{\Omega} + 2q\,\Omega^2 x\,\hat{\boldsymbol{x}} - \Omega^2 z\,\hat{\boldsymbol{z}} - \frac{\boldsymbol{v}_i - \boldsymbol{u}}{t_{\rm stop}} + \boldsymbol{F}_g \tag{2.3}$$

where ρ_g denotes the gas mass volume density, P_g is the gas pressure, and $\mu \equiv \rho_d/\rho_g$ is the ratio of the local dust mass density to the gas mass density. The velocity of the gas is represented by $\boldsymbol{u}$, and the velocity of an individual dust particle is $\boldsymbol{v}_i$, where the subscript i identifies the ith dust particle. We use an isothermal equation of state, $P_g = \rho_g c_s^2$, where c_s is the sound speed.

The gas and the dust are coupled together by the terms $\mu(\overline{\boldsymbol{v}} - \boldsymbol{u})/t_{\text{stop}}$ and $-(\boldsymbol{v}_i - \boldsymbol{u})/t_{\text{stop}}$ in the gas and dust momentum equations, respectively. The notation $\overline{\boldsymbol{v}}$ represents the mass-weighted average velocity of the dust particles in the gas cell (though in our simulations all dust particles have the same mass). The stopping time of the dust particle, t_{stop}, is a timescale that characterizes the rate at which momentum is exchanged between the gas and dust. In the Epstein drag regime (Epstein 1924), where the particle size is smaller than the mean free path of the gas, this parameter is given by

$$t_{\text{stop}} = \frac{\rho_s s}{\rho_g c_s} \tag{2.4}$$

where ρ_s is the bulk solid density of the particles (approximately $2.6\,\mathrm{g\,cm^{-3}}$ for silicates (Moore & Rose 1973)) and s is the radius of the dust grains if we assume they can be approximated with a spherical shape. In protoplanetary disks, the Epstein drag regime applies to dust particles everywhere except the very inner part of the disk (Birnstiel et al. 2016), so we use this drag formalism.

In the local frame described by (x, y, z), which rotates with the Keplerian rotation with the disk, there is a background velocity flow due to differential rotation in the radial direction. The angular velocity is a power law in the disk radius, $\Omega \propto r^{-q}$, and we model Keplerian rotation, where $q = 3/2$. In our co-ordinates, the rotation vector is oriented along the z-axis, $\boldsymbol{\Omega} = \Omega\,\hat{\boldsymbol{z}}$, which leads to a background velocity flow given by $(q\Omega x)\hat{\boldsymbol{y}}$, where x is the local radial co-ordinate.

2.2.1 Numerical methods

We simulate this system with the public C-version of the ATHENA hydrodynamics grid code (Stone et al. 2008). We employ the HLLC Riemann solver to compute the numerical fluxes and the cornered transport upwind (CTU) integrator to evolve the equations in time (Stone et al. 2008; Stone & Gardiner 2009). Dust is modeled following ATHENA (Bai & Stone 2010b) with the semi-implicit integrator and the triangular-shaped cloud (TSC) scheme to interpolate particle properties to and from the gas grid. The gravity solver was modified to include dust self-gravity. Otherwise, what follows are standard ATHENA options.

The orbital advection scheme separates the background flow velocity from the fluctuations, leading to a more computationally expedient and accurate algorithm (Masset 2000; Johnson et al. 2008; Stone & Gardiner 2010). Thus the momentum equation for the dust particles which is integrated in our simulations has the background shear flow subtracted, and is of the form

$$\frac{d\boldsymbol{v}_i'}{dt} = 2(v_{iy}' - \eta v_K)\Omega\hat{\boldsymbol{x}} - (2-q)v_{ix}'\Omega\hat{\boldsymbol{y}} - \Omega^2 z\hat{\boldsymbol{z}} - \frac{\boldsymbol{v}_i' - \boldsymbol{u}'}{t_{\rm stop}} + \boldsymbol{F}_g \tag{2.5}$$

where $\boldsymbol{v}' = \boldsymbol{v} - (q\Omega x)\hat{\boldsymbol{y}}$ and $\boldsymbol{u}' = \boldsymbol{u} - (q\Omega x)\hat{\boldsymbol{y}}$.

To maintain this shear flow at the radial boundary, our simulations employ shearing box boundary conditions, where the azimuthal (y-direction) and vertical (z-direction) hydrodynamic boundary conditions[2] are purely periodic, and the radial (x-direction) boundary conditions are shear periodic (see Hawley et al. 1995; Stone & Gardiner 2010). The radial periodic zones move along the y-direction with velocities of magnitude $q\Omega L_x$. Once the periodic zones have moved beyond the extent of the computational domain in the y-direction, the motion resets and the shear periodic boundary conditions become momentarily purely periodic. The time period for this is given by $t_n = nL_y/(q\Omega L_x)$,

[2] The boundary conditions are slightly different for the gravity solver, see Section 2.2.1

where for each $n = 0, 1, 2...$ the radial boundary conditions are purely periodic, and for all intermediate times the are boundaries are not perfectly aligned, according to the shear periodic scheme. Here, L_x and L_y are the extent of the box in the x-direction and y-direction, respectively.

Another essential component of the streaming instability is large-scale, radial pressure gradients in the gas disk, which has a surface density profile that decreases with radius. This pressure gradient is responsible for maintaining a persistent difference between the radial component of the velocity of the dust and the velocity of the gas. Only the gas feels the radially-outward pointing hydrodynamic force due to this pressure gradient, which causes the gas to orbit at slightly sub-Keplerian speeds (Armitage 2020). The dust does not feel this force, and orbits at the Keplerian speed. The difference in these radial velocities is small, but it is persistent, which means there is a persistent momentum exchange between the dust and gas via the drag force, hence why this gradient is a key component of the streaming instability (Youdin & Goodman 2005).

Including this radial pressure gradient directly in the gas phase within the simulations would create a discontinuity between the inner and outer radial boundaries of the domain. Hence, when including this effect in Athena, Bai & Stone (2010b) approximate the effect of the pressure gradient as a constant force within the shearing box. However, instead of applying an outward radial (positive x) force to the gas, a constant inward radial (negative x) force is added to the particles. This is the $\boldsymbol{F}_{\mathrm{grad}} = -2\eta v_k \Omega \hat{\boldsymbol{x}}$ term in equation 2.5. The factor ηv_k measures the amount by which the azimuthal component of the dust and gas is modified from the Keplerian velocity. Given a disk model with a radial pressure profile $P_g \propto r^{-n}$ and an isothermal equation of state,

$$\eta = n \frac{c_s^2}{v_k^2}. \tag{2.6}$$

With the gas scale height defined as $H_g \equiv c_s/\Omega$, then $\eta \sim \mathcal{O}(H_g/r)^2$, and in many models of PPDs, e.g. minimum mass solar nebula (Hayashi 1981), $H_g/r \sim 0.05$, and a typical value for η is ~ 0.003. In ATHENA (Bai & Stone 2010b), this factor η in the radial pressure gradient force $\boldsymbol{F}_{\rm grad} = -2\eta v_k \Omega \hat{\boldsymbol{x}}$ is parameterized via the dimensionless factor $\eta v_k / c_s$, and the simulations in this study use a value of $\eta v_k / c_s = 0.05$ (see Section 2.2.2).

Particle self-gravity

Exploring the creation of bound clumps requires the gravitational acceleration due to dust particles,

$$\boldsymbol{F}_g = -\nabla \Phi_d \tag{2.7}$$

where the potential due to dust, Φ_d, is the solution of Poisson's equation,

$$\nabla^2 \Phi_d = 4\pi G \rho_d, \tag{2.8}$$

where G is the gravitational constant. The TSC interpolation scheme is used to compute the dust density, ρ_d (used for drag and gravity).

Following prior work (e.g. Simon et al. 2016), we neglect the self-gravity of the gas whose local density perturbations are relatively small and also the effect of gravity on gas which is small compared to other forces. These assumptions can be justified by examining the gaseous Toomre (1964) parameter, $Q \equiv c_s \Omega / (\pi G \Sigma) \sim 32$ for our simulations and thus the gas disk is very gravitationally stable (see also equation 2.13 and associated discussion).

We use the Poisson solver implemented in the public (C-version) of ATHENA by C.-G. Kim (Kim & Ostriker 2017), with shear-periodic horizontal boundary conditions (Gammie 2001) and vacuum (open) boundary conditions in the vertical direction (Koyama & Ostriker 2009). We show tests confirming the correct behaviour of dust with self-gravity in our simulations in Appendix Appendix 2.A.

2.2.2 Initial conditions & parameters

Our choice for the parameters that control the dust mass, dust grain size, radial pressure gradient, and ratio of gravitational and rotational shear strength are either identical or very similar to choices from previous work (Simon et al. 2016; Schäfer et al. 2017; Johansen et al. 2012; Li et al. 2018; Gole et al. 2020). These parameters are summarized in the bottom row Table 2.1 and are defined in this section.

The gas is initialized with a Gaussian profile in the vertical direction

$$\rho_g(z) = \rho_{g,0} \exp\left(-\frac{z^2}{2H_g^2}\right) \tag{2.9}$$

where $\rho_{g,0}$ is the gas density in the midplane and H_g is the gas scale height. We set the units of our model so that $\rho_{g,0} = H_g = \Omega = c_s = 1$. The dust particle positions are initialized with a random number generator based on a uniform distribution in the x-y plane, and a Gaussian profile in the z direction with a scale height $H_d = 0.02H_g$. The number of particle resolution elements in each simulation is equal to the number of grid resolution elements in the domain. As seen in Table 2.1, we ran multiple simulations with identical domain sizes and resolutions, each of which labelled with a letter `a`, `b`, `c`, or `d`. The dust particles in these otherwise identical simulations were initialized with different random number seeds, changing the individual particle positions. This leads to different outcomes in the planetesimal formation process during the non-linear evolution of the streaming instability (explored in Section 2.3).

The size of the dust grains, s, controls the strength of the drag coupling between dust and gas. This sets the dimensionless stopping time,

$$\tau_s \equiv t_{\rm stop}\Omega. \tag{2.10}$$

In all our simulations, we choose $\tau_s = 0.314$. In terms of orbital periods, $T_{\rm orb} = 2\pi/\Omega$, we have $t_{\mathrm{stop}}/T_{\mathrm{orb}} \approx 0.05$. The mass of the dust particles is controlled by the ratio of dust mass surface Σ_d density to the gas mass surface Σ_g density

$$Z \equiv \frac{\Sigma_d}{\Sigma_g} \tag{2.11}$$

and we use $Z = 0.02$, a slightly super-solar solid mass ratio. The radial pressure gradient parameter η (see equation 2.6), is parametrized via

$$\Pi \equiv \frac{\eta v_K}{c_s} \tag{2.12}$$

and for this parameter we choose $\Pi = 0.05$. Lastly, the strength of gas self-gravity versus tidal shear is captured by

$$\widetilde{G} \equiv \frac{4\pi G \rho_{g,0}}{\Omega^2}. \tag{2.13}$$

The value of this parameter sets the relative importance of self-gravity versus tidal shear. Varying $\widetilde{G}$ is equivalent to moving through different radial portions of the disk. For our simulations, as in the fiducial simulation from Simon et al. (2016), we set $\widetilde{G} = 0.05$, equivalent to a Toomre Q of 32. For a disk model where these quantities are power laws in the disk radius r, i.e. $\Sigma_g \propto r^{-a}$, $H_g \propto r^b$, $\Omega \propto r^{-q}$, then $\widetilde{G} \propto r^{-a-b+2q}$. For $a = 1$, $q = 3/2$, and, as in the minimum mass solar nebula (MMSN) model (Hayashi 1981), $b = 5/4$, then $\widetilde{G} \propto r^{3/4}$ and varies with radial position within the disk.

2.2.3 Simulation domain

In our study, we consider simulation domains of various sizes, as well as multiple runs of simulations with identical physical parameters to investigate the variance planetesimal formation process via the streaming instability. The domain sizes are summarized in Table 2.1.

We employ simulations with $L_x = L_y = L_z = 0.2$, as well as $L_x = L_y = 0.4,\ L_z = 0.2$

TABLE 2.1: Simulation parameters.

Run name	Domain Size $(L_x \times L_y \times L_z)/H_g$	Grid Resolution $N_{\text{cell}} = N_x \times N_y \times N_z$
`L02a`	$0.2 \times 0.2 \times 0.2$	$120 \times 120 \times 120$
`L02b`	$0.2 \times 0.2 \times 0.2$	$120 \times 120 \times 120$
`L02c`	$0.2 \times 0.2 \times 0.2$	$120 \times 120 \times 120$
`L02d`	$0.2 \times 0.2 \times 0.2$	$120 \times 120 \times 120$
`L04a`	$0.4 \times 0.4 \times 0.2$	$240 \times 240 \times 120$
`L04b`	$0.4 \times 0.4 \times 0.2$	$240 \times 240 \times 120$
`L08`	$0.8 \times 0.8 \times 0.2$	$480 \times 480 \times 120$

$N_{\text{par}}/N_{\text{cell}}$	τ_s	Z	$\widetilde{G}$	Π
1	0.314	0.02	0.05	0.05

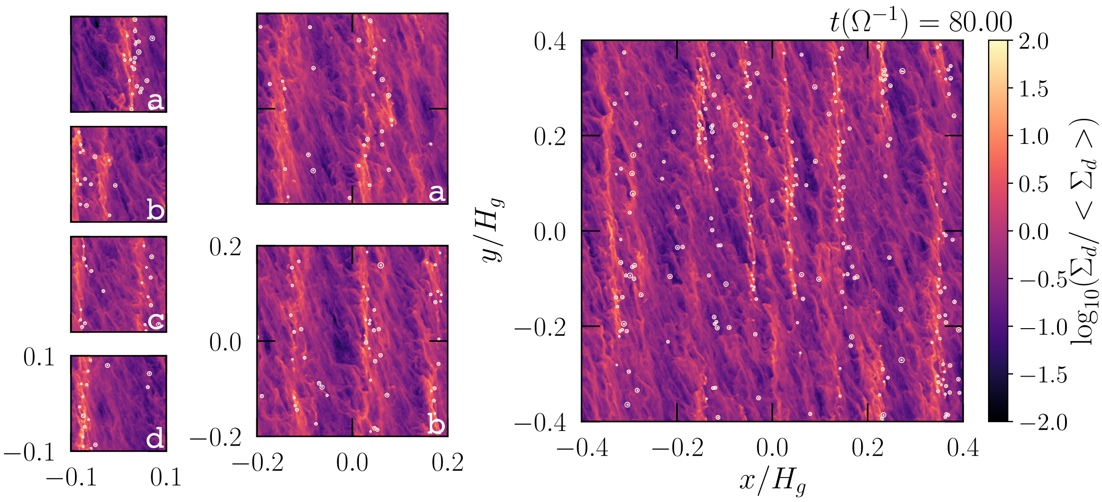

FIGURE 2.1: Dust surface density in the x-y plane for each of the 7 simulations. The colour represents the logarithm of the dust surface density normalized by the mean dust surface density. Bound planetesimals identified by the group finder are highlighted by the white circles, where the radii of the circles is equal to the Hill radius (equation 2.18). Each snapshot represents the simulation at time $t = 80$ in units of the inverse orbital frequency, Ω^{-1}.

and $L_x = L_y = 0.8$, $L_z = 0.2$, where all above lengths are in units of the gas scale height, H_g. We introduce a shorthand for the simulations with the previously described domain sizes, and refer to them as `L02`, `L04` and `L08`, respectively.

We maintain an equivalent numerical resolution (in terms of cells per length) between runs. In our smallest domains, the `L02` runs, which matches the size of the domains from Simon et al. (2016), we use a moderate resolution of $(N_x, N_y, N_z) = (120, 120, 120)$. This results in cubic resolution elements in our simulation grids, with a side length of $0.2H_g/120 \approx 0.00167H_g$. We maintain this resolution in our larger simulations, hence the `L04` runs have $(N_x, N_y, N_z) = (240, 240, 120)$ and the `L08` runs have $(N_x, N_y, N_z) = (480, 480, 120)$.

We note that, according to Simon et al. (2016), for these dust parameters our resolution of $\sim 0.001667H_g$ is sufficient to adequately sample the planetesimal distribution, typically providing several planetesimals per `L02` sized box. At higher resolutions, the dust particles can collapse to smaller length scales because gravity is discretized at the grid cell scale, and thus smaller mass planetesimals can be formed, and a greater number of planetesimals overall. At lower resolutions, only a few planetesimals per `L02` box can form.

While the ratio of the dust-to-gas mass surface density is $Z = 0.02$, the ratio of the midplane dust mass density and dust gas density, given by,

$$\frac{\rho_{d,0}}{\rho_{g,0}} \equiv \frac{\Sigma_d}{\Sigma_g}\frac{H_g}{H_d} = Z\left(\frac{H_d}{H_g}\right)^{-1}, \tag{2.14}$$

is actually rather high once the dust settles to the midplane. The ratio H_d/H_g approaches ~ 0.05, which gives $\rho_{d,0}/\rho_{g,0} \sim 0.4$, approaching unity. Also, as shown in the next section, the relationship between the total dust mass and the total gas mass in the simulation domain is $M_{\rm dust,T} = 0.25M_{\rm gas,T}$. This is because the vertical extent of the box is $0.2H_g$, which excludes a significant portion of the gas mass in this small patch of the protoplanetary disk, while all the dust mass in the vertical dimension is included within the domain (recall $H_{d,0} = 0.02H_g$).

2.2.4 Physical unit conversion

Following Simon et al. (2016) and Johansen et al. (2012) we convert to physical units by considering a mass unit given by $M_0 = \rho_{g,0}{H_g}^3$, and then use the MMSN model (Hayashi 1981) for the gas scale height as a function of disk radius, $H_g(r) \sim 0.033(r/\mathrm{AU})^{5/4}$. With $r = 3$ AU, we have $M_0 = 6.7 \times 10^{26}$ g. For our smallest (`L02`) boxes, the total amount of gas in the box is $M_{\mathrm{gas,T}} \approx 0.008M_0$. With $\Sigma_g = \sqrt{2\pi}\rho_{g,0}H_g$, $\Sigma_d = M_{\mathrm{dust,T}}/(L_xL_y)$, we have $M_{\mathrm{dust,T}} = \sqrt{2\pi}(L_x/H_g)(L_y/H_g)ZM_0$. Again, for the `L02` boxes, this gives $M_{\mathrm{dust,T}} \approx 0.002M_0 = 0.25M_{\mathrm{gas,T}}$ and with the conversion for M_0 to physical units, assuming a global disk radius of $r = 3$ AU, the total mass of dust in the `L02` boxes under these assumptions is $M_{\mathrm{dust,T}} = 1.34 \times 10^{24}$ g $\approx 1.5M_{\mathrm{Ceres}}$.

With the same MMSN prescription for $H_g(r)$ as above, $0.2H_g$ (the side length of our smallest domain) converts to ~ 0.025 AU if we place the simulation box at $r = 3$ AU. At the same radius, our resolution unit of $\sim 0.00167H_g$ converts to $\sim 2 \times 10^{-4}$ AU, or $32,000$ km.

2.2.5 Computational resources

Every simulation in this study was integrated to at least $t = 200\Omega^{-1}$ in Athena. The number of CPU hours used to integrate to $t = 200\Omega^{-1}$ was ∼3500 for each `L02` simulation, ∼8200 for each `L04` simulation, and 27400 for the `L08` simulation. All simulations were run on the ComputeCanada Niagara cluster.

2.2.6 Planetesimal mass distribution characterization

In this section we describe the methods we used to quantify the mass distribution of planetesimals formed in our simulations. The cumulative mass distribution, $N_>(m_p)$, is the number N is the number of planetesimals of greater or equal mass than m_p. Following Simon et al. (2017), we estimate the differential mass distribution via,

$$\left.\frac{dN}{dm_p}\right|_i = \frac{2}{m_{p,i+1} - m_{p,i-1}}. \tag{2.15}$$

where i denotes the ith planetesimal ranked in increasing mass. We use the maximum likelihood estimator (MLE) of Clauset et al. (2009) to estimate the power-law index p such that $\frac{dN}{d\,m_p} \propto m_p^{-p}$. This gives,

$$p = 1 + n\left[\sum_{i=1}^{n} \ln\left(\frac{m_{p,i}}{m_{p,\min}}\right)\right]^{-1}, \tag{2.16}$$

where n is the number of planetesimals in the set of planetesimal masses, $\{m_{p,i}\}$, and $m_{p,\min}$ is the minimum planetesimal mass in the set. The error in the estimate for p is,

$$\sigma = \frac{p-1}{\sqrt{n}}. \tag{2.17}$$

Other studies (Schäfer et al. 2017; Li et al. 2019) characterized the mass distribution with a variety of functions that contain more parameters, including some that combined a power-law fit with an exponential cut-off. Since we use only moderate resolution and thus have lower planetesimal numbers than the high-res simulations from Simon et al. (2016), we choose to only fit our data with a single power law.

2.2.7 Group finding

We employ the group finding algorithm SKID (Stadel 2001) to identify gravitationally bound clumps in our particle data, which we refer to as planetesimals in our study.

The Hill radius, R_H, characterizes the roughly spherical region where a planetesimal's gravity dominates over shear (Armitage 2020). This radius can be expressed as,

$$R_H = \left(\frac{m_p G}{3\Omega^2}\right)^{1/3}, \tag{2.18}$$

which gives the Hill density for a planetesimal with mass m_p,

$$\rho_H \equiv \frac{3}{4\pi}\frac{m_p}{R_H^3} = 9\frac{\Omega^2}{4\pi G}. \tag{2.19}$$

The SKID algorithm computes a mass density estimate on the dust particle data, and we consider any clumps with densities above ρ_H and with a sufficiently large mass m_p so that the Hill radius for that clump is greater than the width of the hydrodynamic grid cell, $\Delta x = L_x/N_x$. These are the same conditions used in Li et al. (2019) and Gole et al. (2020), who likewise employed a clump finding algorithm on the dust particle data to identify planetesimals. We note that the results of our study are not sensitive to these cut-offs as most of the identified planetesimals are massive enough that their Hill radius R_H is much larger than Δx, and the densities of the particles in these clumps are well clear of ρ_H, confirming that these particles are unambiguously gravitationally bound.

2.3 Planetesimal mass distribution

In this section we examine the variability in the formation of planetesimal via the streaming instability. We explore this via simulations with domains of varying sizes and re-runs of otherwise identical simulations with different random seeds used to distribute the dust particles (see Section 2.2.2).

Figure 2.1 shows the dust surface density in the x-y plane for each of our simulations at $t = 80\Omega^{-1}$. We choose to present the dust surface density and perform our mass distribution analyses at $t = 80\Omega^{-1}$ because at this time, enough planetesimals have formed to sample the distribution well, but this is also before planetesimals have grown substantially[3]. The planetesimals in Figure 2.1 are highlighted with white circles. Visually, it is clear that the distribution of dust varies significantly amongst the simulations with the same domain size and different random seeds. For the larger domain runs (such as `L08`), regions that have the same area as an entire `L02` run may contain many more or many fewer planetesimals at the same state of evolution.

2.3.1 Cumulative number distributions

For these data, we subdivide the larger simulations (`L04a`, `L04b`, `L08`) into regions with the same area as the `L02` runs. The cumulative number distributions for each sub-region are shown as separate lines in Figure 2.2. Explicitly, there are 4 such sub-domains for each `L04` run and 16 for `L08`.

Figure 2.2 demonstrates the large variability in the cumulative number distribution for the planetesimal masses at $t = 80\Omega^{-1}$ in these equal area regions. At the mass $m_p/M_{t,02} = 0.03$, the spread in the number of planetesimals within the different `L02` simulations is 14 to 22, and in the `L04` simulations the spread is 6 to 14, and in the `L08` the spread is 6 to 29. This spread–most easily seen in the `L08` simulation, which represents largest total area with 16 `L02`-sized boxes–demonstrates the variable behavior in the planetesimal formation process via the streaming instability that is not represented well by even a few `L02` simulations.

There is also variation in how these planetesimals are distributed in mass. There are many planetesimals between 0.02 M_{Ceres} and 0.03 M_{Ceres} in the `L02a` run and between

[3] In Section 2.4 we discuss how the cross-sections of the bound dust objects in the simulations in this study (and all similar studies) are unrealistically large, and how this impacts the mass distribution over time.

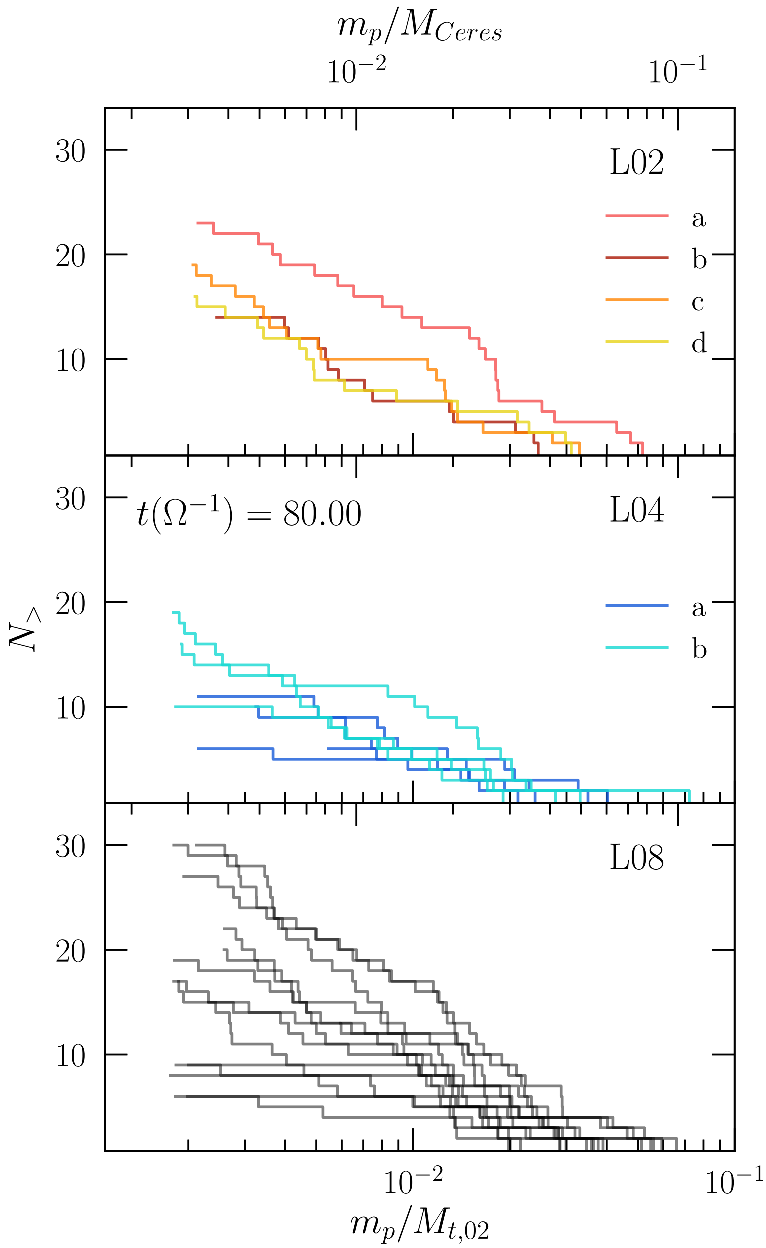

FIGURE 2.2: Cumulative number distributions of the planetesimal mass at time $t = 80\Omega^{-1}$. For the L04 and L08 data, the simulation domains have been subdivided into smaller boxes equivalent in size to the L02 domains (see Section 2.3.1). The data represents the planetesimal distribution at the simulation time $t = 80\Omega^{-1}$, the same snapshot considered in Figures 2.1 and 2.3. The planetesimal masses are given in units of the total mass of the dust in an L02-sized domain on the bottom x-axis and the mass of Ceres on the top x-axis (see Section 2.2.4 for physical unit conversions).

0.01 M_{Ceres} and 0.02 M_{Ceres} in the `L02c` run, but the other `L02` runs do not have many planetesimals at these masses. This trend is observed in the samples of `L02`-sized domains within the larger boxes as well.

2.3.2 Differential number distributions

Figure 2.3 shows the differential mass distributions, estimated as described in 2.2.6. Each symbol in the top panel represents dN/dM for just one of the four `L02` simulations. However, the indicated power-law index p was computed with all four runs. The same procedure was used for the `L04` runs in the middle panel.

We find power-law indices of $p_{02} = 1.73 \pm 0.09$, $p_{04} = 1.64 \pm 0.07$, $p_{08} = 1.60 \pm 0.04$ for the different domain sizes. The decreasing uncertainty reflect the larger total area. Within this modest uncertainty, the different cases agree with each other and are also generally in agreement with values reported in Simon et al. (2016), Simon et al. (2017) and Johansen et al. (2015).

The mass distribution of the planetesimals changes over the course of the simulations and this is reflected in the indices as shown in Figure 2.4. When considering the small domain simulations individually, as in the top panel, there is a lot of variance in the value of p, typically ranging from 1.5 to 2.0, and upper and lower limits exceeding that. This partly reflects the total numbers in each sample being in the range of 10-30 at the chosen resolution. There is a general trend to less variation at later times and smaller p values.

In the bottom panel, when the larger domains are considered and the planetesimal populations from the multiple `L02` and `L04` runs are combined, there is much less variance in the value for p. The steady, decreasing trend with time is readily apparent. At $t = 50\Omega^{-1}$, when enough planetesimals have formed to compute a reliable value for p, the values range between 1.6 and 2.0 across the different sized simulations, and well

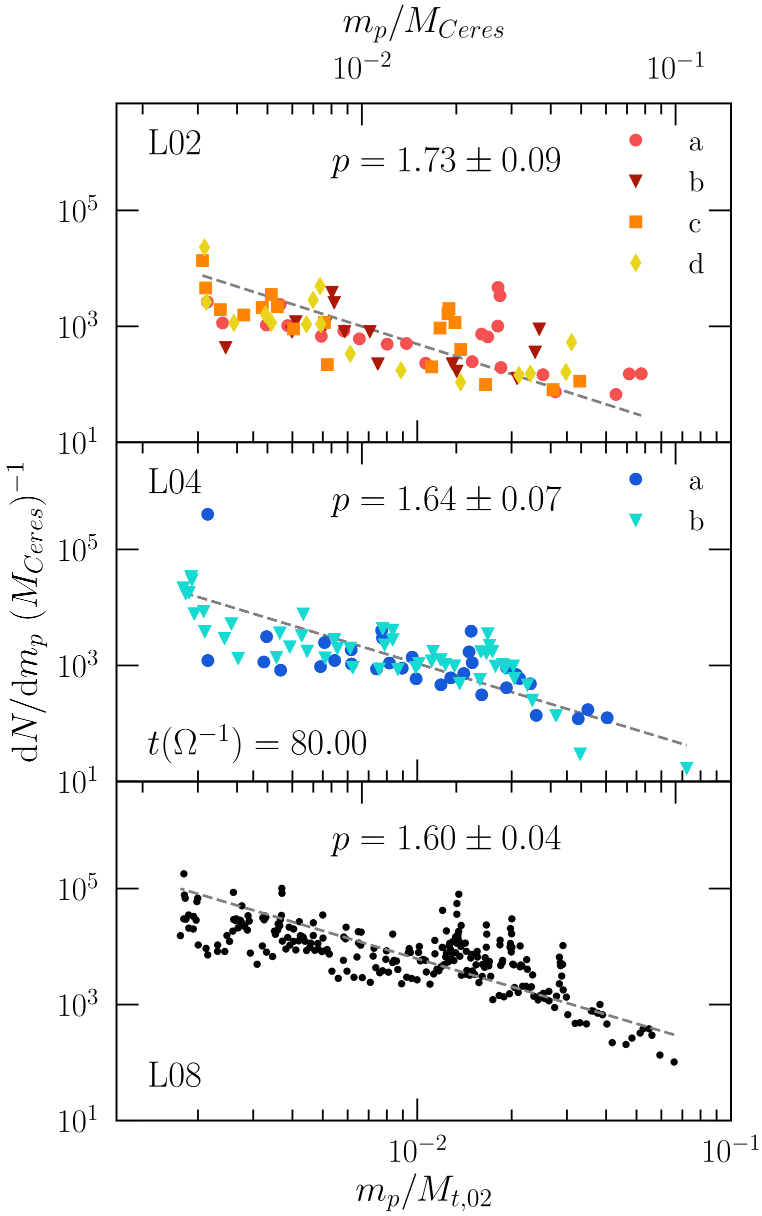

FIGURE 2.3: Differential number distributions of the planetesimal mass, computed according to equation 2.15. The data for each of the 7 simulations is plotted individually. The grey dashed lines are power-law fits, where the slopes are calculated according to equation 2.16. The calculation for the fit in the `L02` panel includes every data point for all four simulations, and the fit in the `L04` panel includes every data point in the two simulations. The data represents the planetesimal distribution at the simulation time $t = 80\Omega^{-1}$, the same snapshot considered in Figures 2.1 and 2.2. The planetesimal masses are given in units of the total mass of the dust in an `L02`-sized domain on the bottom x-axis and the mass of Ceres on the top x-axis. See Section 2.2.4 for details on the conversion to physical units (see Section 2.2.4 for physical unit conversions).

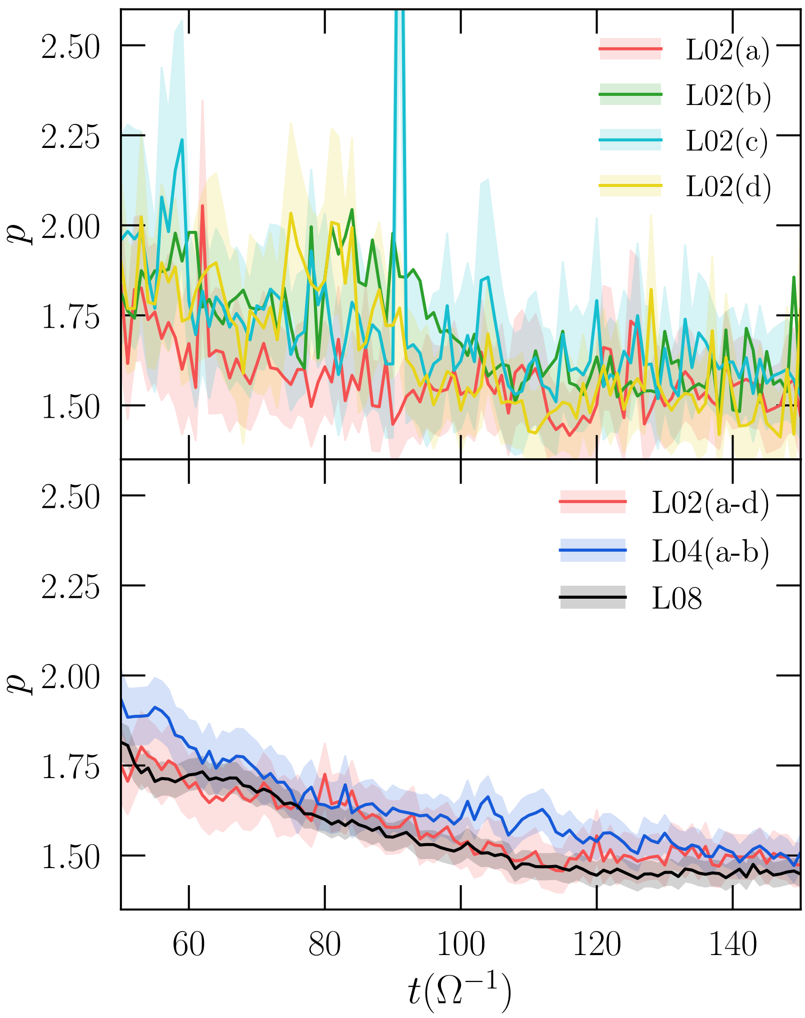

FIGURE 2.4: The slope of the power-law fit to the dN/dm_p mass distributions over time. The power-law index p is calculated according to equation 2.16. *Top.* The data for the `L02` simulations. *Bottom.* The data for all 7 simulations. As in Figure 2.3, when computing the power-law index, every data point in all of the `L02` simulations is included in the calculation for p, and the same goes for the `L04` data. *Both.* The shaded region represents σ, the error in p, calculated according to equation 2.17.

after planetesimals have formed, at $t = 150\Omega^{-1}$, the values are between 1.4 and 1.6. A decrease in p represents a shift towards fewer and more massive planetesimals at late times.

A trend toward larger masses with time is somewhat expected. However, a clear demonstration of this trend has not been demonstrated in previous studies. In Figure 3 from Simon et al. (2017), the authors show data for p over time in their simulations, but only over a relatively narrow range of time[4]. Similarly, Schäfer et al. (2017) show how the values of their fit parameters change over time, but also only for a narrow window. This decrease in distribution fit parameters emphasizes that care is needed when attempting to extract a single value for the power-law index or a single set of parameters that describes the mass distribution of planetesimals formed by the streaming instability. The mass distribution is transient and should be expected to evolve indefinitely, albeit as a slowing rate, particularly when a larger simulation domain provides for more material as shown in the next section.

2.3.3 Total mass of dust in planetesimals and the onset of planetesimal formation

Figure 2.5 shows the total mass of the planetesimals in the simulations over time. As in Figure 2.2, the larger domain simulations are divided into smaller sub-domains with the same area as the `L02` runs. The `L08` run shows the largest variance in these data. After $t = 40\Omega^{-1}$, the spread in the total dust mass in planetesimals in any of the sub-domains from the `L08` run spans 5% to 45% of the total mass of dust in a single sub-domain. The data from the `L02` and `L04` runs generally fit within the maximum-minimum bounds of the `L08` run. Once again we note that simply re-running these simulations with a different random seed leads to significantly different consequences for planetesimals

[4] Our physical dust parameters very closely match the simulation from the middle panel of their Figure 3.

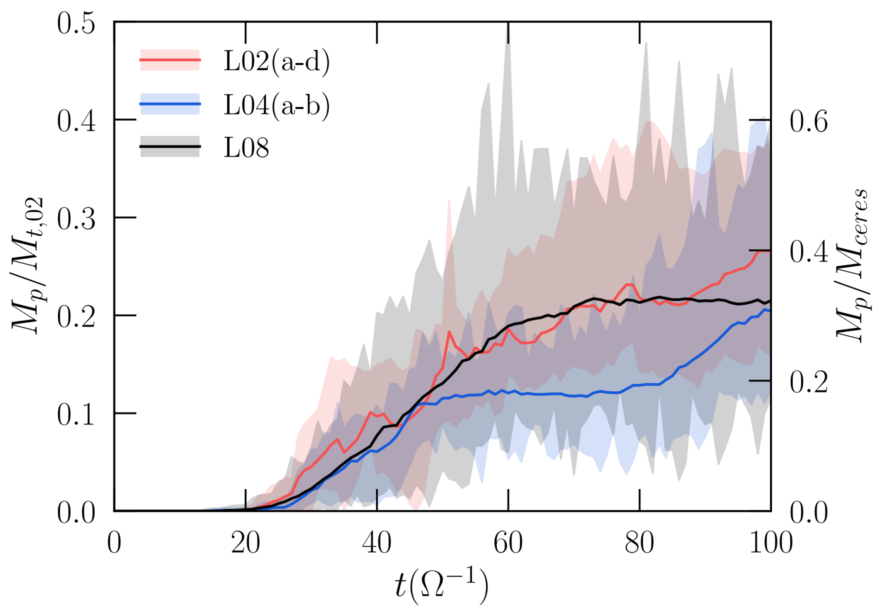

FIGURE 2.5: The total mass of the planetesimals M_p in the simulations over time. For the `L04` and `L08` data, the simulation domains have been divided into smaller boxes equivalent in size to the `L02` domains (see Section 2.3.1). For the `L02` data, all four of the small domain simulations are considered simultaneously, and the `L04` data considers both of the intermediate sized simulations. The solid line represents the average mass of planetesimals for all the `L02` or `L02`-sized boxes, and the shaded region is bounded by the maximum and minimum values in this set. The planetesimal masses are given in units of the total mass of the dust in an `L02`-sized domain on the left y-axis and the mass of Ceres on the right y-axis. See Section 2.2.4 for details on the conversion to physical units.

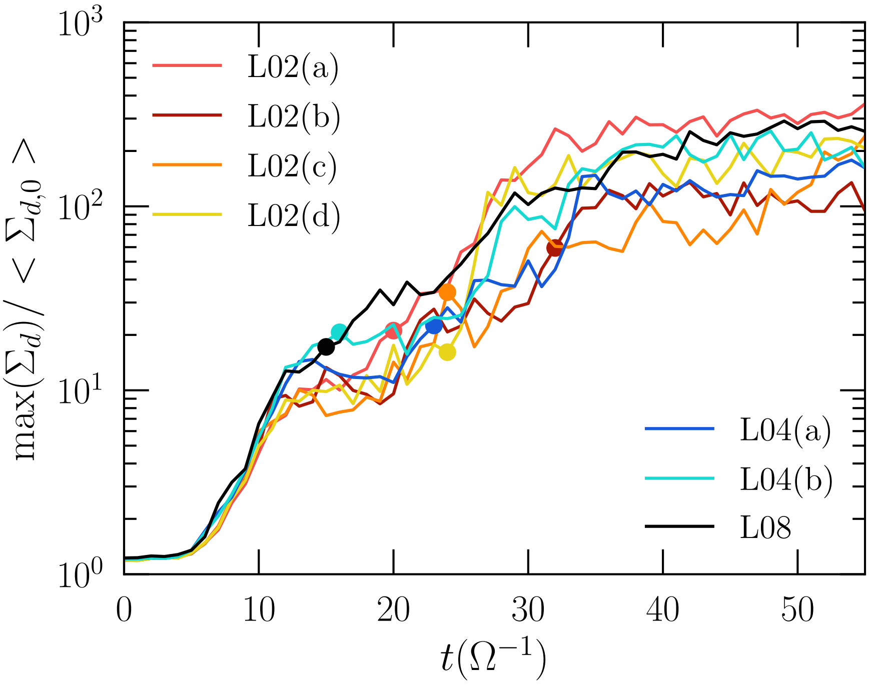

FIGURE 2.6: Maximum value for the dust surface density in the x-y plane of the 7 simulations over time, normalized by the mean dust surface density. The circles represent the point in time where each simulation first formed planetesimals.

formation, shown here directly by the wide spread denoted by the red shaded region that is quite similar to the region-to-region variation in the larger domains.

Figure 2.6 shows the maximum value of the dust surface density, $\max(\Sigma_d)$, in the x-y plane over the course of all 7 simulations. Before approximately $t \sim 10\Omega^{-1}$, all simulations evolve quite similarly, however, between about $t \sim 10\Omega^{-1}$ to $t \sim 20\Omega^{-1}$, the larger domain simulations have the highest values of $\max(\Sigma_d)$. After this time highly turbulent motions are present in the dust dynamics and the chaotic evolution of the dust density leads to diverging tracks.

The point where planetesimals first form in each simulation (denoted by the circles in Figure 2.6) spans a range of $t = 15\Omega^{-1}$ to $35\Omega^{-1}$. This is another representation of the non-linear nature of the streaming instability: even among nearly identical simulations, the dust surface density can evolve differently, which affects the timing for planetesimal formation. Also, the first formation of planetesimals tends to occur earlier in the bigger domains. This is likely related to the observation that the value of $\max(\Sigma_d)$ is higher in the larger domains from $t \sim 10\Omega^{-1} - 20\Omega^{-1}$. Planetesimal formation requires large over-densities, and the simulations that first reach dust densities sufficient for gravitational collapse will be the first to form planetesimals. The large domain simulations can more quickly reach high dust over-densities because large scale dynamical modes can enable a faster growth to more extreme local density maxima. The influence of these large scale modes can also be seen in the variation in the spatial distribution of the planetesimals at $t = 80\Omega^{-1}$ in Figures 2.1 and 2.2. The smaller `L02` domains cannot represent the large scale modes available in the `L08` domains. We will quantify and discuss the presence of these large scale modes in an upcoming paper in this series.

2.4 Summary & Discussion

In this study we used 3D simulations of patches of protoplanetary disks to study the formation of planetesimals from the gravitational collapse of dust over-densities generated by the streaming instability. We employ simulations that use larger domains than most studies and higher resolution than a study that used similar sized domains. Also, we re-run simulations with identical physical parameters except for the randomized placement of the dust particles–a novel approach for these kinds of simulations. Both the larger domains and re-run simulations allow us to probe the variability in the population of planetesimals which is caused by the non-linear nature of the streaming instability. Our main results are as follows:

(i) The cumulative number distribution for the planetesimal mass in any of the single `L02` domains (which represent the maximum domain size used by most similar studies) or `L02`-sized sub-domains within the larger simulations exhibits large variability. The re-run `L02` simulations exhibit a spread in the total number of planetesimals that ranges from 14 to 22, and this spread is 6 to 29 in the sub-domains within the `L08` simulation. That is, there is greater variability in the planetesimal distribution in the larger domain simulations than the smaller domains. The number of planetesimals at specific masses is also highly varied within the different `L02` or `L02`-sized domains.

(ii) Variability in the planetesimal formation process can also be seen in the total mass of dust converted to planetesimals within these domains. In the case of re-run `L02` simulations, the mass conversion rate to planetesimals varies between 5 and 25%, and within the domain of the `L08` simulation this conversion is between 5 and 45%. Spatial variability in the planetesimal formation process has not previously been reported in other studies.

(iii) In our study we characterize the differential number mass distribution of planetesimals with a single parameter: a power-law index. The value of this parameter is consistent across our three different choices of domain size when all planetesimals for each domain size are considered together, and our values as consistent with the index measured by other studies. However, we find these indices decrease over time, by as much as $\sim 10\%$ over the course of several orbits. This is representative of the planetesimal population becoming more top-heavy, i.e. the largest planetesimals disproportionately increase in mass over the course of the simulation. Thus, identifying a single choice of parameters that describes the mass distribution may be intrinsically difficult in our simulations and similar set-ups.

(iv) The dust surface density in the radial-azimuthal plane in the `L08` simulation displays box-scale structure in the azimuthally oriented filaments. In this large domain, the filaments do not span the full azimuthal extent as in the smaller domain simulations. The distribution of planetesimals is also clearly unevenly distributed in the azimuthal directions. This implies large-scale dynamical modes which are not present in the small domains are contributing to the highly variable planetesimal formation process observed in the `L08` simulation. In subsequent work, we intend to quantify these larger-scale modes and their role.

(v) The maximum surface density grows quicker and planetesimals form earlier in larger domains simulations. This suggests an active role for larger-scale dynamical modes that exists in the larger domains but cannot be represented by the smaller domains. Again, we defer a detailed exploration of large-scale modes to a upcoming work where we will consider filament evolution leading up to planetesimal formation.

2.4.1 Ongoing challenges and future work

When characterizing the planetesimal mass distribution in our simulation, and in all studies that employ similar techniques, a fundamental issue arises due to limited computational power. At the resolution in our study, the minimum length scale that is resolved, i.e. the cell-size, converts to approximately $\sim 30,000$ km in physical units (see Section 2.2.4). The gravitational force is discretized at this length scale, meaning this is the smallest sized bound object that can represented in our simulation. We should aim to probe kilometre and tens of kilometres length scales: the true length scale of planetesimals, extrapolated from observations of asteroids and Kuiper Belt objects. If we kept the same domain sizes from this study, we would require some 1000 times better resolution, or 1000 times more grid points in each dimension. This is beyond the reach of current computational capabilities. Our conclusion then is the smallest planetesimals in our study (and all studies of this variety) do not accurately represent what we would expect to be the true smallest planetesimal mass in nature. Simon et al. (2016) use higher resolution simulations in their study and the minimum planetesimal mass in that study is not converged. This means that the low-mass end of the planetesimal mass distribution in such studies is still an open question. The minimum size of the planetesimals is an important parameter in studies that model the interior evolution of the planetesimals to constrain the planetesimal formation timescales in the early Solar system (Lichtenberg et al. 2018).

A second effect of the large grid cell size is the enhancement of planetesimal-planetesimal interactions such as mergers and planetesimal-disk interactions such as the accumulation of dust material post-formation, compared to what would occur in nature. As mentioned in our summary point (iii) above, we observe that the mass distributions become increasingly top-heavy over time, but this phenomenon is likely more pronounced in this and all similar work due to artificially large interaction cross-sections. Planetesimals could accrete mass after formation, but not with effective collisional cross-sections of $\sim$ 1 billion km^2. To combat this issue, Gole et al. (2020) use a clump-tracking algorithm to identify planetesimal masses at the moment they are formed in their simulation. This probes the "birth" mass distribution, and avoids including planetesimals that may have grown artificially large. Johansen et al. (2015) and Schäfer et al. (2017) replace bound dust objects with sink particles but find this does not substantially change the mass distribution. The objective of our study, which used moderate resolution, was not to definitely explore the planetesimal mass distribution itself, so we do not employ these more advanced techniques. Instead, we study how these outcomes vary due to larger domain simulations and across a sample of re-run simulations. Our methods are sufficiently accurate for those purposes and illustrate the impact of domain size and intrinsic variation.

Characterizing the azimuthally-oriented dust filaments formed by the non-linear SI (readily visible in Figure 2.1) will be essential for establishing a broader understanding of planetesimal formation via the SI. These filaments are where dust over-densities become large enough to gravitationally collapse, hence they comprise the material reservoirs for planetesimal formation. Key characteristics include their radial width, and radial separation. The non-linear physics that produces these filaments makes a priori predictions from analytical theory difficult. A few studies have empirically investigated these length scales (Yang & Johansen 2014; Gerbig et al. 2020). Of particular interest is whether scales significantly larger than typical simulation boxes could affect filaments and consequent planetesimal formation. In a subsequent paper in this series, we will explore the origin and impact of characteristic dust filament lengths scales and the role of large-scale dynamical modes.

Appendix 2.A Self-gravitating shearing wave test

To test our implementation of self-gravity applied to the dust particles, we used the shearing wave test from Section 2.2.2 of Simon et al. (2016) and Section 1.3.1 of the Supplementary Information from Johansen et al. (2007), which is based on methods from Goldreich & Lynden-Bell (1965). In this set-up, the initial condition is a plane wave perturbation in the x-y (radial-azimuthal) plane and uniform properties in the z direction, and the amplitude of the wave is small compared to the background follows so that the evolution of the amplitude can be described by a linear approximations to the hydrodynamic equations. As in Simon et al. (2016) and Johansen et al. (2007), we compare the evolution of the amplitudes from the numerical integration in Athena to a semi-analytical Runge-Kutta integration of the amplitudes computed using the `solve_ivp` routine from the `scipy.integrate` module of SciPy ver. 1.1.0 (Virtanen et al. 2020).

The numerical integration used the shearing box configuration in Athena with purely periodic boundary conditions in y and z and shear-periodic boundaries conditions in x. Also, to isolate the influence of the self-gravity forces on the wave, we eliminate the back-reaction of the aerodynamic drag of the dust particles on the gas, which is akin to considering a dust-gas mixture with a very low dust-to-gas mass ratio, μ (see equation 2.2). The equations that describe the full self-gravitating dust fluid in this case are thus,

$$\frac{\mathrm{d}\rho_d}{\mathrm{d}t} = -\rho_g(\nabla \cdot \boldsymbol{v}), \tag{2.A1a}$$

$$\frac{\mathrm{d}\boldsymbol{v}}{\mathrm{d}t} = -\nabla\Phi - \frac{\Omega}{\tau_s}(\boldsymbol{v} - \overline{\boldsymbol{u}}), \tag{2.A1b}$$

$$\nabla^2\Phi = 4\pi G\rho_d, \tag{2.A1c}$$

where $\overline{\boldsymbol{u}}$ is the background gas velocity, but going forward we will set this velocity to zero, placing the integration in the frame of the background gas fluid, leaving the drag term above proportional only the to dust fluid velocity w.r.t. to this background, stationary gas fluid.The other symbols represent the same quantities as Section 2.2.1. In the frame of the shearing flow, given by $((3/2)\Omega x)\hat{\boldsymbol{y}}$, we have,

$$\frac{\mathrm{d}\rho_d}{\mathrm{d}t} - \frac{3}{2}\Omega x \frac{\partial \rho_d}{\partial y} = -\rho_d \nabla \cdot \boldsymbol{v}, \tag{2.A2a}$$

$$\frac{\mathrm{d}\boldsymbol{v}}{\mathrm{d}t} - \frac{3}{2}\Omega x \frac{\partial \boldsymbol{v}}{\partial y} = 2\Omega v_y \hat{x} - \frac{1}{2}\Omega v_x \hat{y} - \nabla\Phi - \frac{\Omega}{\tau_s}\boldsymbol{v}, \tag{2.A2b}$$

$$\nabla^2\Phi = 4\pi G \rho_d. \tag{2.A2c}$$

Now, following Goldreich & Lynden-Bell (1965), we transform to sheared axes, which we denote with a $'$,

$$x' = x \tag{2.A3a}$$

$$y' = y + (3/2)\Omega x t \tag{2.A3b}$$

$$t' = t \tag{2.A3c}$$

and the derivatives in terms of these axes are,

$$\frac{\partial}{\partial x} = \frac{\partial}{\partial x'} + (3/2)\Omega t' \frac{\partial}{\partial y'} \tag{2.A4a}$$

$$\frac{\partial}{\partial y} = \frac{\partial}{\partial y'} \tag{2.A4b}$$

$$\frac{d}{dt} = \frac{d}{dt'} + (3/2)\Omega x' \frac{\partial}{\partial y\prime}. \tag{2.A4c}$$

The linear perturbations to the fluid properties are of the form,

$$\rho_d = \rho_{d0}[1 + \delta\rho_d], \tag{2.A5}$$

$$\boldsymbol{v} = \overline{\boldsymbol{v}} + \delta\boldsymbol{v}, \tag{2.A6}$$

thus, we note that $\delta\rho_d$ is a dimensionless quantity. The functional form the perturbations is a plane wave in the sheared axes,

$$\delta f(x', y') = \widetilde{f}\exp[i(k_x x' + k_y y' - \omega t)]. \tag{2.A7}$$

Lastly, still following Goldreich & Lynden-Bell (1965), we denote a dimensionless shear time parameter

$$\tau \equiv (3/2)\Omega t' - k_x/k_y, \tag{2.A8}$$

and we will track the temporal evolution of the wave according to this parameter τ. Returning to the shearing-frame fluid equations from eq. 2.A2, applying the linear, small-amplitude perturbations and discarding non-linear terms, we have the equations that describe the evolution of the amplitudes of the wave with the dimensionless time τ:

$$\frac{d\delta\rho_d}{d\tau} = -i\frac{2k_y}{3\Omega}(\delta v_x \tau + \delta v_y), \tag{2.A9a}$$

$$\frac{d\delta v_x}{d\tau} = \frac{4}{3}\delta v_y + i\frac{2}{3\Omega}\tau\frac{4\pi G}{k_y(1+\tau^2)}\rho_{d,0}\delta\rho_d - \frac{2}{3\tau_s}\delta v_x, \tag{2.A9b}$$

$$\frac{d\delta v_y}{d\tau} = -\frac{1}{3}\delta v_x + i\frac{2}{3\Omega}\frac{4\pi G}{k_y(1+\tau^2)}\rho_{d,0}\delta\rho_d - \frac{2}{3\tau_s}\delta v_y. \tag{2.A9c}$$

We choose the following parameters for the numerical (Athena) and semi-analytic integrations: $\tau_s = \rho_{d,0} = k_y = G = 1.0$, and the initial conditions: $\tau_0 = -2$, $\delta v_x(\tau_0) =$

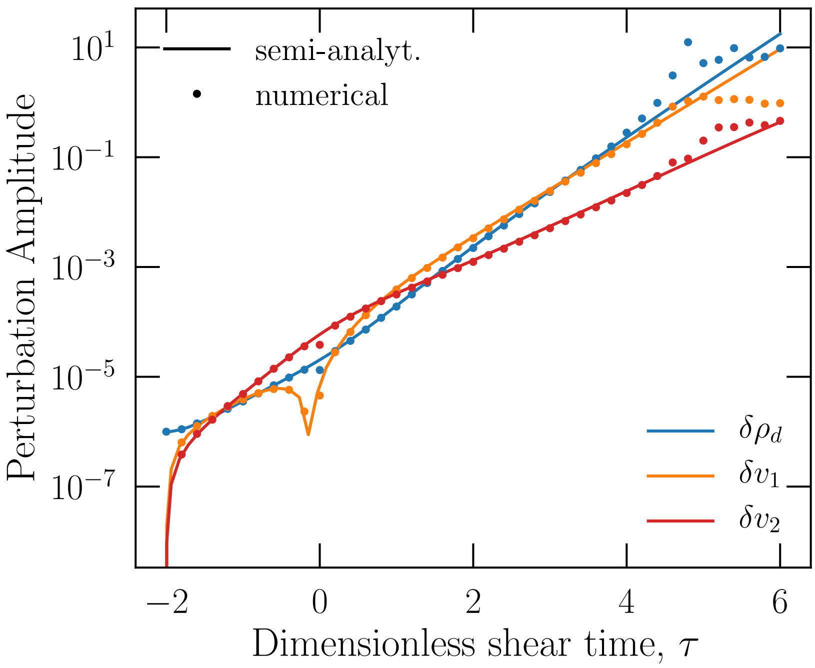

FIGURE 2.A1: Evolution of the amplitudes of the self-gravitating dust fluid from the shearing wave test. The solid lines represent the evolution from a semi-analytical Runge Kutta integration, and the dots represent the evolution from the numerical (ATHENA) integration. The time axis is units of the dimensionless shearing time parameter τ.

$\delta v_y(\tau_0) = 0$, $\delta\rho_d(\tau_0) = 10^{-6}$. The domain in ATHENA is set-up with $(L_x,L_y,L_z) = (2\pi,2\pi,0.2)$ and $(N_x,N_y,N_z) = (256,256,2)$.

The evolution of the amplitudes of the sheared wave is shown in Figure 2.A1. The numerical and semi-analytic solutions agree strongly until $\tau \sim 4$, when the $\delta\rho_d/\rho_{d,0}$ amplitude approaches 0.1, and the perturbation becomes non-linear. At this point the linearized equations no longer describe the non-linear behavior captured in the numerical integration. This confirms that our implementation of self-gravity for the dust particles follows the expected behavior.

Acknowledgements

These simulations were performed on the Niagara system operated by SciNet and Compute Canada. JW thanks NSERC for funding support.

Chapter 3

Streaming instability on different scales. II. Filaments and dynamics

The following presents work towards a paper to be submitted to the Monthly Notices of the Royal Astronomical Society (MNRAS), by J. Rucska and J. Wadsley.

Abstract

We present numerical simulations of strong dust clumping via the non-linear streaming instability (SI). We focus on the dust filaments in the pre-planetesimal formation phase. The dense filaments represent the mass reservoir available to planetesimals, and are an under-studied component of the SI. We model patches of protoplanetary disks with varying physical sizes, and find the small domains common to prior work predict filaments that are globally ring-like, yet in large domains these filaments are azimuthally truncated. Fourier spectra reveal dynamics at large scales inaccessible to smaller domains. The natural radial filament spacing length also occurs at a scale where the small domains have limited spectral resolution, forcing the organization of the dust into limited

configurations not seen in larger simulations. A mock filament profile fitting procedure shows that small variations in the filament spacing can explain aspects of the simulations spectra that are otherwise difficult to model. Our results suggests large domain simulations of the SI are useful tools for constraining properties of the mass reservoir available to planetesimal formation via the SI.

3.1 Introduction

The formation of rocky planetary cores begins with the micron-sized grains the protoplanetary disc inherits from the interstellar medium. These micron-sized grains grow via collisions to pebbles in the size range of millimetres to centimetres (Birnstiel et al. 2016). Recent observations of these pebbles in protoplanetary discs have revealed a stunning diversity in disc size and structure (e.g. Ansdell et al. 2016; Andrews et al. 2018; van der Marel et al. 2021). An open question concerns how these pebbles grow to become kilometre-sized planetesimals–the precursors to protoplanets, full sized rocky planets, and the cores of some gas giants. In protoplanetary discs, collisions between dust objects of approximately a centimetre in size are believed to occur at relative velocities large enough that the collisions are primarily destructive (Zsom et al. 2010; Güttler et al. 2010; Windmark et al. 2012). Further, objects near a metre in size will drift rapidly into the central star due to the headwind they feel from the gaseous component of the disc (Weidenschilling 1977a). Hence, a mechanism for the rapid formation of planetesimals directly from pebbles is required to overcome these barriers.

The streaming instability (SI, Youdin & Goodman 2005) is a leading mechanism for this process. In the disc midplane, dust pebbles orbit at slightly different speeds from the gas, which is subject to a radial pressure force (Nakagawa et al. 1986). Under these conditions, the dust and gas constantly exchange momentum via aerodynamic coupling. This coupling is a key driver of SI dynamics. For pebble-sized grains in environments with high local dust mass concentrations, the SI growth rates are substantial, leading to the rapid, spontaneous concentration of dust (Johansen & Youdin 2007; Bai & Stone 2010b). In stratified disc models, the settling of dust to a dense midplane layer can initiate other hydrodynamic instabilities such as the Kelvin-Helmholtz instability (KHI), which can interact with SI and drive dust clumping (Gerbig et al. 2020; Lin 2021). The dust clumps created by the SI can easily grow to high densities that are unstable to gravtiational collapse, resulting in the formation of bound planetesimals from pebble clouds in just tens of orbits (Johansen et al. 2007).

Before planetesimals form, the non-linear phase of the streaming instability collects dust into extended, azimuthally-oriented filaments. These filaments have been seen in 3D simulations of the SI under a wide range of physical conditions (Johansen et al. 2007; Bai & Stone 2010a; Simon et al. 2016; Simon et al. 2017; Li et al. 2018; Abod et al. 2019; Carrera et al. 2021). It is primarily within these filaments that the highest local dust densities are achieved. Thus, these filaments represent the reservoirs of dust mass available for planetesimal formation, and characterizing their properties–such as key length scales: width, separation, and the total mass in these structures–is essential to characterizing planetesimal formation via the SI more broadly.

Once planetesimals are formed, the subsequent phase in planet formation is the growth of protoplanetary cores. Recent models have directly incorporated outcomes from the non-linear SI to inform their input planetesimal populations (Liu et al. 2019; Jang et al. 2022). Useful predictions from the SI include the shape of the planetesimal mass distribution, the characteristic planetesimal mass, and the maximum and minimum planetesimal mass. Constraining these quantities has the been the focus of much prior work (Johansen et al. 2015; Simon et al. 2016; Simon et al. 2017; Schäfer et al. 2017; Abod et al. 2019; Li et al. 2019; Gole et al. 2020). By comparison, the filaments that represent the mass reservoir planetesimals are born from has been relatively understudied.

This is partially because a robust characterization of the length scales and timescales of the non-linear streaming instability across a wide range of physical conditions has remained elusive. The analytic theory for the linear mode of the SI assumes the perturbations are both axisymmetric and oriented in the radial-vertical direction (Youdin & Goodman 2005; Youdin & Johansen 2007; Bai & Stone 2010b; Squire & Hopkins 2018). Thus, progress on characterizing the filaments seen in the non-linear SI in 3D has come through empirical measurements of simulation data. Yang & Johansen (2014) and Li et al. (2018) represent the most dedicated studies to date. Both explore how the vertical dynamics of the non-linear SI can affect outcomes in the disc midplane relevant to planetesimal formation. Gerbig et al. (2020) connect properties of the non-linear dust dynamics to length scales and time scales associated with the KHI and report on measurements of some filament properties.

There remains much to explore regarding SI filaments. Yang & Johansen (2014) and Li et al. (2018) modelled SI dynamics without the gravitational collapse of bound objects. In prior work (Rucska & Wadsley 2021), we find that the formation of planetesimals disrupts the filament structures, which suggests the filament-dominated phase is temporary and difficult to identify in models that cannot conclusively delineate the beginning of planetesimal formation. Further, an in-depth exploration of Fourier spectra of the dust surface density can effectively highlight key length scales in the system dynamics, and Li et al. (2018) are the only study to our knowledge to provide a brief exploration of Fourier modes in the dust density.

In this paper, we conduct an expanded analysis on a data set first studied in a previous paper (Rucska & Wadsley 2021, hereafter Paper I). Our simulation suite is composed of multiple runs of varying domain size. We use self-gravitating models to identify the pre-planetesimal, dust filament dominated phase of the SI. We conduct in-depth analyses of Fourier spectra, and discuss a novel technique using mock 1D filament profiles which can explain unique features of the simulation's surface density Fourier spectra.

Our paper is organized as follows. In Section 3.2, we briefly summarize our model, numerical methods, and physical parameters. In Section 3.3 we analyze the real-space dust surface density features with a focus on the filaments. In Section 3.4 we discuss properties of 1D Fourier spectra in both the radial and azimuthal direction. In Section 3.5 we describe a procedure for generating mock filament profiles, and how their spectra compare to our simulation data spectra. Finally, in Section 3.6 we summarize our results, discuss their impact on the field and prospects for future work. Appendix Appendix 3.A summarizes a small parameter sweep to provide loose constraints of filament properties with our mock signal procedure. In Appendix Appendix 3.B we repeat our analyses at different numerical resolutions, and conclude that the level of resolution common to prior work struggles to capture the filament properties explored in our study.

3.2 Methods and initial conditions

The numerical methods, set-up, and parameter choices for this study are identical to those used in Paper I. Hence, here we provide only a summary of our methods and direct readers seeking a more detailed description to Paper I.

We model the dynamics of a local region of a protoplanetary disc, which involves a gas phase coupled to a solids or dust phase via aerodynamic drag. The disc is localized using the shearing sheet approximation (Goldreich & Lynden-Bell 1965), in which a local Cartesian frame (co-ordinates x, y, z) co-rotates with the Keplerian rotation in the disc.

The following equations describe the gas and dust evolution:

$$\frac{\partial \rho_g}{\partial t} + \nabla \cdot (\rho_g \boldsymbol{u}) = 0, \tag{3.1}$$

$$\begin{aligned}\frac{\partial \rho_g \boldsymbol{u}}{\partial t} &+ \nabla \cdot (\rho_g \boldsymbol{u}\boldsymbol{u}) = -\nabla P_g \\ &+ \rho_g \left[-2\boldsymbol{\Omega} \times \boldsymbol{u} + 2q\,\Omega^2 x\,\hat{\boldsymbol{x}} - \Omega^2 z\,\hat{\boldsymbol{z}} + \mu \frac{\overline{\boldsymbol{v}} - \boldsymbol{u}}{t_{\text{stop}}} \right],\end{aligned} \tag{3.2}$$

$$\frac{d\boldsymbol{v}_i}{dt} = 2\boldsymbol{v}_i \times \boldsymbol{\Omega} + 2q\,\Omega^2 x\,\hat{\boldsymbol{x}} - \Omega^2 z\,\hat{\boldsymbol{z}} - \frac{\boldsymbol{v}_i - \boldsymbol{u}}{t_{\text{stop}}} + \boldsymbol{F}_g, \tag{3.3}$$

where ρ_g denotes the gas mass volume density, P_g is the gas pressure, $\mu \equiv \rho_d/\rho_g$ is the ratio of the local dust mass density to the gas mass density, $\boldsymbol{u}$ is the velocity of the gas, and $\boldsymbol{v}_i$ is the velocity of an individual dust particle, which tracks a clump of dust mass. We use an isothermal equation of state, $P_g = \rho_g c_s^2$, where c_s is the sound speed. The parameter q is the exponent for the power-law of angular rotation frequency with radial position in the disc, $\Omega \propto r^{-q}$, which in Keplerian rotation has the value $q = 3/2$.

The magnitude of the drag term and dynamical timescale for the exchange of momentum between the gas and dust is set by the stopping time of the dust particle, t_{stop}. In the Epstein drag regime (Epstein 1924), where the particle size is smaller than the mean free path of the gas, this parameter is given by

$$t_{\text{stop}} = \frac{\rho_s s}{\rho_g c_s} \tag{3.4}$$

where ρ_s is the bulk solid density of the particles (approximately $2.6\,\mathrm{g\,cm^{-3}}$ for silicates, Moore & Rose 1973) and s is the radius of the dust grains. In protoplanetary discs, the Epstein drag regime applies to dust particles everywhere except the very inner part of the disc (Birnstiel et al. 2016).

3.2.1 Numerical methods

Our simulations employ the Athena hydrodynamics grid code (Stone et al. 2008; Stone & Gardiner 2009) with the Lagrangian particles module to model the dust (Bai & Stone 2010b). Our hydrodynamic scheme uses the HLLC Reimann solver and the cornered transport upwind (CTU) integrator. For the dust momentum evolution, we use a semi-implicit integrator, as well as the triangular-shaped cloud (TSC) scheme to interpolate particles to and from the gas grid.

The background Keplerian radial shear velocity is integrated separately from the fluctuations to the shear. This common technique increases numerical accuracy and decrease computational run time (Masset 2000; Johnson et al. 2008; Stone & Gardiner 2010). Thus, the dust momentum equation that is integrated by the simulation has the background shear flow subtracted,

$$\frac{d\boldsymbol{v}_i'}{dt} = 2(v_{iy}' - \eta v_K)\Omega\hat{\boldsymbol{x}} - (2-q)v_{ix}'\Omega\hat{\boldsymbol{y}} - \Omega^2 z\hat{\boldsymbol{z}} - \frac{\boldsymbol{v}_i' - \boldsymbol{u}'}{t_{\text{stop}}} + \boldsymbol{F}_g \tag{3.5}$$

where $\boldsymbol{v}' = \boldsymbol{v} - (q\Omega x)\hat{\boldsymbol{y}}$ and $\boldsymbol{u}' = \boldsymbol{u} - (q\Omega x)\hat{\boldsymbol{y}}$. This background shear flow requires the use of shearing box boundary conditions across the radial (x-direction) numerical domain boundary (see Hawley et al. 1995; Stone & Gardiner 2010). The azimuthal (y-direction) and vertical (z-direction) boundary conditions are purely periodic.

As in prior work (Bai & Stone 2010b), we model the influence of the radially outward pointing gas pressure gradient with a constant inward radial force term applied to the dust, $\boldsymbol{F}_{\text{grad}} = -2\eta v_k \Omega\hat{\boldsymbol{x}}$. The parameter η is related to the strength of the radial pressure gradient, and is give by,

$$\eta = n\frac{c_s^2}{v_k^2}. \tag{3.6}$$

where n is the exponent of the radial pressure profile $P_g \propto r^{-n}$. The value of η (and n) is ultimately set by another parameter, Π (see equation 3.12).

We include the gravitational acceleration from the dust density field in the dust fluid momentum calculations. This permits the collapse of high-density regions and the formation of bound dust clumps. Though the focus of this study is not on the clumps or planetesimals themselves, we include the effects of self-gravity so that we can accurately model and analyze the environment they are actively formed in. This acceleration is given by,

$$\boldsymbol{F}_g = -\nabla\Phi_d \tag{3.7}$$

where the gravitational potential due to the dust density field, Φ_d, comes from the solution to Poisson's equation,

$$\nabla^2\Phi_d = 4\pi G\rho_d, \tag{3.8}$$

where G is the gravitational constant. To solve this equation we use an FFT method implemented by C.-G. Kim (Kim & Ostriker 2017), with shear-periodic horizontal boundary conditions (Gammie 2001) and vacuum (open) boundary conditions in the vertical direction (Koyama & Ostriker 2009).

3.2.2 Initial conditions & parameters

As with Paper I, our choice for the parameters for the dust mass, dust grain size, radial pressure gradient, and ratio of gravitational and rotational shear strength are either identical or very similar to choices from previous work (Johansen et al. 2012; Simon et al. 2016; Schäfer et al. 2017; Li et al. 2018; Gole et al. 2020). These parameters are summarized briefly discussed in this section, and our choices for those values are in the bottom row of Table 3.1.

The initial gas density is set to be uniform in the x-y plane and with a Gaussian profile in the vertical direction

$$\rho_g(z) = \rho_{g,0}\exp\left(-\frac{z^2}{2H_g^2}\right) \tag{3.9}$$

where $\rho_{g,0}$ is the gas density in the midplane and H_g is the gas scale height. We set the units of our model so that $\rho_{g,0} = H_g = \Omega = c_s = 1$. Following section 2.4 of Paper I, if we choose the disc model from Hayashi (1981) with $H_g(r) \sim 0.033(r/\mathrm{AU})^{5/4}$ and place our local shearing-box model at $r = 3$ AU, then the total mass of dust in the simulation domain is 1.34×10^{24} g $\approx 1.5 M_{\mathrm{Ceres}}$, and the $0.2H_g$ side length of our smallest domain converts to ~ 0.025 AU.

The dust particle positions are initialized with a random number generator that sets a similar initial density profile to the gas: uniform in the x-y plane, and a Gaussian profile in the z direction with a scale height $H_d = 0.02H_g$. We re-run simulations with identical physical parameters but different initial random seeds (labelled with a letter `a`, `b`, `c`, or `d` in Table 3.1), which changes the exact initial placement of the dust particles and sets a differential initial noise field in the dust density. Through the non-linear nature of the streaming instability, the differences in these initial perturbation leads to macroscopic differences in the high-density dust features such as filaments and planetesimals. This procedure from Paper I probes the variability in the non-linear SI.

We parameterize the drag stopping time (t_{stop}, see equation 3.4) via a dimensionless parameter,

$$\tau_s \equiv t_{\mathrm{stop}}\Omega, \tag{3.10}$$

and we choose $\tau_s = 0.314$, which is the same stopping time from Paper I and many other studies. The mass of the dust particles is controlled by the ratio of dust mass surface Σ_d density to the gas mass surface Σ_g density,

$$Z \equiv \frac{\Sigma_d}{\Sigma_g}, \tag{3.11}$$

TABLE 3.1: Simulation parameters.

Run name	Domain Size $(L_x \times L_y \times L_z)/H_g$	Grid Resolution $N_{\rm cell} = N_x \times N_y \times N_z$
L02a	$0.2 \times 0.2 \times 0.2$	$120 \times 120 \times 120$
L02b	$0.2 \times 0.2 \times 0.2$	$120 \times 120 \times 120$
L02c	$0.2 \times 0.2 \times 0.2$	$120 \times 120 \times 120$
L02d	$0.2 \times 0.2 \times 0.2$	$120 \times 120 \times 120$
L04a	$0.4 \times 0.4 \times 0.2$	$240 \times 240 \times 120$
L04b	$0.4 \times 0.4 \times 0.2$	$240 \times 240 \times 120$
L08	$0.8 \times 0.8 \times 0.2$	$480 \times 480 \times 120$
L16	$1.6 \times 1.6 \times 0.2$	$960 \times 960 \times 120$

$N_{\rm par}/N_{\rm cell}$	τ_s	Z	$\widetilde{G}$	Π
1	0.314	0.02	0.05	0.05

and we use $Z = 0.02$, a slightly super-solar solid mass ratio. The radial pressure gradient parameter η (see equation 3.6), is parametrized via,

$$\Pi \equiv \frac{\eta v_K}{c_s}, \tag{3.12}$$

and for this parameter we choose $\Pi = 0.05$, applicable to a wide range of disc models (Bai & Stone 2010a). Lastly, the strength of self-gravity versus tidal shear is captured by

$$\widetilde{G} \equiv \frac{4\pi G \rho_{g,0}}{\Omega^2}. \tag{3.13}$$

The value of this parameter sets the relative importance of self-gravity versus tidal shear. We choose $\widetilde{G} = 0.05$, equivalent to a Toomre (1964) Q parameter of 32.

3.2.3 Simulation domain

As with Paper I, we consider simulation domains of various sizes: $L_x = L_y = L_z = 0.2$; $L_x = L_y = 0.4,\ L_z = 0.2$; $L_x = L_y = 0.8,\ L_z = 0.2$; and include one larger simulation with $L_x = L_y = 1.6,\ L_z = 0.2$. All lengths are in units of the gas scale height, H_g. We introduce a shorthand for the simulations with the previously described domain sizes, and refer to them as L02, L04, L08, L16, respectively. We also study multiple runs of the L02 and L04 simulations with identical physical parameters but different initial dust density fields, as described in the previous section. The simulation parameters are summarized in Table 3.1. We maintain an equivalent numerical resolution (in terms of cells per length) between runs which equates to a cell size of $0.2H_g/120 \approx 0.00167H_g$.

3.3 Dust surface density features

In this section we examine the features of the dust surface density from our simulations with a dedicated focus on the filaments in Section 3.3.1.

Figure 3.1 shows the (radial-azimuthal) dust surface density for all 8 simulations at time $t = 40\Omega^{-1}$. As this early time, the dominant dust features are the azimuthally-oriented filaments, and we can readily see differences in these filamentary features between simulations with different domain sizes. In the smaller L02 and L04 boxes, the filaments seem to span the full azimuthal length, while the filaments in the larger L08 and L16 runs are broken up along this dimension before they reach across the full box length. In the proceeding section we provide a quantitative assessment of this observation.

We choose $t = 40\Omega^{-1}$ as a representative time for our analyses, as this is when the filaments have become prominent features, yet before planetesimal formation has begun in earnest. Figure 3.2 shows the dust surface density in the L04a simulation over time. We see that the coherent, box-scale filaments do not form until about $t = 35\Omega^{-1}$, and they persist until about $t = 50\Omega^{-1}$, at which point the planetesimals detach from the filaments and disrupt the filament structure. Figure 3.3 shows the total dust mass in structures with a surface density above the mean (our proxy for filaments, see Section 3.3.1) and the total mass in planetesimals over time[1]. We see that the mass in filaments saturates early, and the first bound clumps appear at about $t =$

[1]Planetesimals are identified using a group finding algorithm (Stadel 2001), see Section 2.7 in Paper I for details

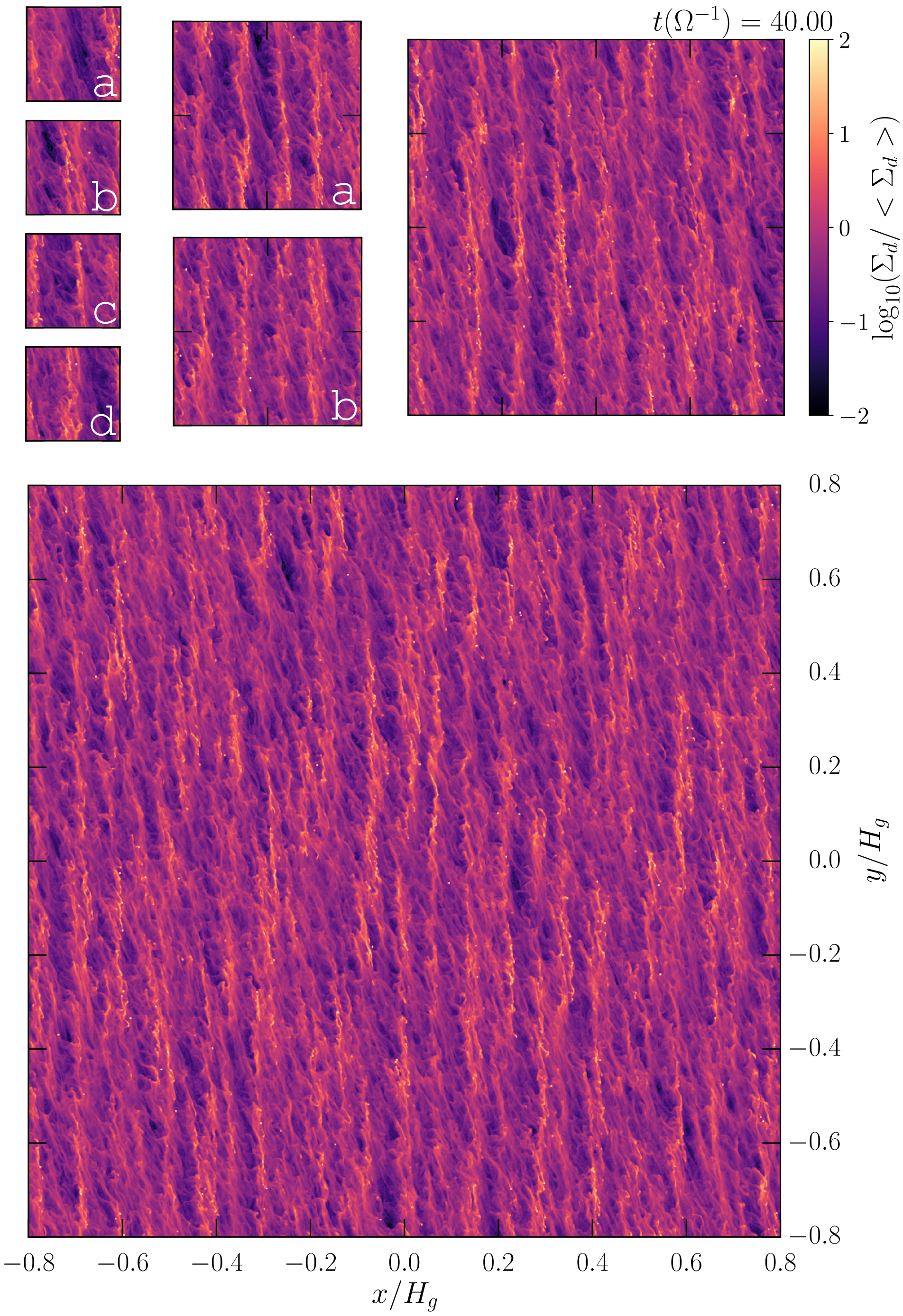

FIGURE 3.1: Dust surface density in the x-y (radial-azimuthal) plane for each of the 8 simulations. The colour represents the logarithm of the dust surface density normalized by the mean dust surface density. Each snapshot represents the simulation at time $t = 40$ in units of the inverse orbital frequency, Ω^{-1}.

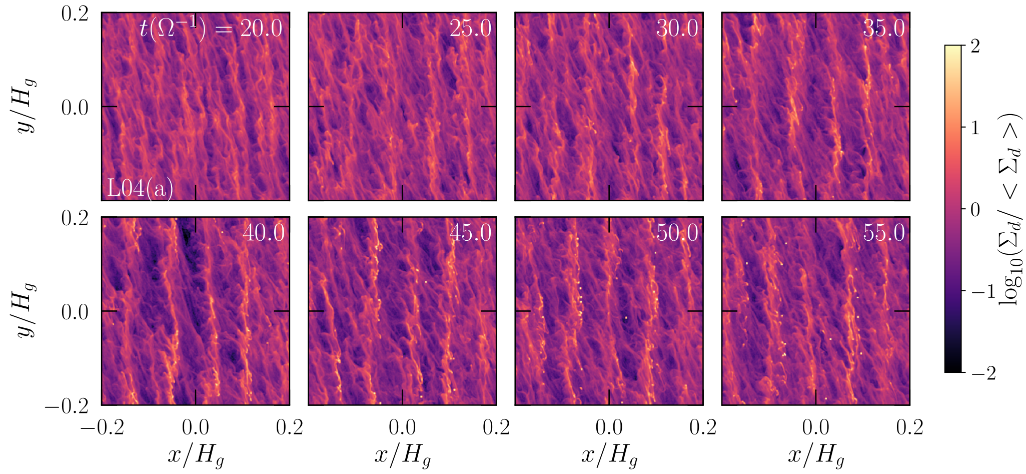

FIGURE 3.2: Dust surface density in the x-y plane for the `L04(a)` simulation over time.

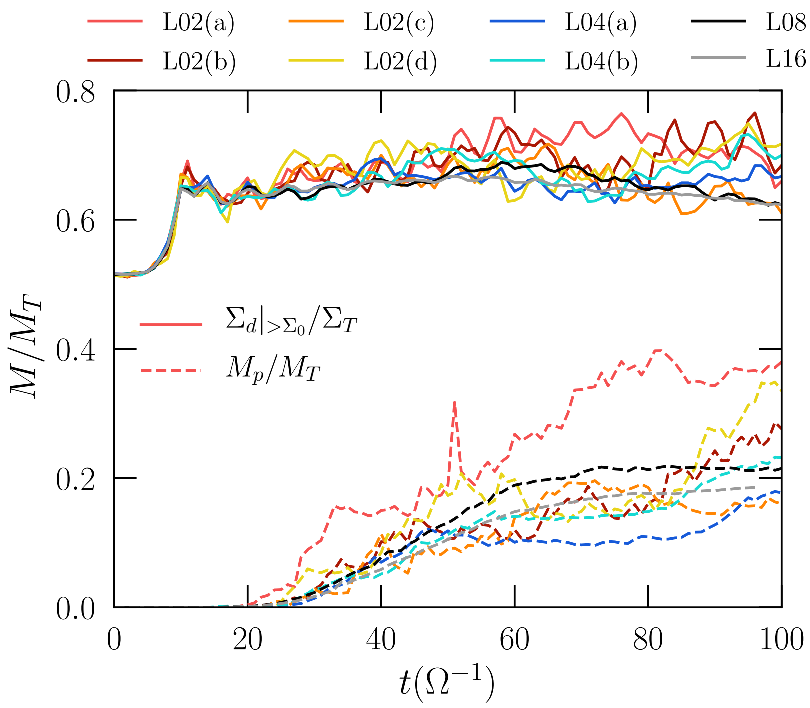

FIGURE 3.3: Total dust mass in planetesimals (M_p/M_T, dashed lines) and in over-dense structures above the mean surface density ($\Sigma_d|_{>\Sigma_0}/\Sigma_T$, solid lines) over time, for each simulation. The dust mass in these structures are normalized to the total dust mass in the box. The over-dense structures are a proxy for the filaments (see Section 3.3.1).

$20\Omega^{-1}$. Combining conclusions from Figures 3.2 and 3.3, we identify $t = 40\Omega^{-1}$ as a snapshot where the quasi-stable filaments have formed and planetesimal formation has not substantially altered their structure. Thus, we focus our analyses in this study on $t = 40\Omega^{-1}$ or a time average from $t = 40 - 50\Omega^{-1}$. The techniques we discuss are general and apply at other times, but at these times the signals we aim to measure are the strongest.

3.3.1 Filament lengths

In this section we first briefly summarize our procedure for identifying dust filaments, and then discuss our measurements of the azimuthal lengths of the filaments.

We identify filaments as contours/continuous objects that are more dense than the mean surface density in the simulation, after applying a Gaussian smoothing filter to the dust surface density. We approximate the width of the filament features as $\sim 0.0012H_g$, and set the standard deviation of the Gaussian filter as one sixth of this width. Or, equivalently, 6-σ is set as $0.0012H_g$ or 7.2 resolution elements. Our results are not strongly dependent on this choice. The smoothing filter makes the filaments/contours more continuous in shape, and thus our length analysis less noisy. Our main results hold without the filter.

To calculate the contours, we use the ASTRODENDRO Python package[2]. We do not use any advanced features of the software to identify substructures or dendrogram trees within the filaments, we simply make use of the contour-finding capabilities of this package. We choose the mean surface density of the simulation as the threshold above which to trace contours. The mean is a logical choice since the initial dust surface density is uniform in the x-y plane, so by definition this value represents the boundary between concentrated and depleted regions of dust mass. Lastly, we ignore any contours

[2] Available at `http://www.dendrograms.org`.

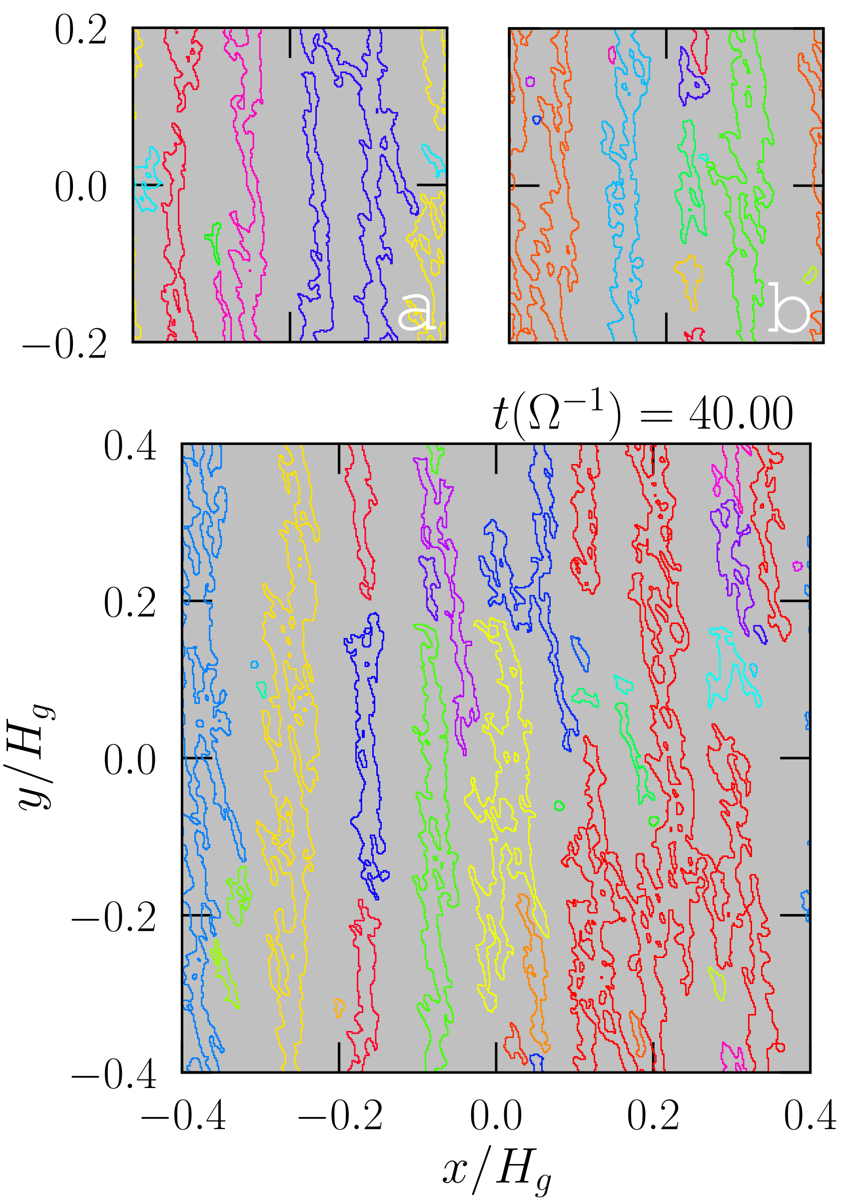

FIGURE 3.4: Identified dust filaments in the `L04(a)`, `L04(b)` (top) and `L08` (bottom) simulations. The coloured outlines represent individual filaments, defined as contours in the dust surface density at the mean surface density (see Section 3.3.1). The different colours distinguish adjacent filaments. The positions of the identified filaments/contours can be compared to the features seen in the surface density in Figure 3.1, which also represents the same simulation time $t = 40\Omega^{-1}$.

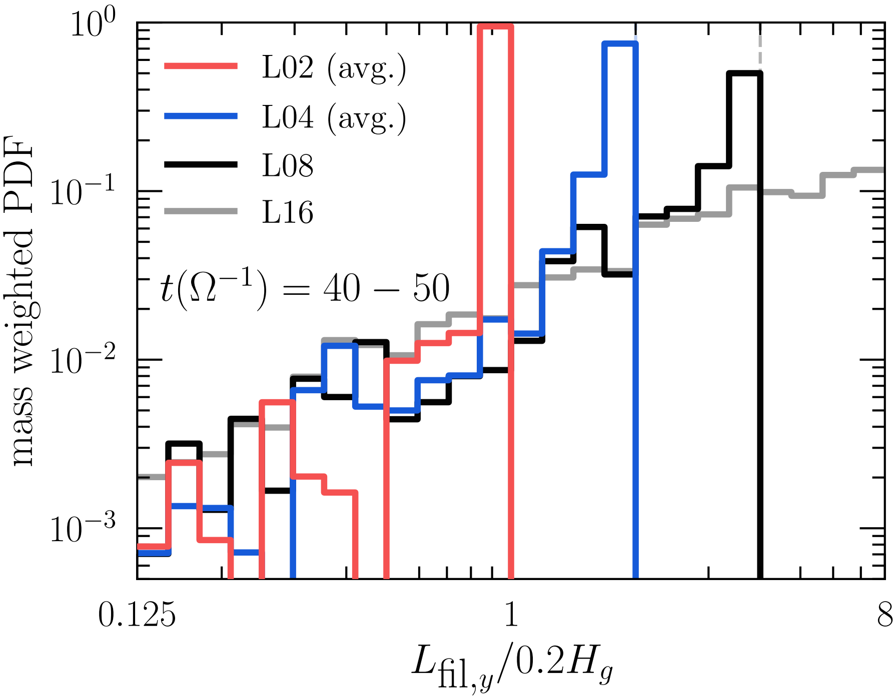

FIGURE 3.5: Mass weighted probability density functions (PDF) for the azimuthal (y-dir.) lengths of the dust filaments. Filaments are identified as contours at the mean surface density, see Section 3.3.1 for details of this procedure and Figure 3.4 for a demonstration the output from our identification scheme. The filament lengths are normalized by 0.2 H_g, the side length of the `L02` simulations. The PDFs are time averaged over the interval $t = (40 - 50)\Omega^{-1}$ and averaged over the multiple `L02` and `L04` simulations. For all simulations except for the largest one, `L16`, there is a strong peak at the respective box-length scales, indicating the smaller simulations preferentially form filaments that span the full azimuthal length of the simulation. For the `L02` data, the peak bin value at $L_{\mathrm{fil},y} = 0.2$ (i.e. their full box length) is greater than 95%. See Table 3.2 for more specific values from the PDFs.

TABLE 3.2: Specific values from the probability density functions of azimuthal filament lengths from Figure 3.5.

	L02	L04	L08	L16
$\geq 0.2\ H_g$	0.949	0.951	0.944	0.904
$\geq 0.4\ H_g$	—	0.750	0.822	0.794
$\geq 0.8\ H_g$	—	—	0.500	0.556
$\geq 1.6\ H_g$	—	—	—	0.134

that are below 10 pixels in total area, which removes isolated planetesimals from our filament-focused analysis.

Figure 3.4 demonstrates the results of our procedure. Individual filaments are highlighted by the different colours. These contours can be compared with the raw surface density maps in Figure 3.1. Note, due to the smoothing filter that we apply to the surface density before we locate the contours, the filaments in Figure 3.4 are slightly wider and smoother than the filaments in Figure 3.1.

With the filaments identified, we compute their azimuthal length. The mass-weighted, time-averaged probability distribution functions (PDFs) of the filament lengths in the different simulations are shown in Figure 3.5. We can immediately see that the smaller domain simulations primarily produce filaments that span the full azimuthal width of the domain. The distributions in Figure 3.5 from the `L02`, `L04`, and `L08` simulations are all very strongly peaked at their respective box scales. The peak of the `L16` distribution is also at its box scale, but the peak is not nearly as strong as with the other simulations (note that the y-axis in Fig. 3.5 has logarithmic scaling). In Table 3.2, we provide specific numbers from the PDFs in Fig. 3.5. The numbers along the diagonal show the values from the respective box length scales: $\sim$ 95% for `L02`, 75% for `L04`, 50% for `L08`, and $\sim$ 14% for `L16`.

Given the periodic boundary conditions across the azimuthal boundary, box-scale filaments imply ring-like structures globally. The larger domains produce more truncated filaments along this dimension, hinting that there are dynamical modes in the non-linear streaming instability (for these grain sizes/stopping times) which break up the filaments at length scales that the smaller `L02`, $0.2H_g$-sized boxes cannot capture. We explore these ideas further using Fourier spectra of the dust surface density in Section 3.4.1.

Also shown in Table 3.2 is the sum of the total mass in filaments above the various box scales in the simulation suite, as fraction of the total filament mass at all length scales. For example, the top row shows the total mass in filaments above $0.2H_g$, the `L02` box scale. We see fairly consistent values among the different rows in this Table, which shows that the overall segregation of filament mass is consistent across the different simulation domain sizes. All simulations have between 90% and 96% of the filament mass in filaments with azimuthal lengths above $0.2H_g$. In the `L08` and `L16` simulations, approximately 50% of the filament mass is at or above the $0.8H_g$ length scale. This result shows that, although the commonly used $0.2H_g$ domain size from prior work does not capture the azimuthal length of the filaments accurately, the mass segregation in filaments at or above $0.2H_g$ appears to be consistent with runs with larger domains.

3.4 Dust surface density power spectra

In this section we explore the spectral power in the dust surface density using Fourier transforms. Fourier analysis provides insight on key dynamical length scales that shape the distribution of dust. We focus specifically on comparing the large-scale dynamical modes between the simulations with different domain sizes, the peak radial length scale associated with the dust filaments, and the variance in the real-space dust surface density, which quantifies the degree to which the dust mass is concentrated into dense structures.

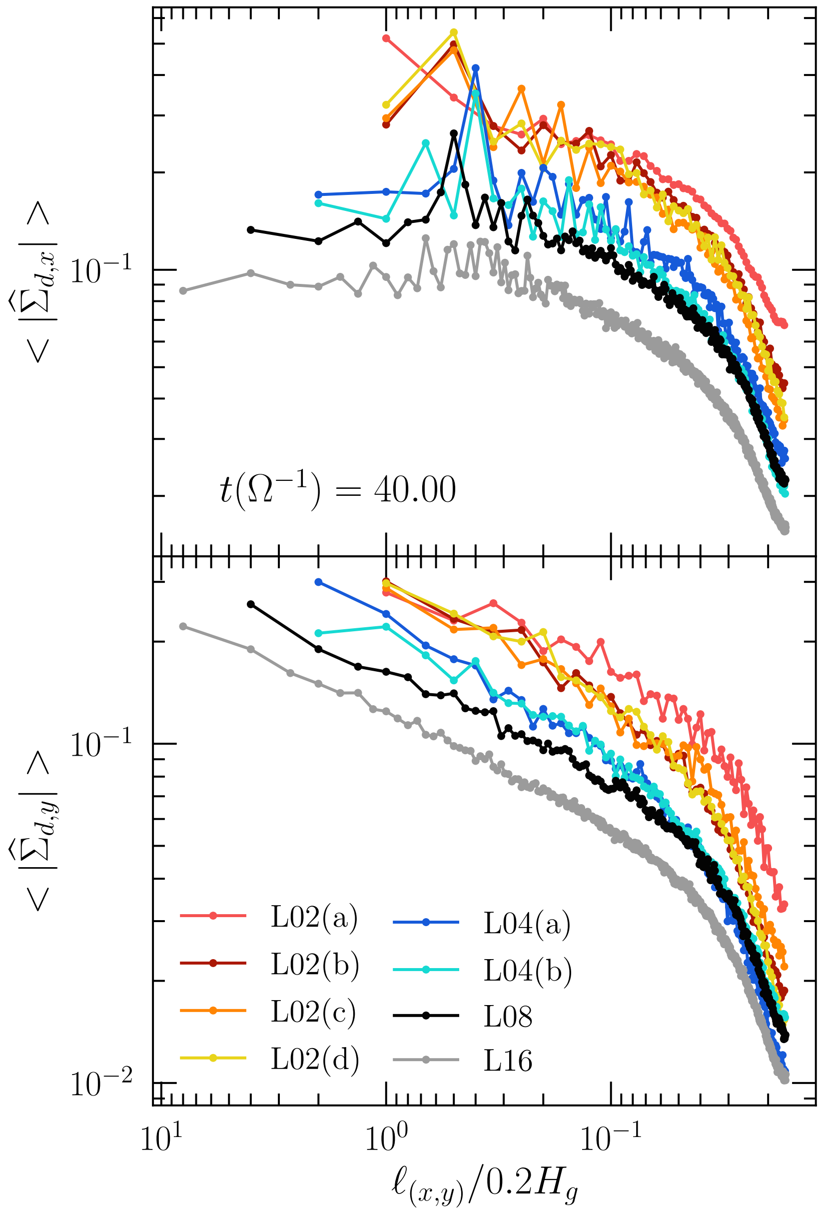

FIGURE 3.6: Average of 1D Fourier transform magnitudes through the x and y dimensions for all 8 simulations. For the top panel, each line represents the average magnitudes for each single row of the dust surface density at a specific y grid coordinate (i.e. along the x-direction). The average (mean) is taken for all x-direction rows. The bottom panel represents analogous data, where rows of Fourier transform magnitudes are averaged along the y-direction. There is a strong peak in the radial (x-dir., top panel) spectra, representing the radial filament separation length scale. This peak length scale is plotted over time in Figure 3.7.

3.4.1 Fourier spectra and large length scale power

Increasing the radial and azimuthal domain lengths above the $0.2H_g$ domain size common to prior work permits dynamics on longer length scales. Figure 3.6 shows our representation of the averaged 1D Fourier transform magnitudes, or Fourier spectra. To compute this spectra, we first calculate the (complex-valued) Fourier transform amplitudes for a single row of dust surface density, e.g., for the x direction:

$$\widehat{\Sigma}_{d,x}(k_x) = \frac{1}{N_x} \sum_{x_j=0}^{N_x-1} \Sigma_{d,x}(x_j) \ \exp\Big(-2\pi i \frac{x_j k_x}{N_x} \Big), \tag{3.14}$$

and then we compute the magnitude of the amplitudes (for a complex signal $\hat{a}$, $|\hat{a}| = \sqrt{\hat{a} \cdot \hat{a}^*}$) and take the average of those magnitudes across the other dimension,

$$< |\widehat{\Sigma}_{d,x}| >\equiv \frac{1}{N_y} \sum_{y_j=0}^{N_y-1} |\widehat{\Sigma}_{d,x}(y_j)|. \tag{3.15}$$

Unlike projecting 2D Fourier amplitudes, this procedure is a non-linear averaging that avoids phase interference, and highlights the strong peak feature in the x-direction spectra. The normalization of $1/N$ in equation 3.14 ensures that we are able to directly compare the spectra across the simulations with different box sizes. We compute these averaged transforms along the rows/columns in both the x and y directions, and plot the spectra for all simulations versus physical length scale $\ell_{(x,y)} = 1/k_{(x,y)}$ in Figure 3.6.

The dominant feature of the radial direction spectra (top panel) are the peaks that (primarily) occur below the full-length box scale for each simulation, in the vicinity of $0.1H_g$. This value corresponds to the spacing between the filaments in the radial direction (cf. Fig. 3.1). We explore this peak feature in more detail in Section 3.4.2.

In the azimuthal (y) direction, the spectra steadily increase in power from small length scales to large length scales in all simulations. For all simulations (except `L04b`) the full-domain length scale has the most power. This is consistent with earlier observations from Figure 3.5, that the filaments generally occur on the largest length scales accessible to the simulation. The large-scale structure and organization in the dust density suggest that the SI generates dynamics on large scales that can lead to this structure. Perhaps in even larger domains there would be a turn-over in these spectra beyond or near $1.6H_g$, and in the mass-weighted PDF of length scales (Fig. 3.5), signalling a preferred azimuthal filament length similar to what is seen in the radial direction. Such a simulation would be computationally expensive, however.

In both directions, the larger domain sizes provide an increase of spectral resolution. The larger simulations can capture dynamics at various length scales that smaller simulations cannot. For example, at its largest scale, the `L02` sims can capture modes at $0.2H_g$ and $0.1H_g$. The `L16` simulation can represent 8 dynamical modes between $[0.2H_g, 0.1H_g)$. This effect has interesting consequences for the radial spacing of the filaments, which, according to the peak values from the top panel of Figure 3.6, appears to prefer a length scale near $0.1H_g$. At this scale, the `L02` simulation–a common box length from the literature–has limited spectral resolution. We explore this idea further in the proceeding section.

3.4.2 Spacing between dust filaments: peak spectra length scales

The peak near $0.1H_g$ in the radial Fourier spectra at $t = 40\Omega^{-1}$ (Fig. 3.6) is a robust feature that persists over time. In Figure 3.7, we plot the peak length scale $\max(\ell_x)$ over time.

We see that, at early times, and at late times, $\max(\ell_x)$ can vary substantially. Before $t \sim 30\Omega^{-1}$, the filaments have yet to become the dominant features, and dust surface density is less ordered when compared to slightly later times (cf. Fig. 3.2). Beyond $t \sim 60\Omega^{-1}$, the planetesimals disrupt the filaments substantially (cf. Figure 1 from Paper I, the surface density at $t = 80\Omega^{-1}$). Between $t \sim 35 - 55\Omega^{-1}$, the peak length

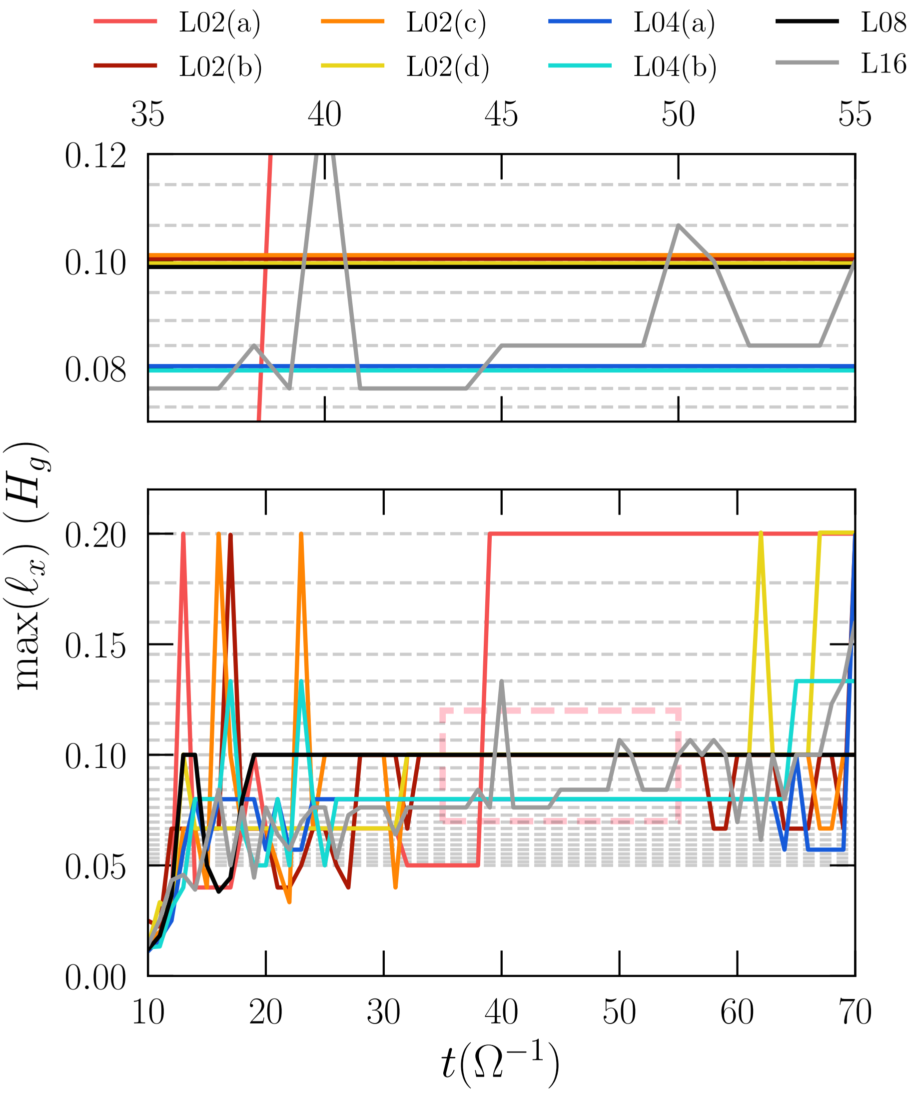

FIGURE 3.7: Peak Fourier spectra radial (x) length scales over time (i.e. the peak ℓ_x from the top panel of Fig 3.6). The top panel is a zoom-in of the region bounded by the rectangle with light pink dashed line in the bottom panel. The data in the top panel have been vertically shifted to make the individual lines at the $0.1H_g$ and $0.08H_g$ length scales visible. The horizontal dashed lines in the bottom panel represent each dynamical move available to the `L16` simulation over the range $[0.2, 0.05H_g]$.

scale and the filamentary structures are the most stable, which is the reason we focus our analyses on these times.

From Figure 3.7, we see that the $\sim 0.1H_g$ peak length scale from the spectra at $t = 40\Omega^{-1}$ (Fig. 3.6) is consistent over $t \sim 35 - 55\Omega^{-1}$. Each of the `L02b-d` and the `L08` simulations peak exactly at this scale without variation, and the `L04a,b` peaks are at $0.08H_g$. The `L02a` peak length begins at $0.05H_g$ and then jumps to $0.2H_g$ near $t = 38\Omega^{-1}$. This large jump demonstrates limitations of the smaller domain sizes. Every simulation can numerically represent dynamical modes at integer divisions its domain size. For the `L02` simulations, this corresponds to (in H_g): $0.2, 0.1, 0.05, 0.25...$ etc. That is, there are only 3 dynamical length scales for these simulations in the range $[0.2, 0.05H_g]$. The numbers of modes available to the `L16` simulation over this range, each one represented by a grey, horizontal dashed line in Figure 3.7, is 17.

The limited number of large-scale dynamical modes influences the macroscopic organization of dust in real space. The peak length scale can be translated into the number of filaments present in each simulation. In the vicinity of the apparent preferred filament radial separation length scale near $0.1H_g$, the `L02` simulations are forced into a configuration with either 1 filament ($0.2H_g$ separation), 2 filaments ($0.1H_g$), or 3 ($0.05H_g$). As seen in the dust surface density (Fig. 3.1), in our sample, 3 of the `L02` simulations (`b-d`) organize into a 2-filament ($0.1H_g$) configuration, while the `L02a` has just one filament. The `L02`-sized simulation from Simon et al. (2016) as well as the `L02`-sized, 128^3 run from Schäfer et al. (2017) (see their Table 2[3]) both organize into 1 filament. Our 1 filament simulation forms a higher number of planetesimals than the other `L02` simulations (Fig. 2 of Paper I), and has more total mass in planetesimals (Fig. 3.3) than its 2-filament counterparts, suggesting that there is indeed an enhanced amount of dust locally concentrated into the `L02a` filament, and hence an increased opportunity for planetesimal

[3]This observation was made at $t \approx 250\Omega^{-1}$, well after planetesimal formation would have distrupted the filament structure (see Figure 1 of Paper I).

formation.

The `L04` simulations, which, near $0.1H_g$, can represent 5 filaments ($0.08H_g$), 4 ($0.1H_g$), or 3 ($0.133H_g$), have constant peak length scales at $0.08H_g$ in Figure 3.7. This represents a configuration with 2.5 filaments per `L02` box length, which is a smaller linear filament density than is seen in the `L02` simulations in our sample[4]. Interestingly, in terms of both number of planetesimals and total mass in planetesimals, the `L04` simulations are generally less active in terms of planetesimal formation than any of the `L02` simulation. These results—which, admittedly, represent a limited sample size—suggest limited spectral resolution can even impact outcomes such as planetesimal formation.

From Figure 3.7, the peak radial length scale for the `L16` simulation does not stay at one mode between $t \sim 35 - 55\Omega^{-1}$, but wanders among modes in the vicinity of $0.1H_g$. In Figure 3.6, the relative peak amplitude for the `L16` is the smallest among our simulation suite. The radial organization of the filaments at this domain size–even when probed row-by-row as in our analysis–is less ordered and constant, though the predominant structure is still filaments spaced roughly $0.08 - 0.1H_g$ apart.

The preferred filament separation length scale of $\sim 0.1H_g$ from our analyses is fairly consistent with similar results from the literature. Yang & Johansen (2014) report measurements of the filament separations using stencils. For simulations with resolution at a similar level to our study (their $640{H_g}^{-1}$ linear cell density, our equivalent value is $600{H_g}^{-1}$), they find a stable filament separation of $0.1H_g$ at early times. Li et al. (2018) use a similar procedure as our Section 3.4.1 for computing peak radial direction length scales using Fourier power spectra. They find a preferred filament separation of $\sim 0.15H_g$. Also, inspecting the real-space density data in their Figures 9-11 at early times (before $t = 10P_{\mathrm{orbit}} \approx 62.8\Omega^{-1}$, to match their Fourier analysis in the pre-strong clumping phase), a filament spacing between near $0.1H_g$ appears to match their data.

[4]Further, following our discussion on dynamical resolution, the `L02` domain size would not be capable of forming 2.5 equally spaced filaments, and would instead need to organize into 2 or 3.

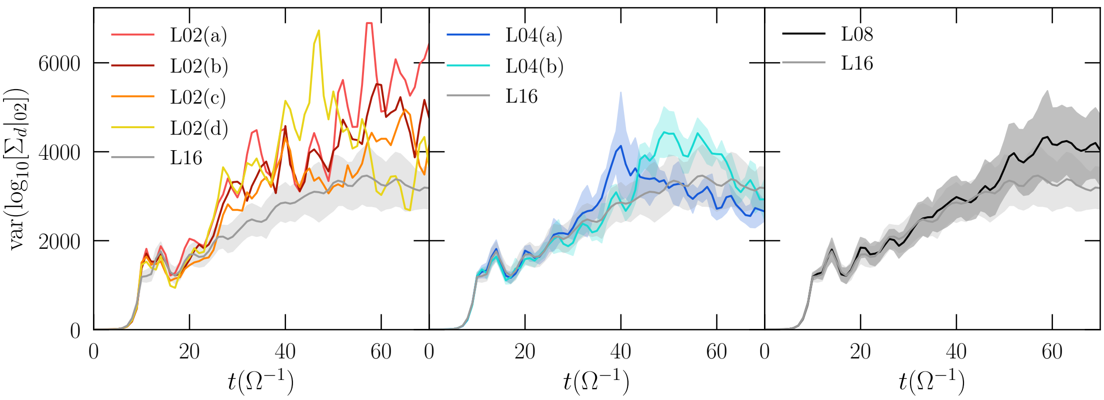

FIGURE 3.8: Variance in the logarithm of the dust surface density over time (equation 3.16). The larger simulation domains have been divided into smaller domains equivalent in size the `L02`-sized domains, and the curves for these simulations show the mean in the solid lines and the standard deviation from the average in the shaded regions.

It is important to note that most of the simulations in Yang & Johansen (2014) used resolutions lower than $640{H_g}^{-1}$, and that Li et al. (2018) used an equivalent of $320{H_g}^{-1}$. We explore the effects of resolution on our results in Appendix Appendix 3.B, and conclude that a resolution of $600{H_g}^{-1}$ (120^3 in a $(0.2H_g)^3$ box) is required to achieve converged results regarding the filament structures.

3.4.3 Variance

Through Parseval's Theorem, a related quantity to the integrated spectral power of a signal (e.g., 2D, discrete $a(x_i, y_i)$) is the variance:

$$\mathrm{var}(a) = \sum_{x_i} \sum_{y_i} \left(a(x_i, y_i) - \overline{a}\right)^2, \tag{3.16}$$

where $\overline{a}$ is the mean of the signal. We plot the variance of the logarithm of the dust surface density in Figure 3.8. We compute the variance on the logarithmic values in order to down-weight the influence of the planetesimals (and deeply depleted regions), which are not the focus of this study. From Figure 3.1, the filament features appear to represent densities within 1 and 10 times the mean surface density. We also divide each larger simulation into subdomains equivalent in size to the `L02`, similar to our analyses from Paper I. For the larger simulations, the mean values (solid line) and standard deviation (shaded region) for the set of `L02`-sized regions are plotted. For each curve, the variance is zero at the beginning of the simulation when the dust density is uniform, and then rises sharply with a narrow standard deviation in the early onset of the streaming instability near $t = 10\Omega^{-1}$. Once the non-linear SI and dramatic variations in density develop beyond $t =\sim 30\Omega^{-1}$ (cf. Fig. 3.2), the data become more variable, with wide standard deviations in the larger simulations.

As seen in the averaged Fourier magnitude spectra in Figure 3.6, the `L02` simulations have the highest vertical offsets, then the `L04`, `L08` and `L16`.

We can see immediately that $\mathrm{var}(\log_{10}[\Sigma_d])$ is the largest for the `L02` simulations, and the variance generally decreases with domain size. This tracks the order of the vertical offsets in the Fourier magnitude spectra in Fig. 3.6. This means the surface density distribution in the smaller simulation contains more deviations from mean values, and is overall less smooth than in the larger simulations. This may be due to the periodic boundary conditions having a stronger reinforcing effect on the dynamics of the smaller domains due to the shorter crossing times for these domains.

3.5 Filament properties via mock signals

In this section, we describe a novel procedure for exploring properties of the SI-formed filaments via Fourier spectra and mock signals. Gerbig et al. (2020) measured the widths of filaments in 1D, radially oriented, azimuthally integrated surface density profiles. They identify filaments as continuous structures above the mean (integrated) surface density, similar to our 2D contour method for measuring azimuthal filament lengths (Sections 3.3.1). As with Gerbig et al. (2020), we focus on the radially oriented, 1D surface density profile from one of our simulations. Along this axis, the filaments stand

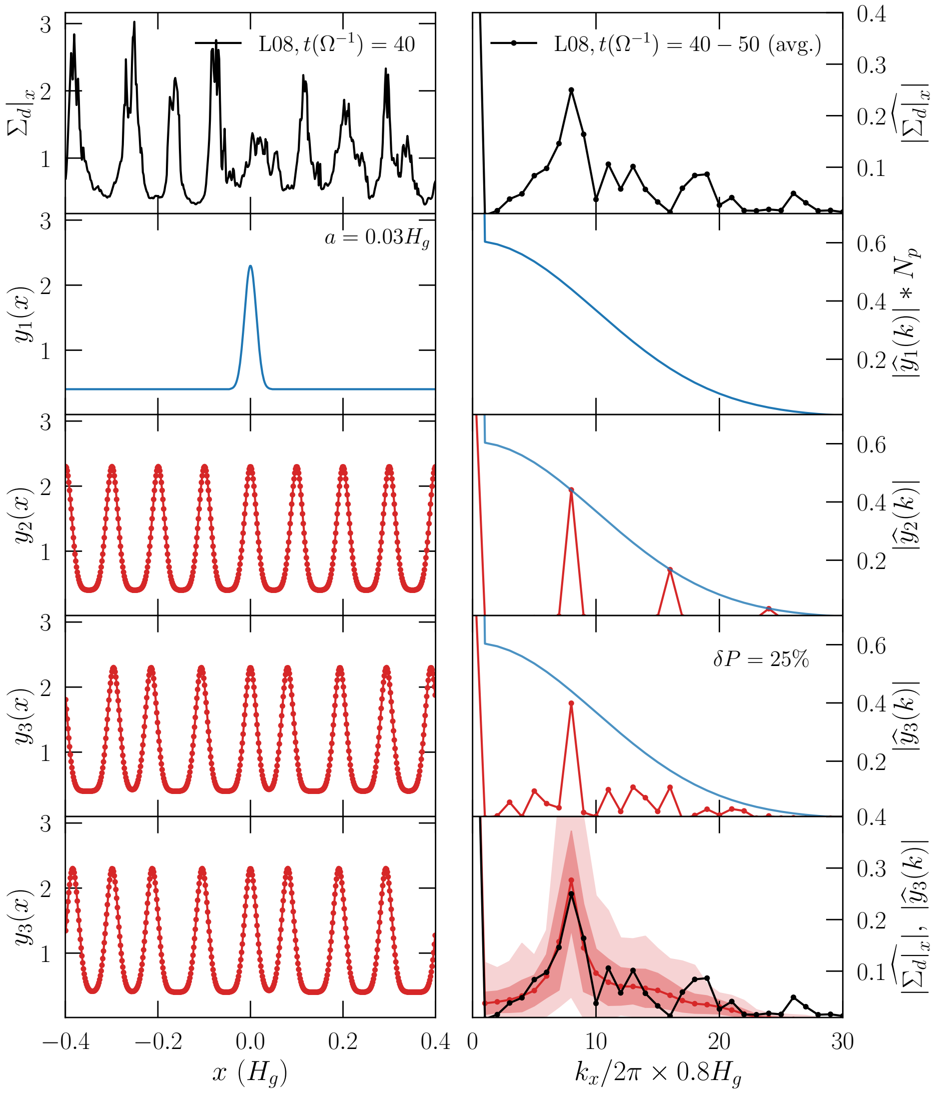

FIGURE 3.9: A summary of our mock signal procedure (Section 3.5). *Top row.* The azimuthally averaged dust surface density at $t = 40\Omega^{-1}$ on the left and the magnitude of the Fourier transform amplitudes, time averaged from $t = 40 - 50\Omega^{-1}$ on the right. *2nd row.* A single Gaussian pulse with a full width at half maximum (FWHM) of $a = 0.03H_g$. *3rd row.* A series of 8 equally spaced Gaussian pulses. *4th row.* A series of 8 Gaussian pulses with periods perturbed from the equal-spaced value by $\delta P = 25\%$ (eq. 3.18). In rows 2-4, the spectra of each signal is shown on the right panels. The blue line in these rows is the spectra of the single pulse from row 2, a sinc envelope with the amplitude multiplied by the number of pulses in the mock signals for comparison purposes. *Bottom row.* On the left, another example of the same kind of mock signal from the 4th row. On the right, the spectra of 100 iterations of mock signals with randomly selected spacings versus the spectra from the simulation. The solid red line represents the mean spectra from the 100 iterations, the darker shaded region represents 1 standard deviation above and below the mean, the light shaded region shows the maximum and minimum values from the sample.

out as distinct peaks. Our procedure compares the Fourier spectrum of that 1D signal against the spectra from a series of mock signals. The goal of this method is to offer an explanation for some of the erratic features of the simulation spectral signal. In Appendix Appendix 3.A, we apply our procedure within a parameter sweep to suggest loose bounds on specific filament properties.

We define the 1D, azimuthally averaged dust, radially oriented dust surface density profile as,

$$\Sigma_d\big|_x(x_i) \equiv \frac{1}{N_y}\sum_{y_i}\Sigma_d(x_i, y_i). \tag{3.17}$$

We plot this profile at $t = 40\Omega^{-1}$ and the magnitude of the Fourier spectra of that signal ($|\widehat{\Sigma_d\big|_x}|$, eq. 3.14) for the `L08` simulation in the top row of Figure 3.9. The Fourier spectra are time averaged over multiple snapshots from $t = 40 - 50\Omega^{-1}$ to reduce noise. As seen in the full power spectra in Figure 3.6, there is a well-defined peak corresponding to the $k_x = 8$ mode (in inverse box-length units, the same as the x-axis of Figure 3.9)[5]. The strength of this mode comes from the strongest features of the real-space data, namely the 8 roughly equally spaced filaments that are readily visible in the full 2D surface density (Fig. 3.1) and the $\Sigma_d\big|_x$ signal at these times.

This spectrum displays strong off-peak power at $k_x = 7, 9$, and local peaks at $k_x = 11, 13, 18, 19, 26$. Our attempts to explain all of these features with simple analytic functional fits proved unsatisfactory. Instead, we construct mock signals using a series of Gaussian pulses–i.e. narrow Gaussian functions–which individually resemble the peaks from the real-space simulation. We find that pulses with uneven spacing could plausibly explain the erratic features of the simulation spectra.

Figure 3.9 summarizes our mock signal procedure. The left column shows real space signals, and the right column shows the spectra of these signals, which are the magnitude

[5]For the rest of this section, values for k_x in the text will be given in units of the inverse box length, though we will no longer explicitly state so.

of the Fourier amplitudes as a function of k_x. The spectrum of a single pulse, shown in the second row, is close to that of a sinc function[6]: $\mathrm{sinc}(kL) \equiv \sin(kL)/(kL)$. When the signal is composed of a regularly spaced series of pulses (third row), the spectra is zero everywhere except the at spatial frequencies that correspond to the number of pulses (i.e. the fundamental mode), as well as harmonics of that frequency. The amplitude of the mock signal at the fundamental and harmonic modes follows the envelope set by the single-pulse spectrum. (In the figure, the envelope amplitude is multiplied by the number of pulses in order to be directly comparable to the spectra from multiple peaks.) Note that at the harmonic frequencies ($k_x = 16, 24...$) the simulation spectrum has relatively low signal, which was one of the main difficulties in our attempts at analytical functional fits. Also, the amplitude of the Gaussian pulses in the real space signals $y_2(x)$ and $y_3(x)$ are set so that the mean value of these signals is equal to the mean of the simulation signal.

In the fourth row, the series of pulses are no longer exactly equally spaced, but perturbed from the equal-spaced period value of $P_0 \equiv L_x/N_p$. The pulses are assigned spacing values from a random uniform distribution bounded by

$$P = P_0(1 \pm \delta P). \tag{3.18}$$

In Figure 3.9, the value of δP chosen is 0.25 or 25%. Adding variation to the spacing between the pulses pushes spectral power to off-harmonic values. As a consequence, the power at $k_x = 8, 16, 24...$ does not reach the envelope set by the blue line, unlike in the third row. Further, for this particular pulse arrangement ($y_3(x)$ in the fourth row), there are peaks in power at $k_x = 11, 13, 16$. Thus, we conclude that the power at $k_x = 11, 13, 18, 19$ in the simulation spectra could be due to unequal spacing between the dust filaments.

[6]If the pulse were a square wave, the spectrum would be exactly be a sinc function.

The bottom right panel of Figure 3.9 summarizes the results of multiple iterations of mock signals. Taking unique set of spacings determined by equation 3.18 will produce a slightly different arrangement of pulses and hence a different spectra for that one particular mock signal (the left panels in the fourth and fifth rows show two iterations of mock signals). To characterize the effect of this random placement on the spectra, 100 iterations of randomly generated mock signals and associated spectra were generated, and the solid red line from this panel represents the mean spectra, while the dark and light shaded regions represent 1 standard deviation from the mean and the max./min. bounds from the set of 100 spectra, respectively.

The degree to which power is leaked to off-harmonic frequencies by the variation in pulse spacing depends on the value of δP. The zero-values of the sinc function envelope in k-space are inversely proportional to the width of the pulse in real space, so the decay of the spectra at high k_x is determined by the thickness of the pulses. Here, a is the Gaussian full width at half maximum (FWHM)). In Appendix Appendix 3.A, we repeat this procedure with different values of δP and a to demonstrate these effects, and suggest constraints on those properties based on the fits of the mock spectra to the simulation spectra.

Lastly, we note that our analysis in this section is focused on the spectrum from the `L08` simulation because the larger domain permits better spectral resolution (i.e. a larger number of modes) at modes near the `L02` box scale than the `L02` and `L04`. However, we do not use the even larger `L16` run the peaks in the radial spectra from this simulation are less well defined. We believe this is due in part to the first step of the procedure, the azimuthal average of the dust surface density. As can been seen in the 2D dust surface density (Fig. 3.1), and based on results from our azimuthal filament length analysis (Fig. 3.5), the filaments in the `L16` are less contiguous than in any of the other simulations. Azimuthally averaging the dust surface density blurs together many filaments that are separated by large azimuthal distances but are near adjacent in radial projections. Even when the spectra are taken row-by-row (Section 3.4), dominant radial modes are difficult to identify (Fig. 3.6) and this peak mode varies more than in other simulations, even at times when the filaments are dominant features (Fig. 3.7). Thus, we identify the `L08` as the appropriate simulation from our suite for this procedure.

3.6 Discussion

In this study, we present an expanded analysis of numerical models of patches of protoplanetary discs from our previous study, Rucska & Wadsley (2021) (Paper I). In Paper I, we highlighted the effects of larger domains and different random initial perturbations to quantify the variability in the properties of planetesimals formed via the SI. Here, we focus on the filaments in the pre-planetesimal formation stage. The filaments represent the reservoirs of mass available to form planetesimals, and hence are an essential component of the planetesimal formation process. Prior work in the literature has studied filament properties in large numerical domains (Yang & Johansen 2014; Li et al. 2018; Schäfer et al. 2017; Gerbig et al. 2020), albeit with lower numerical resolution. We find that an increased number of grid points compared to that primarily used in older studies is required to accurately represent the filament properties we characterize (see Appendix Appendix 3.B).

Also, in prior work where filaments where were a primary focus (Yang & Johansen 2014; Li et al. 2018), models without self gravity (and hence the gravitational collapse of dense clouds into planetesimals) were used. Self gravity likely does not strongly influence the large-scale properties of filaments, as they are generally at densities well below the gravitational collapse threshold. However, following the dense clumps to gravitational collapse useful for defining the end of the filament-dominated phase of the SI, as we discuss in beginning of Section 3.3. In Yang & Johansen (2014) and Li et al. (2018), their analysis either focused on late times, well beyond when planetesimal formation would have occurred in earnest and disrupted the filament structure, or they had to make estimates of when the pre-strong clumping phase occurs. Here, by using models that incorporate self gravity we are able to conclusively define the pre-planetesimal, filament-dominated epoch of the SI.

A summary of our primary results are as follows:

1. We identify the dust filaments as objects bound by contours in the dust surface density above the mean value, i.e. the uniform dust surface density in the initial conditions. We find that smaller simulation domains preferentially form filaments that span the full azimuthal extent of the box, which denotes ring-like structures globally. In the smallest domains (a size common to much prior work), over 90% of the filament mass is in such ring-like structures. However, in the largest simulation from our suite (8 times the size of the smallest in the radial and azimuthal directions), less than 15% of the filament mass is in filaments that span the full azimuthal width, suggesting that the smaller domains are not capable of representing the true azimuthal length of the filaments. However, the filament mass segregation at the various domain sizes from our simulation suite is fairly consistent across all simulations.

2. There is significant power in the largest length scale (i.e. box-scale) modes. In the azimuthal direction in particular, the peak power is at this full box scale. This suggests that capturing the full dynamical behaviour of the non-linear streaming instability requires the use of domains that permit these large scale modes that can result in the organization of dust on large scales. These modes are likely responsible for the disruption of filaments in the azimuthal direction in the large simulations as discussed in point (i). They may also contribute to the variance in the spatial distribution of planetesimals observed in Paper I.

3. The Fourier spectra in the radial direction reveal a dominant peak length scale of $\sim 0.08 - 0.1H_g$ (gas scale heights), which corresponds to the radial spacing of the filaments. This peak is consistent across a range of domain sizes during the pre-planetesimal formation stage in which filaments are the dominant feature of dust mass. Our value is consistent with prior calculations of this length scale (Yang & Johansen 2014; Li et al. 2018).

4. Like Li et al. (2018), we conclude that the $0.2H_g$ sized simulations (`L02`) struggle to represent the radial filament separation length scale from point (iii). We build on this observation through discussion of the limited dynamical resolution available to these simulations at this scale, which forces the dust mass into specific configurations of filaments. We find 3 of the 4 `L02` simulations form two filaments, giving a spacing of $0.1H_g$ that is consistent with other domains, while the other `L02` run forms just one filament, implying a spacing that is double that size. Other runs of equivalent `L02`-sized simulations from the literature also find a configuration with one filament (Simon et al. 2016; Schäfer et al. 2017). Thus, similar to conclusions from Paper I, we see large variability in the non-linear SI, and evidence that single runs of `L02`-sized simulations cannot capture the full range of outcomes when it comes to the formation of filaments. For these reasons, like Li et al. (2018), in future studies of filaments formed by the SI, we recommend large numerical domains that can accurately represent the radial separation length scale.

5. Through a novel procedure that makes use of randomized mock filament density profiles and Fourier spectra, we find that the arrangement of filaments in our larger $0.8H_g$ simulation (in radial and azimuthal extent) are best described as peaks that are perturbed by $\sim 25\%$ from an arrangement where the peaks are exactly evenly spaced. This variance in peak placement best describes the radial Fourier spectra of the simulation data.

6. A small parameter sweep the properties of the mock filaments from point (v) in addition to an alternate mock signal procedure of manually placing peaks provides loose constraints on the filament width of approximately $0.03H_g$. This value is consistent with filament width measurements from Gerbig et al. (2020), and the length scale associated with the radial pressure gradient.

3.6.1 Implications and future work

In prior work on planetesimal formation via the SI in 3D simulations, much of the focus has been on constraining the properties of the planetesimals themselves. The mass distribution is an essential input for models of how the population of planetesimals evolves via gravitational interactions into protoplanets post-formation (e.g. Pollack et al. 1996). However, the environment that planetesimals are formed from–the dust filaments–remains relatively understudied.

Recent work on planetesimal population evolution (Liu et al. 2019; Jang et al. 2022) has used properties of dust filaments from 3D simulations of the SI. They assume the mass reservoir available for planetesimal formation is a single SI filament that forms a continuous dust ring around the full circumference of the disc. In this study, we have shown with larger numerical domains that the filaments do not primarily span the full circumferential length of the disc. Rather, the mass reservoir available for planetesimal formation is best described by a more complex picture where several filaments exist simultaneously within a local region. These filaments are truncated azimuthally and are (roughly) spaced evenly apart in the radial dimension. Liu et al. (2019) and Jang et al. (2022) also assume that the width of the filament is set by the radial pressure gradient length scale. This is roughly consistent with our loose constraints on the filament width, but, to our knowledge, this correlation has not been explicitly explored.

Indeed, the qualities of the dust surface density and filaments may vary with the strength of the radial pressure gradient (Abod et al. 2019) as well as grain size (Simon et al. 2017). Specifically, from Simon et al. (2017), smaller grains produce wider, less clumpy filaments that may actually be coherent over larger azimuthal lengths than the pebbles studied here. Smaller dust grains have yet to be studied in larger numerical domains to confirm whether this is true.

However, despite the fact that the qualities of the filaments are different in larger domains, based on our previous study (Rucska & Wadsley 2021), the spread in planetesimal formation outcomes such as the mass distribution and the total mass converted to planetesimals is consistent between several re-run small-domain simulations and larger domain simulations. Given our observations that the small simulations appear to struggle to represent the natural radial filament spacing (in agreement with Li et al. 2018), large domain simulations with different physical properties such as grain size, total dust mass, radial pressure gradient, etc., would be useful tools for constraining the properties of the planetesimal mass reservoir across a variety of disc conditions.

Also, Yang & Johansen (2014) and Li et al. (2018) show in simulations without self gravity that larger vertical domain lengths can lead to different outcomes in dust clumping and the organization of dust filaments in the late-stages of the non-linear SI. How these vertical domain lengths influence the pre-planetesimal formation filaments as well as the planetesimal formation process itself remains unstudied. Due to computational expense, we kept the vertical extent of the domains constant at 0.2 gas scale heights. Exploring simulations with large physical extents in all three dimensions at the fiducial resolution from this study would be an interesting avenue for future research.

Acknowledgements

These simulations were performed on the Niagara supercomputing cluster operated by SciNet and Compute Canada. JW thanks NSERC for funding support.

Appendix 3.A Filament properties from mock signals

In this section we explore results of repeating the same mock signal procedure of Section 3.5, culminating in the plot in the bottom right panel of Figure 3.9, but for different values of the Gaussian pulse full width at half maximum (FWHM), a, and the pulse spacing perturbation factor δP (eq. 3.18). We compute 100 iterations of the mock signal spectra for each combination of a and δP. Our results are summarized in Figure 3.A1.

Visually, it appears the spectra with ($\delta P = 25\%$, $a = 0.03 H_g$), and ($\delta P = 25\%$, $a = 0.02 H_g$) fit the simulation data spectra the best. When δP is smaller than 25%–that is, as the pulse spacing closer resembles an evenly spaced signal (3rd/middle row of Figure 3.9)–there is too much power near the harmonic frequencies ($k_x = 16, 24...$) which does not fit the simulation spectrum well. When $a = 0.02 H_g$, there is too much power at high k_x, and for $a = 0.04 H_g$, there is too much power at low k_x. The parameter a sets the zeros of the sinc envelope in k-space. We quantify these fits with the χ^2 statistic, using the mean simulation spectra (solid red lines in Fig. 3.A1),

$$\chi^2 = \sum_{i=0}^{N_x} \frac{\left(\mathrm{mean}(|\widehat{y_3}(k_{x,i})|) - |\widehat{\Sigma_d}|_x(k_{x,i})|\right)^2}{|\widehat{\Sigma_d}|_x(k_{x,i})|}. \tag{3.A1}$$

These values confirm our visual observations: the $a = 0.03 H_g$, and $\delta P = 25\%$ parameter choice is the best fit to the simulation spectrum.

3.A.1 Manual mock

Alternatively, we can remove the randomness and statistical focus of our previous analyses and instead manually construct mock signals with Gaussian pulses manually placed at the locations of peak in the simulation data. Figure 3.A2 shows 3 mock signals with varying FWHM (a) and their associated spectra. We see that there is substantial off-harmonic power (i.e. away from $k_x = 8, 16, 24...$) in the mock spectra, as in the simulation signal. The average spacing between the centres of the manual mock pulses

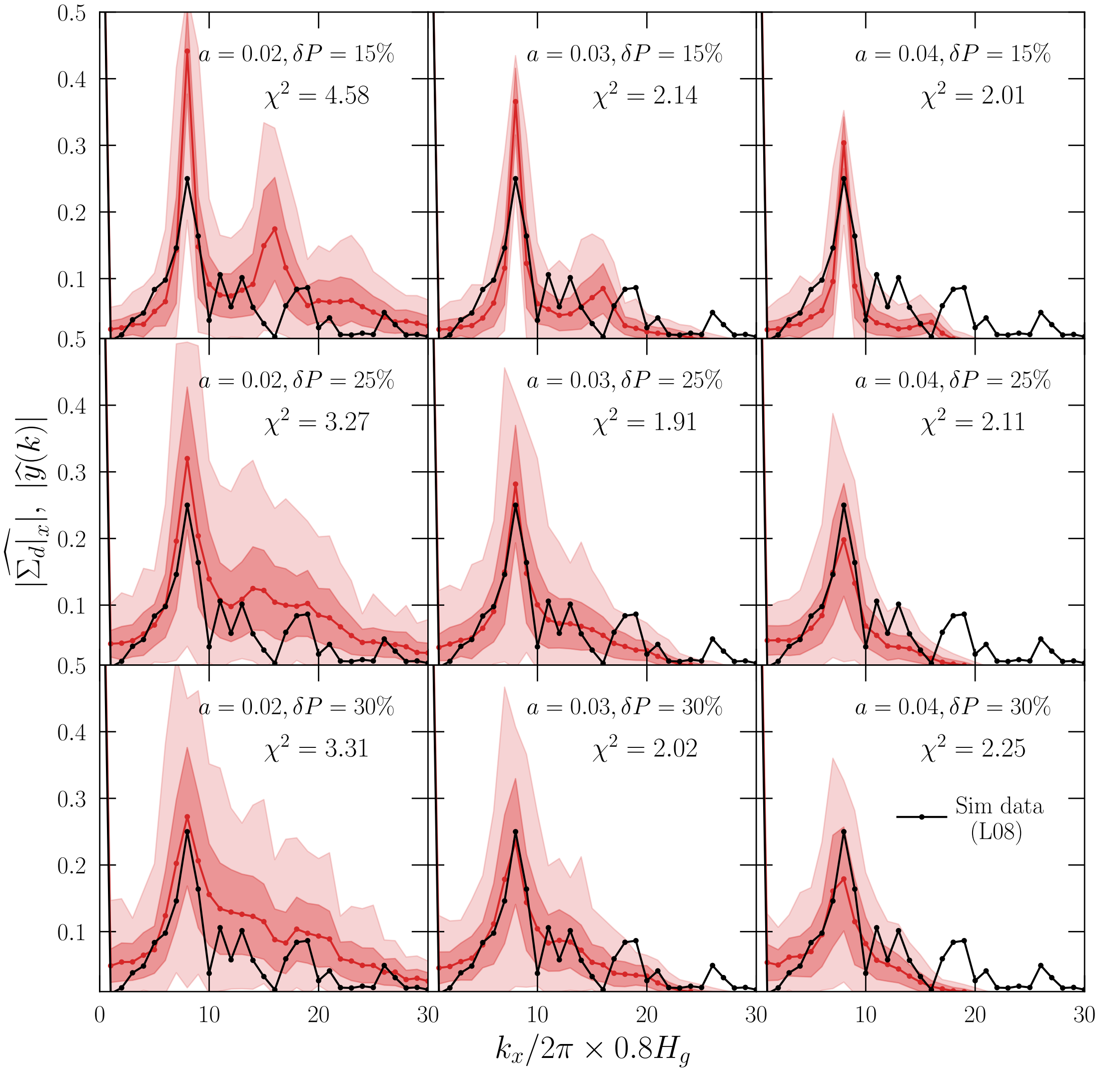

FIGURE 3.A1: Results of the 100 iteration mock signal procedure (Sec. 3.5) for signals with different Gaussian full width at half maximum values (a, all in units of the gas scale height H_g) and different values for the variance in the spacing between the pulses (δP, eq. 3.18). As in Figure 3.9, the solid red line represents the mean spectra from the 100 iterations, the darker shaded region represents 1 standard deviation above and below the mean, the light shaded region shows the maximum and minimum values. The *chi*-square statistic (equation 3.A1) for each mock signal mean curve is also shown for each set of parameters. The panel in the middle is the same data as in Figure 3.9.

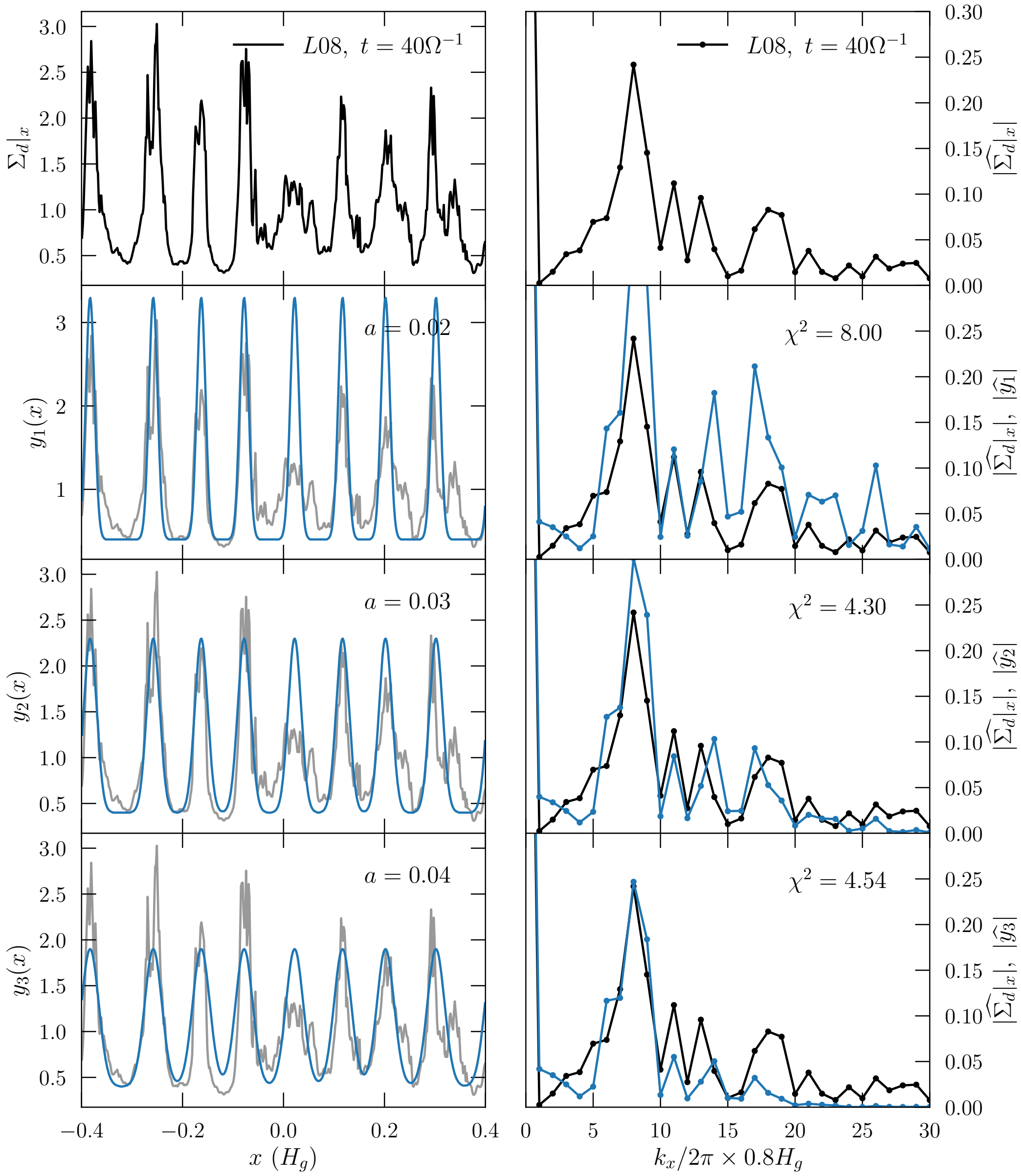

FIGURE 3.A2: A series of mock signals with Gaussian pulses manually fit (by eye) to the peaks in the azimuthally averaged dust surface density from the L08 simulation. *Top.* The 1D, radial surface density profile in real space (left) and in Fourier space (right). *2nd to 4th rows.* Three different mock signals and their spectra, with three different full width at half maximum values for the Gaussian pulses (a, in units of the gas scale height H_g). The centres of the pulses are manually adjusted to roughly match the simulation signal. The amplitudes of the pulses are set such that the total integrated area (i.e. mass) for the mock signals is the same as the area under the simulation signals. The χ-square statistic (equation 3.A1) for each mock signal spectra and the simulation spectra is also shown, for each choice of a.

is $P = 0.101 \pm 0.013H_g$, where $0.013H_g$ is the standard deviation in the set of spacings. Interestingly, for the procedure from Section 3.5 with sets of 100 mock signals with random spacings, when $\delta P = 0.25$, the average standard deviation from the 100 mock signal spacings is also approximately $0.013H_g$. Thus, there is agreement between the variation in the pulse spacings predicted by this manual procedure and from the multiple iterations of randomized mock signals with varied pulse parameters from Section Appendix 3.A. Further, the χ^2 values comparing the various manual mock signal spectra suggest that $a = 0.03H_g$ provides the best fit, also corroborating predictions from the previous section.

This value roughly agrees with prior work. For the choice of the radial pressure gradient parameter from this study, Gerbig et al. (2020) measure the width of the most dense dust filaments in their simulations to be $\sim 0.03 \pm 0.01 H_g$[7]. They used a different procedure of measuring the widths of the filament from their base in the azimuthally averaged radial surface density profiles. Also, this calculation was only for the densest filament in their simulation, and was calculated at a very late time ($t \approx 240\Omega^{-1}$) compared to our analyses ($t \approx 40 - 50\Omega^{-1}$).

Given our choice of the pressure gradient parameter (eq. 3.12), $\eta v_k/c_s = 0.05$, the length scale set by pressure gradients is $\eta r = 0.05H_g$ (where r is the global disc radius). This length is approximately consistent with the filaments widths calculated here and from Gerbig et al. (2020). It appears plausible that stronger pressure gradients create wider filaments in the pre-planetesimal formation phase of the SI (see Figure 2 of Abod et al. 2019), though, to our knowledge, no study has thoroughly investigated this correlation.

TABLE 3.B1: Simulation parameters for the different resolution runs. The physical parameters are the same as in Table 3.1.

Run name	Domain Size $(L_x \times L_y \times L_z)/H_g$	Grid Resolution $N_{\rm cell} = N_x \times N_y \times N_z$	$N_{\rm cell}$ per H_g
`L08(240)`	0.8 × 0.8 × 0.2	240 × 240 × 60	300
`L08(480)`	0.8 × 0.8 × 0.2	480 × 480 × 120	600
`L08(960)`	0.8 × 0.8 × 0.2	960 × 960 × 240	900

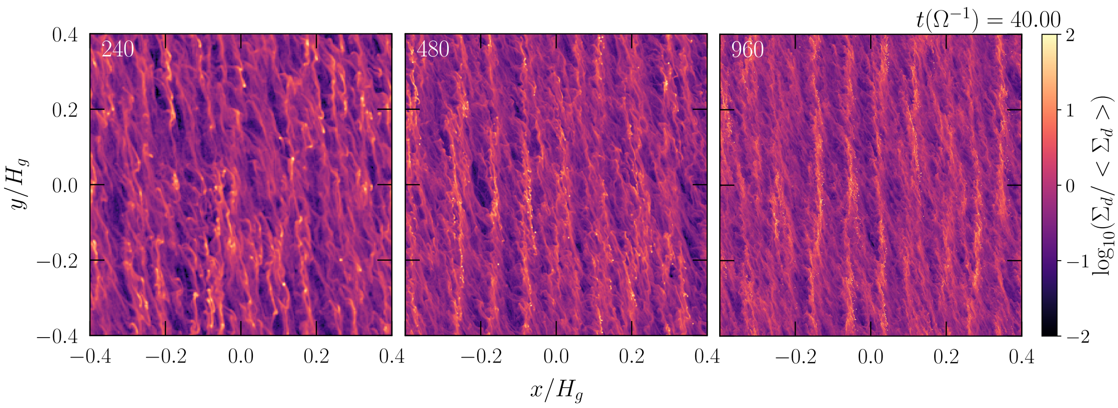

FIGURE 3.B3: Dust surface density in the x-y (radial-azimuthal) plane for each of the 3 `L08` sized simulations, at $t = 40\Omega^{-1}$.

Appendix 3.B Effect of numerical resolution

In this section we discuss how our results vary with numerical grid resolution. We rerun the `L08` simulation at two additional resolutions, one with twice as many grid points and another with half as many, see Table 3.B1. The physical parameters are the same, and we maintain the $N_{\rm par}/N_{\rm cell} = 1$ resolution for the dust particles resolution. Prior work on SI that explored filament properties in 3D simulations (Yang & Johansen 2014; Schäfer et al. 2017; Li et al. 2018; Gerbig et al. 2020) used a cell size resolution near our `L08(240)` run, or lower. We retrace much of our analysis from the main text for each of these simulations.

The radial-azimuthal dust surface density at $t = 40\Omega^{-1}$ for each `L08` simulation is shown in Figure 3.B3. There is a stark, visual difference in the characteristics of the

[7] cf. the top panel of their Figure 8. The relationship between the radial pressure gradient parameter used in this study Π and the similar parameter β from Gerbig et al. (2020) is $2\Pi = \beta$

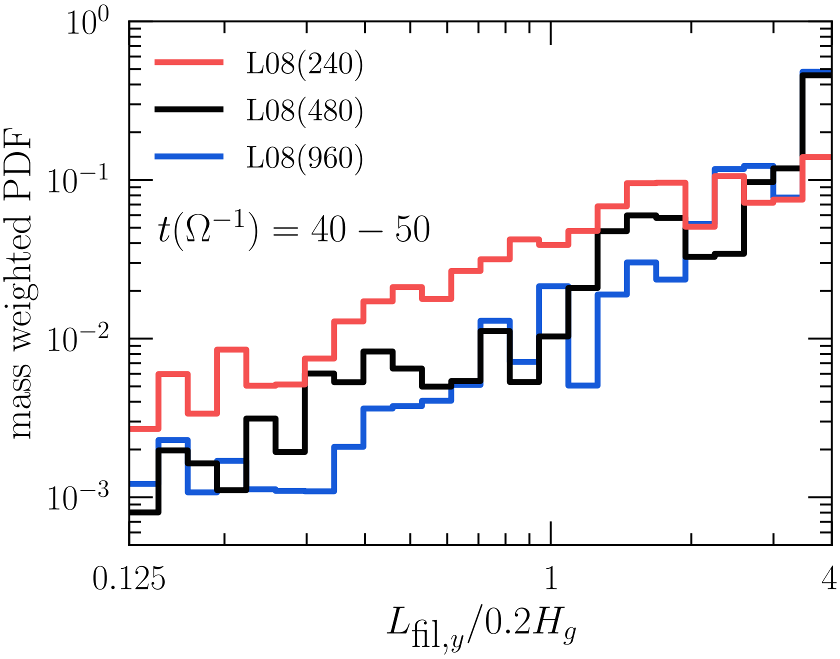

FIGURE 3.B4: Mass weighted probability density functions (PDF) for the azimuthal (y-dir.) lengths of the dust filaments, as in Figure 3.5. Filaments are identified as contours at the mean surface density, see Section 3.3.1. The PDFs are time averaged over the interval $t = (40-50)\Omega^{-1}$.

dense dust features in the lower (240) resolution run. Both the 480 and 960 form long, extended filaments, while the dense features in the 240 run clump on much shorter length scales (cf. Li et al. 2018 Figure 1). This suggests the behavior of the non-linear SI for our dust parameters is consistent for the 480 and 960 resolutions but not at the 240 resolution.

Indeed, when we apply our filament identification and azimuthal length measurement procedure from Section 3.3.1, we find the 240 filaments no longer preferentially span the full azimuthal length of the box. The mass-weighted filament length PDFs for these simulations are shown in Figure 3.B4. Both the 480 and 960 PDFs peak at the box-length $0.8H_g$ length scale, with $\sim 50\%$ of the mass in the runs in filaments at that length scale. The same procedure in the 240 produces a PDF with less than 20% of the mass in box-scale filaments.

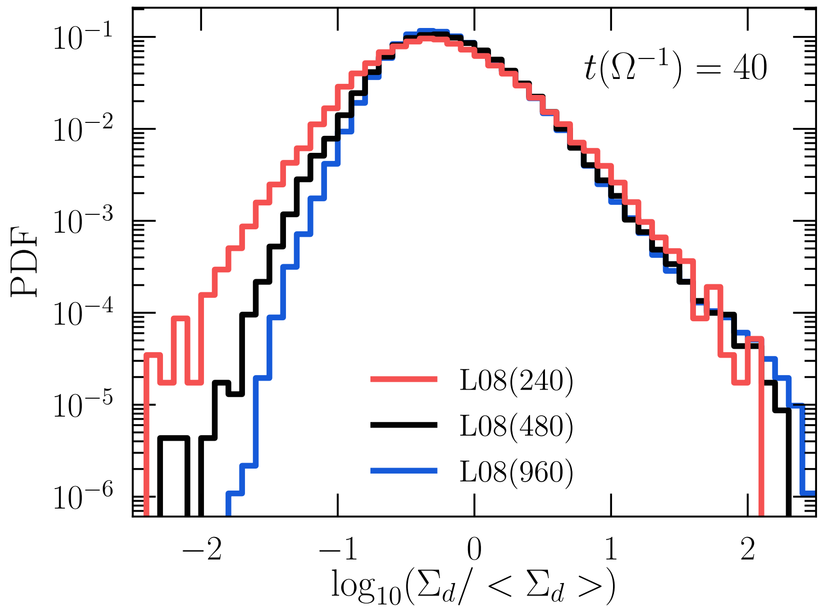

FIGURE 3.B5: Probability density function (PDF) of the surface density in each of the 3 `L08` simulations (cf. Figure 3.B3).

Figure 3.B5 shows (non-mass weighted) PDFs of the dust surface density for these simulations. As resolution increases, there are fewer regions with surface densities below 0.1 of the mean value. There are also more regions with densities above 100 $< \Sigma_d >$, which is a rough proxy for planetesimal formation.

The variance in the logarithm of the dust surface density (Section 3.4.3) is shown in Figure 3.B6. The `960` run follows a similar curve to the `480` run at early times before $t = 10\Omega^{-1}$, though the variance peaks at a higher value before settling into values closer to the `480` run and the `L16` simulation (see Figure 3.8). However, the variance in the `240` simulation differs dramatically from the other two simulations. The curve rises at later times, suggesting the non-linear SI develops slower at this resolution. The `240` run also settles at higher levels of variance. The greater number of low surface density values (Figure 3.B5) is likely is the main contributor to this effect.

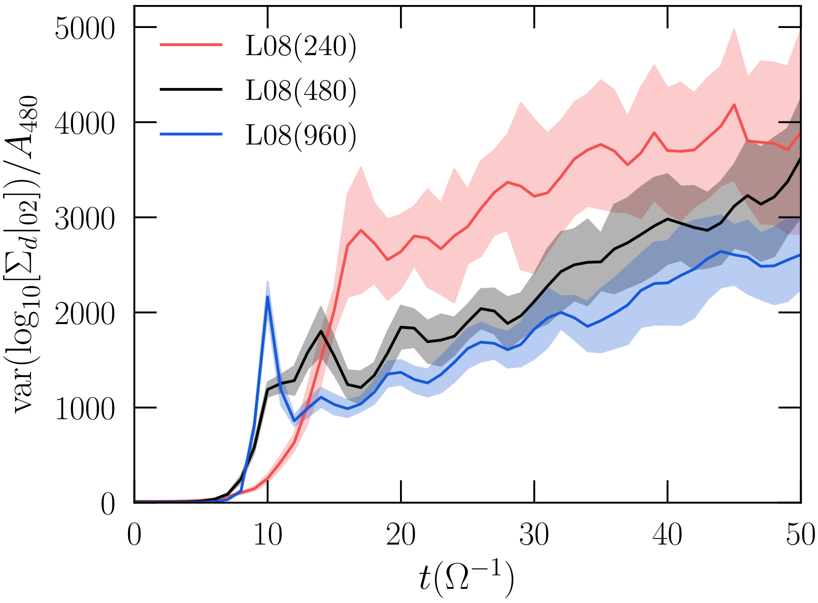

FIGURE 3.B6: Variance in the logarithm of the dust surface density overtime (Section 3.4.3) for the 3 `L08` simulations. As in Figure 3.8, the simulation domains have been divided into smaller domains equivalent in size the `L02`-sized domains. The solid lines represent the mean values and the shaded regions represent one standard deviation from the average. The normalization factor A_{480} accounts for the different number of cells in each sum, and is equal to 0.5, 1.0, and 2.0 for the `240`, `480`, `960` simulations respectively.

Finally, we produce averaged Fourier spectra magnitudes for each simulation, according to the procedure in Section 3.4.1. In the top panel, the strongly peaked feature at $0.1H_g$ (`480`) and $0.08H_g$ (`960`) that represents the radial spacing length scale for filaments does not appear in the `240` data. This is not surprising considering the filaments do not appear strongly in the real space surface density (Fig. 3.B3). In the azimuthal (y) direction, we see the same trend discussed in Section 3.4.1, in that the spectral power climbs steadily to the largest length scales in all simulations. Li et al. 2018 compute the radial power spectra for simulations with a resolution similar to our `240` run, and their data likewise lack a well defined peak as seen in our higher resolution runs.

We conclude that at the 300 grid cells per H_g resolution of the `240` simulation, the properties of the filaments formed by the non-linear SI is unresolved. The `480` run–which is the default resolution for the main results from study–appears to be an appropriate resolution for our analyses.

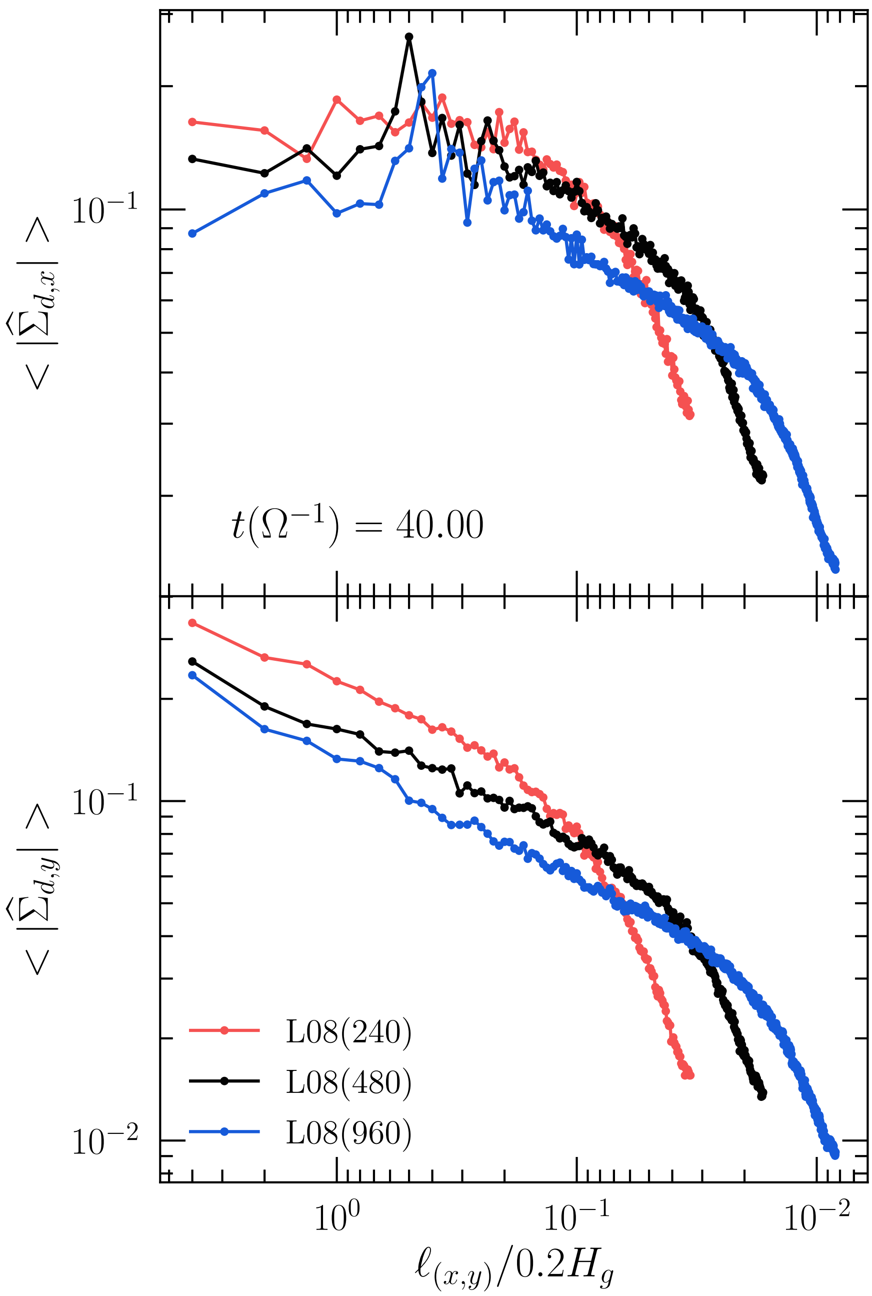

FIGURE 3.B7: Average of 1D Fourier transform magnitudes through the x and y dimensions for the 3 `L08` simulations, as in Figure 3.6. See Section 3.4.1 for details on the anlaysis procedure. *Top.* Average magnitudes for each row of the dust surface density along x-direction. *Bottom.* As in top, but for the y-direction.

Chapter 4

Planetesimal formation via the streaming instability with multiple grain sizes

The following presents work submitted to the Monthly Notices of the Royal Astronomical Society (MNRAS), by J. Rucska and J. Wadsley.

Abstract

The formation of kilometre-sized planetesimals from centimetre-sized pebbles requires a rapid mechanism that can overcome barriers that limit growth. We present 3D numerical simulations of the streaming instability (SI), a mechanism that is capable of directly forming planetesimals via the gravitational collapse of pebble clouds. We model multiple grain sizes simultaneously. These are the first simulations to use a realistic, peaked size distribution based on grain growth predictions. Both multi-size and single-size models form dense, clumped structures. We show observations underestimate the dust surface density due to clumping and optical depth effects. We estimate 20%-80% more dust can be present. The smallest grains in our size distribution do not participate in the

formation of filaments or planetesimals formed by the remaining ∼80% of the dust mass. This implies a size cutoff for pebbles incorporated into asteroids and comets. Our results reveal spatially distinct dust populations. Future work using dynamically varying size distributions would reveal how these populations evolve and interact due to SI-driven grain growth, affecting both the observable properties of protoplanetary discs and planetesimal formation.

4.1 Introduction

In the process of planet formation, planetary embryos grow from the collisions of many millions of 1 km to 100 km sized planetesimals. In turn, planetesimals are born from millimetre-centimetre sized pebbles in protoplanetary discs. However, the formation of planetesimals cannot occur through simple pathways such as the collisional coagulation of progressively larger objects. It is well understood that collisions between objects in the range of 1 cm to 1 m in protoplaneteary disc environments are predominantly destructive, resulting in smaller remnants from the original bodies in the collision (Zsom et al. 2010; Güttler et al. 2010; Windmark et al. 2012). Further, all solid objects orbiting in protoplanetary discs experience a headwind as they orbit through the gaseous component of the disc. At ∼1 m sizes, this process is maximally efficient, and causes the rapid orbital decay of these objects, sending them into the central star on timescales on the order of a few hundred years (Weidenschilling 1977a).

Hence, planet formation requires a mechanism that is capable of rapidly forming planetesimals directly from cm sized pebbles. A leading candidate for this process is known as the streaming instability (SI), first studied by Youdin & Goodman (2005) (see also: Youdin & Johansen 2007; Johansen & Youdin 2007). The SI is a specific example of a broader family of resonant drag instabilities that exist when the aerodynamic drag timescale becomes resonant with another dynamical timescale in the disc (Squire & Hopkins 2018; Squire & Hopkins 2020). In the saturated, non-linear phase of the instability, the SI is capable of producing strong, localized overdensities of clouds of pebble-sized dust that can then gravitationally collapse into planetesimals (Johansen et al. 2007), thus directly overcoming the aforementioned growth barriers.

Since the seminal work from Johansen et al. (2007), over a decade of research has explored planetesimal formation via the SI with high resolution 3D hydrodynamic simulations (Johansen et al. 2009b; Johansen et al. 2012; Johansen et al. 2015; Simon et al. 2016; Simon et al. 2017; Schäfer et al. 2017; Abod et al. 2019; Li et al. 2019; Nesvorný et al. 2019; Nesvorný et al. 2021; Gole et al. 2020; Rucska & Wadsley 2021; Carrera et al. 2021; Carrera et al. 2022; Carrera & Simon 2022). The streaming instability has proven to be a robust mechanism for forming planetesimals, so long as the local protoplanetary disc region meets the prerequisite conditions of enhanced dust mass concentration (i.e. supersolar) and sufficiently large dust grains (Carrera et al. 2015; Yang et al. 2017; Li & Youdin 2021). Protoplanetary discs observed with the Atacama Large Millimeter/submillimeter Array (ALMA) and the Very Large Telescope (VLT)/SPHERE and Subaru/HiCIAO have shown features with concentrated dust mass, such as rings (e.g. Dullemond et al. 2018; Macías et al. 2019; Muto et al. 2012; Avenhaus et al. 2018), non-axisymmetric bumps (e.g. van der Marel et al. 2013; van der Marel et al. 2015; Cazzoletti et al. 2018; van der Marel et al. 2021) and spiral structure (e.g. Benisty et al. 2015; Pérez et al. 2016; Benisty et al. 2017). Some rings may have sufficiently high dust concentrations to initiate planetesimal formation via the SI (Stammler et al. 2019; Maucó et al. 2021). Indeed, Carrera et al. (2021), Carrera et al. (2022) and Xu & Bai (2022a) and Xu & Bai (2022b) show that persistent radial gas pressure maxima, which likely play a role in the formation of the observed large-scale rings (Whipple 1972), can sufficiently concentrate dust to trigger planetesimal formation via the SI.

Observations of minor solar system bodies support the idea that these objects may have been formed via the SI or a similar process. Asteroids are commonly described as "rubble piles": gravitationally bound conglomerates of smaller pebbles with significant bulk porosity (Walsh 2018). Further, results from the Rosetta mission to comet 67P/Churyumov-Gerasimenko suggest this object likely formed from a cloud of millimetre-sized dust particles (Blum et al. 2017; Fulle & Blum 2017). Results from the New Horizons flyby of the Kuiper belt object (486958) Arrokoth suggest that this object, a contact binary with two distinct lobes, is likely a result of the slow decay of a binary orbit, where the two progenitor objects formed via the gravitational collapse of a pebble cloud (McKinnon et al. 2020; Grishin et al. 2020; Marohnic et al. 2021). Nesvorný et al. (2019) and Nesvorný et al. (2021) also show that the gravitational collapse of dense pebble clouds from SI simulations can produce planetesimal binaries with properties similar to binaries observed in the Kuiper belt. Kavelaars et al. (2021) measured the size distribution of objects in the cold classical Kuiper belt and find it is well described by an exponential cut-off at large sizes—a feature predicted by the streaming instability.

The New Horizons mission also observed the craters that cover the 4 billion-year-old surfaces of the Pluto-Charon system, enabling an analysis of the inferred size distribution of the impactors from the early Solar system that produced those craters (Singer et al. 2019; Robbins & Singer 2021; Robbins et al. 2017). Singer et al. (2019) find a deficit of craters at small sizes, for impactors below $\lesssim$ 1-2 km in diameter. Unfortunately, current limits on computational power prevent 3D simulations of the SI from providing any insights on the SI-formed planetesimal size distribution at these small sizes (Simon et al. 2016; Li et al. 2019; see Section 4.1 of Rucska & Wadsley 2021 for further discussion).

Observational constraints on planetesimal formation are difficult to acquire, yet there is a general agreement between observational data and predictions from models of planetesimal formation via the SI. To date, the SI remains a leading candidate for the efficient formation of planetesimals, yet there remains open questions regarding this process, such as how the presence of a distribution of dust grain sizes affects outcomes regarding planetesimal formation.

4.1.1 Dust grain size distributions in protoplanetary discs

Observations reveal that protoplanetary discs in nature have at least two distinct dust populations: $\sim$millimetre-sized pebbles which have settled to the disc mid-plane and are most readily visible via their sub-mm wavelength thermal emission with ALMA (e.g. Andrews et al. 2016; van der Marel et al. 2021; Maucó et al. 2021), and $\sim$micron-sized grains suspended vertically in the disc, seen in infrared scattered light (e.g. Muto et al. 2012; Benisty et al. 2015; Avenhaus et al. 2018). Though these components occur in spatially distinct regions in the disc, they are likely linked, as grain growth theory shows that pebbles can readily grow via coagulation from the micron-size grains that the disc inherits from the interstellar medium (Birnstiel et al. 2011; Birnstiel et al. 2015, see Birnstiel et al. 2016, for a review). Once the grain growth/fragmentation process reaches equilibrium, the predicted outcome from the widely-used Birnstiel et al. (2011) model is a grain size distribution described by multiple power-laws and a distinct peak, so that most of the mass in the distribution is within a factor of two of a specific grain size.

4.1.2 Streaming instability with a distribution of grain sizes

Until recently, there were few studies of the streaming instability with multiple sizes. Johansen et al. (2007) included multiple dust species in a subset of their runs, but the focus of their work was the onset of planetesimal formation rather than the behavior of the different grains. Bai & Stone (2010a) modelled discs with a variety of grain size distributions simultaneously in 3D simulations, and explored the influence of these distributions on properties of the non-linear, saturated state of the SI, pre-planetesimal formation.

Recently, there have been multiple studies on how particle size distributions influence the linear growth phase of the SI (Krapp et al. 2019; Paardekooper et al. 2020; Paardekooper et al. 2021; McNally et al. 2021; Zhu & Yang 2021) and the linear and non-linear phase in 2D numerical simulations (Schaffer et al. 2018; Schaffer et al. 2021; Yang & Zhu 2021). These studies explored linear SI growth rates and the clumping of dust in the non-linear phase for distributions with a wide range of grain sizes. Overall, they conclude that the SI can produce strong dust clumping so long as the local dust-to-gas mass ratio is large, approaching unity, and that the grain size distribution involves sufficiently large grains (near approximately a centimetre in size). In this paper, we study dust that is well within the strong growth regime, and follow the non-linear phase of the SI all the way to planetesimal formation.

We expand prior work by Bai & Stone (2010a) (3D), Schaffer et al. (2018) and Schaffer et al. (2021) (2D) and Yang & Zhu (2021) (2D). The grain size distributions in these studies are power laws, with exponents similar to the fiducial slope for interstellar grains from Mathis et al. (1977). In this study, we sample the grain size distribution of Birnstiel et al. (2011), which is the equilibrium outcome of a grain growth/fragmentation model applicable to the midplane of protoplanetary discs, where planetesimal formation is believed to occur. The Birnstiel et al. (2011) distribution deviates from a single power law and includes a peak at large sizes. Thus, in our discretized version of that grain size distribution, the spacing between the representative grain size for each bin is not equal, in linear or logarithmic space, which is unique from prior work on this subject.

We present the first 3D, vertically stratified simulations of the SI with multiple species of dust grains since Bai & Stone (2010a), and compare the non-linear development of the SI in dust with multiple sizes against data from our prior work which used a single size (Rucska & Wadsley 2021). We highlight the differences in the dust surface density distribution between multi-size and single-size models, along with a novel analysis that reveals the observational consequences of the strong dust clumping seen in our runs, and explore how grains of different sizes participate in planetesimal formation.

Our paper is organized as follows. In Section 4.2 we present our methods and choice of parameters and a discussion about the dust grain size distribution we model. Section 4.3 focuses on the different dust surface density distributions between our multi-size model and prior work with single grain sizes, and the observational consequences of these differences. Section 4.4 focuses on how the different grain sizes participate in the non-linear filament and planetesimal formation process. In Section 4.5 we summarize our key results and discuss how this paper influences the current understanding of planetesimal formation via the SI.

4.2 Methods

We model a local portion of a near-Keplerian protoplanetary disc. We study the dynamics of a gas phase aerodynamically coupled to a dust/solids phase. The specifics of our numerical and hydrodynamic set-up are nearly identical to those described in Rucska & Wadsley (2021), so we briefly summarize those methods here and refer a reader interested in a more detailed discussion to that paper.

We use the shearing sheet approximation of Goldreich & Lynden-Bell (1965) to track the local dynamics of a Cartesian frame co-rotating at the Keplerian orbital velocity. We employ the Athena hydrodynamics code (Stone et al. 2008; Stone & Gardiner 2009) with the solids particle module (Bai & Stone 2010b) to numerically evolve the protoplanetary disc system. Vertically, the box is centred on the disc midplane ($z = 0$), and the co-rotating frame of reference leads to an imposed background velocity in the azimuthal (y) direction described by $(q\Omega x)\hat{\boldsymbol{y}}$. Here x is the radial co-ordinate in the co-rotating frame, with $x = 0$ being the radial centre of the box, and q is the power-law index of the angular velocity with radial position in the disc, $\Omega \propto r^{-q}$, so that in Keplerian discs $q = 3/2$.

The equations that describe the dynamics of the gas and solids (dust) are

$$\frac{\partial \rho_g}{\partial t} + \nabla \cdot (\rho_g \boldsymbol{u}) = 0, \tag{4.1}$$

$$\begin{aligned} \frac{\partial \rho_g \boldsymbol{u}}{\partial t} + \nabla \cdot (\rho_g \boldsymbol{u}\boldsymbol{u}) &= -\nabla P_g \\ &+ \rho_g \left[-2\boldsymbol{\Omega} \times \boldsymbol{u} + 2q\,\Omega^2 x\,\hat{\boldsymbol{x}} - \Omega^2 z\,\hat{\boldsymbol{z}} + \mu \frac{\overline{\boldsymbol{v}} - \boldsymbol{u}}{t_{\text{stop}}} \right], \end{aligned} \tag{4.2}$$

$$\frac{d\boldsymbol{v}_i'}{dt} = 2(v_{iy}' - \eta v_K)\Omega\hat{\boldsymbol{x}} - (2-q)v_{ix}'\Omega\hat{\boldsymbol{y}} - \Omega^2 z\hat{\boldsymbol{z}} - \frac{\boldsymbol{v}_i' - \boldsymbol{u}'}{t_{\text{stop}}} + \boldsymbol{F}_g, \tag{4.3}$$

where ρ_g is the gas mass density, P_g is the gas pressure, $\boldsymbol{u}$, is the velocity of the gas, $\boldsymbol{v}_i'$ is the velocity of an individual dust particle in the frame of the background shear flow, and $\overline{\boldsymbol{v}}$ is the mass-weighted average velocity of the dust in a gas cell. The gas equation of state is isothermal, $P_g = \rho_g c_s^2$, where c_s is the sound speed. The quantity $\mu \equiv \rho_d/\rho_g$ is the local ratio of dust to gas mass density, and η controls the strength of the radially inward drag force on the dust, which is related to the steepness of the radial gas pressure gradient (see Section 4.2.1). The quantity t_{stop} is the time-scale for the exchange of momentum between the dust and gas phase, which depends on a local gas quantities such as density and temperature, and, crucially, the physical size of the dust grains. We discuss this parameter in more detail in Section 4.2.2 as it is central to the context for this paper.

For the numerical algorithms, as in Rucska & Wadsley (2021) we use the standard ATHENA options for the Reimann solver (HLLC), hydrodynamics integrator (corner transport upwind) and a semi-implicit integrator for the dust momentum equations with a triangular-shaped cloud scheme to interpolate the dust particle properties with the simulation grid. In equation 4.3, the background shear flow has been subtracted from the dust and gas velocities. Separating the advection of the shear velocity from local deviations leads to a more efficient and accurate numerical integration (Masset 2000; Johnson et al. 2008). For the hyrdodynamic boundary conditions of the numerical domain, we use the shearing box boundary conditions, which are periodic in the azimuthal (y) and the vertical directions (z) and shear periodic in the radial (x) direction (Hawley et al. 1995; Stone & Gardiner 2010).

The term $\boldsymbol{F}_g$ in equation 4.3 represents the gravitational acceleration. Not all prior work on high-resolution studies of the non-linear SI includes the effects of the dust density field self-gravity, but since our study is in part focused on the properties of planetesimals, it is included here. Self-gravity enables the collapse of dense dust material into gravitationally bound objects (i.e. planetesimals). Following Simon et al. (2016), based on an implementation described and tested in Rucska & Wadsley (2021), this acceleration is computed via the gradient in the gravitational potential from the dust density field, and this potential is computed from the solution to Poisson's equation,

$$\boldsymbol{F}_g = -\nabla\Phi_d, \tag{4.4}$$

$$\nabla^2\Phi_d = 4\pi G\rho_d. \tag{4.5}$$

Here G is the gravitational constant. Our parameterization of this constant is discussed further in the next section (equation 4.9). Note, we neglect the gravitational influence of the gas, since the density perturbations in the gas in these kinds of local protoplanetary disc models are very small (Li et al. 2018). We use the fast Fourier transform Poisson solver available in Athena (Kim & Ostriker 2017) to solve equation 4.5, shear periodic horizontal boundary conditions and vaccuum boundary conditions vertically.

TABLE 4.1: Simulation parameters.

Run names	τ_s - grain stopping time(s)		
S0,S1, S2,S3 (S)	0.314		
M6-0,M6-1,M6-2, M6-3,M6-4 (M6)	0.036, 0.191, 0.270, 0.314, 0.353, 0.412		
M12	0.021, 0.113, 0.170, 0.218, 0.256, 0.284, 0.305, 0.324, 0.342, 0.363, 0.390, 0.437		
M18	18 values between 0.016 and 0.450		
Domain Size $(L_x \times L_y \times L_z)/H_g$ $0.2 \times 0.2 \times 0.2$	Grid Resolution $N_{\text{cell}} = N_x \times N_y \times N_z$ $120 \times 120 \times 120$		
$N_{\text{par}}/(N_{\text{species}} \times N_{\text{cell}})$	Z	$\widetilde{G}$	Π
1	0.02	0.05	0.05

4.2.1 Physical and numerical parameters, initial conditions

In this section we discuss the physical parameters that influence the dynamics of our local protoplanetary disc system. In this study we choose identical or very similar values as previous work on these systems (Simon et al. 2016; Schäfer et al. 2017; Johansen et al. 2012; Li et al. 2018; Gole et al. 2020; Rucska & Wadsley 2021). These parameters and our choices are summarized in Table 4.1 and briefly discussed in this section, with a more in-depth discussion of the stopping time parameter τ_s in Section 4.2.2.

The total mass of the dust particles is controlled by the ratio of dust mass surface density to the gas surface density

$$Z = \frac{\Sigma_d}{\Sigma_g}, \tag{4.6}$$

and we choose $Z = 0.02$, which is a slightly supersolar metal mass ratio. Note that our simulation domains model only a fraction of the vertical gas scale height while capturing the full dust scale height. Thus the effective surface density mass ratio within the simulation domain is higher than 0.02. Following the discussion from Section 2.4 of Rucska & Wadsley (2021), the ratio of total dust mass to total gas mass within the full simulation domain is approximately 0.25.

The radial gas pressure gradient represented by the $-2\eta v_k \Omega$ term equation 4.3 is parameterized via η:

$$\eta = n \frac{c_s^2}{v_K^2}. \tag{4.7}$$

where n is the pressure power law index, $P_g \propto r^{-n}$, the local Keplerian speed is v_K, and the isothermal sound speed is c_s. This pressure gradient shifts the azimuthal component of the dust and gas velocities by ηv_K, and we subtract this shift from our data to conduct analysis in this shifted frame. As with other work, in our simulations η is ultimately controlled by a similar parameter

$$\Pi = \frac{\eta v_k}{c_s}, \tag{4.8}$$

and we choose $\Pi = 0.05$, a typical value that applies to a wide variety of disc models (Bai & Stone 2010a).

The strength of self-gravity versus tidal shear is controlled by

$$\widetilde{G} \equiv \frac{4\pi G \rho_{g,0}}{\Omega^2}. \tag{4.9}$$

Selecting $\widetilde{G} = 0.05$ is equivalent to a Toomre (1964) Q of 32, so the gas phase is gravitationally stable, supporting our exclusion of the gas density field in solving for the gravitational potential (equation 4.5).

In equation 4.9, $\rho_{g,0}$ is the gas midplane density. The gas density is initialized to have a Gaussian profile vertically with a scale height H_g, and a uniform distribution in the radial and azimuthal directions. The dust phase is initialized analogously except with a scale height of $H_d = 0.02H_g$. We set the units of our scale-free model to that $\rho_{g,0} = H_g = \Omega = c_s = 1$. See Section 2.4 of Rucska & Wadsley (2021) for a discussion on how to convert these units to physical units. Using the minimum mass solar nebula model of Hayashi (1981), there is approx 1.5 $M_{\rm Ceres}$ worth of dust mass in our full simulation domain.

The 3D simulation domains we study have equal lengths of $L_x = L_y = L_z = 0.2\ H_g$, and we choose a grid resolution of $N_x = N_y = N_z = 120$. Simon et al. (2016) show that this resolution and Rucska & Wadsley (2021) show that this box size is sufficient to accurately capture the planetesimal formation process with our chosen set of physical parameters. This grid resolution matches that of Rucska & Wadsley (2021).

We choose a dust resolution such that the total number of particles for each grain species is equivalent to the total number of grid points in the gas grid. The millions of dust particles are initially placed so that the overall dust density distribution is uniform in the x-y plane and follows a Gaussian profile vertically. The precise initial positions of the particles are set via a random number generator. As in Rucska & Wadsley (2021), we re-run multiple simulations that are otherwise identical except for the initial seed for the random number generator, which gives a different initial (and very small in amplitude) noise pattern to the dust density in each run. Once the streaming instability develops into the non-linear phase, the initial perturbations result in dramatic variations in the dust density. Thus, re-running simulations with different initial seeds probes the stochastic qualities of the non-linear SI and the variance in the outcomes in a way that a single simulation cannot.

In Table 4.1, the simulation labels `S0,...,S3` denote the simulations which use a single dust grain size (these are the same `L02(a-d)` simulations from Rucska & Wadsley 2021), and analogously the labels `M6-0,...,M6-4` represent the simulations that use multiple grain species simultaneously. The `M12` and `M18` are simulations that sample the same size distribution as the `M6-0,...,M6-4` simulations but with a greater number of grain species/bins. Details on the grain sizes in each simulation are discussed in the proceeding section.

4.2.2 Grain size distribution

We base our distribution of grain sizes on the results from Birnstiel et al. (2011), a widely used model of the collisional growth and fragmentation of dust grains in protoplanetary discs. Dynamics such as local turbulence, vertical settling, and radial drift affect the relative velocities between dust grains and can lead to grain growth or fragmentation via destructive collisions, depending on local conditions (for a review, see Birnstiel et al. 2016).

Birnstiel et al. (2011) conclude that the dust grain population will equilibrate towards a size distribution with a shape that depends quite strongly on properties of the disc (see their Fig. 6). Properties such as the gas surface density, midplane temperature, the Shakura & Sunyaev (1973) α turbulent viscosity parameter, and a fragmentation threshold velocity for the grains. The authors also provide an online tool for exploring different combinations of disc quantities. For the distribution shape we study, we choose $\Sigma_g = 100$ g/cm^2, $T_{\mathrm{mid}} = 100$ K, roughly equivalent to a radial position of ~ 5 AU for a disc with $\Sigma_g(r) = 1000\ (r/\mathrm{AU})^{-3/2}$ g/cm^2 (e.g. minimum mass solar nebula model; Weidenschilling 1977b) and $T_{\mathrm{mid}} = 200\ (r/\mathrm{AU})^{-3/7}$ K (e.g. Chiang & Goldreich 1997). For other parameters we choose $\alpha = 1 \times 10^{-4}$, $v_{\mathrm{frag}} = 3$ m/s. These choices lead to a distribution that peaks towards $\sim$4 cm.

However, it is not the grain size that is a direct input for our simulation model, but the characteristic time scale for the aerodynamic coupling between the dust and gas, t_{stop} (equations 4.2 and 4.3). There are different forms for this stopping time depending on the regime of drag one considers, but for protoplanetary discs, almost all grains are in the Epstein (Epstein 1924) drag regime (Birnstiel et al. 2016), where the size of the dust grains is smaller than the mean free path of the gas particles. The form of $t_{\rm stop}$ in this regime is

$$t_{\rm stop} = \frac{\rho_s}{\rho_g c_s} s, \tag{4.10}$$

where ρ_s is the material density of the particles (approximately $2.6\,{\rm g\,cm^{-3}}$ for silicates; Moore & Rose 1973), ρ_g is the local gas density, c_s is the local sound speed, which depends on the gas temperature, and s is the size of the dust grains. Thus, for the same gas properties, the grain size sets $t_{\rm stop}$. In our models, as with other studies of the streaming instability, we model the drag coupling between the dust and gas with a dimensionless parameter $\tau_s = t_{\rm stop}\Omega$,

$$\tau_s = \frac{\Omega \rho_s s}{\rho_g c_s}. \tag{4.11}$$

In an α-disc model, the midplane gas density is $\rho_{g,0} = (1/\sqrt{2\pi})(\Sigma_g/H_g)$ and $H_g = c_s/\Omega$ (Armitage 2020), so that $\tau_s = (\rho_s/\Sigma_g)s$. With our above choices for the disc properties in the grain size distribution, the previous mentioned size peak of 4 cm grains translates to $\tau_s \sim 0.1$. In this study, we wish to directly compare our results to both our previous study (Rucska & Wadsley 2021) and prior work which has focused on a single stopping time of $\tau_s = 0.314$. Thus, we maintain the original shape of this particular Birnstiel et al. (2011) distribution from our chosen disc parameters, but slightly shift the peak to $\tau_s = 0.314$, which is analogous to considering a different radial position in the disc. Setting the distribution to peak at our previous single grain size value is the most logical method for comparing these two different representations of the dust environment.

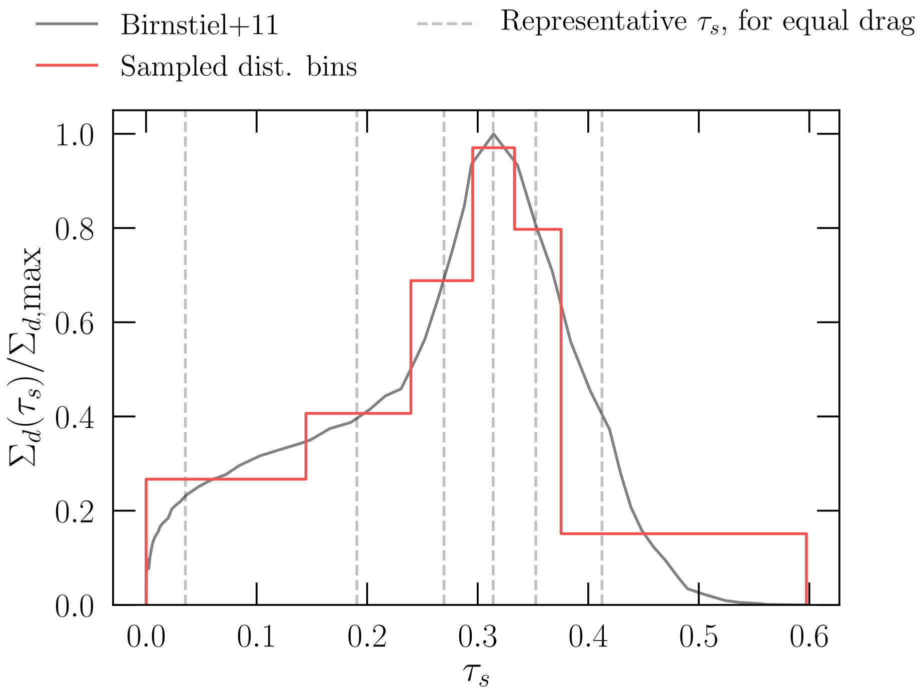

FIGURE 4.1: Grain size distribution sampled for this study. The grey curve represents the surface density distribution as a function of grain size according to a grain growth model in collision-fragmentation equilibrium (Birnstiel et al. 2011). The red curve represents our sampling of the distribution with six bins, and the vertical dashed lines are the representative τ_s selected for each bin (See Section 4.2.2).

Sampling the Birnstiel et al. (2011) distribution

Figure 4.1 shows the dust mass surface density distribution that we sample, as a function of τ_s. The six different bins (red curve), used for the five `M6-0...M6-4` simulations, are chosen such that there is roughly an equal number of mass in each bin while enforcing that one bin is centred on the peak at $\tau_s = 0.314$. Since the streaming instability is driven by the aerodynamic coupling between the dust and gas, we chose the representative τ_s for each bin so that there is the same total drag force (proportional to Σ_d/τ_s) in each bin as in the original distribution. This requires us to satisfy the equality

$$\int_{\tau_{\mathrm{bin,l}}}^{\tau_{\mathrm{bin,r}}} \frac{\Sigma_d(\tau_s)}{\tau_s{}'} d\tau_s{}' = \frac{\Sigma_{\mathrm{bin}}}{\tau_{\mathrm{bin}}}(\tau_{\mathrm{bin,r}} - \tau_{\mathrm{bin,l}}), \tag{4.12}$$

where $\tau_{\mathrm{bin,(r,l)}}$ are the right and left τ_s values in each bin, Σ_{bin} is the mean height of the distribution in that bin, and τ_{bin} is the representative size in that bin which we solve for. We see from Figure 4.1 that τ_{bin} in the bins for $\tau_s > 0.1$ roughly tracks the half-mass point of the $\Sigma_d(\tau_s)$ curve, but in the bin for the smallest grains, τ_{bin} is closer to the leftmost, small-τ_s edge of the bin, because the drag force per unit mass scales as $1/\tau_s$.

Table 4.1 lists the exact values of τ_{bin} (hereafter just referred to by τ_s) modelled simultaneously by our simulations, with each species given a roughly equal amount of the total dust mass in the simulation domain[1]. Note that these values of τ_s are not equally spaced, linearly or logarithmically, which is different from the distributions modelled by prior work (Johansen et al. 2007; Bai & Stone 2010a; Schaffer et al. 2018; Yang & Zhu 2021) which also used equal-mass bins in their discretized distributions.

[1] We could not simultaneously ensure that our sample has one bin with a representative τ_{bin} exactly at the peak $\tau_s = 0.314$ and have the bins contain exactly equal mass. However all bin total masses are within 10% of each other.

Increasing the number of grain species

To accompany our main `M6-0...M6-4` simulations which use 6 bins, we also run two simulations with more species of grains/bins in order to test how our results are affected by the number of species present. We ran one with 12 bins and the other with 18 bins, which we denote `M12` and `M18` respectively. When creating these samples with additional bins, we decide to subdivide each of the original 6 bins into 2 and 3 bins, again keeping an equal mass in each bin. This maintains the original bin edges from the 6-bin sample and thus allows for a more straightforward comparison of the results between the different discrete distributions. Once the new (additional) bin edges are computed, the same procedure of equal drag from eqaution 4.12 is used to select a representative τ_s for each bin.

4.2.3 Planetesimal/clump identification

To quantify how the different sized grains participate in the formation of planetesimals in our simulations, we must first identify which grains are a part of bound planetesimals. For this study, we accomplish this with a dust density cut. The Hill radius denotes a region where the gravity of an object in a circumstellar disc dominates over the shear due to the velocity gradient of the background Keplerian rotation. This shear is the only force that directly opposes the gravitational collapse of the dust. As described in Rucska & Wadsley (2021), we can covert the Hill radius into a Hill density, above which a dust clump is unstable to gravitational collapse. In the physical parameters of our model, this Hill density is given by,

$$\rho_H = 9\frac{\Omega^2}{4\pi G}. \tag{4.13}$$

With our choices of parameters, $\rho_H = 180$.

We identify all particles within cells with dust densities greater than ρ_H as being a part of bound planetesimals, All adjacent cells above this threshold are considered the same planetesimal. The triangular shaped cloud scheme that translates particle data to the gas grid smooths the dust density on the length scale of a single grid cell. As a result, some cells with relatively few particles have a dust density above ρ_H because there are tens of thousands of particles in the neighbouring cells. We also average clump-related data over the multiple `M6-0...M6-4` simulations, removing some of the influence of the stochastic nature of the non-linear SI from our results concerning planetesimals. For reasons of computational expense from the large number of particles in our simulations, we do not opt for a more sophisticated clump finding algorithm as in Rucska & Wadsley (2021).

4.3 Dust surface density at different grain sizes

In this section we examine the dust surface density in the multiple-grain simulations (`M6-0,...,M6-4`, hereafter referred to collectively as `M6`) and compare them with the surface density from the single-grain simulations (`S0,...,S3`, hereafter `S`). We inspect the surface density maps visually and then present a quantitative analysis of rudimentary observational consequences resulting in differences from these maps.

The dust surface density in the 6 different sizes or species of dust grains at $t = 100\Omega^{-1}$ in the `M6-0` simulation is shown in Figure 4.2. We present all data from single snapshots at $t = 100\Omega^{-1}$ because at this stage planetesimal formation has begun in earnest, but the planetesimals have not yet disrupted the other features in the dust such as the filaments. As we discuss in detail in Section 4.1 of Rucska & Wadsley (2021), the numerical cross-sections of the planetesimals in our simulations (and all similar simulations in the literature) are unphysically large, which causes the planetesimals to post-formation interact more strongly with the other dust particles than we would expect in nature. Thus, the true final state of the dust surface density post planetesimal formation is uncertain.

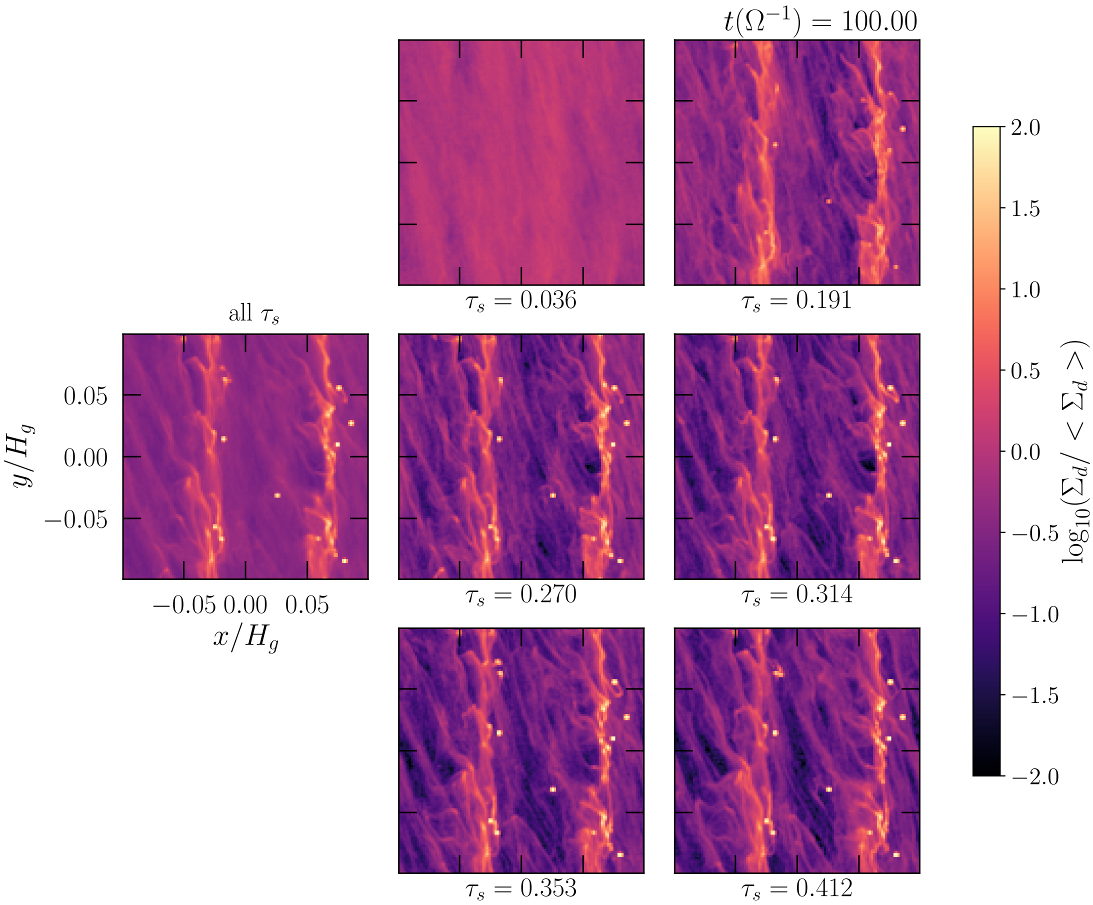

FIGURE 4.2: Dust surface density in the x-y (radial-azimuthal) plane for each species of grain in the `M6-0` simulation. The two right columns represent the surface density in the individual species, each identified by their grain size which here is represented by the dimensionless stopping time, τ_s (see equation 4.11 and surrounding discussion). The lone panel in the left column represents the full dust surface density in the simulation, with all grain species. The colour represents the logarithm of the dust surface density normalized by the mean dust surface density. The mean and normalization is computed in each panel individually. These data represents the simulation at time $t = 100$ in units of the inverse orbital frequency, Ω^{-1}.

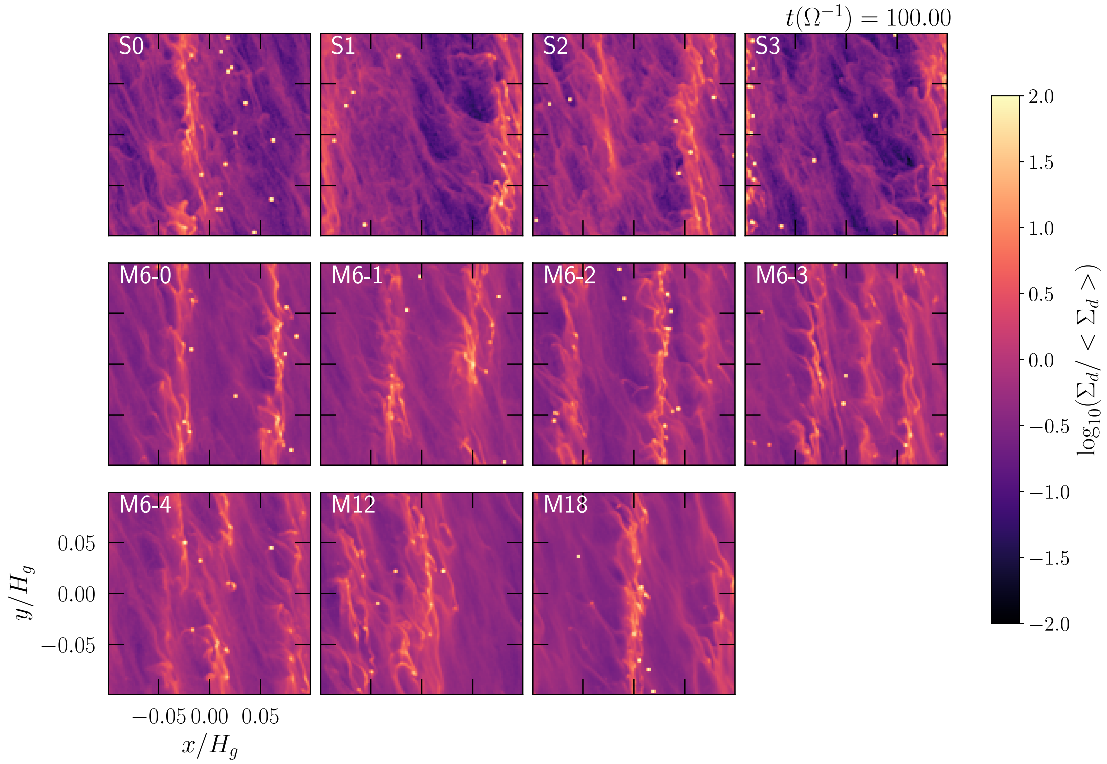

FIGURE 4.3: Dust surface density at $t = 100\ \Omega^{-1}$ in the x-y (radial-azimuthal) plane for all simulations. The `S` simulations use a single grain size, and the `M6` simulations use multiple sizes simultaneously. See Table 4.1 for a summary of the simulation parameters.

We pick $t = 100\Omega^{-1}$ as a compromise to capture the coexistence of the planetesimals and the filaments, which we believe to be the most realistic representation of the saturated stage of the non-linear streaming instability.

We notice immediately in Figure 4.2 that the smallest sized dust grains (lowest τ_s) do not readily collect into filaments or planetesimals at all, even when the larger grains are producing dense feature simulatenously. All grains with $\tau_s > 0.1$ participate in the structure of the filaments, while the distribution of the $\tau_s = 0.0355$ grains is smooth with relatively little spatial variation. Secondly, with a more careful visual inspection of the $\tau_s = 0.191$ surface density map, one can see that the brightest, $\sim$2-3 cell wide objects in the largest grains–which represent the planetesimals–are less bright than in the $\tau_s > 0.2$ grains, suggesting the $\tau_s = 0.191$ grains do not form into planetesimals as readily (for more quantitative results concerning clumping, see Section 4.4). In the full dust surface density, which includes all grains ("all τ_s" panel), we see altogether the filaments, planetesimals, and the smooth, dispersed quality of the smallest grains which is most apparent in the space between filaments. Similar visual observations can be seen in other studies of the non-linear SI with multiple grain sizes (cf. Yang & Zhu 2021 Figures 4 and 6, Bai & Stone 2010a Figure 2, Johansen et al. 2007 Figure 2).

We can make similar observations when comparing the surface density maps of the `M6` and `S` simulations, shown in Figure 4.3. The `S` use one grain size of $\tau_s = 0.314$ and thus more closely resemble the $\tau_s = 0.270$ to 0.412 grains from the `M6` simulations, in that the dust mass at these sizes is predominantly concentrated into planetesimals and filaments which are separated by relatively empty regions with surface densities $\lesssim$10% of the mean surface density. The smaller grains in the `M6` simulations fill these empty regions.

More quantitative confirmation of these observations can be seen in the probability distribution functions (PDFs) of the dust surface density, in Figure 4.4. The top panel

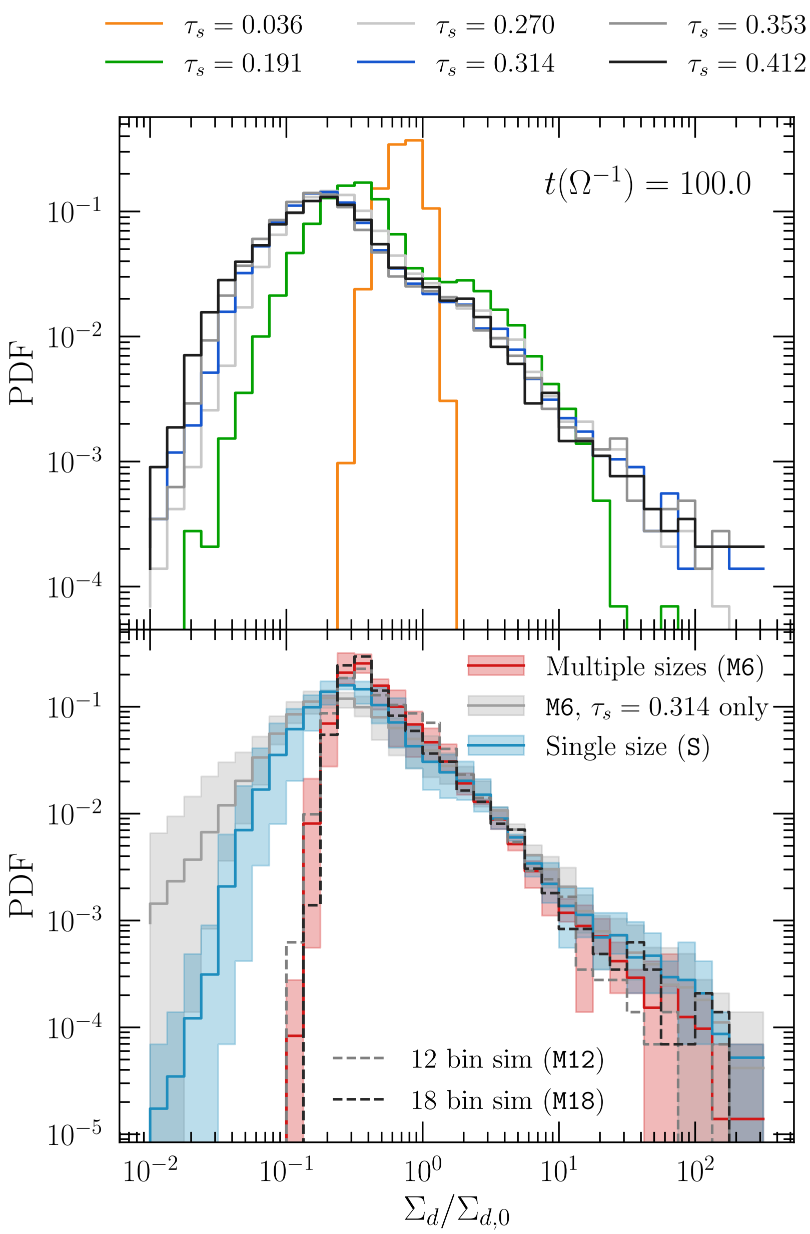

FIGURE 4.4: Probability distribution functions (PDFs) of the dust surface density in our simulations at $t = 100\Omega^{-1}$. *Top.* PDF for the `M6-0` simulation for each τ_s (grain size) bin (cf. Figure 4.2). The normalization by the mean surface density is computed for each grain species individually. *Bottom.* PDFs for all simulations (cf. Figure 4.3). The red (blue) shaded regions represent the maximum and minimum bounds among all `M6` (`S`) simulations, and solid line represents the mean PDFs. Analogously, the grey shaded data and solid line represent the $\tau_s = 0.314$ grains from the `M6` simulations only. The dashed curves are the PDFs for the `M12` and `M18` simulations.

shows the PDFs for the individual grains from the M6-0 simulation at $t = 100\Omega^{-1}$. Here, we quantify what is observable in Figure 4.2: the distribution of surface density in the $\tau_s = 0.036$ grains is narrow, peaking around the mean, $\Sigma_{d,0}$. The $\tau_s = 0.191$ distribution is wider by an order of magnitude in each direction, which is a sign that these grains are participating in filaments. Yet only the grains with $\tau_s > 0.2$ extend out to surface densities greater than $100\Sigma_{d,0}$–a (rough) proxy for planetesimals. The PDFs of the particle volume density from Yang & Zhu (2021) Figure 8 show similar segregation by grain size.

The bottom panel of Figure 4.4 highlights how this affects the overall surface density in the M6 simulations. The PDFs extend only as low as $0.1\Sigma_{d,0}$, while the distributions from the single size $\tau_s = 0.314$ simulations extend out to $0.01\Sigma_{d,0}$. Interestingly, when looking at the $\tau_s = 0.314$ grains from the M6 simulations on their own, these PDFs show there are more low surface density areas in these grains than there are in the S simulations at the this size. This suggests that the presence of different-sized dust grains in the M6 results in more empty or lower surface density regions than if the $\tau_s = 0.314$ grains were left to evolve on their own.

The PDFs for the M12 and M18 simulations–which have more grain size bins than the M6 simulations–are also shown in the bottom panel of Figure 4.4. These PDFs follow the M6 data closely, suggesting that the number of grain species does not affect how the dust surface density is distributed.

The differences in the S (blue) and M6 (red) PDFs have interesting observational consequences. There many more regions with low surface density in the S simulations and (on average) more regions at higher surface densities. Depending on the opacity of the dust, this could lead to a lower estimate of the total dust mass from observations due to optical depth effects. We explore this idea in the next section.

4.3.1 Observational consequences

Observations of some bright rings in protoplanetary discs have come to the interesting conclusion that the thermal emission from the dust in these rings is likely not optically thick (Dullemond et al. 2018; Huang et al. 2018; Cazzoletti et al. 2018; Macías et al. 2019; Maucó et al. 2021). Other studies have shown that, with a parameterized model of planetesimal formation via the streaming instability, this can be explained by pebble-sized dust mass in rings being converted into planetesimals, which do not contribute to mm wavelength emission (Stammler et al. 2019; Maucó et al. 2021). Taking this idea a step further, Scardoni et al. (2021) took the dust surface density profiles from 2D simulations of the SI and explored how the dust clumping would affect observations. They use a complex model for the dust opacity (Birnstiel et al. 2018) and find general agreement between their calculations of observed properties of discs such as the fraction of the emission that is optically thick and the spectral index. They also conclude that planetesimal formation can reduce the optical depth of emission at mm wavelengths.

In this, section we construct two mass correction factors which quantify the observational implications of the varying degrees of dust clumping seen in our simulations[2]. We explore how these mass correction factors vary with optical depth ($\tau_{\rm opt} = \kappa\Sigma_{d,0}$)[3], and how they evolve over time. We forgo a detailed mock observational treatment and complicated calculations of the dust opacity in favour of a technique that primarily highlights the differences in emission from our single grain size and multiple grain size models versus a uniform dust surface density map without clumping due to the SI.

[2]Note, the dust features created by the SI occur on length scales well below 1 AU, and are hence unresolvable by any contemporary observational facility.

[3]We vary $\tau_{\rm opt}$ by holding $\Sigma_{d,0}$ fixed and varying κ in units of $(\Sigma_{d,0})^{-1}$.

The intensity of emission (I) from a source of radiation (source function S, assumed constant with dust physical properties, etc.), can be written in integrated form as,

$$I(\tau) = S(1 - e^{-\tau_{\rm opt}}), \tag{4.14}$$

where $\tau_{\rm opt}$ is the optical depth, and the wavelength dependence of all quantities has been ignored. We consider a simple prescription for the optical depth, $\tau_{\rm opt} = \kappa\Sigma$, where κ is the dust opacity and Σ is the dust surface density. For optically thin emission (low opacity, and/or small amount of mass), $\tau_{\rm opt} \ll 1$, and then $I \approx S\kappa\Sigma$ and one can convert that emission to an estimate of the surface density if S and κ are known: $\Sigma_{\rm est} = I/S\kappa$. However, if we consider that this underlying emission I may or may not be optically thick (equation 4.14), e.g. due to clumping, then we have,

$$\Sigma_{\rm est} = \frac{(1 - e^{-\kappa\Sigma})}{\kappa}, \tag{4.15}$$

which is the (potentially erroneous) surface density one would compute under the assumption the emission was optically thin (If $\kappa \ll 1$, then $\Sigma_{\rm est} \sim \Sigma$). This expression is useful as it does not require knowledge of the source function.

We take the surface density map from our simulations (Σ) and compute an converted surface density map $\Sigma_{\rm est}$ via equation 4.15. We do a wide sweep of values of κ, acknowledging that there are large uncertainties in the values of dust opacity (Birnstiel et al. 2018). We then take the spatial average of that converted surface density, $< \Sigma_{\rm est} >$, to model the fact that all features in our simulations would be unresolved and hence smoothed by the observational beam.

Finally, we construct two dust mass correction factors from these average estimate surface densities. First, using a ratio of the true averaged surface density of the simulation Σ_{actual} (i.e. the mean surface density $\Sigma_{d,0}$),

$$C = \frac{\Sigma_{\text{actual}}}{< \Sigma_{\text{est}} >}. \tag{4.16}$$

This factor quantifies ignorance about the optical depth of the emission as well as unresolved clumping.

Perhaps more interestingly, we can compute the $< \Sigma_{\text{est}} >$ for a *uniform* dust density distribution at Σ_{actual}, and then divide that by the $< \Sigma_{\text{est}} >$ for our simulations, which display strong clumping in the dust surface density. This leads to a second correction factor

$$C_{\text{clump}} = \frac{< \Sigma_{\text{est,uniform}} >}{< \Sigma_{\text{est}} >} = \frac{C}{C_{\text{uniform}}}. \tag{4.17}$$

This ratio excludes any ignorance about the optical depth, and instead isolates the effects of dust clumping via the streaming instability. If one is confident about the optical depth of an observed source, C_{clump} represents the factor the inferred dust surface density should be multiplied by if the SI is believed to have caused significant clumping in that region of the disc.

The top panel of Figure 4.5 shows C as a function of τ_{opt}. At low τ_{opt}, $C_1 \sim 1$ for all simulations, since in this regime the optically thin assumption is valid by definition. At high τ_{opt}, all simulations converge to $C_1 \sim \tau_{\text{opt}}$ since the exponential term in equation 4.15 vanishes, removing any dependence in C on the surface density distribution in the simulations and hence any influence of clumping. It is at intermediate values of τ_{opt} where differences between the sets of simulations are apparent.

To better observe these differences, we use our second correction factor C_{clump}, seen in the bottom panel of Figure 4.5. This factor is the ratio of C for each simulation (coloured

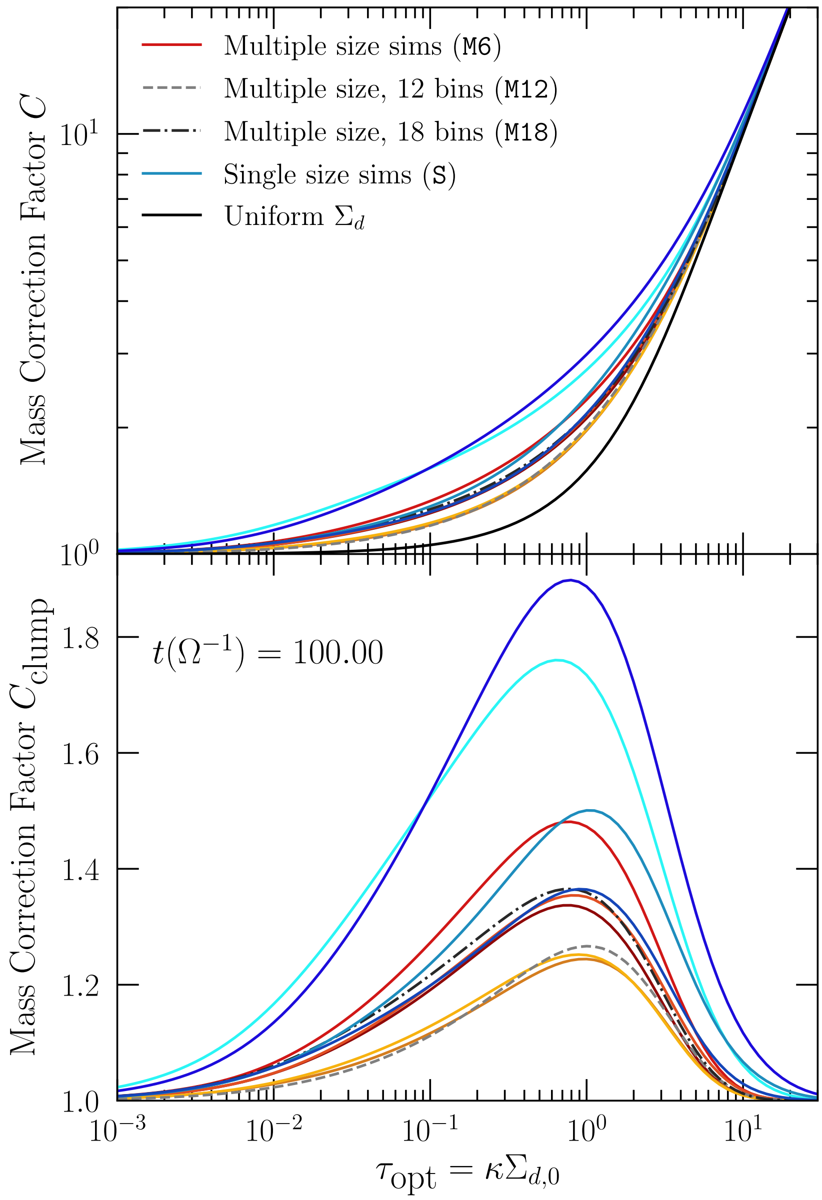

FIGURE 4.5: Observational dust mass correction factors, C and $C_{\rm clump}$. Details on how these factors are defined are in Section 4.3.1. *Top.* Comparing the mean surface density from the simulation ($\Sigma_{d,0}$) to surface densities converted from mock emission of the simulation dust surface density maps (Figure 4.3), viewed at varying optical depth (or, equivalently, dust opacity). *Bottom.* Mass correction factor due to the effects of strong clumping from the streaming instability. Comparing observed mean surface densities converted from simulation surface density maps to a uniform surface density. These data are equivalent to dividing the coloured and dashed curves by the solid black curve in the top panel.

and dashed lines, top panel) to the C for a spatially uniform dust surface density distribution at $\Sigma_{d,0}$ (black line, top panel[4]). Hence, what $C_{\rm clump}$ highlights is the influence of the different amount of clumping in the dust surface density maps/distributions between the two sets of simulations (Figure 4.3 and 4.4). If the optical depth is well constrained (e.g. from grain properties), it is the factor one would multiply a dust surface density inferred from observations by in order to account for the (unresolved) dust clumping from our simulations.

We note that $C_{\rm clump}$ peaks near $\tau_{\rm opt} = 1$ for all simulations, with peak values generally higher for the single size simulations `S` than the `M6` simulations with multiple sizes. As we discussed earlier in Section 4.3, when compared the simulations with multiple grains, the dust in the `S` sims is more heavily concentrated into filaments and planetesimals, and the spaces between filaments have much lower surface density. As a consequence, in our simple model, the dust emission from the `S` models is overall less bright than the `M6` models, as there is relatively less dust mass in the inter-filament space, and there is more dust in the filaments and planetesimals, where the emission is saturated at intermediate optical depths. Said another way, more of this dust mass is "hidden" in the `S` simulations, requiring a higher mass correction factor $C_{\rm clump}$ to account for this effect.

The peak values of $C_{\rm clump}$ are between $\sim 1.2 - 1.5$ for the `M6` and `M12` and `M18` simulations, which we believe to be more representative of protoplanetary disc grain size distributions in nature rather than a single size. Thus, for dust grains described by a Birnstiel et al. (2011) grain size distributions with stopping times peaked at $\tau_s = 0.314$, observational estimates of the dust mass from protoplanetary discs could be off by a factor of $20 - 50\%$ in regions of the disc where the streaming instability is active. If the grain size distribution were instead much more strongly peaked at a single size–i.e., closer to the `S` models than `M6`–then this mass correction factor could be as high as 80%.

[4]This curve is simply a plot of $\tau_{\rm opt}/(1 - \exp(-\tau_{\rm opt}))$.

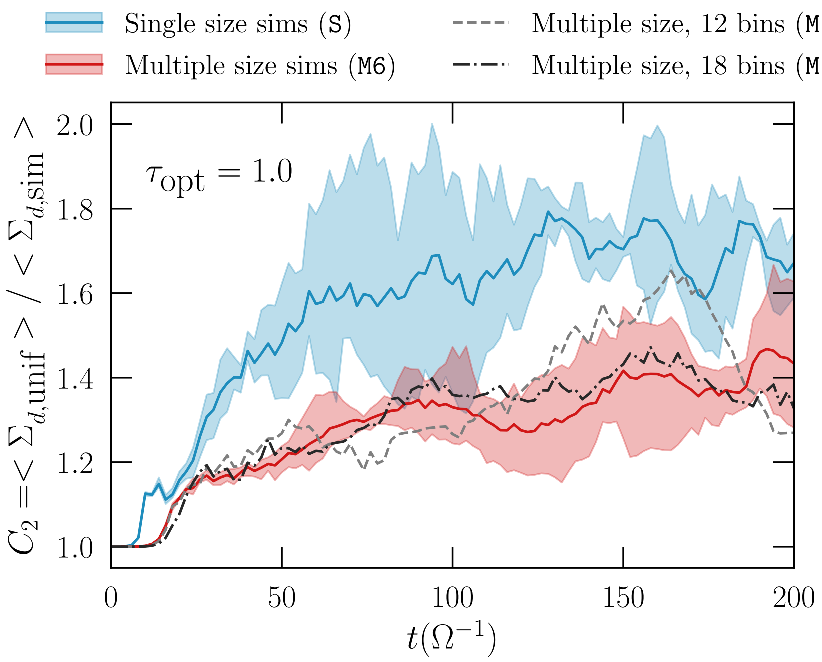

FIGURE 4.6: The dust mass correction factor $C_{\rm clump}$ over time in all simulations, at an optical depth of $\tau_{\rm opt} = 1.0$. The shaded regions are bounded by the maximum and minimum values across the sample of multiple simulations, and the solid curves represent the means of that sample.

The values of C_{clump} at $\tau_{\text{opt}} = 1.0$ over time, plotted in Figure 4.6, are fairly stable over the course of our simulations. Once planetesimal formation begins, the main features of the dust surface density which influence C_{clump} persist over dozens of dynamical timescales. Note that the single snapshot values of C_{clump} presented in Figure 4.5 are from $t = 100\Omega^{-1}$, and in Figure 4.6 this is one of the rare times where there is significant overlap between the single size and multiple size sims. At most other times the curves in Figure 4.5 do not overlap at all. Similar to the single snapshot data, the curves for the `M12` (12 bins) and `M18` (18 bins) simulations in Figure 4.6 are consistent with the `M6` simulations, suggesting incorporating more grain species does not influence our results.

Note, we do not plot C over time as it has the same shape of C_{clump}, since the difference in normalization between C and C_{clump} (at a specific optical depth) are just different constant factors. C uses $\Sigma_{d,0}$ as a reference point, and, for the purposes of Figure 4.6, C_{clump} uses $< \Sigma_{d,\text{unif}} > (\tau_{\text{opt}} = 1.0)$.

4.4 Planetesimal composition: grain size

The bright cells in the surface density maps in Figure 4.3 suggest that all simulations from our study produce dense, gravitationally bound clumps. As described in Section 4.2.3, we identify bound clumps (i.e. planetesimals) as regions where the 3D dust volume density (ρ_d) exceeds the Hill density (ρ_H)–the density threshold above which the dust mass is unstable to gravitational collapse. All grid cells with $\rho_d > \rho_H$ that are adjacent to each other are identified as the same plantesimal. In this section we explore the composition of these clumps in terms of the various dust species within them, as well as the composition of the dust mass that lost from each clump from simulation snapshot to snapshot.

The fraction of mass in clumps for each grain size is shown in Figure 4.7. The different coloured bands represent the mass in each grain size bin. Table 4.2 shows the

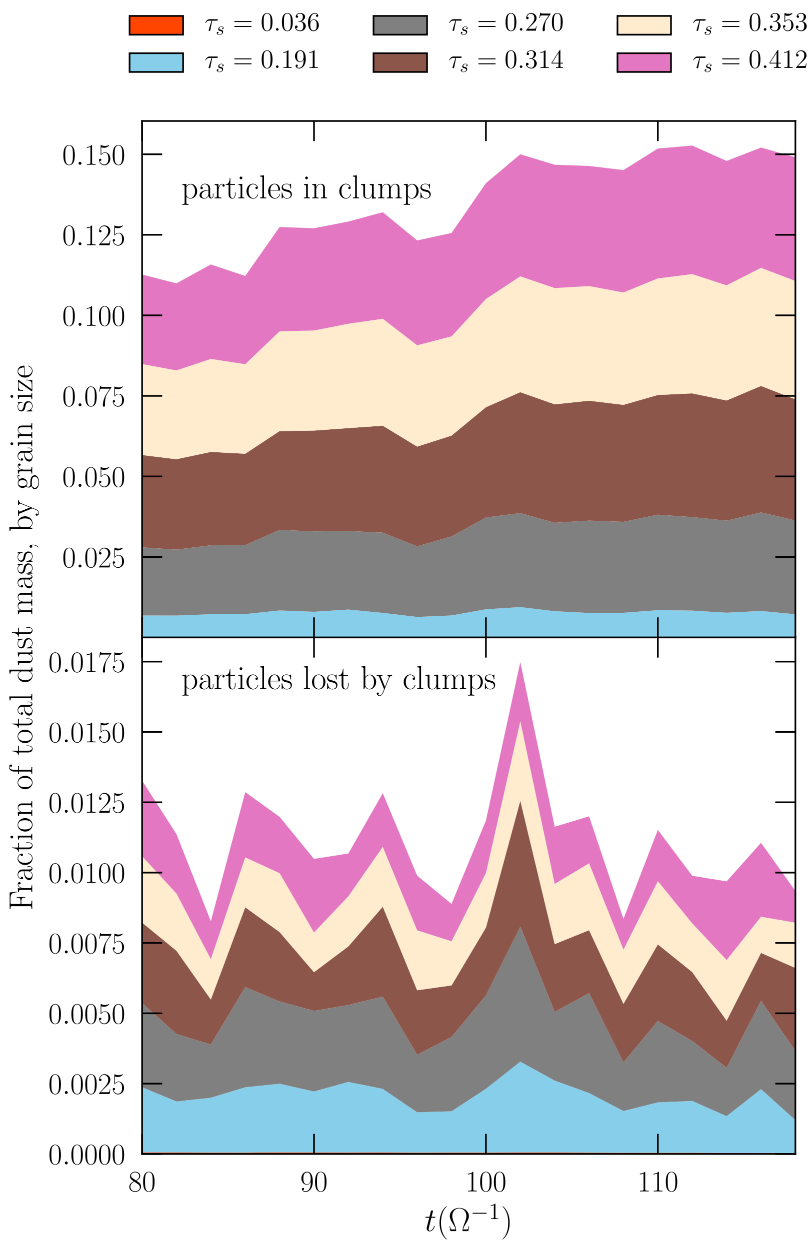

FIGURE 4.7: Fraction of total dust mass for particles in bound clumps or lost by clumps, for each τ_s (grain size) bin. These data represent an average over the whole group of `M6` simulations. The coloured bands represent the fractional mass for each τ_s. The data for each grain size are vertically stacked so that the total mass in clumps (or lost by clumps) for all dust grains is tracked by the top of the pink shaded region. The data for $\tau_s = 0.036$ are too small to be seen on this scale; see Table 4.2 for time-averaged values of these data for all τ_s, and for the data from the `M12` and `M18` simulations.

TABLE 4.2: Time averages ($t = 80 - 120\Omega^{-1}$) of the total dust mass in bound clumps and lost by clumps, split by τ_s (grain size) (cf. Figure 4.7).

(A) Dust mass in bound clumps (as fraction of total dust mass).

τ_s	6 bin sims	12 bin	18 bin
0.036	4.90×10^{-5}	4.38×10^{-4}	5.84×10^{-4}
0.191	7.73×10^{-3}	7.47×10^{-3}	1.08×10^{-2}
0.270	2.60×10^{-2}	1.81×10^{-2}	3.20×10^{-2}
0.314	3.38×10^{-2}	2.29×10^{-2}	4.23×10^{-2}
0.353	3.30×10^{-2}	2.24×10^{-2}	4.33×10^{-2}
0.412	3.43×10^{-2}	2.06×10^{-2}	4.46×10^{-2}

(B) Dust mass lost by clumps (as fraction of total dust mass).

τ_s	6 bin sims	12 bin	18 bin
0.036	4.71×10^{-5}	2.74×10^{-4}	3.52×10^{-4}
0.191	2.04×10^{-3}	1.99×10^{-3}	2.70×10^{-3}
0.270	2.78×10^{-3}	2.51×10^{-3}	3.83×10^{-3}
0.314	2.43×10^{-3}	2.21×10^{-3}	3.38×10^{-3}
0.353	1.95×10^{-3}	1.75×10^{-3}	2.73×10^{-3}
0.412	1.93×10^{-3}	1.72×10^{-3}	2.55×10^{-3}

time averages for these data over the range of time across the full x-axis in Figure 4.7. As seen in the top panel and in Table 4.2a, the majority of the mass in clumps ($> 90\%$) is in the grains with $\tau_s > 0.2$. A small fraction of the clumps are composed of $\tau_s = 0.191$ grains and there is effectively no clump mass associated with the $\tau_s = 0.035$ grains. These results corroborate earlier observations from Figure 4.2 regarding the decreased prominence or total lack of visible planetesimals in the surface density maps for these grain sizes.

Some particles that are within in a clump in one snapshot are not within that same clump[5] in the consecutive snapshot. These particles may be loosely bound at the edge of the gravitational influence of the planetesimal (i.e. near the Hill radius) or simply passing through the high-density grid cells that are identified as planetesimals. We explore these

[5]Planetesimals in concurrent simulation snapshots which share over 50% of the same unique particles (determined by particle ID numbers) are determined to be the same clump.

TABLE 4.3: Residence time (equation 4.18) for the different dust grains in the M6 simulations.

τ_s	Mass in clumps	Mass lost from clumps	Residence time (Ω^{-1})
0.036	4.90×10^{-5}	4.71×10^{-5}	2.08
0.191	7.73×10^{-3}	2.04×10^{-3}	7.60
0.270	2.60×10^{-2}	2.78×10^{-3}	18.7
0.314	3.38×10^{-2}	2.43×10^{-3}	27.8
0.353	3.30×10^{-2}	1.95×10^{-3}	33.9
0.412	3.43×10^{-2}	1.93×10^{-3}	35.6

ideas with velocity and vertical position data in Section 4.4.2. For the purposes of this analysis, we identify these transient clump particles as "lost", and plot the composition of this lost dust mass in the bottom panel of Figure 4.7 and provide the time averages of these data in Table 4.2b. The lost dust mass is nearly evenly distributed among the grains at $\tau_s > 0.1$, with the highest proportion involving the $\tau_s = 0.270$ grains. Note that on average, approximately 10% of all the mass in clumps is consistently lost between snapshots.

We can combine the results from the two panels of Figure 4.7 into a single idea known as the residence time–a quantity that estimates how long the dust mass of a particular grain species will remain in clumps given how quickly that mass is lost. This is represented simply by,

$$\text{Residence time} = \Delta t_{\text{snap}} \left(\frac{\text{Mass in clumps}}{\text{Mass lost btwn. snapshots}} \right), \tag{4.18}$$

where Δt_{snap} is the amount of time between data outputs and in this study is equal to $2.0\ \Omega^{-1}$. The residence time is hence equivalent to diving the data in Table 4.2a by the data in Table 4.2b and multiplying by Δt_{snap}.

We present calculations of the residence time in Table 4.3. This table confirms our prior conclusions when considering both panels of Figure 4.7 together: the largest grains are the most bound, longest-lived components of the planetesimals. All grains with

$\tau_s > 0.2$ have residence times above 18 Ω^{-1}, and this quantity increases monotonically with τ_s. The smallest grains at $\tau_s = 0.036$ have residence times comparable to Δt_{snap}, suggesting they form only a transient component of the clump mass[6].

Interestingly, the $\tau_s = 0.191$ grains have an intermediate residence time of $\sim 8\ \Omega^{-1}$. We can also observe from the dust surface density maps for each grain species (Fig. 4.2) and the PDF of those surface densities (top panel Fig. 4.4) that the $\tau_s = 0.191$ grains exhibit behavior that is not like the smallest grains or the larger grains. The smallest grains do not participate in any kind of dust clumping, and the larger grains readily form gravitationally unstable planetesimals. Our results suggest the $\tau_s = 0.191$ grain behavior in the non-linear evolution of the streaming instability is somewhere in-between these two regimes.

We can see evidence of this in-between behavior for the $\tau_s = 0.191$ grains in Figure 4.8, which shows the amount of dust mass above a certain density threshold at each grain size at $t = 100\ \Omega^{-1}$. In the bottom panel, the threshold is ρ_H, and hence these data are equivalent to (a single time/vertical slice of) the data from the top panel of Figure 4.7. We see similar conclusions as before: the $\tau_s > 0.2$ grains dominate the clump mass budget, the $\tau_s = 0.036$ grains are not a part of the clumps at all, and the $\tau_s = 0.191$ make up a small fraction of the mass at clump densities.

In the top panel of Figure 4.8, the threshold is $\rho_{g,0}$, the mid-plane gas density. In our simulations and those like it from the literature, the gas density displays little variation, even when the streaming instability develops strong dust clumps and filaments (Li et al. 2018). So the $\rho_{g,0}$ threshold effectively marks the boundary where the dust density dominates the total local mass density ($\rho = \rho_d + \rho_g$), an important regime for the streaming instability (Youdin & Goodman 2005). We see that the $\tau_s = 0.036$ grains are

[6]A more sophisticated clump-finding approach may definitely determine these small grains to be kinematically unbound. However, our simpler (and less expensive) analysis reaches the same conclusion to the degree of precision suitable for our study.

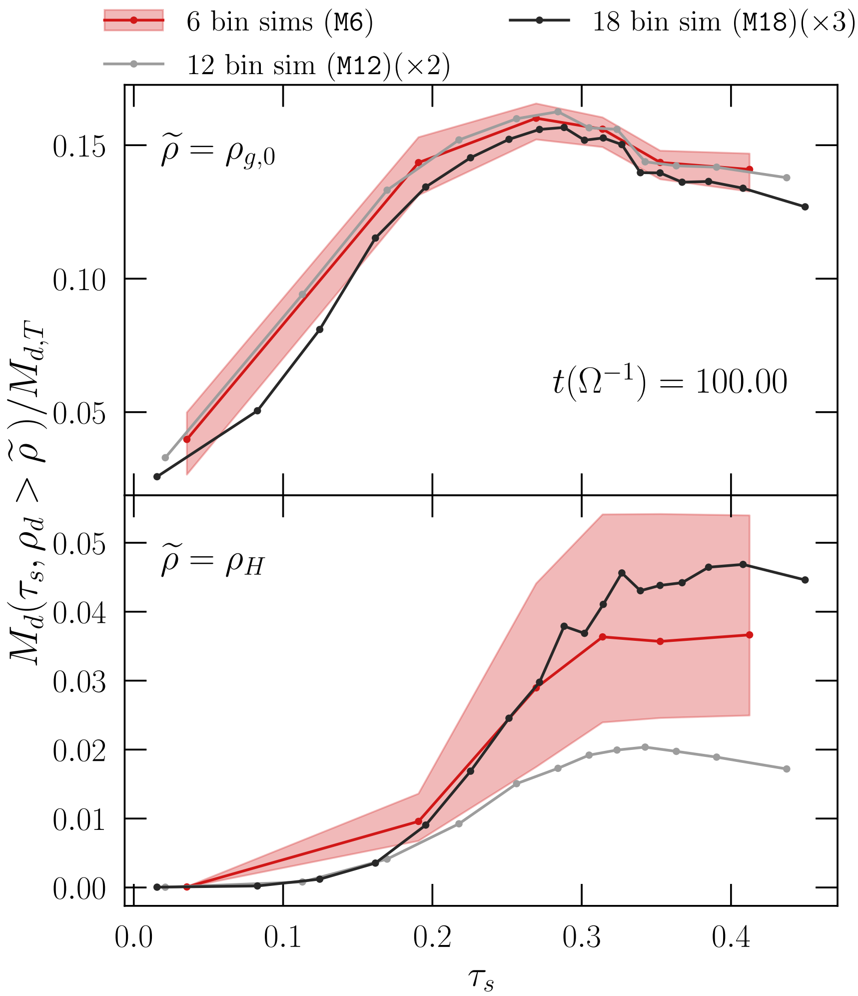

FIGURE 4.8: Total dust mass above certain density thresholds as a function of grain size (τ_s), normalized by the total dust mass in the simulation domain. In the top panel the threshold is the initial midplane gas density $\rho_{g,0}$ and the bottom panel the threshold is the Hill density (equation 4.13), the threshold above which dust forms gravitationally bound planetesimals. The shaded regions represent the bound for the maximum and minimum across the five `M6` simulations. The `M12` and `M18` data are shown with grey and black curves, with multiplications by 2 and 3 to allow for a direct comparison with the `M6` simulations, which have fewer bins and hence more dust mass per bin.

proportionally underrepresented even at the lower threshold of $\rho_{g,0}$, representing $\sim 7\%$ of all dust mass. Meanwhile, the $\tau_s = 0.191$ grains contribute just as much mass above this threshold as the larger grains.

Including observations from the dust surface density at each grain size (Fig. 4.2), we can interpret the data in Figure 4.8 as supporting the idea that the $\tau_s = 0.191$ grains form filaments but not strong clumps, while the smaller $\tau_s = 0.036$ grains form neither. In other words, the $\rho_{g,0}$ threshold appears to delimit the dust density boundary for the filamentary features.

4.4.1 Simulations with larger numbers of species

As with the results from Section 4.3, using a larger number of grain species to sample the grain size distribution does not change our results. In Table 4.2, we include time averages of the mass in clumps and lost by clumps for the `M12` and `M18` simulations. As discussed in Section 4.2.2, the larger bin samples are created by sub-sampling the 6 bins from the `M6` simulations, so that we can easily combine the sub-sampled bins to match the τ_s bin boundaries from 6 bin sample for the purposes of comparison. The overall conclusions from the `M12` and `M18` data are the same: the larger $\tau_s > 0.2$ grains dominate the clump mass budget, while the dust mass lost is more evenly spread among the $\tau_s > 0.1$ grains. Also, the shape of the curves from Figure 4.8 are within the bounds set by the `M6` simulations.

We note that, as a whole, including Figure 4.5, the `M12` has slightly lower mass in clumps and dense structures than the `M6` average, while the `M18` data is slightly above this average. We do not interpret these differences as evidence that an increased number of bins affects planetesimal formation in a deterministic way. Rather, we view these differences are a consequence of the non-linear nature of the developed stage of the streaming instability. The variability in the SI is immediately observable as the range

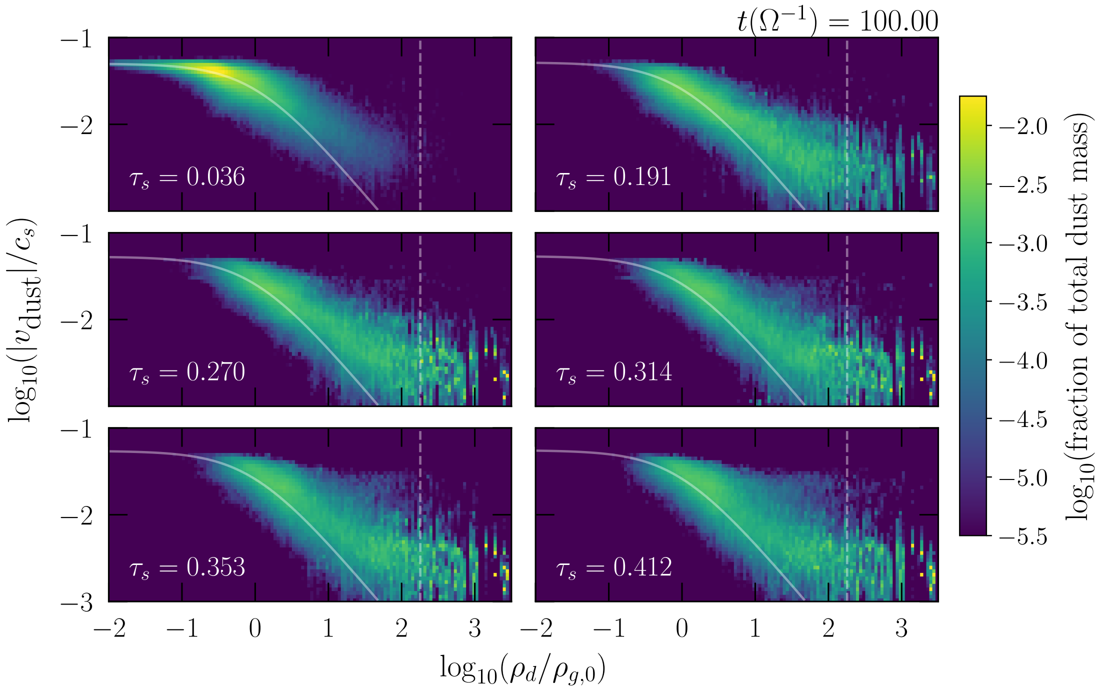

FIGURE 4.9: 2D histogram in the dust density-velocity phase space for the different grains in the `M6-0` simulation at $t = 100\Omega^{-1}$. Each panel is the histogram for the individual grain species. Note that all dust velocities are measured with respect to the background Keplerian flow. The (logarithmic) colourbar is normalized to the total dust mass in the simulation. The darkest bins do not contain any particles; a minimum value is applied for aesthetic purposes. The solid white curve represents the NSH equilibrium velocity (Nakagawa et al. 1986; see also equations 7 in Youdin & Johansen 2007) and the vertical white dashed line represents the Hill density in our simulation units (equation 4.13). The NSH velocity is a function of τ_s and the local dust-to-gas mass ratio, $\epsilon = \rho_d/\rho_g$. Since $\rho_g \approx 1$ throughout our simulation domain, we use ρ_d as a proxy for ϵ.

of outcomes among the individual `M6` and `S` simulations, and is the overarching theme of our previous study (Rucska & Wadsley 2021).

4.4.2 Dust velocity

In this section we use velocity data to further explore the differences in behavior between the smaller and larger dust grains in our simulations, and the consequences this has on planetesimal formation.

A 2D histogram of the dust particles in the dust volume density (ρ_d) and individual particle velocity ($|v_{\rm dust}|$) phase space, for the `M6-0` run, is shown in Figure 4.9. Also plotted is the magnitude of the equilibrium drift velocity for the dust (Nakagawa et al. 1986) as the white curve, which tracks the expected steady-state drift rates of the dust (in the absence of complex dynamics like the non-linear SI). We see at large ρ_d, the expected drift velocity falls to 0, predicting that the dust fully decouples from the dust-gas equilibrium and orbits at the Keplerian velocity, and at low ρ_d the drift velocity approaches to the radial pressure gradient offset $\sim \eta v_K$ with a factor of order unity that depends on τ_s.

The smallest $\tau_s = 0.036$ dust grains have most of their mass below $\rho_{g,0}$, which is in line with conclusions regarding Figure 4.8. Nearly all of the dust at this size–which does not form filaments or clumps–follows the NSH equilibrium curve closely. This provides further evidence that these smallest grains do not participate in highly non-linear behavior that deviates from analytical, steady-state expectations.

Most of the $\tau_s = 0.191$ grains do not exist at densities above $\rho_H = 180$, but between 30 and $100\rho_{g,0}$, which corroborates earlier discussions in Section 4.4 which conclude these grains predominantly participate in filament formation but not clump formation. The lower density dust between ~ 0.3 and $10\rho_{g,0}$ primarily follows the NSH equilibrium curve.

For the larger $\tau_s > 0.2$ grains, most of their mass exists at large densities well above ρ_H. Dust in the centre of planetesimals can be seen as the bright yellow pixels at $\rho_d \geq 10\rho_H$. The lines of above and below these brightest pixels show that the dust resolution element superparticles can have slightly different velocities within a single grid cell. As with the $\tau_s = 0.191$ grains, the lower density dust is centered around the NSH expectations.

Note that for all grains with dust densities above $\sim 30\rho_{g,0}$, the bulk of the mass

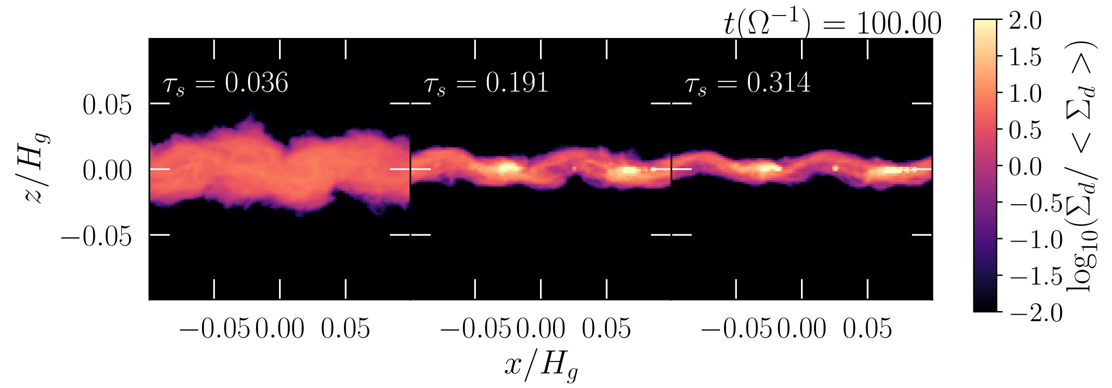

FIGURE 4.10: Dust surface density in the x-z (radial-vertical) plane for a subset of grains from the M6-0 simulation at $t = 100\Omega^{-1}$.

deviates substantially from the NSH equilibrium, settling at velocities between ~ 0.001 and $0.01c_s$. This is evidence of small amplitude, local turbulence, likely driven in part by the dense dust clumps near the midplane imparting substantial momentum onto the gas over small length scales. The width of the histogram about the NSH curve at lower densities is likely a result of this more disperse dust interacting with stirred up midplane gas.

4.4.3 Vertical position

We can further highlight the different behavior between the different sized dust grains by briefly exploring the properties of the vertical (out of midplane) dynamics. Figure 4.10 shows the dust surface density in the radial-vertical (x-z) plane. We can see the that small grains have a much more extended vertical profile than any of the larger grains, with no bright features. Comparatively, the $\tau_s = 0.314$ grains (which look nearly identical to the other grains in the largest four sizes, which are not shown) are distributed very closely to the midplane. The $\tau_s = 0.191$ are slightly more extended with slightly broader features than the large grains, and the bright planetesimal between $x = 0.0$ and $0.05H_g$ is not very bright in these grains. Yet, the filament features are readily visible.

We can further quantify these observations by computing the dust scale height, defined as,

$$H_p = \sqrt{\frac{1}{N_{\rm par}} \sum_i^{N_{\rm par}} (z_i - \overline{z})^2}, \tag{4.19}$$

and a similar (and related) quantity, the root mean-square (RMS) z velocity,

$$v_{z,\rm rms} = \sqrt{\frac{1}{N_{\rm par}} \sum_i^{N_{\rm par}} (v_{z,i} - \overline{v_z})^2}. \tag{4.20}$$

These values for all dust grains in the `M6-0` simulation are presented in Table 4.4. The H_p data confirm what is visible in the vertical surface density: the smallest grains have by far the most vertically extended scale heights, and the scale height monotonically decreases with τ_s. The scale height is directly related to the RMS of the vertical dust velocity since it is only through turbulent motions–which provide a constant source of vertical velocity dispersion–that the dust can maintain a persistent scale height (Youdin & Lithwick 2007). Similar to observations made by Schaffer et al. (2018) and Schaffer et al. (2021) in their 2D simulations of the SI with multiple grains, it appears in our simulations that the larger grains stir up turbulence near the midplane, which causes the smaller grains, which are more tightly coupled to the gas aerodynamically (short drag stopping times), to remain suspended at relatively large scale heights. The vertical RMS velocity for the gas near the midplane is 4.13×10^{-3} (in units of c_s), which is very close to $v_{z,\rm rms}$ for the small $\tau_s = 0.036$ grains.

4.5 Conclusions and discussion

In this study we model a patch of a protoplanetary disc in 3D numerical hydrodynamics simulations. We model the dust component of the disc with multiple grain sizes simultaneously under conditions that are unstable to the streaming instability, and track the non-linear development of the SI to the formation of bound planetesimals. This paper

TABLE 4.4: Particle scale height and vertical RMS velocity for the different dust grains in the `M6-0` simulation at $t = 100\Omega^{-1}$.

τ_s	H_p (H_g)	$v_{z,\mathrm{rms}}$ (c_s)
0.036	11.7×10^{-3}	4.16×10^{-3}
0.191	4.47×10^{-3}	2.87×10^{-3}
0.270	3.40×10^{-3}	2.50×10^{-3}
0.314	3.03×10^{-3}	2.31×10^{-3}
0.353	2.77×10^{-3}	2.29×10^{-3}
0.412	2.64×10^{-3}	2.37×10^{-3}

extends previous work that used multiple grain sizes in simulations of the non-linear phase of the SI (Johansen et al. 2007; Bai & Stone 2010a; Schaffer et al. 2018; Schaffer et al. 2021; Yang & Zhu 2021). Most prior work used a grain size distribution with a number density described by a single power law, but in our study we sample a distribution that is the output of a widely-used model of grain growth and fragmentation applicable to midplane of protoplanetary discs (Birnstiel et al. 2011). To compare our multi-species results to prior work which modelled the dust with a single species, we match the peak of the size distribution to the grain size studied in Rucska & Wadsley (2021).

Our main results are as follows:

1. Only larger grains with dimensionless stopping times $\tau_s > 0.1$ participate strongly in the non-linear SI, producing filaments and regions with large dust densities that gravitationally collapse into planetesimals. The smaller grains do not form filaments or clumps at all, despite the fact they are embedded in an environment where roughly 5/6 of the dust mass is forming dense structures. This confirms a basic property of the multi-species SI at the non-linear stage (Bai & Stone 2010a; Yang & Zhu 2021), which remains true for a realistic protoplanetary disc grain size distribution from Birnstiel et al. (2011). The net result is there is more dust mass in the regions between the filaments in the multi-species simulations when compared

to the single grain simulations, and slightly less mass in the dense structures.

2. Clumping of dust via the SI on sub-AU length scales reduces the average surface brightness for a given amount of dust. This confirms in 3D models that the SI could explain the lower than expected (order unity) optical depths seen in observed protoplanetary disc rings (see Section 4.3.1 for details). We estimate that 20%-80% more dust may be present than in uniform mass distribution models. The effect is less severe for multi-size versus single-size models.

3. We identify bound clumps and dense dust features. Larger $\tau_s \gtrsim 0.2$ grains form clumps, $\tau_s \lesssim 0.04$ grains do not form clumps or filaments. Intermediate sizes are somewhat in between, forming filaments but not clumps. The velocities of the smallest grains are quite different from the larger grains in clumps and filaments, suggesting that these small grains—with a short drag stopping time that enforces tight coupling to the gas—simply sweep by the planetesimals rather than becoming incorporated into them. This implies a size cutoff for pebble and dust grains incorporated into asteroids and comets.

4. The main group of the multi-species runs in this study used 6 bins or species to sample of the grain size distribution. We test 12 and 18 bins to show convergence. More bins appears to have no measurable effect on the results for the multi-species simulations and we conclude that 6 bins is sufficient to study peaked grain size distributions.

4.5.1 The future of planetesimal formation via the SI with multiple grain sizes

Including multiple sizes in models of the non-linear SI effects not just planetesimal formation but also the observable properties of protoplanetary discs. Most prior work on the SI has modelled the dust with a single grain size. However, recent observations of protoplanetary discs (see Andrews 2020, for a review) and results from grain growth theory (Birnstiel et al. 2011; Birnstiel et al. 2015) suggest that there is a distribution of dust grain sizes within discs. An important consideration then is what the shape of this distribution should be.

In this paper we have shown that just an order of magnitude difference in grain size can determine whether grains are fully active in the SI all to way to planetesimal formation, or whether they do not even form filaments. This observation motivates further exploration of the grain size distribution parameter space. Our study represents a single instance of the Birnstiel et al. (2011) distribution for a specific set of disc conditions. In our results, most of the species participate in planetesimal formation. Shifting the distribution peak to smaller sizes—equivalent to considering different radial positions in the disc—would move dust mass from species that undergo strong clumping towards species that do not participate in planetesimal formation or primarily form only filaments. Presumably, this would result in an overall decrease in the total dust mass that is converted to planetesimals. Extending our work to a broader range of distributions would reveal how planetesimal formation varies in conditions at different radial locations in the disc.

Of particular interest is a distribution with a more equal mix of SI-active and SI-inactive grains. These conditions likely describe the onset of the SI and planetesimal formation. Early in the disc lifetime, most of the dust in the midplane may be too small ($\tau_s \lesssim 0.04$) to participate in planetesimal formation initially, and then grow through mutual collisions (e.g. Birnstiel et al. 2011) to involve sizes that are unstable to the SI. However, the time scales for grain growth are typically $> 10^4$ yr (e.g. Birnstiel et al. 2012), while the timescale for planetesimal formation via the SI is much shorter[7].

[7]For the timescales in our study, $100\Omega^{-1} \approx 16$ orbital periods, which is equivalent to ~200 years at 5 AU around a solar mass star.

Thus, for initially small grains, planetesimal formation may occur as grains grow. It would be interesting to explore this initial planetesimal formation phase with a dust size distribution that includes a larger proportion of smaller, SI-inactive grains.

More realistically, however, it is likely grain growth and the streaming instability occur simultaneously. Dust growth and fragmentation is driven by collisions between dust grains. The source of the relative velocity for these collisions in models such as Birnstiel et al. (2011) is an underlying turbulence that may be driven by large scale hydrodynamic instabilities (see Lyra & Umurhan 2019, for a review). The streaming instability generates its own turbulence locally (e.g. Li et al. 2018) that drives relative velocities between dust, especially when a distribution of sizes is considered (Bai & Stone 2010a). How these SI-driven collisions influence grain growth remains unstudied. A possible technique may be a model where the dust size can change based on collisions and expectations of growth/fragmentation. These dynamic grain size models have been applied to global models of disc evolution (e.g. Gonzalez et al. 2017; Drążkowska et al. 2021), yet have not appeared in high resolution studies of the SI.

Our results show that, under the SI, a distribution of sizes will segregate spatially. The larger, pebble-sized dust settles to the midplane and undergoes vigorous non-linear dynamics leading to filament and planetesimal formation, while the smaller grains remain vertically suspended and occupy the space between filaments. Thus, the influence of grain growth likely varies spatially as well. Perhaps the small, vertically suspended grains could grow to sizes that are more SI-active, settle towards the midplane, and participate in planetesimal formation. The dense, dust-dominated regions within filaments could promote the growth of pebbles to larger sizes than is possible in gas-dominated regimes. Or, the pebbles in filaments could fragment to smaller SI-inactive grains and reduce the efficiency of planetesimal formation. These smaller sized, fragmented remnants would be created at low scale heights near the midplane, and it is unclear how those grains would interact with clumps and pebble-rich filaments. Such possibilities could be explored in dynamic grain size models.

Incorporating grain growth introduces models dependent on physical units (e.g. fragmentation threshold velocity). This breaks the scale-free property of the common shearing box model used in high-resolution studies of the SI that allows, for example, the translation of $\tau_s = 0.314$ dust to represent different physical grain sizes depending on the disc model and radial position. This means multiple simulations will be required to model how grain growth theory interacts with the local dynamics of the streaming instability under different disc conditions.

The composition of grains could also influence both grain growth and the aerodynamic coupling between the solids and gas phase. Icy grains can stick together at larger collisional velocities than silicate grains (e.g. Gundlach & Blum 2015), and since icy grains are, generally speaking, larger than dry grains, they can radially drift through protoplanetary discs at different rates (Drążkowska & Alibert 2017). If both dry and icy grains co-exist in a disc region that is unstable to the SI (in the vicinity of a disc ice line), our results suggest the two populations could become spatially separated. The small, dry grains would preferentially remain suspended above the disc midplane while the larger, SI-active icy grains would form filaments and planetesimals. This would distinguish the chemical composition of the planetesimals from the overall dust population within which they are formed.

Improving numerical resolution to near planetesimal (∼10 km) length scales could confirm our interpretation of our results that small grains do not participate in clump formation because they are tightly coupled to the gas which flows around the plantesimals. An increase in resolution to this scale is not possible with the methods applied to the streaming instability thus far, but may be approachable with adaptive resolution techniques and/or zoom-in simulations with small domains.

The ability of the available numerical schemes to model an aerodynamically coupled solids-gas system with a dynamic grain size distribution also remains unexplored. Bai & Stone (2010a) suggested that 1 dust superparticle per grid cell per grain species is adequate to capture the non-linear SI, and this has been the literature standard since. It is unclear how this would translate to a dust phase with a continuous, dynamic size range. Difficulties and uncertainties aside, we believe a dynamic dust size distribution could be a promising avenue for approaching a more realistic model of planetesimal formation via the streaming instability.

Acknowledgements

These simulations were performed on the Niagara supercomputing cluster operated by SciNet and Compute Canada. JW thanks NSERC for funding support.

Chapter 5

Critical conditions for strong clumping via the streaming instability in 3D

In this chapter we probe the conditions where strong clumping of dust via the streaming instability is possible. We run a suite of 3D numerical simulations to conduct a parameter sweep over the two most influential parameters to the streaming instability: the amount of dust mass and the aerodynamic drag stopping time (a proxy for the grain size). We build on prior work based on 2D simulations.

5.1 Introduction

The streaming instability is a mechanism capable driving dust clumping in protoplanetary discs. The strength of this clumping varies with the local dust mass as well as the drag stopping time. The growth rates of plane wave perturbations in the linear SI are largest for high dust-to-gas mass ratios ≥ 1 and for drag stopping times (t_{stop}) that are resonant with the orbital dynamical timescale (Ω^{-1}) in the disc (Youdin & Goodman 2005; Youdin & Johansen 2007; Squire & Hopkins 2018). Figure 1.9 shows growth rates for different dust conditions. The amount of dust mass and the stopping time have a similar influence on dust clumping in the saturated, non-linear phase of the SI (Johansen & Youdin 2007; Bai & Stone 2010b). In an influential study, Johansen et al. (2007) showed that for large grains with $t_{\rm stop}\Omega \sim 1$, and a slightly super-solar concentration of solids, a local region of a protoplanetary disc is unstable to dust clumping via the SI. Dense dust filaments form on the order of tens of orbits, and within these structures highly dense clumps collapse under their own self-gravity to form planetesimals. This result identified the streaming instability as a leading mechanism to overcome growth barriers for solid material in protoplanetary discs, such as the destructive collisions barriers for centimetre sized dust pebbles (see Blum 2018, for a review) and the rapid radial drift barrier of metre sized objects due to aerodynamic headwind (Weidenschilling 1977a).

Hence, there is interest in understanding under what conditions the streaming instability operates within protoplanetary discs. Through empirical analyses of numerical simulations suites, a series of studies (Carrera et al. 2015; Yang et al. 2017; Li & Youdin 2021) has sought to define boundaries for dust clumping via the SI. These boundaries are summarized roughly as curves through a parameter space set by the local dust-to-gas surface density ratio and drag stopping time. Semi-analytical models of the evolution of global protoplanetary discs have made use of these results to determine when the SI is active and planetesimal formation occurs (e.g. Drążkowska et al. 2016; Drążkowska & Dullemond 2018; Cridland et al. 2022).

One limitation of the studies by Carrera et al. (2015), Yang et al. (2017), and Li & Youdin (2021) is their simulation suite was based on 2D simulations in the radial-vertical plane, primarily to limit computational cost. This follows analytical studies of the linear SI (e.g Youdin & Goodman 2005) which used axisymmetric perturbations with radial-vertical modes only (Fig. 1.9). Recent work has demonstrated that the SI can promote dust clumping in the 2D radial-azimuthal plane as well, both in linear perturbations (Pan

& Yu 2020) and in numerical simulations of the non-linear, saturated phase (Schreiber & Klahr 2018). However, many 3D studies of the SI demonstrate the formation of dust structure in all 3 dimensions (Johansen et al. 2007; Bai & Stone 2010a; Simon et al. 2016; Simon et al. 2017; Li et al. 2018; Abod et al. 2019; Carrera et al. 2021). Structure in 2D radial-vertical domains denotes rings globally, and thus cannot accurately model localized clumping along the circumferential length that is likely an essential component of planetesimal formation. Thus, our motivation for this work is to probe the boundary for strong clumping via the SI and hence planetesimal formation in a more physically realistic 3D model that includes dynamics in the 3rd dimension.

5.2 Methods

We use the Athena hydrodynamics code (Stone et al. 2008; Bai & Stone 2010b) with the same localized protoplanetary disc model and numerical methods as our prior work, so we direct readers interested in discussion of the equations we solve and the numerical schemes to Section 2.2 of this thesis. In this section, we summarize the key components of our methods relevant to this chapter.

Our simulation domains span 0.2 gas scale heights[1] in each dimension, with a resolution of 256^3 total grid cells. We do not include the effects of self-gravity on the dust as in our prior studies, because we believe self-gravity does not strongly affect the first stage of planetesimal formation, which is strong clumping via the non-linear SI. Indeed, for reasons of computational expediency, some studies on planetesimal formation waited to initiate self-gravity until strong clumping was initiated by the SI (e.g. Simon et al. 2016). Following prior work (Li & Youdin 2021), we define clumping sufficient for planetesimal formation via a density threshold (equation 5.6).

[1]Both the gas and dust are initialized with a Gaussian density profile along the vertical direction.

The parameter Z sets the total dust mass in the simulation domain,

$$Z = \frac{\Sigma_d}{\Sigma_g}, \tag{5.1}$$

which is the ratio of the dust-to-gas mass surface density. As discussed in Section 1.1.1, this is different from the common definition of metallicity, which is the mass ratio of elements heavier than helium to the total gas mass. For our purposes, we are interested in the mass content of the solid material that can participate in the streaming instability and planetesimal formation, Z_{solids}. In the outer protosolar disc, beyond the ice lines of volatile gases, $Z_{\text{solids}} \approx 0.015$, and in the inner disc, $Z_{\text{solids}} \approx 0.005$ (Lodders 2003). A value of $Z = 0.005$ is quite low in the context of the streaming instability, and in most cases from Li & Youdin (2021), this amount of dust will not produce strong clumping. Hence, the streaming instability typically requires a preexisting mechanism to enhance local dust concentrations, such as pressure bumps (Carrera et al. 2021; Carrera et al. 2022), vortices (Lyra et al. 2008), magnetically driven zonal flows (Johansen et al. 2009a; Bai & Stone 2014), ice lines (Drążkowska et al. 2016; Drążkowska & Dullemond 2018), or radial drift (Birnstiel et al. 2012).

As with prior work, we conduct a parameter sweep, with Z representing one of the axes. We can translate this mass ratio to 3D densities in the midplane, which is more relevant to the whether the SI is capable of large growth rates (Fig. 1.9). The midplane gas density is set by

$$\rho_{g,m} = \frac{1}{\sqrt{2\pi}} \frac{\Sigma_g}{H_g}, \tag{5.2}$$

where H_g is the gas scale height. If we approximate the vertical settled dust density profile as a Gaussian, then the ratio of the midplane dust to gas density is,

$$\frac{\rho_{d,m}}{\rho_{g,m}} = \frac{H_g}{H_d} \frac{\Sigma_d}{\Sigma_g} = Z \left(\frac{H_d}{H_g} \right)^{-1}. \tag{5.3}$$

The dust scale height in vertically settled states of the non-linear SI in stratified protoplanetary discs is typically within the range of $0.005 - 0.02H_g$ (Bai & Stone 2010a; Li et al. 2018; Gerbig et al. 2020). In this study, we will sweep through values of Z within the range of $\sim 0.004 - 0.04$, so in some runs we will have $\rho_{d,m}/\rho_{g,m} \gtrsim 1$, which is the physically pertinent condition for strong clumping via the SI (Gole et al. 2020). This condition is achieved indirectly through a sufficiently large value of Z.

The second main parameter in our study is the characteristic timescale for the aerodynamic coupling between the dust and the gas, or more simply, the drag stopping time, $t_{\rm stop}$. There are different regimes of drag that results in different forms for $t_{\rm stop}$, but in our work we only consider the Epstein drag regime (Epstein 1924), where the dust grain size is smaller than the mean free path of the gas. This drag regime is believed to apply for all but the very inner parts of the protoplanetary disc (Birnstiel et al. 2016). In the Epstien regime, the drag stopping time is

$$t_{\rm stop} = \frac{\rho_s}{\rho_g c_s} s, \tag{5.4}$$

where ρ_s is the material density of the particles, ρ_g is the local gas density, c_s is the local sound speed—a function of the gas temperature—and s is the radius of the dust grains, if the grains are approximated as spheres. In this form, we can see that for constant gas properties, the grain size controls $t_{\rm stop}$. In all work on the SI, $t_{\rm stop}$ is incorporated into the model protoplanetary disc units via a dimensionless parameter $\tau_s = t_{\rm stop}\Omega$, where Ω is the disc orbital dynamical timescale, so that the orbital period is $P = 2\pi/\Omega$.

We can convert τ_s to a physical size by invoking a disc model with physical units. If we consider the disc midplane, with the the gas density given by equation 5.2 and the gas scale height set by $H_g = c_s/\Omega$ (Armitage 2020), we get $\tau_s = (\rho_s/\Sigma_g)s$. Li & Youdin (2021) find that the lowest Z for which there is still strong clumping via SI occurs for grains with $\tau_s \approx 0.314$. For silicates, $\rho_s \approx 2.6\,{\rm g\,cm^{-3}}$ (Moore & Rose 1973),

TABLE 5.1: Simulation suite parameters.

τ_s - drag stopping time	Z dust-to-gas surface density ratio
0.01	0.0133, 0.02, 0.04
0.03	0.02, 0.04
0.1	0.01, 0.0133, 0.02
0.3	0.003, 0.004, 0.006, 0.01, 0.0133, 0.02
1.0	0.004, 0.005, 0.0075, 0.01, 0.0133, 0.02
2.0	0.02, 0.04

and if we take $\Sigma_g(r) = 1000\ (r/\mathrm{AU})^{-3/2}$ g/cm^2 (e.g. minimum mass solar nebula model; Weidenschilling 1977b), then at 5 AU, $\tau_s = 0.314$ corresponds to ~ 11 cm.

Our simulation suite consists of a parameter sweep in τ_s–Z. The values considered are summarized in Table 5.1. Note that the computational expense limits the total number of parameter choices we can consider, especially for $\tau_s \lesssim 0.01$, which have slower growth rates (see Fig. 1.9). Our choices reflect those of Li & Youdin (2021).

The last quantity we introduce here is the density threshold above which dust is unstable to gravitational collapse. The Hill radius, R_H, delimits the region around a massive object (mass m_p) where the gravity of the object dominates over rotational shear set by the central star (Armitage 2020). This radius can be expressed as,

$$R_H = \left(\frac{m_p G}{3\Omega^2}\right)^{1/3}, \tag{5.5}$$

where G is the gravitational constant. This also sets a Hill density for a planetesimal with mass m_p,

$$\rho_H \equiv \frac{3}{4\pi}\frac{m_p}{R_H^3} = 9\frac{\Omega^2}{4\pi G}. \tag{5.6}$$

If the dust density locally increases beyond ρ_H, the dust clump is unstable to gravitational collapse. For our choice of physical parameters and simulation units, $\rho_H = 180$. If any simulation in our suite achieves $\rho_d > \rho_H$ anywhere in the simulation domain, we consider that simulation to have strong clumping (as in Li & Youdin 2021).

5.3 Results

The main results of our study can be summarized with a plot in the τ_s–Z plane labelling which conditions produce strong clumping capable of producing planetesimals and which do not. We present these results in Figure 5.1 alongside other results probing strong dust clumping from the literature.

We plot the value of the maximum dust density $\max(\rho_d)$ over time for all simulations in Figure 5.2. If $\max(\rho_d) > \rho_H$ (equation 5.6) for a particular run, we determine that combination of (τ_s, Z) to have produced strong clumping, which sets whether the parameter pair is represented by a green circle or red `X` in Figure 5.1.

Figure 5.3 shows the simulations that border the boundary between clumping and no clumping. We immediately see structure in all three dimensions. For dust with $\tau_s \geq 0.1$ that shows strong clumping, there are dense, azimuthally-oriented filaments that roughly span the full azimuthal length of the domain and which have settled to a vertically thin region at the disc midplane. For the smaller grains, $\tau_s = 0.01, 0.03$, the clumps appear as bright groups with short azimuthal lengths in the radial-azimuthal (x-y) plane. In the case of no clumping, for the dust with $\tau_s \geq 0.1$, there are no filaments or extended coherent structures in the x-y plane. Filaments are visible in the no clumping case for the smallest two grains, but they are much less dense than the filaments seen in larger grains that display clumping.

From Figure 5.2, we see for some simulations $\max(\rho_d)$ crosses above and then below

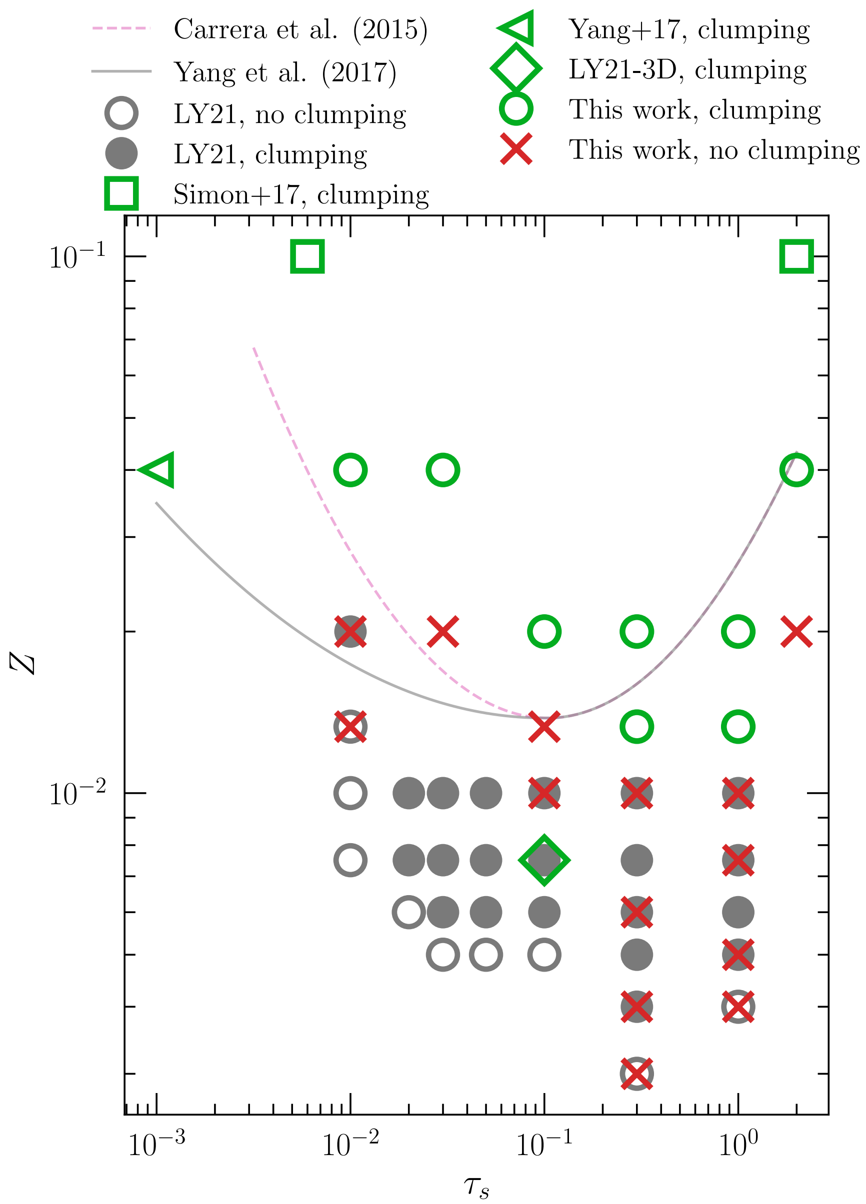

FIGURE 5.1: A summary of which combination of the parameters (τ_s,Z) produce strong clumping in our 3D simulations. Green and red symbols represent 3D simulations with strong clumping and no clumping, respectively, with circles and X's for our runs. The grey filled/unfilled circles are 2D results from Li & Youdin (2021), and the green diamond represents their single 3D run. Other 3D simulations from the literature (Yang et al. 2017; Simon et al. 2017) that display clumping are also shown. The two lines summarize the clumping boundary from Carrera et al. (2015) and Yang et al. (2017).

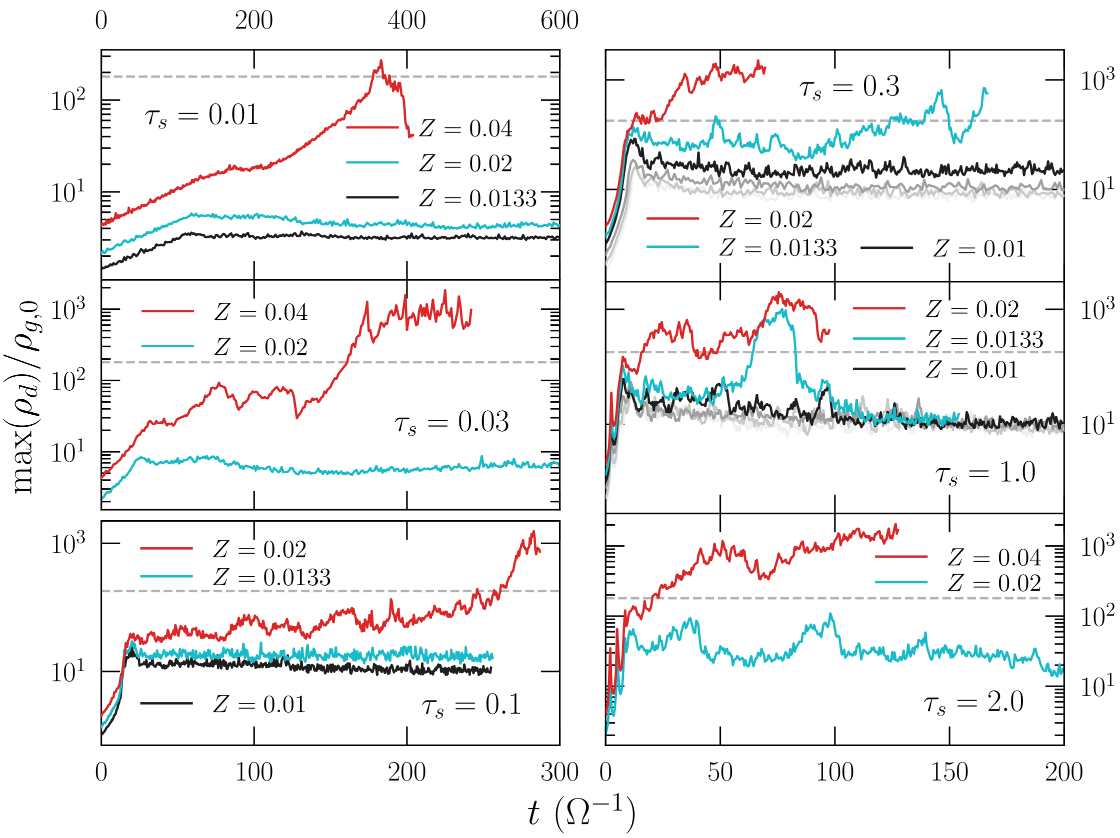

FIGURE 5.2: The maximum dust density in each simulation from our suite over time. Each panel represents a different value of τ_s, each colour a different value of Z. The horizontal dashed line represents $\rho_H = 180$ (equation 5.6), the threshold for planetesimal formation and hence our definition of strong clumping for Figure 5.1.

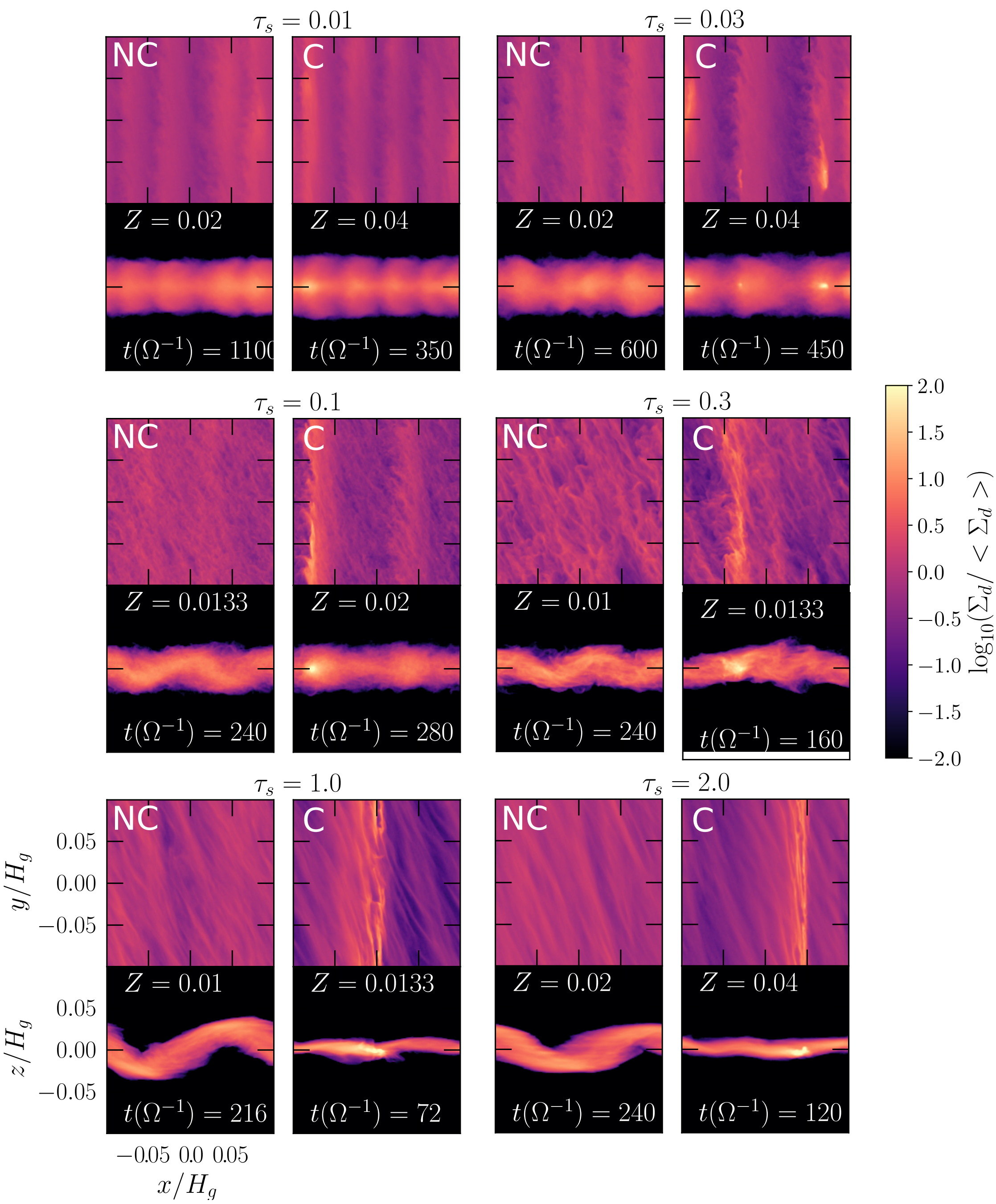

FIGURE 5.3: The dust surface density in the radial-azimuthal (x-y) and radial-vertical (x-z) planes for various simulations from our suite. For each τ_s, we present two choices of Z in columns: the highest Z for which there is no clumping on the left (labelled with "NC"), and the lowest value of Z for which there is strong clumping on the right (labelled with "C").

the ρ_H threshold. This transient behaviour would not appear in simulations with self-gravity as the dense clumps would gravitationally collapse and remain above ρ_H (see Section 4.4). We plot the dust surface density over time across the transient $\max(\rho_d)$ behaviour for these particular simulations in Figure 5.4. As in Figure 5.3, there is azimuthal structure in the dust density in all cases. In the ($\tau_s = 0.01$,$Z = 0.04$) and ($\tau_s = 0.3$,$Z = 0.0133$) cases (top, middle rows), the clumps in the middle columns have short azimuthal lengths. The larger grain case ($\tau_s = 1.0$,$Z = 0.0133$) produces an azimuthally coherent filament as seen in the larger grains in Figure 5.2.

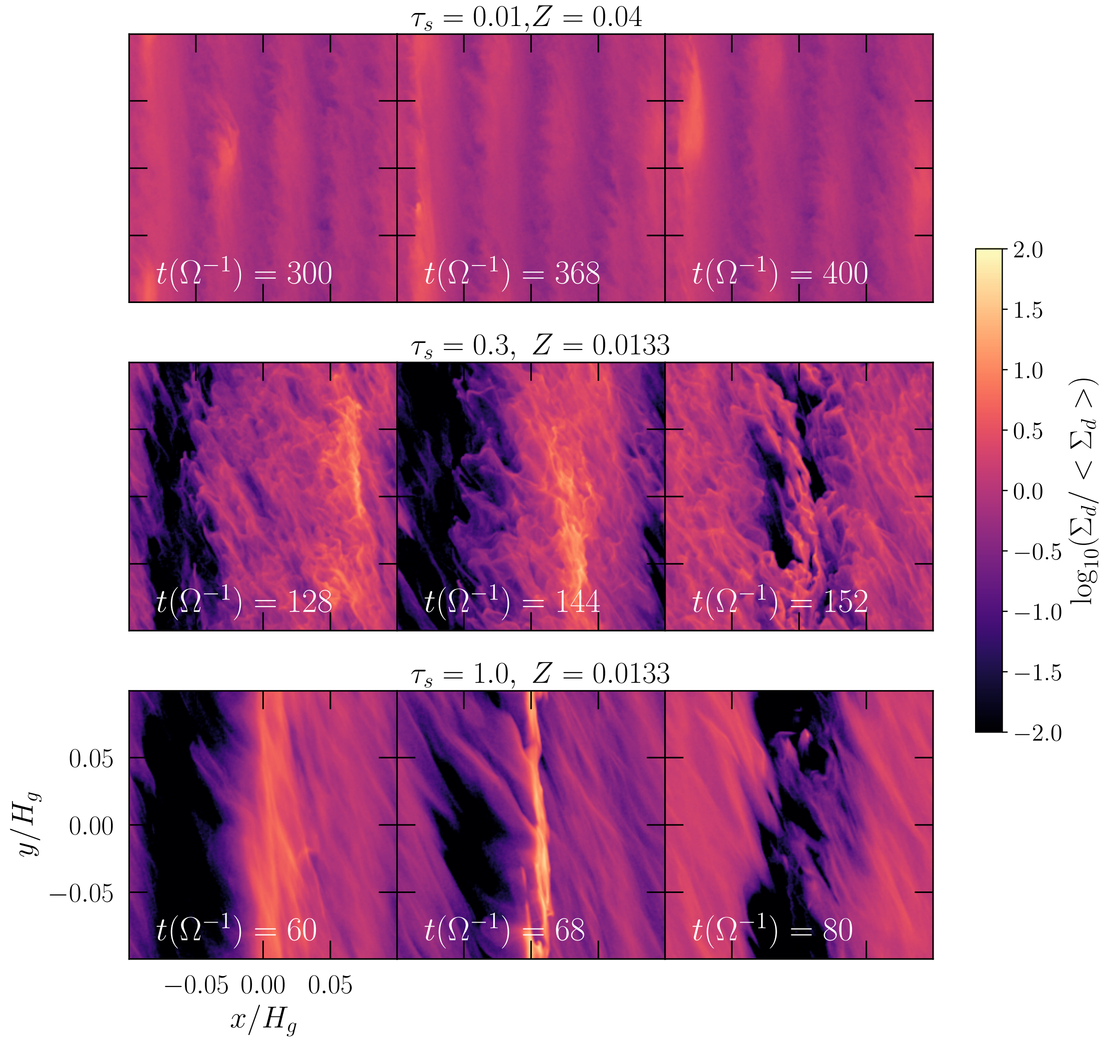

FIGURE 5.4: Dust surface density in the radial-azimuthal plane for a few select runs which display a transient phase of strong clumping (cf. Figure 5.2). Each row represents a unique simulation at three different times, just before strong clumping (left), during strong clumping (middle), and after strong clumping (right).

5.4 Discussion

The most interesting observation from this study is the disagreement between our predictions for the boundary between strong clumping and no clumping in τ_s–Z space and that same boundary from Li & Youdin (2021), Carrera et al. (2015), and Yang et al.

(2017). In general, the 2D results from Li & Youdin (2021) predicts a lower critical Z for the same τ_s than our 3D simulations. Here we discuss some possible reasons.

First, we discuss the differences in modelling all three dimensions versus only two. In the 2D, radial-vertical simulations from Li & Youdin (2021), clumps represent rings in the global disc geometry. Dust mass is confined to a single value of (r, z) with no variation in the azimuthal direction. Our 3D models capture the 3D dynamics of the non-linear SI and show that the filaments, while azimuthally oriented, display a variety of non-axisymmetric structure that is not well described by uniform rings. Perhaps most relevant to dust clumping is the truncation of filaments and other dense features azimuthally, resulting in clumps with short azimuthal lengths and azimuthal gradients of density along filaments. Such features can be seen in Figures 5.3 and 5.4. With this in mind, one might expect for a given τ_s that 3D simulations would produce clumping at lower values of Z than the same simulation in 2D. Carrera et al. (2015) and Yang et al. (2017) both use 2D models, and for $\tau_s = 0.3, 1.0$, our results do predict a lower Z clumping threshold than their studies. However, at ($\tau_s = 0.03$,$Z = 0.02$), our models do not produce clumping, contrary to their predictions, and at ($\tau_s = 0.03$,$Z = 0.02$), we predict no clumping above the Yang et al. (2017) line. Yang et al. (2017) use an improved algorithm for stiff drag forces at short stopping times (Yang & Johansen 2016) that may contribute to this discrepancy. Our discrepancy with the Li & Youdin (2021) results may come from other differences, given they did run one set of parameters in 3D which displays strong clumping below the boundary from our results.

Second, Li & Youdin (2021) also used different hydrodynamic boundary conditions (BCs) for the vertical domain boundary. They employ outflow conditions (Simon et al. 2011; Li et al. 2018) where gas momentum is permitted to leave through the boundary, and then the mass in the domain is renormalized at every timestep to keep the gas mass in the box constant. We use periodic BCs, where any material that leaves through one boundary returns to the domain through the opposite side. Explicitly, the implied configuration of the disk model under periodic BCs is the numerical domain interacts with copies of itself through both the bottom and top boundary. Under outflow conditions, there is nothing beyond the vertical domains, and mass is artificially replaced. Both numerical treatments necessarily produce artefacts, and it is possible they contribute to whether the SI produces strong clumps, and hence the differences between our results and Li & Youdin (2021). Both Carrera et al. (2015) and Yang et al. (2017), used periodic BCs as well, and their results are, broadly speaking, closer to our boundary than that in Li & Youdin (2021).

The cycling of vertical gas momentum in periodic BCs can slightly stir up particles in the midplane, leading to higher scale heights and weaker clumping (Li et al. 2018). Indeed, from Figure 14 in Li & Youdin (2021), for conditions near their clumping boundary, they find outflow conditions predict a lower critical Z. Similarly, increasing the vertical height of the domain can cause less stirring in the midplane, promoting clumping and different predictions for the clumping boundary. Li et al. (2018) conduct a thorough investigation of the effects of vertical domain size and boundary conditions in the case of strong clumping in 3D, albeit at a numerical resolution where some properties of the dust filaments are not resolved (See Appendix 3.B). It would be useful to apply a similar, 3D investigation with varied BCs near the clumping boundary to determine the influence of the aforementioned numerical choices.

Lastly, Li & Youdin (2021) use 4 times longer domain extents in the radial direction, which permits multiple filaments for larger grains. As seen in Figure 2 from Li & Youdin (2021), capturing multiple filaments permits interactions and mergers between the filaments that can drive strong clumping. From our suite, for dust with $\tau_s \geq 0.3$, there is only one filament in the cases where strong clumping occurs (Figure 5.3). We discuss in Chapter 3 how the $(0.2H_g)^3$ box size for $\tau_s = 0.314$ (and $Z = 0.02$) struggles to represent what appears to be the preferred filament spacing of $0.1H_g$ for dust grains of that size. This restricts the domain to a configuration with either 1 or 2 filaments. As Z is lowered to near the critical clumping threshold, the one-filament configuration enforces a relatively large radial distance between itself across the shear-periodic boundary, which may result in decreased interactions and hence less intense clumping than in models with multiple filaments present.

The most effective tool for probing the boundary for strong clumping via the SI may be simulations with very large vertical extents to remove the influence of the vertical boundary conditions and radial extents wide enough for multiple filaments. However, 3D simulations at moderate to high resolutions and large domains are computationally expensive. Especially in the application of probing the SI clumping boundary, which may require incredibly long run times (Yang et al. 2017; Li & Youdin 2021). This cost would limit the number of runs in a parameter sweep study such as this work or in Li & Youdin (2021). However, our work and that of Carrera et al. (2015), Yang et al. (2017) and Li & Youdin (2021) could serve as a guide for what choices of τ_s and Z—such as those where there is disagreement—should be explored first.

The fact remains that determining what conditions produce strong clumping via the streaming instability is invaluable to the field of planet formation, and worthy of intense scrutiny. The boundary between strong and no clumping determines where planetesimals can form within a protoplanetary disc (Drążkowska et al. 2016; Drążkowska & Dullemond 2018; Cridland et al. 2022). Once planetesimals form, they are no longer strongly affected by radial drift due to their large inertia (Weidenschilling 1977a), and these stationary planetesimal populations could set the locations for the formation of rocky protoplanets in models of planetesimal accretion (Wallace & Quinn 2019; Liu et al. 2019; Jang et al. 2022). If the growing planet reaches a few Earth masses it can open a gap in the gaseous disc, and the exchange of torque between the planet and the disc can cause the planet to migrate. The magnitude of the torque is a strong function of the radius of the planet (Tanaka et al. 2002; Jiménez & Masset 2017), and hence the initial radial position of this planet could significantly influence the final location of the planet within the disc, as well as its final mass, chemical composition, etc. (Alessi et al. 2020; Alessi & Pudritz 2022). Planet formation is an interlinked, cascading process spanning many orders of magnitude in length scales. Precise information about the early stages such as planetesimal formation, refined by studies of the boundary for strong clumping via the SI, can lead to tighter constraints on the population of the final planets.

Another interesting consequence of the strong clumping boundary in the SI is that, for a fixed solids-to-gas surface density ratio, small grains can grow from SI-inactive regions to SI-active regions. Thus, models of grain growth globally within discs (Birnstiel et al. 2012; Gonzalez et al. 2017; Drążkowska et al. 2021) can determine the global distribution of SI-active grains, which then feeds into localized planetesimal formation via the SI and the aforementioned processes. Local grain growth (e.g. Birnstiel et al. 2011) coupled with constraints on the SI clumping boundary can also inform models of planetesimal formation within dust rings observed by ALMA (Stammler et al. 2019; Maucó et al. 2021), which is a proposed explanation for the intermediate optical depths seen in numerous dust rings (Dullemond et al. 2018; Huang et al. 2018; Cazzoletti et al. 2018; Macías et al. 2019; Maucó et al. 2021).

Chapter 6

Conclusions

In this thesis, we have studied planetesimal formation via the streaming instability (SI) in simulations of previously unexplored configurations. We model the evolution of aerodynamically coupled gas and dust in high-resolution, 3D numerical simulations of patches of protoplanetary discs in shearing boxes. All simulations were computed with the Athena hydrodynamic code (Stone et al. 2008; Bai & Stone 2010b).

The streaming instability has been shown to be an effective mechanism for forming planetesimals directly from the gravitational collapse of dense pebble clouds in the midplane of protoplanetary discs. Once the dust pebbles settle to the midplane and dominate the local mass budget of the protoplanetary disc, the instability develops rapidly, producing azimuthally extended dust filaments that further clump to form planetesimals. Such a mechanism must exist in nature due to well-documented barriers that impede the growth of millimetre/centimetre sized pebbles beyond ∼10 cm sizes. Much remains to be understood about how efficiently and under which conditions the SI can operate. Progress on the planetesimal formation phase of the SI has primarily come from empirical studies of high-resolution simulations. The contributions of this thesis to the existing literature continue this process, exploring new behaviors of the streaming instability until filaments and planetesimals form, and reporting on our discoveries.

Here, we synthesize our main results, and discuss our ideas for future progress in this field in the proceeding section.

Our work in Chapters 2 and 3 is based on a simulation suite with small and large domains. Much prior work in the literature has made use of cubic domains with a side length of 0.2 gas scale heights, which matches the smallest domain in our suite. Expanding the domain lengths in the radial and azimuthal directions permits larger-scale dynamics, and the co-existence of multiple filaments. Interactions between the filaments can drive strong dust clumping and initiate planetesimal formation. Filament interactions are not captured in the smallest domains that form one filament in one of our runs. We also explored re-runs of simulations with otherwise identical properties except for the initial random perturbation to the dust density distribution. Under the non-linear dynamics of the SI, the slightly varied perturbations grow to different macroscopic outcomes. This technique probes the variability in the planetesimal formation process, and was novel to the field at the time Chapter 2 was published.

In Chapter 2, we focus on the properties of the planetesimals formed in our simulation suite. In our analysis, we subdivide the larger domains simulation into subdomains equivalent in size to the smallest domains, and find dramatic variation between the cumulative number distributions among the individual small domains sims and the subdomains within the larger simulation. Further, the amount of dust mass converted to planetesimals varies across the same regions. Within the largest domain in this study, with 16 smaller subdomains, the spread in mass conversion varies as much as 5% to 45% of the total dust mass in the subdomain. These results demonstrate that accurate assessments of planetesimal properties requires either multiple small simulations or large domains. There is a large spread in planetesimal formation outcomes intrinsic to the SI that cannot be observed in single small domain runs.

Following prior work (e.g. Simon et al. 2016), we characterize the differential number distribution (dN/m_p) of the population of all planetesimals in the largest domain, and the combined populations of the multiple smaller simulations, and we find that the power-law slopes at each domain size are consistent with each other, and with prior work. Thus, combining the results across multiple smaller simulations and using the full domain in large simulations, the degree of variability decreases, and there is a convergent answer in the power-law slope. This suggests that there is some equivalency in the mass distribution as sampled by multiple small domains and larger domains.

However, in Chapter 3, we find different properties across different sized domains in the azimuthally oriented filaments that dominate the dust surface density in the pre-planetesimal formation phase of SI. We identify filaments as contours in the dust surface density maps above the mean surface density. We find that, in the smallest domains, filaments preferentially span the full azimuthal length of the simulation domain, implying ring-like structures globally. In larger domains, progressively less of the filament mass is at the full box scale, demonstrating that the filaments are naturally truncated at larger sizes. The filaments are an essential intermediate step in planetesimal formation. They represent the mass reservoir available to planetesimals form. Our results suggest the properties of this mass reservoir is not accurately represented by the small domains in our study.

We observe that the small domain simulations are locked into configurations of either 1 or 2 filaments, while the domain that is 4 times as wide (run `L08`) forms 8 filaments. The 1D Fourier transform magnitudes in the radial-direction displays a strong peak associated with the filament spacing scale. The peak length scale in the `L08` is persistent during the filament-dominated phase of the SI, which suggests the natural spacing length of the filaments is approximately 0.1 scale heights. This length scale represents half the radial width of the smallest domain, and hence the spectral/dynamical resolution of these runs is limited at this scale. We conclude this offer an explaination for why these simulations are forced into configurations of one or two filaments–radial spacings of 0.2 or 0.1 scale heights, respectively. Other simulations from the literature with similar dust parameters also see dust configurations with a single filament at this box size (Simon et al. 2016; Schäfer et al. 2017). This variation of a factor of 2 the filament spacing is not seen in the largest domains, and is evidence that the smallest domains struggle to represent filament properties in the radial direction, in addition to the azimuthal direction, as discussed above. Fourier spectra in the azimuthal direction confirm that the peak power is in the box-scale mode, which is an indicator of large-scale dynamics that truncates the filaments and cannot be captured by the smaller simulations.

One filament property that is consistent across domain sizes is the segregation of dust mass at the various box-scale sizes. There is roughly equal mass in filaments that are longer than 0.2 gas scale heights (smallest domain) in all larger domains, and equal mass at 0.4 scale heights and above, etc. This consistency in how the SI segregates mass azimuthally may be related to the consistency in the spread in total planetesimal mass across the various domain sizes seen in Chapter 1. The spatial variation in the filaments across domain sizes (i.e. azimuthal truncation) echoes the variation in the spatial distribution of planetesimals.

We also use a novel procedure of manual mock signals to demonstrate that the filaments in the 0.8 scale height (`L08`) simulation are best described as being roughly equally spaced, but not exactly so. The spectra of the simulation filament profile reveal off-harmonic power that resists analytical functional fits but is readily described by a mock signal with randomly shifted peaks. In the appendix, we vary properties of the mock signal to suggest loose constraints on the filament width that is roughly consistent with prior work.

Combing our results from Chapter 1 and 2 together, we conclude, for the purposes of quantifying the planetesimal mass distribution and the total mass converted to planetesimals, running multiple small simulations is roughly equivalent to running large simulations. For characterizing the mass reservoir available for planetesimal formation—the filaments—we believe larger domains should be used. The filament properties in small domains are too inconsistent with the properties seen in the large domains. Further, based on a resolution study from Appendix 3.B in Chapter 2, a resolution of at least 600 cells per gas scale height should be used for our dust properties. Constraining these properties is useful for studies that wish to model the post-formation evolution of the planetesimals into protoplanets (e.g. Liu et al. 2019; Jang et al. 2022).

In Chapter 4, we run a different suite of simulations that models the dust with multiple grain sizes (or species) simultaneously. Recent models of the SI with multiple sizes have explored both the linear phase and the non-linear saturated phase in 2D. Older work (Bai & Stone 2010a) studied 3D stratified discs, but without self-gravity/planetesimal formation. All prior studies of the multi-species non-linear SI used a grain size distribution described by a single power-law, in line with models of dust grains from the interstellar medium (ISM). However, in the midplane of protoplanetary discs, equilibrium between grain growth and fragmentation can result in a grain size distribution with a distinct peak (Birnstiel et al. 2011). In our study, we use a discrete sampling to model the Birnstiel et al. (2011) distribution in the context of a 3D patch of a protoplanetary disc. Our work represents the first multi-species dust treatment in this context since Bai & Stone (2010a) and the only multi-species non-linear SI study to model the Birnstiel et al. (2011) distribution that is a more realistic grain size distribution for protoplanetary discs than the distribution applicable to the ISM.

Our sample consists of grains between roughly 4mm and 5 cm in size. We place the peak of our grain size distribution to match the single-size runs considered by our prior work (Ch. 2 and 3) and directly compare the two models to quantify the influence on the SI of multi-species dust.

In the multi-species runs, the larger dust grains readily form filaments and clumps while the smaller grains do not, despite being embedded in a dust environment that is primarily composed of dense dust structures. This results in a greater amount of dust mass in the inter-filament space than is seen in the comparable single-size models. This general behavior is seen in other models of the multi-species non-linear SI (Bai & Stone 2010a; Yang & Zhu 2021).

Depending on the opacity of the dust, the different spatial distributions of dust mass could have significant observational consequences. Thermal emission from the clumped dust features from our simulation will saturate at intermediate optical depths $\gtrsim$1. To quantify this effect, we compute mass conversion factors based on the dust surface density maps in our simulations—a new analysis for 3D studies of the SI. We find that the single-size models with greater amounts of clumping require correction factors between 40-90% percent to account for the saturated emission. The multi-size models, which clump less, and are hence overall brighter, require correction factors of 20-50%. It is interesting to note that the dust sizes we model are very similar to the sizes seen by ALMA observations, and some studies have explained the low optical depth seen in some dust rings as evidence for ongoing planetesimal formation via the SI (Stammler et al. 2019; Maucó et al. 2021). In these cases a mass correction factor to accurately estimate the mass of the dust ring from the dust surface density is likely required. Our results provide bounds on what these factors may be, depending on the size of grains present and how strongly peaked the grain distribution is.

Second, we investigate the composition of planetesimals by grain size. We identify bound clumps (i.e. planetesimals) as dust that is above the gravitational collapse density threshold. We find that the smallest ∼mm size grains do not participate in clump formation at all, and display kinematic behavior to suggest they merely stream past the planetesimals without becoming gravitationally bound. The clump masses are dominated by the four largest species in our sample. For the second smallest species, at $\sim$2.5 cm if the size at the distribution peak is 4cm, these grains display an in-between behavior. They readily form filaments but do not participate in clump formation. The segregation of clump composition by size suggests that planetesimals will primarily be made up of grains that undergo strong clumping via the SI, a prediction that can be tested by meteorite measurements and observational inferences of the composition of asteroids.

In Chapter 5, we probe the boundary between strong clumping via the SI and no clumping, building on prior work by Carrera et al. (2015), Yang et al. (2017) and Li & Youdin (2021). We explore the parameter space set by drag stopping time (linear in grain size) and the dust-to-gas mass surface density ratio. Prior studies used 2D simulations. Inspired by the evident azimuthal dynamics seen in the 3D SI (and quantified in our study in Chapter 3), we conduct our parameter sweep in cubic 3D domains with a side length of 0.2 scale heights.

Interestingly, our results disagree with the recent study from Li & Youdin (2021). These authors predict a lower critical surface density threshold (for fixed stopping time) than is seen our suite, sometimes lower by more than a factor of 2. Our results are in closer agreement to the previous studies of Carrera et al. (2015) and Yang et al. (2017). We interpret these differences as a demonstration that the nature of the SI clumping boundary is sensitive to choices in the numerical set-up.

Likely candidates are 1) the longer radial domains studied by Li & Youdin (2021), which permit multiple filaments and hence filament interactions that can drive clumping and lower surface density thresholds, 2) larger vertical extents (for some parameter choices), which permits momentum in the gas to leave the midplane, and hence promoting dust settling and clumping, or 3) their choice of outflow vertical boundary conditions which promotes settling for similar reasons as taller vertical boundaries. Additional exploration of the effects of the above choices may be required. Accurately probing the clumping boundary for the SI with numerical simulations appears to be a difficult task. The best tool for this problem may be 3D simulations with moderate radial extents and tall vertical domains that limit the influence of artefacts that come from any choice of boundary conditions.

6.1 Future Work

A key short-coming of all models of planetesimal formation via the SI to date is the inability to properly resolve dynamics on the physical planetesimal length scale. We cannot simultaneously model both the filaments and the final collapse phase of the bound dust clumps, which in our models are resolved at the level of the Hill radius—the length scale for the region around the clump where the gravitational influence of the clump dominates over the rotational shear. Explicitly, we find a radial filament spacing length scale of approximately 0.1 gas scale heights for the dust parameters we model in Chapter 3. For a typical protoplanetary disc model (e.g. Hayashi 1981), at $\sim$3 AU, this filament separation scale corresponds to $\sim 10^6$ km—some 4 to 5 orders of magnitude larger the physical planetesimal size. No current computational facility, nor any in the near future, is capable of simultaneously resolving those length scales with a fixed grid scale (i.e. brute force). This means the final spin of the clumps, or what fraction of clumps form binaries or multiple bodies—both quantities that can be compared to measurements from Kuiper belt objects—is not calculated within the filament environment. As in Nesvorný et al. (2019) and Nesvorný et al. (2021), the SI-formed clump particle distribution can be exported to a separate simulation, which can then follow the collapse phase fully. This strategy excludes the environment surrounding the clump from potentially participating in the collapse, such as the smaller grains that preferentially flow through clumps at relatively large relative velocities in our models.

Including these grains would alter the final size distribution within the aggregate clump, and potentially the chemical composition of the clump as well, if it were formed in the vicinity of an ice line where larger grains are icy and small grains are bare silicates.

Further, these resolution limitations result in unphysically large numerical cross section of the clumps. The post-formation growth of these objects is likely enhanced compared to what we would expect in nature. Thus, in quantifying planetesimal properties such as the mass distribution, we are required to pick a time before the objects have substantially interacted with the rest of the mass in the domain. The overall behavior of the planetesimals is correct, in that they detach from the filaments and experience less radial drift due to their substantial inertia, but the details are unknown. Of great interest is how a 10 km sized object interacted with a dense filament of dust pebbles that is 10,000 times wider. Johansen et al. (2015) show with a semi-analytical model that planetesimals can grow substantially via the accretion of pebbles. It would be fascinating to explore this in resolved numerical simulations.

Resolving the smallest length scales would also permit constraints on the low mass end of the size distributions. Simon et al. (2016) show that as numerical resolution is increased, the smallest planetesimals formed also decreases. Information on the minimum planetesimal size formed via the SI constrains models of the internal geological evolution of solid bodies and consequently the timescale of planetesimal formation in the solar system (Lichtenberg et al. 2018). This would also allow for direct comparisons to data from the crater size distribution on Pluto and Charon that predict a minimum size in primordial minor solar system bodies near 1-2 km.

Of course, if resolving this minimum scale were simple, conceptually or technologically, then it would have been done already. But that does not mean it is impossible.

There may be avenues for future work on zoom-in simulations of dust filaments–if accurate localized models of filaments could be reproduced on planetesimal scales. Alternatively, adaptive dust-gas methods (Huang & Bai 2022) may be able to simultaneously resolve relevant small and large scales. Though this would also likely require some novel ideas for domain sizes, as no refinement techniques could simultaneously capture the 4 orders of magnitude between the aforementioned filament spacing length scale and the 10 km planetesimal scale, for instance.

Another interesting avenue for further research is in exploring various grain size distributions in the local protoplanetary disc shearing box context. Our results from Chapter 4 represent just one iteration of possible grain size distributions. More interestingly, one could also consider a dynamic grain size model, where the grain size for each dust resolution is a variable, constantly evolution due to collisions with other dust. Dynamic grain size distributions have been studied in global models of protoplanetary discs (e.g. Gonzalez et al. 2017; Drążkowska et al. 2021) but not in the dynamic environment of a shearing box that is unstable to the SI. Most models of grain growth (including Birnstiel et al. 2011, from which we base our grain size distribution from Chapter 4) use a model of global disc turbulence to drive dust collisions. In our models, and others like it in the literature, the non-linear SI drives its own turbulence in the disc midplane. As this turbulence has not been thoroughly characterized in the literature, how it would affect grain growth is poorly explored.

In our opinion, the most exciting possibilities for future research on the streaming instability in high-resolution shearing boxes exist in creative conceptions of the size of the numerical domain and the dust grain size model. We are excited to see what comes next in the field of planetesimal formation.

Bibliography

Abod, C. P. et al. (2019). *ApJ*, **883**, 192.

Adams, F. C., Lada, C. J., & Shu, F. H. (1987). *ApJ*, **312**, 788.

Alessi, M. & Pudritz, R. E. (2018). *MNRAS*, **478**, 2599–2617.

Alessi, M. & Pudritz, R. E. (2022). *MNRAS*, **515**, 2548–2577.

Alessi, M., Pudritz, R. E., & Cridland, A. J. (2020). *MNRAS*, **493**, 1013–1033.

ALMA Partnership et al. (2015). *ApJ*, **808**, L3.

Andre, P., Ward-Thompson, D., & Barsony, M. (2000). In: *Protostars and Planets IV*. Ed. by V. Mannings, A. P. Boss, & S. S. Russell, 59.

Andrews, S. M. (2020). *ARA&A*, **58**, 483–528.

Andrews, S. M. et al. (2016). *ApJ*, **820**, L40.

Andrews, S. M. et al. (2018). *ApJ*, **869**, L41.

Ansdell, M. et al. (2016). *ApJ*, **828**, 46.

Ansdell, M. et al. (2018). *ApJ*, **859**, 21.

Armitage, P. J. (2020). *Astrophysics of Planet Formation*. 2nd ed. Cambridge Univ. Press.

Avenhaus, H. et al. (2018). *ApJ*, **863**, 44.

Ayliffe, B. A. & Bate, M. R. (2012). *MNRAS*, **427**, 2597–2612.

Backus, I. & Quinn, T. (2016). *MNRAS*, **463**, 2480–2493.

Bai, X.-N. & Stone, J. M. (2010a). *ApJ*, **722**, 1437–1459.

Bai, X.-N. (2015). *ApJ*, **798**, 84.

Bai, X.-N. & Stone, J. M. (2010b). *ApJS*, **190**, 297–310.

Bai, X.-N. & Stone, J. M. (2010c). *ApJ*, **722**, L220–L223.

Bai, X.-N. & Stone, J. M. (2014). *ApJ*, **796**, 31.

Balbus, S. A. & Hawley, J. F. (1991). *ApJ*, **376**, 214.

Bally, J., O'Dell, C. R., & McCaughrean, M. J. (2000). *AJ*, **119**, 2919–2959.

Benisty, M. et al. (2015). *A&A*, **578**, L6.

Benisty, M. et al. (2017). *A&A*, **597**, A42.

Benisty, M. et al. (2022) , arXiv:2203.09991.

Benisty, M. et al. (2021). *ApJ*, **916**, L2.

Benz, W. et al. (2014). In: *Protostars and Planets VI.* Ed. by H. Beuther et al., 691.

Béthune, W., Lesur, G., & Ferreira, J. (2016). *A&A*, **589**, A87.

Birnstiel, T., Fang, M., & Johansen, A. (2016). *Space Sci. Rev.*, **205**, 41–75.

Birnstiel, T., Klahr, H., & Ercolano, B. (2012). *A&A*, **539**, A148.

Birnstiel, T., Ormel, C. W., & Dullemond, C. P. (2011). *A&A*, **525**, A11.

Birnstiel, T. et al. (2015). *ApJ*, **813**, L14.

Birnstiel, T. et al. (2018). *ApJ*, **869**, L45.

Blum, J. & Wurm, G. (2008). *ARA&A*, **46**, 21–56.

Blum, J. (2018). *Space Sci. Rev.*, **214**, 52.

Blum, J. et al. (2017). *MNRAS*, **469**, S755–S773.

Bohlin, R. C., Savage, B. D., & Drake, J. F. (1978). *ApJ*, **224**, 132–142.

Brandenburg, A. et al. (2021). *J. Open Source Softw.*, **6**, 2807.

Brauer, F., Dullemond, C. P., & Henning, T. (2008). *A&A*, **480**, 859–877.

Calvet, N. et al. (1994). *ApJ*, **434**, 330.

Carrera, D., Johansen, A., & Davies, M. B. (2015). *A&A*, **579**, A43.

Carrera, D. & Simon, J. B. (2022). *ApJ*, **933**, L10.

Carrera, D. et al. (2021). *AJ*, **161**, 96.

Carrera, D. et al. (2022). *ApJ*, **927**, 52.

Cazzoletti, P. et al. (2018). *A&A*, **619**, A161.

Chen, K. & Lin, M.-K. (2020). *ApJ*, **891**, 132.

Chiang, E. & Youdin, A. N. (2010). *Annual Review of Earth and Planetary Sciences*, **38**, 493–522.

Chiang, E. I. & Goldreich, P. (1997). *ApJ*, **490**, 368–376.

Clauset, A., Shalizi, C. R., & Newman, M. E. J. (2009). *SIAM Rev.*, **51**, 661–703.

Cleeves, L. I. et al. (2015). *ApJ*, **799**, 204.

Cridland, A. J. et al. (2022). *A&A*, **662**, A90.

Cuzzi, J. N., Hogan, R. C., & Bottke, W. F. (2010). *Icarus*, **208**, 518–538.

Cuzzi, J. N. et al. (2001). *ApJ*, **546**, 496–508.

Dawson, R. I. & Johnson, J. A. (2018). *ARA&A*, **56**, 175–221.

Dipierro, G. et al. (2015). *MNRAS*, **453**, L73–L77.

Dong, R., Liu, S.-Y., & Fung, J. (2019). *ApJ*, **870**, 72.

Dong, R., Zhu, Z., & Whitney, B. (2015). *ApJ*, **809**, 93.

Draine, B. T. (2011). *Physics of the Interstellar and Intergalactic Medium.*

Drążkowska, J. & Alibert, Y. (2017). *A&A*, **608**, A92.

Drążkowska, J., Alibert, Y., & Moore, B. (2016). *A&A*, **594**, A105.

Drążkowska, J. & Dullemond, C. P. (2014). *A&A*, **572**, A78.

Drążkowska, J. & Dullemond, C. P. (2018). *A&A*, **614**, A62.

Drążkowska, J., Stammler, S. M., & Birnstiel, T. (2021). *A&A*, **647**, A15.

Drążkowska, J. et al. (2022) , arXiv:2203.09759.

Dullemond, C. P. & Dominik, C. (2005). *A&A*, **434**, 971–986.

Dullemond, C. P. et al. (2018). *ApJ*, **869**, L46.

Epstein, P. S. (1924). *Phys. Rev.*, **23**, 710–733.

Fischer, D. A. et al. (2014). In: *Protostars and Planets VI.* Ed. by H. Beuther et al., 715.

Flaherty, K. M. et al. (2017). *ApJ*, **843**, 150.

Francis, L. & van der Marel, N. (2020). *ApJ*, **892**, 111.

Fulle, M. & Blum, J. (2017). *MNRAS*, **469**, S39–S44.

Fulton, B. J. & Petigura, E. A. (2018). *AJ*, **156**, 264.

Fulton, B. J. et al. (2017). *AJ*, **154**, 109.

Galametz, M. et al. (2019). *A&A*, **632**, A5.

Gammie, C. F. (2001). *ApJ*, **553**, 174–183.

Gerbig, K. et al. (2020). *ApJ*, **895**, 91.

Gingold, R. A. & Monaghan, J. J. (1977). *MNRAS*, **181**, 375–389.

Ginzburg, S., Schlichting, H. E., & Sari, R. (2018). *MNRAS*, **476**, 759–765.

Goldreich, P. & Lynden-Bell, D. (1965). *MNRAS*, **130**, 125.

Goldreich, P. & Tremaine, S. (1980). *ApJ*, **241**, 425–441.

Gole, D. A. et al. (2020). *ApJ*, **904**, 132.

Gonzalez, J. .-., Laibe, G., & Maddison, S. T. (2017). *MNRAS*, **467**, 1984–1996.

Greene, T. P. et al. (1994). *ApJ*, **434**, 614.

Greenstreet, S. et al. (2019). *ApJ*, **872**, L5.

Grishin, E. et al. (2020). *Nature*, **580**, 463–466.

Gullbring, E., Barwig, H., & Schmitt, J. H. M. M. (1997). *A&A*, **324**, 155–160.

Gundlach, B. & Blum, J. (2015). *ApJ*, **798**, 34.

Güttler, C. et al. (2010). *A&A*, **513**, A56.

Haffert, S. Y. et al. (2019). *Nature Astronomy*, **3**, 749–754.

Haisch Karl E., J., Lada, E. A., & Lada, C. J. (2001). *ApJ*, **553**, L153–L156.

Hartlep, T. & Cuzzi, J. N. (2020). *ApJ*, **892**, 120.

Hartmann, L. et al. (1998). *ApJ*, **495**, 385–400.

Hawley, J. F., Gammie, C. F., & Balbus, S. A. (1995). *ApJ*, **440**, 742.

Hayashi, C. (1981). *Progress of Theoretical Physics Supplement*, **70**, 35–53.

Huang, J. et al. (2018). *ApJ*, **869**, L42.

Huang, P. & Bai, X.-N. (2022) , arXiv:2206.01023.

Ida, S. & Lin, D. N. C. (2004). *ApJ*, **616**, 567–572.

Jang, H., Liu, B., & Johansen, A. (2022) , arXiv:2205.10103.

Jiménez, M. A. & Masset, F. S. (2017). *MNRAS*, **471**, 4917–4929.

Johansen, A. & Youdin, A. (2007). *ApJ*, **662**, 627–641.

Johansen, A., Youdin, A., & Klahr, H. (2009a). *ApJ*, **697**, 1269–1289.

Johansen, A., Youdin, A. N., & Lithwick, Y. (2012). *A&A*, **537**, A125.

Johansen, A. et al. (2007). *Nature*, **448**, 1022–1025.

Johansen, A. & Lambrechts, M. (2017). *Annual Review of Earth and Planetary Sciences*, **45**, 359–387.

Johansen, A., Youdin, A., & Mac Low, M.-M. (2009b). *ApJ*, **704**, L75–L79.

Johansen, A., Youdin, A., & Mac Low, M.-M. (2009c). *ApJ*, **704**, L75–L79.

Johansen, A. et al. (2015). *Science Advances*, **1**, 1500109.

Johnson, B. M., Guan, X., & Gammie, C. F. (2008). *ApJS*, **179**, 553–555.

Johnson, J. A. et al. (2010). *PASP*, **122**, 905.

Kama, M. et al. (2020). *A&A*, **634**, A88.

Kataoka, A. et al. (2013). *A&A*, **557**, L4.

Kavelaars, J. J. et al. (2021). *ApJ*, **920**, L28.

Keppler, M. et al. (2018). *A&A*, **617**, A44.

Kim, C.-G. & Ostriker, E. C. (2017). *ApJ*, **846**, 133.

Kokubo, E. & Ida, S. (1996). *Icarus*, **123**, 180–191.

Koyama, H. & Ostriker, E. C. (2009). *ApJ*, **693**, 1316–1345.

Krapp, L. et al. (2019). *ApJ*, **878**, L30.

Lada, C. J. & Wilking, B. A. (1984). *ApJ*, **287**, 610–621.

Lada, C. J. (1987). In: *Star Forming Regions*. Ed. by M. Peimbert & J. Jugaku. Vol. 115, 1.

Leya, I. et al. (2008). *Earth and Planetary Science Letters*, **266**, 233–244.

Li, R. & Youdin, A. N. (2021). *ApJ*, **919**, 107.

Li, R., Youdin, A. N., & Simon, J. B. (2018). *ApJ*, **862**, 14.

Li, R., Youdin, A. N., & Simon, J. B. (2019). *ApJ*, **885**, 69.

Lichtenberg, T. et al. (2018). *Icarus*, **302**, 27–43.

Lichtenberg, T. et al. (2021). *Science*, **371**, 365–370.

Lin, D. N. C. & Papaloizou, J. (1986). *ApJ*, **309**, 846.

Lin, M.-K. (2021). *ApJ*, **907**, 64.

Lin, M.-K. & Hsu, C.-Y. (2022). *ApJ*, **926**, 14.

Liu, B., Ormel, C. W., & Johansen, A. (2019). *A&A*, **624**, A114.

Lodders, K. (2003). *ApJ*, **591**, 1220–1247.

Long, F. et al. (2017). *ApJ*, **844**, 99.

Lynden-Bell, D. & Pringle, J. E. (1974). *MNRAS*, **168**, 603–637.

Lyra, W. et al. (2008). *A&A*, **491**, L41–L44.

Lyra, W. & Umurhan, O. M. (2019). *PASP*, **131**, 072001.

Macías, E. et al. (2019). *ApJ*, **881**, 159.

Manara, C. F. et al. (2022) , arXiv:2203.09930.

Marohnic, J. C. et al. (2021). *Icarus*, **356**, 113824.

Masset, F. (2000). *A&AS*, **141**, 165–173.

Mathis, J. S., Rumpl, W., & Nordsieck, K. H. (1977). *ApJ*, **217**, 425–433.

Maucó, K. et al. (2021). *ApJ*, **923**, 128.

Mayer, L. et al. (2004). *ApJ*, **609**, 1045–1064.

Mayor, M. & Queloz, D. (1995). *Nature*, **378**, 355–359.

McKinnon, W. B. et al. (2020). *Science*, **367**, aay6620.

McNally, C. P., Lovascio, F., & Paardekooper, S.-J. (2021). *MNRAS*, **502**, 1469–1486.

Moore, G. S. M. & Rose, H. E. (1973). *Nature*, **242**, 187.

Morbidelli, A. et al. (2009). *Icarus*, **204**, 558–573.

Müller, A. et al. (2018). *A&A*, **617**, L2.

Muto, T. et al. (2012). *ApJ*, **748**, L22.

Nakagawa, Y., Sekiya, M., & Hayashi, C. (1986). *Icarus*, **67**, 375–390.

Nesvorný, D. et al. (2019). *Nature Astronomy*, **3**, 808–812.

Nesvorný, D. et al. (2021). *PSJ*, **2**, 27.

Okuzumi, S. et al. (2016). *ApJ*, **821**, 82.

Owen, J. E. & Wu, Y. (2017). *ApJ*, **847**, 29.

Paardekooper, S. .-., Baruteau, C., & Kley, W. (2011). *MNRAS*, **410**, 293–303.

Paardekooper, S.-J., McNally, C. P., & Lovascio, F. (2020). *MNRAS*, **499**, 4223–4238.

Paardekooper, S.-J., McNally, C. P., & Lovascio, F. (2021). *MNRAS*, **502**, 1579–1595.

Paardekooper, S.-J. et al. (2022) , arXiv:2203.09595.

Pan, L. & Yu, C. (2020). *ApJ*, **898**, 7.

Pascucci, I. et al. (2022) , arXiv:2203.10068.

Pérez, L. M. et al. (2016). *Science*, **353**, 1519–1521.

Pérez, S., Casassus, S., & Benítez-Llambay, P. (2018). *MNRAS*, **480**, L12–L17.

Perri, F. & Cameron, A. G. W. (1974). *Icarus*, **22**, 416–425.

Pineda, J. E. et al. (2022) , arXiv:2205.03935.

Pinilla, P. et al. (2016). *A&A*, **585**, A35.

Pinte, C. et al. (2016). *ApJ*, **816**, 25.

Pinte, C. et al. (2018). *ApJ*, **860**, L13.

Pollack, J. B. et al. (1996). *Icarus*, **124**, 62–85.

Price, D. J. et al. (2018). *Publ. Astron. Soc. Australia*, **35**, e031.

Raymond, S. N., Quinn, T., & Lunine, J. I. (2006). *Icarus*, **183**, 265–282.

Ribas, Á. et al. (2014). *A&A*, **561**, A54.

Rice, W. K. M. et al. (2003). *MNRAS*, **346**, L36–L40.

Riols, A. & Lesur, G. (2018). *A&A*, **617**, A117.

Robbins, S. J. & Singer, K. N. (2021). *PSJ*, **2**, 192.

Robbins, S. J. et al. (2017). *Icarus*, **287**, 187–206.

Rogers, P. D. & Wadsley, J. (2011). *MNRAS*, **414**, 913–929.

Rucska, J. J. & Wadsley, J. W. (2021). *MNRAS*, **500**, 520–530.

Rucska, J. J. (2018). Numerical Investigations of the Early Stages of Planet Formation. Master's thesis. McMaster University.

Scardoni, C. E., Booth, R. A., & Clarke, C. J. (2021). *MNRAS*, **504**, 1495–1510.

Schäfer, U., Yang, C.-C., & Johansen, A. (2017). *A&A*, **597**, A69.

Schaffer, N., Johansen, A., & Lambrechts, M. (2021). *A&A*, **653**, A14.

Schaffer, N., Yang, C.-C., & Johansen, A. (2018). *A&A*, **618**, A75.

Schreiber, A. & Klahr, H. (2018). *ApJ*, **861**, 47.

Schwamb, M. E. et al. (2019). *ApJS*, **243**, 12.

Shakura, N. I. & Sunyaev, R. A. (1973). *A&A*, **24**, 337–355.

Shankman, C. et al. (2016). *AJ*, **151**, 31.

Simon, J. B., Beckwith, K., & Armitage, P. J. (2012). *MNRAS*, **422**, 2685–2700.

Simon, J. B., Hawley, J. F., & Beckwith, K. (2011). *ApJ*, **730**, 94.

Simon, J. B. et al. (2013). *ApJ*, **775**, 73.

Simon, J. B. et al. (2015). *MNRAS*, **454**, 1117–1131.

Simon, J. B. et al. (2016). *ApJ*, **822**, 55.

Simon, J. B. et al. (2017). *ApJ*, **847**, L12.

Singer, K. N. et al. (2019). *Science*, **363**, 955–959.

Smith, N. et al. (2005). *AJ*, **129**, 382–392.

Speedie, J., Booth, R. A., & Dong, R. (2022a). *ApJ*, **930**, 40.

Speedie, J. et al. (2022b). *MNRAS*, **510**, 6059–6084.

Squire, J. & Hopkins, P. F. (2018). *MNRAS*, **477**, 5011–5040.

Squire, J. & Hopkins, P. F. (2020). *MNRAS*, **498**, 1239–1251.

Stadel, J. G. (2001). Cosmological N-body simulations and their analysis. PhD thesis. University of Washington.

Stammler, S. M. et al. (2019). *ApJ*, **884**, L5.

Stone, J. M. & Gardiner, T. (2009). *New Astron.*, **14**, 139–148.

Stone, J. M. & Gardiner, T. A. (2010). *ApJS*, **189**, 142–155.

Stone, J. M. et al. (2008). *ApJS*, **178**, 137–177.

Tanaka, H., Takeuchi, T., & Ward, W. R. (2002). *ApJ*, **565**, 1257–1274.

Teague, R., Bae, J., & Bergin, E. A. (2019). *Nature*, **574**, 378–381.

Teague, R. et al. (2018a). *ApJ*, **860**, L12.

Teague, R. et al. (2018b). *ApJ*, **864**, 133.

Tominaga, R. T., Inutsuka, S.-i., & Takahashi, S. Z. (2018). *PASJ*, **70**, 3.

Tominaga, R. T., Takahashi, S. Z., & Inutsuka, S.-i. (2020). *ApJ*, **900**, 182.

Toomre, A. (1964). *ApJ*, **139**, 1217–1238.

Trapman, L. et al. (2020). *A&A*, **640**, A5.

Turner, N. J. & Drake, J. F. (2009). *ApJ*, **703**, 2152–2159.

Umurhan, O. M., Estrada, P. R., & Cuzzi, J. N. (2020). *ApJ*, **895**, 4.

van der Marel, N. et al. (2015). *ApJ*, **810**, L7.

van der Marel, N. & Mulders, G. D. (2021). *AJ*, **162**, 28.

van der Marel, N. et al. (2013). *Science*, **340**, 1199–1202.

van der Marel, N. et al. (2021). *AJ*, **161**, 33.

Virtanen, P. et al. (2020). *Nature Methods*, **17**, 261–272.

Wadsley, J. W., Keller, B. W., & Quinn, T. R. (2017). *MNRAS*, **471**, 2357–2369.

Wallace, S. C. & Quinn, T. R. (2019). *MNRAS*, **489**, 2159–2176.

Walsh, K. J. (2018). *ARA&A*, **56**, 593–624.

Warren, P. H. (2011). *Earth and Planetary Science Letters*, **311**, 93–100.

Weidenschilling, S. J. (1977a). *MNRAS*, **180**, 57–70.

Weidenschilling, S. J. (1977b). *Ap&SS*, **51**, 153–158.

Weidenschilling, S. J. (2011). *Icarus*, **214**, 671–684.

Wetherill, G. W. & Stewart, G. R. (1989). *Icarus*, **77**, 330–357.

Whipple, F. L. (1972). In: *From Plasma to Planet.* Ed. by A. Elvius, 211.

Williams, J. P. & Cieza, L. A. (2011). *ARA&A*, **49**, 67–117.

Windmark, F. et al. (2012). *A&A*, **540**, A73.

Xu, Z. & Bai, X.-N. (2022a). *ApJ*, **924**, 3.

Xu, Z. & Bai, X.-N. (2022b) , arXiv:2207.08858.

Yang, C.-C. & Johansen, A. (2014). *ApJ*, **792**, 86.

Yang, C.-C. & Johansen, A. (2016). *ApJS*, **224**, 39.

Yang, C.-C., Johansen, A., & Carrera, D. (2017). *A&A*, **606**, A80.

Yang, C.-C. & Zhu, Z. (2020). *MNRAS*, **491**, 4702–4718.

Yang, C.-C. & Zhu, Z. (2021). *MNRAS*, **508**, 5538–5553.

Youdin, A. & Goodman, J. (2005). *ApJ*, **620**, 459–469.

Youdin, A. & Johansen, A. (2007). *ApJ*, **662**, 613–626.

Youdin, A. N. (2011). *ApJ*, **731**, 99.

Youdin, A. N. & Lithwick, Y. (2007). *Icarus*, **192**, 588–604.

Zeng, L. et al. (2019). *Proceedings of the National Academy of Science*, **116**, 9723–9728.

Zhang, K., Blake, G. A., & Bergin, E. A. (2015). *ApJ*, **806**, L7.

Zhu, Z. & Yang, C.-C. (2021). *MNRAS*, **501**, 467–482.

Zsom, A. et al. (2010). *A&A*, **513**, A57.